Physics Reports 1075 (2024) 1–137

Contents lists available at ScienceDirect

Physics Reports

journal homepage: www.elsevier.com/locate/physrep

Topology in soft and biological matter

Luca Tubiana [1,2,*], Gareth P. Alexander [3], Agnese Barbensi [4], Dorothy Buck [5], Julyan H.E. Cartwright [6,7], Mateusz Chwastyk [8], Marek Cieplak [8], Ivan Coluzza [9], Simon Čopar [10], David J. Craik [11], Marco Di Stefano [12], Ralf Everaers [13], Patrícia F.N. Faísca [14,15], Franco Ferrari [16], Achille Giacometti [17,18], Dimos Goundaroulis [19,20], Ellinor Haglund [21], Ya-Ming Hou [22], Nevena Ilieva [23], Sophie E. Jackson [24], Aleksandre Japaridze [25], Noam Kaplan [26], Alexander R. Klotz [27], Hongbin Li [28], Christos N. Likos [29], Emanuele Locatelli [29,30,31], Teresa López-León [32], Thomas Machon [33], Cristian Micheletti [34], Davide Michieletto [35,36], Antti Niemi [37,38], Wanda Niemyska [39], Szymon Niewieczerzal [40], Francesco Nitti [41], Enzo Orlandini [30,31], Samuela Pasquali [43], Agata P. Perlinska [40], Rudolf Podgornik [44,45,46], Raffaello Potestio [1,2], Nicola M. Pugno [47,48], Miha Ravnik [10,49], Renzo Ricca [50,51], Christian M. Rohwer [52,53], Angelo Rosa [34], Jan Smrek [29], Anton Souslov [54], Andrzej Stasiak [55,56], Danièle Steer [41,42], Joanna Sułkowska [40], Piotr Sułkowski [57], De Witt L. Sumners [58], Carsten Svaneborg [59], Piotr Szymczak [57], Thomas Tarenzi [60], Rui Travasso [61], Peter Virnau [62], Dimitris Vlassopoulos [63,64], Primož Ziherl [10,49], Slobodan Žumer [10,49]

[1] *Physics Department, University of Trento, via Sommarive 14, I-38123, Trento, Italy*
[2] *INFN-TIFPA, Trento Institute for Fundamental Physics and Applications, I-38123 Trento, Italy*
[3] *Department of Physics and Centre for Complexity Science, University of Warwick, Coventry CV4 7AL, United Kingdom*
[4] *School of Mathematics and Physics, University of Queensland, St Lucia, QLD 4067, Australia*
[5] *Department of Mathematics & Department of Biology, Duke University, 120 Science Dr, Durham, NC 27710, USA*
[6] *Instituto Carlos I de Física Teórica y Computacional, Universidad de Granada, 18071 Granada, Spain*
[7] *Instituto Andaluz de Ciencias de la Tierra, CSIC-Universidad de Granada, 18100 Armilla, Granada, Spain*
[8] *Institute of Physics, Polish Academy of Sciences, al. Lotnikow 32/46, 02-668 Warsaw, Poland*
[9] *Center for Theoretical Biological Physics, Rice University, 77005, Houston, TX, United States*
[10] *Faculty of Mathematics and Physics, University of Ljubljana, Jadranska 19, SI-1000, Ljubljana, Slovenia*
[11] *Institute for Molecular Bioscience, Australian Research Council Centre of Excellence for Innovations in Peptide and Protein Science, The University of Queensland, Brisbane Queensland 4072, Australia*
[12] *Institute of Human Genetics, Université de Montpellier, CNRS, Laboratoire de Chromatine et Biologie Cellulaire, 34094 Montpellier, France*
[13] *École Normale Supérieure (ENS) de Lyon, CNRS, Laboratoire de Physique and Centre Blaise Pascal de l'ENS de Lyon, F-69342 Lyon, France*
[14] *BioISI – Instituto de Biossistemas e Ciências Integrativas & Departamento de Física, Faculdade de Ciências, Campo Grande, C8 bdg, Lisboa 1749-016, Portugal*
[15] *Department of Physics, Faculty of Sciences, University of Lisbon, Lisbon 1749-016, Portugal*
[16] *Centre for Advanced Studies in Astrobiology and Related Topics and Institute of Physics, University of Szczecin, Wielkopolska 15, 70-451 Szczecin, Poland*
[17] *Department of Molecular Sciences and Nanosystems, Ca' Foscari University of Venice, Via Torino 155, 30172, Venice, Italy*
[18] *European Centre for Living Technology (ECLT) Ca' Bottacin, 3911 Dorsoduro Calle Crosera, 30123, Venice, Italy*

* Corresponding author at: Physics Department, University of Trento, via Sommarive 14, I-38123, Trento, Italy.
E-mail address: luca.tubiana@unitn.it (L. Tubiana).

https://doi.org/10.1016/j.physrep.2024.04.002

[19] Department of Molecular and Human Genetics, Baylor College of Medicine, 1 Baylor Plaza, Houston, TX 77030, USA
[20] Center for Theoretical and Biological Physics, Rice University, 6100 Main Str, Houston, TX 77005, USA
[21] University of Hawaii at Manoa, Department of Chemistry, 2545 McCarthy Mall, Honolulu, HI 96822-2275, USA
[22] Department of Biochemistry and Molecular Biology, Thomas Jefferson University, Philadelphia, PA 19107, USA
[23] Institute of Information and Communication Technologies, Bulgarian Academy of Sciences, 25A, Acad. G. Bonchev Str., Sofia, 1113, Bulgaria
[24] Yusuf Hamied Department of Chemistry, Lensfield Road, Cambridge CB2 1EW, UK
[25] Department of Bionanoscience, Kavli Institute of Nanoscience Delft, Delft University of Technology, Van der Maasweg 9, 2629 HZ Delft, The Netherlands
[26] Department of Physiology, Biophysics & Systems Biology, Rappaport Faculty of Medicine, Technion Israel Institute of Technology, 1 Efron St., Haifa, Israel
[27] California State University, Long Beach, 1250 Bellflower Blvd, Long Beach, CA, 90840, USA
[28] Department of Chemistry, University of British Columbia, Vancouver, BC V6T 1Z1, Canada
[29] Faculty of Physics, University of Vienna, Boltzmanngasse 5, 1090 Vienna, Austria
[30] Department of Physics and Astronomy, University of Padova, Via Marzolo, 8 - 35131 Padova, Italy
[31] INFN, Sezione di Padova, Via Marzolo 8, 35131 Padova, Italy
[32] UMR CNRS 7083 Gulliver, École Supérieure de Physique et de Chimie Industrielles de la Ville de Paris, PSL Research University, 75005 Paris, France
[33] HH Wills Physics Laboratory, University of Bristol, Tyndall Avenue, BS81TL Bristol, UK
[34] Scuola Internazionale Superiore di Studi Avanzati (SISSA), via Bonomea 265, 34136 Trieste, Italy
[35] School of Physics and Astronomy, University of Edinburgh, Peter Guthrie Tait Road, Edinburgh, EH9 3FD, UK
[36] MRC Human Genetics Unit, Institute of Genetics and Cancer, University of Edinburgh, Edinburgh EH4 2XU, UK
[37] NORDITA, Stockholm University & Uppsala University, Sweden
[38] School of Physics, Beijing Institute of Technology, Beijing, People's Republic of China
[39] Institute of Informatics, University of Warsaw, 02-097 Warsaw, Banacha 2, Poland
[40] Centre of New Technologies, University of Warsaw, Banacha 2c, 02-097, Warsaw, Poland
[41] Université Paris Cité, CNRS, Astroparticule et Cosmologie, F-75013 Paris, France
[42] Laboratoire de Physique de l'École Normale Supérieure, ENS, CNRS, Université PSL, Sorbonne Université, Université Paris Cité, 75005, Paris, France
[43] Université Paris Cité, Laboratoire Biologie Fonctionelle et Adaptative, CNRS UMR 8251, INSERM ERL U1133, 35 rue Hélène Brion, 75013 Paris, France
[44] Wenzhou Institute, University of Chinese Academy of Sciences Wenzhou, Zhejiang 325001, People's Republic of China
[45] School of Physical Sciences and Kavli Institute for Theoretical Sciences, University of Chinese Academy of Sciences, Beijing 100049, People's Republic of China
[46] Beijing National Laboratory for Condensed Matter Physics and Laboratory of Soft Matter Physics, Institute of Physics, Chinese Academy of Sciences Beijing 100190, People's Republic of China
[47] Laboratory for Bioinspired, Bionic, Nano, Meta Materials & Mechanics, Department of Civil, Environmental and Mechanical Engineering, University of Trento, Via Mesiano 77, 38123 Trento, Italy
[48] School of Engineering and Materials Science, Queen Mary University of London, Mile End Road, London E1 4NS, UK
[49] Jožef Stefan Institute, Jamova ulica 39, SI-1000, Ljubljana, Slovenia
[50] Department of Mathematics and Applications, University of Milano-Bicocca, via Cozzi 55, 20125 Milano, Italy
[51] Faculty of Science, Beijing University of Technology, 100 Pingleyuan, Beijing 100124, People's Republic of China
[52] Department of Mathematics and Applied Mathematics, University of Cape Town, 7701 Rondebosch, Cape Town, South Africa
[53] Max Planck Institute for Intelligent Systems, Heisenbergstr. 3, 70569 Stuttgart, Germany
[54] T.C.M. Group, Cavendish Laboratory, University of Cambridge, Cambridge, CB3 0HE, UK
[55] Center for Integrative Genomics, University of Lausanne, Lausanne, Switzerland
[56] SIB Swiss Institute of Bioinformatics, Lausanne, Switzerland
[57] Institute of Theoretical Physics, Faculty of Physics, University of Warsaw, Pasteura 5, 02-093 Warsaw, Poland
[58] Department of Mathematics, Florida State University, 1017 Academic Way, Tallahassee, FL 32306-4510, USA
[59] Department of Physics, Chemistry and Pharmacy, SDU, University of Southern Denmark, Campusvej 55, DK-5230, Odense M, Denmark
[60] School of Chemistry, University of Birmingham, Birmingham B15 2TT, United Kingdom
[61] CFisUC (Centre for Physics of the University of Coimbra), Department of Physics, University of Coimbra, Rua Larga, 3004-516 Coimbra, Portugal
[62] Institute of Physics, Johannes Gutenberg-Universität Mainz, Staudingerweg 9, Mainz 55128, Germany
[63] Institute of Electronic Structure and Laser, Foundation for Research and Technology – Hellas (FORTH), GR-70013, Crete, Greece
[64] Department of Materials Science and Technology, University of Crete, GR-70003, Crete, Greece

ARTICLE INFO

Article history:
Received 15 April 2022
Received in revised form 16 January 2024
Accepted 1 April 2024
Available online xxxx
Editor: Henri Orland

Keywords:
Topology in soft condensed matter
Polymers and polymer melts
Topology in living matter — protein folding
Entangled proteins

ABSTRACT

The last years have witnessed remarkable advances in our understanding of the emergence and consequences of topological constraints in biological and soft matter. Examples are abundant in relation to (bio)polymeric systems and range from the characterization of knots in single polymers and proteins to that of whole chromosomes and polymer melts. At the same time, considerable advances have been made in the description of the interplay between topological and physical properties in complex fluids, with the development of techniques that now allow researchers to control the formation of and interaction between defects in diverse classes of liquid crystals. Thanks to technological progress and the integration of experiments with increasingly sophisticated numerical simulations, topological biological and soft matter is a vibrant area of research attracting scientists from a broad range of disciplines. However, owing

DNA topology & genome organization
Topologically complex fluids

to the high degree of specialization of modern science, many results have remained confined to their own particular fields, with different jargon making it difficult for researchers to share ideas and work together towards a comprehensive view of the diverse phenomena at play. Compelled by these motivations, here we present a comprehensive overview of topological effects in systems ranging from DNA and genome organization to entangled proteins, polymeric materials, liquid crystals, and theoretical physics, with the intention of reducing the barriers between different fields of soft matter and biophysics. Particular care has been taken in providing a coherent formal introduction to the topological properties of polymers and of continuum materials and in highlighting the underlying common aspects concerning the emergence, characterization, and effects of topological objects in different systems. The second half of the review is dedicated to the presentation of the latest results in selected problems, specifically, the effects of topological constraints on the viscoelastic properties of polymeric materials; their relation with genome organization; a discussion on the emergence and possible effects of knots and other entanglements in proteins; the emergence and effects of topological defects and solitons in complex fluids.

This review is dedicated to the memory of Marek Cieplak.

Contents

1. Introduction

Most of the materials we interact with in our daily life, like plastics, biological tissues, food, and living matter, do not behave as simple liquids or crystalline solids. Instead, they show properties usually associated with both, like the ability to maintain a shape at rest while flowing when a stress is applied for a sufficiently long time. These materials are collectively called soft matter.

At the microscopic level, soft matter is composed of complex, structurally diverse molecules, held together by weak intermolecular forces. These molecules have sizes in the range of a few nm up to several μm (even cm in the case of chromosomes), are subject to thermal motion, and their geometrical conformation and relative arrangements can be reshaped by energies of the order of $\sim k_B T$. The characteristics and behaviour of soft materials are thus dictated by a complex interplay of energy and entropy, leading to a high degree of geometrical variability.

In general, the exact chemical details of the constituent molecules can be ignored when modelling soft matter, leading to theories that highlight universal behaviours. For example, several properties of linear polymeric systems can be described considering just the length of the polymers, their self-attraction or self-repulsion, and their concentration. In the same way, the properties of a liquid crystal (LC) are dictated by the orientational arrangement of its constituents, which can be described as a vector field, regardless of their nature, from single elongated molecules, living matter such as viruses and bacteria, to micron-scale colloidal particles. Often, even the precise geometric conformation of the constituents can be ignored, for example as they are disrupted by thermal motions or external fields. In these cases, the behaviour of the material can be characterized through its *topological properties*.

Topology investigates those properties of an object that do not depend on its specific geometrical shape and are unaffected by changes that do not alter its integrity. To visualize these seemingly abstract properties, consider a knitted scarf. It can be stretched, compressed, and twisted, so as to assume a multitude of different shapes. Yet, as long as we do not affect its integrity by cutting the yarn, the topological properties of the scarf, like the number and the arrangement of the stitches, do not change. Furthermore, different types of stitches give different characteristics to the textile: e.g., more or less elasticity, robustness, or a preferred twist. This simple example highlights some fundamental aspects of topological features: they are defined on a whole object, i.e., they are global properties, they are invariant under continuous deformations of this object and independent of scale, and they affect its physical behaviour. Topology allows us to define a discrete set of equivalence classes, identified by *topological invariants*, over the continuum of geometrical conformations of a soft object. A fixed topological class, or topological constraint, reduces the number of available conformations and consequently influences the physical properties of a system.

Topological constraints appear often in soft matter from the micro- to the macro-scale. For example, polymers can form knots and links, which affect their behaviour, and the viscoelastic properties of a melt of polymers change drastically when the polymers are circularized into rings, independently of their exact conformation. In liquid crystals, topological properties can emerge both as singularities or as solitons in the field of orientation of their constituent molecules and affect the optical properties of the material.

Topological constraints are also found in biological matter, often with profound consequences. For example, knots and links can appear both in proteins and in DNA filaments; their emergence and properties can impact biological processes and are studied to improve the physical models of these biopolymers. The fact that double-stranded DNA (dsDNA) is formed of two intertwined and linked chains is actively exploited by cells to regulate their access to genetic information. At larger scales, the appearance of chromosome domains in the human genome can be explained by the fact that, during the lifetime of a cell, chromosomes do not equilibrate and thus behave as if they were unconcatenated rings. At a whole-cell level, only the directional, anisotropic nature of the material can be considered, and topological defects in active LC play a key role in many biological self-assembly processes, such as mitotic spindle assembly.

Interest in topological soft materials is also related to the possibility of using topological constraints to design materials with controllable physical properties. In this respect, recent years have seen significant advances in our ability to manipulate and synthesize complex molecules and to apply our knowledge of topological constraints to the development both of advanced single-molecule apparatuses and of novel materials with remarkable physical properties. For example, soft materials made of linked rings, such as kinetoplast DNA (kDNA), have captured the attention of researchers for their exceptional elastic properties. In LC much research has focused on the controlled assembly of knotted and linked disclination lines stabilized by colloidal particles or boundary conditions, and research on blue phases has opened the possibility of making novel displays with better response time than existing LCDs.

More importantly, in terms of physics, topology can provide a general framework for the characterization of soft materials, offering connections between very different systems. A prominent example is the famous Călugăreanu–White theorem, which relates the *linking number* of two closed curves, a topological invariant, to their local and global geometric properties. This theorem and its generalizations have been applied to dsDNA rings, linked proteins, LC, and even vortices in fluids. More generally, topology offers distinct possibilities to researchers in soft and biological matter, independent of the particular system under consideration. First, one can assay the topological properties of a material, for example the frequency with which knots appear in some polymeric system, to characterize its physical properties. The emergence of different topological classes can also be used to test physical models. Secondly, one can consider the case in which a topological class has been fixed, limiting the geometrical conformations accessible to the system, and study its effects on the system's properties. Thirdly, the ability to control the topology of a system can be used to tune its physical properties. Finally, the emergence and control of topological constraints is a fundamental problem in living systems, particularly in DNA, and their study can offer insight into their biological functions.

Due to advances in experimental techniques and computational capabilities, the last two decades have seen a substantial increase in the number of studies dedicated to topology in soft and biological matter. However, the high specialization of modern science means that most research is divided into different sub-fields, each with its own jargon, making it difficult for researchers to share ideas and obtain a comprehensive view of the different phenomena at play, despite their underlying similarities. This review aims to soften this problem and to favour cross-pollination between different communities by presenting an overview of different sub-fields while highlighting their common aspects. In writing it, we took particular care not only to present a selection of relevant problems in different sub-fields but, moreover, to introduce the fundamental mathematical concepts in an accessible yet sufficiently complete fashion and to highlight the common aspects underlying the emergence and effects of different topological objects across soft and biological matter systems.

The review is aimed in particular at physicists working in soft matter and biophysics as well as mathematicians interested in knowing the latest applications of topology to a wide range of physical systems. In this respect, the number of authors and the range of their scientific activities allowed us to present and connect results from different communities that often appear in different specialized journals, while fruitful discussions between authors from different sub-fields allowed us to distill a broad yet coherent presentation.

The material is organized to help the reader navigate the transdisciplinary subject of topological soft matter with its different sub-fields, and to present the specialist with the latest developments in selected topics. The main topological objects appearing in polymeric and continuum systems, such as knots, links, defects, and solitons, are formally introduced in Section 2. Here, we also discuss recent developments in mathematics that aim to go beyond the limits of the current models and adapt them to recent developments in physics. Section 2 can be used both as a reference while reading the rest of the review and as a primer in knot theory and topological properties of fields for physicists. Section 3 provides an overview of where and how these topological objects arise in different soft and bio-materials and what their consequences are. These two sections constitute the core of the review and aim to present selected examples from different sub-fields in an introductory way, referring the interested reader to the more specialized reviews that are referenced throughout the text. The rest of this review, Sections 4 to 7, provides focused deep-dive presentations of specialized topics that constituted the core scientific interests of the European Topology Interdisciplinary Action (EUTOPIA) COST Action, a collaborative European research network. Section 4 covers the rheological effects of topological constraints in polymer melts; Section 5 focuses on the role of topology in shaping the organization of the genome; Section 6 discusses the current understanding of the role of knots and other topological entanglements in proteins; and Section 7 offers a detailed overview of the latest advancements in the topological properties of complex fluids. Throughout the review, we have taken care to present experimental results first, complemented by computational and theoretical ones.

2. Mathematical introduction

2.1. Topology in soft materials: basic knot theory, field defects and solitons

In this section, we introduce the mathematical concepts that will be used in the rest of the review. We start by describing more intuitive topological objects, like knots and links. We then present the topological aspects of field theories, which provide a natural formalism to describe the behaviour of complex fluids, such as liquid crystals. Specifically, Section 2.2 introduces the mathematical concept of knots and links as non-intersecting closed curves, their tabulation, and their topological invariants, including in particular knot polynomials whose construction is briefly discussed. Section 2.3

introduces tangle calculus. Section 2.5 discusses the famous Călugăreanu–White theorem, using the Frenet frame description of curves introduced in Section 2.4. Sections 2.6 and 2.7 go beyond the standard mathematical definition of knots; the former by considering a class of self-intersecting curves, θ-curves, and the latter by relaxing the condition that knots are closed curves. Section 2.8 introduces the topology of field defects and of solitons, presenting the most relevant objects appearing in complex fluids such as liquid crystals. Section 2.8.2 introduces the concept of helicity, and offers a connection with the Călugăreanu–White theorem for curves. Finally, Section 2.9 discusses the path-integral formulation of polymers, and how knots and links might be introduced in it. This last subsection is more formal and intended for the advanced reader. The presentation is from a physicist's point of view. Whenever necessary, we refer the reader to the mathematical literature, where a rigorous treatment can be found.

2.2. Knots and links as mathematical objects

Knots and links are common objects in everyday life. We use a knot to tie our shoelaces and a chain to lock our bicycle. Knots have long been used to hold sutures, stop ropes from sliding, hold weights, as decoration, and even to store information, as in the case of quipus, Inca civilization devices in which records were stored as different knots on fibres [1]. Physical knots are defined by their characteristic weaving. For example, a bowline knot (Fig. 1**A**) remains a bowline knot no matter the thickness of the rope nor small deformations, as long as the termini of the rope do not slip out and unravel the knot.

The mathematical theory of knots is built by considering knots tied in infinitely thin, perfectly flexible closed rings. In this way, since there are no termini, a knot cannot be untied without cutting open the ring (Fig. 1**C,D**), and its type can be identified with an equivalence class of such objects. Specifically, a *knot* is defined as an embedding of the circle[1] S^1 into Euclidean space $\mathbb{R}^3$, and a *link* is defined as a disjoint collection of knots in $\mathbb{R}^3$. More informally, the images of such embeddings in $\mathbb{R}^3$ are also called knots and links. This convention allows us to state that two closed curves K_1 and K_2 represent the same knot, or are *equivalent*, if there exists a suitable transformation that maps the coordinates of one curve onto the other. Such a transformation is called an *ambient isotopy*, which intuitively is a continuous function that simultaneously transform a knot and the space around it. Formally, an ambient isotopy is a map $F : \mathbb{R}^3 \times [0, 1] \longrightarrow \mathbb{R}^3$, such that $F_t := F(-, t)$ is a *homeomorphism*[2] for every $t \in [0, 1]$ and with $F(K_1, 0) = K_1$ and $F(K_1, 1) = K_2$. The existence of an ambient isotopy F between two knots K_1 and K_2 is equivalent to having an *orientation preserving* homeomorphism of S^3 sending K_1 into K_2 [2].

Continuous isotopies can be quite ill-behaved, and might give rise to pathological behaviours, such as making a knot increasingly tighter until it disappears [2]. Physical knots, on the contrary, are limited by their support, be it a rope or a vector field. Physical knots cannot be bent past a certain curvature, and their size cannot be reduced indefinitely. For this reason, to avoid pathological behaviours, we will refer in the following only to knots which can be represented by polygonal closed curves, the so-called *tame knots*, and we will only consider piece-wise linear maps (isotopies and homeomorphisms) between them. An example of a piece-wise linear homeomorphism is given by triangular moves (Fig. 1**E**). For all purposes, the piece-wise linear segments in a knot can be considered small enough to closely approximate smooth curves. With this definition, *we can classify all equivalent knots as the same topological object*: a knot or link *type* is an equivalence class of closed curves in 3-dimensional space under a piece-wise linear homeomorphism or ambient isotopy.

Knot theory distinguishes and tabulates knot and link types up to this equivalent relation. Throughout this review, and as is customary in the literature, we will often drop the word *type* and use the terms knots and links to refer both to the topological types and to explicit embeddings. Within this framework an open curve cannot be knotted, as it is always possible to find a continuous transformation that brings it to a straight line; in other words, under ambient isotopy, all the piece-wise linear embeddings of an arc $[0, 1]$ are equivalent. We discuss three different ways of extending this approach to define knots in open curves in Section 2.7: *closure schemes*, in which a suitable closure of an open curve is used to circularize it (Section 2.7.1), *knotoids*, a topological equivalence class on projection of open curves based on an extension of the Reidemeister moves (Section 2.7.3), and *intrinsic entanglement measures*, which generalize polynomial invariants to open curves (Section 2.7.4).

2.2.1. Tabulating knots and links: knot diagrams

Knots may be analysed through their *diagrams*. Knot diagrams are regular[3] planar projections of three-dimensional curves, where undercrossings are depicted as interruptions and encode information on which strand is over- or under-passing (Fig. 2**A**). These two-dimensional diagrams are fundamental pictorial representations of knots and links, and they allow us not only to gain intuition about them, but also to prove their equivalence. To check whether two knots

[1] By *embedding* we mean a continuous map that is a *homeomorphism* onto its image, i.e., which is injective and with a continuous inverse defined on its image. This implies that knots have no self-intersections.

[2] A homeomorphism is a bijective, continuous map, whose inverse is also continuous.

[3] A projection is called regular if all the intersections are isolated, double crossing points, like the ones shown in Fig. 5**A**. For example, a diagram where a one strand runs on top of another so that they appear as only one line is not regular.

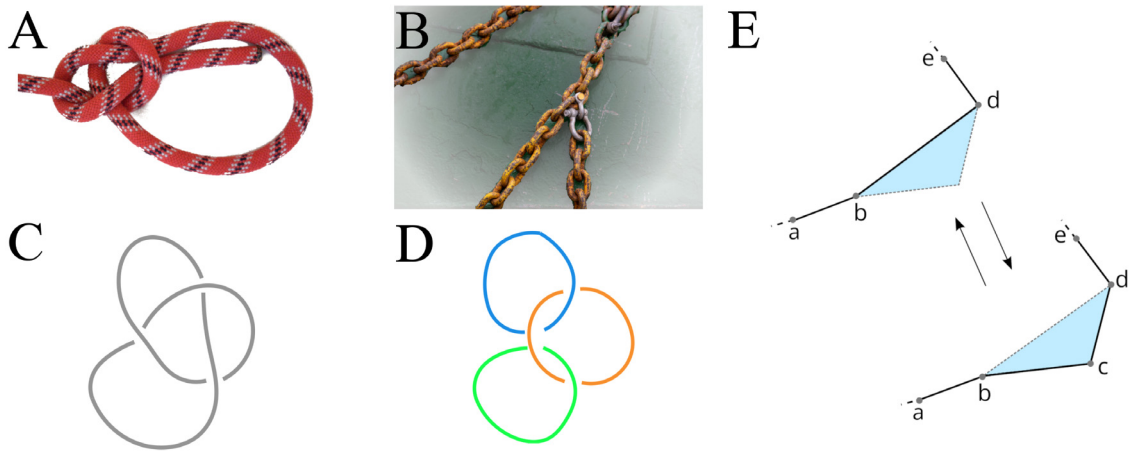

Fig. 1. **A** A physical bowline knot (source: Wikipedia). **B** Example of physical links in a chain **C** and **D** Mathematical knots and links defined on closed curves. **E** A homeomorphism between piecewise-linear curves is provided by triangular moves. These consist in either deleting or adding a vertex on the curve under the condition that no edges of the curve cross the triangle *bcd* identified by the deleted/added vertex, or (not shown) moving a vertex, e.g., vertex c, to a new position c' under the condition that no edges cross the triangles bcc' and dcc'.
Source: **B** adapted from: "Boat chain" by Henry Söderlund.

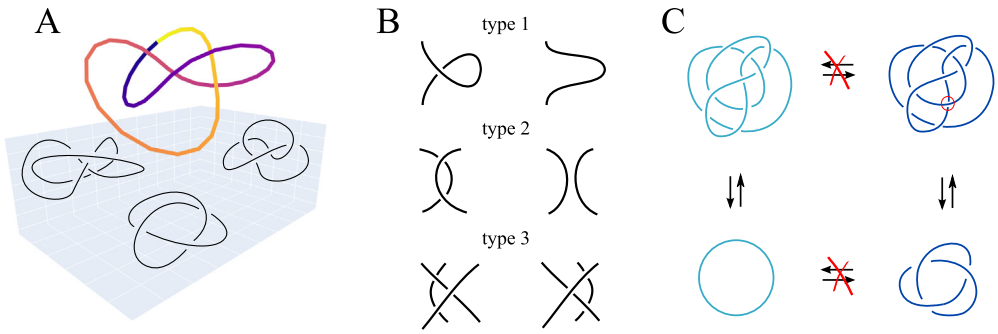

Fig. 2. **A** An embedding of the trefoil knot in $\mathbb{R}^3$, and the three knot diagrams obtained by taking projections on the *xy*, *yz* and *xz* planes. **B** Reidemeister moves. **C** The two diagrams on the left both represent an unknotted circle since they can be transformed one into the other through a sequence of Reidemeister moves. In the same way, both diagrams on the right represent a trefoil knot; the difference between the two top diagrams is highlighted by the circled crossing. No sequence of moves exists that can transform the diagrams on the left into the ones on the right.

are equivalent, one can analyse the corresponding knot diagrams, and a minimal set of local moves on them, called *Reidemeister moves* (Fig. 2**B**).

A fundamental result in knot theory states that the three Reidemeister moves modify a diagram without changing its topology, and that, together with isotopy of the plane,[4] they cover all possible topology-preserving diagram transformations. In other words, whenever one diagram can be transformed into another with a finite sequence of Reidemeister moves, they represent the same knot (Fig. 2**C**), and there is always a finite sequence of Reidemeister moves connecting any pair of diagrams of the same knot type. In particular, this allows removing all the crossings in a diagram representing the simplest case, the *unknot* (Fig. 3A) by a finite sequence of Reidemeister moves.

The ability to demonstrate whether two diagrams represent the same or different knots or links also allows one to represent knots in a standardized fashion [3]. A natural way of doing this is choosing a diagram with the lowest possible number of crossings, called the *minimum crossing number*, C. The minimal crossing number is used to tabulate knots and links from the simplest to the most complex. This organization leads to so-called *Rolfsen notation* in which each knot is assigned a label of the corresponding minimal crossing number and a subscript to distinguish knots having the same value of C. So the unknot is labelled 0_1, the trefoil 3_1, the figure of eight 4_1, the first two knots with 5 crossings are labelled 5_1 and 5_2, etc. The simplest knots and links, which are the object of most studies in soft and biological matter, are shown in Fig. 3**A–B**. Links are tabulated following a similar convention, with the addition of a superscript reporting the number of components.

[4] An isotopy of the plane is a homeomorphism of the plane preserving crossings in the diagram.

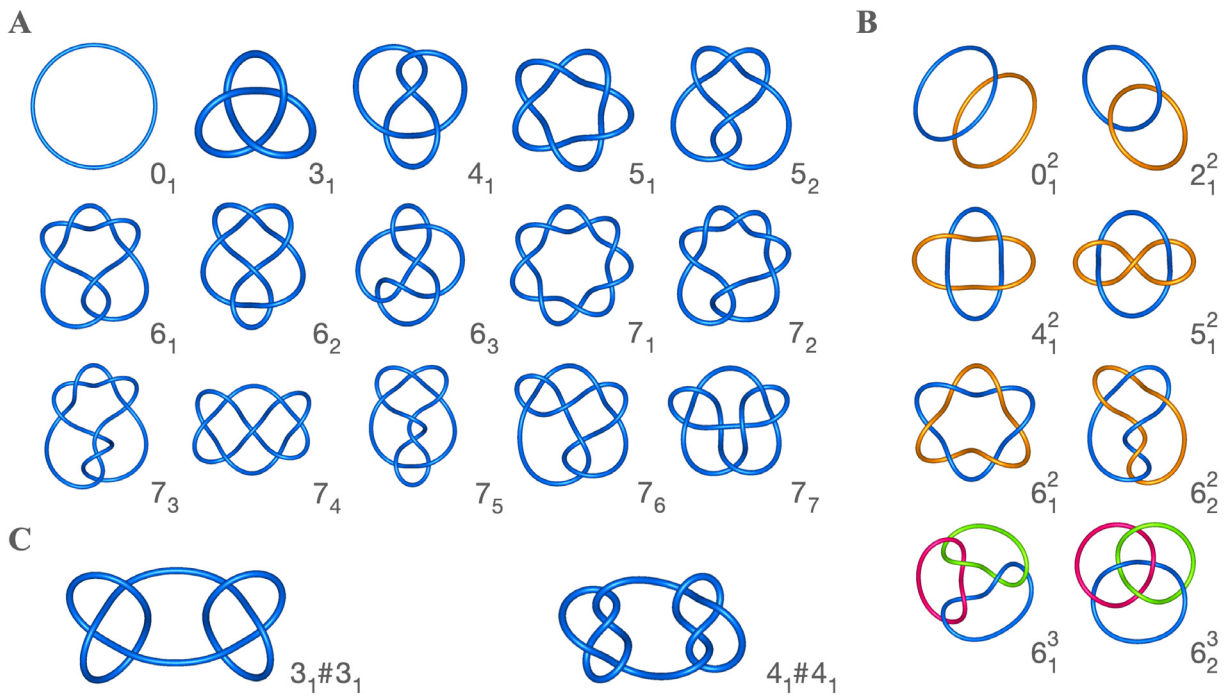

Fig. 3. **A** Prime knots up to 7 crossings. Among them the *unknot*, 0_1, the *trefoil knot*, 3_1, the *figure-of-eight knot*, 4_1, and the *stevedore's knot*, 6_1. **B** A few examples of links. Among them the *unlink* of two links, 0_1^2, the *Hopf link*, 2_1^2, and the *Borromean rings*, 6_2^3. The latter become unlinked upon removal of any of the three rings. **C** Two composite knots made up by the connected sum of 3_1 and 4_1 knots.

2.2.2. Knot families, prime and composite knots

Knots can be grouped into different families based on their properties. We can distinguish *prime knots* (Fig. 3**A**) and *composite knots* (Fig. 3**C**). The former are knots that cannot be decomposed into simpler knots. The latter are the mathematical equivalent of tying several knots on the same string and then joining its ends. As depicted in Fig. 3**C**, they can be obtained as the *connected sum* of two or more prime knots.

As will become clear in this review, two other important families of prime knots in biophysics and soft matter can be distinguished based on the way in which the knot is tied. The first is that of *torus knots*, including knots 3_1, 5_1, 7_1, and all knots that can be formed by winding a curve around a torus as illustrated in Fig. 4**A–B**. The second is that of *twist knots*, including 4_1, 5_2, 6_1, which can be tied by first twisting a ring in the middle and then clamping together its two extremities (Fig. 4**C–E**). 3_1 is both a torus and a twist knot. As we will see in Section 3.2.2, the relative abundance of torus and twist knots in a physical or biological system can be used to probe its properties.

2.2.3. Topological invariants

One of the main problems of knot theory is to understand whether two different knots are equivalent or not. This task is often achieved by defining and computing *topological invariants*, i.e., maps from the set of knots into mathematical objects, for example polynomials, taking the same value on different embeddings of the same knot type. Topological invariants are fundamental in knot theory, as they allow us to recognize knots and links independently of their specific geometric arrangement. Several such invariants have been defined; here we introduce those most commonly used in the soft-matter and biophysics literature.

A first, simple, example of a topological invariant is given by the minimum crossing number C of a knot defined in Section 2.2.1. C is by definition independent of the choice of a knot diagram, and thus of the specific geometrical configuration assumed by the knot. Note, however, that C is a weak invariant: while there is only one knot with $C = 3$ and one with $C = 4$, the number of knots having the same value of C grows exponentially with it (Fig. 3**A**). As of 2023, 352 152 252 distinct prime knots with up to 19 crossings have been tabulated [4] .

Another simple, yet fundamental, invariant is the *unknotting number*, i.e., the minimum number of crossings, among all the possible diagrams representing a knot, that need to be swapped, exchanging the over-passing and under-passing strands, in order to reduce a knot diagram to a diagram of the unknot 0_1. This notion is useful when discussing the effect of enzymes that modify the topology of DNA, as we discuss in Section 3.3.7. Using the knot diagrams reported in Fig. 3**A**, one can verify that the 3_1, 4_1, 5_2, and 6_1 knots have unknotting number 1, while 5_1 and 6_3 have unknotting number 2. One can see by looking at Fig. 4**E** that all twist knots have unknotting number one.

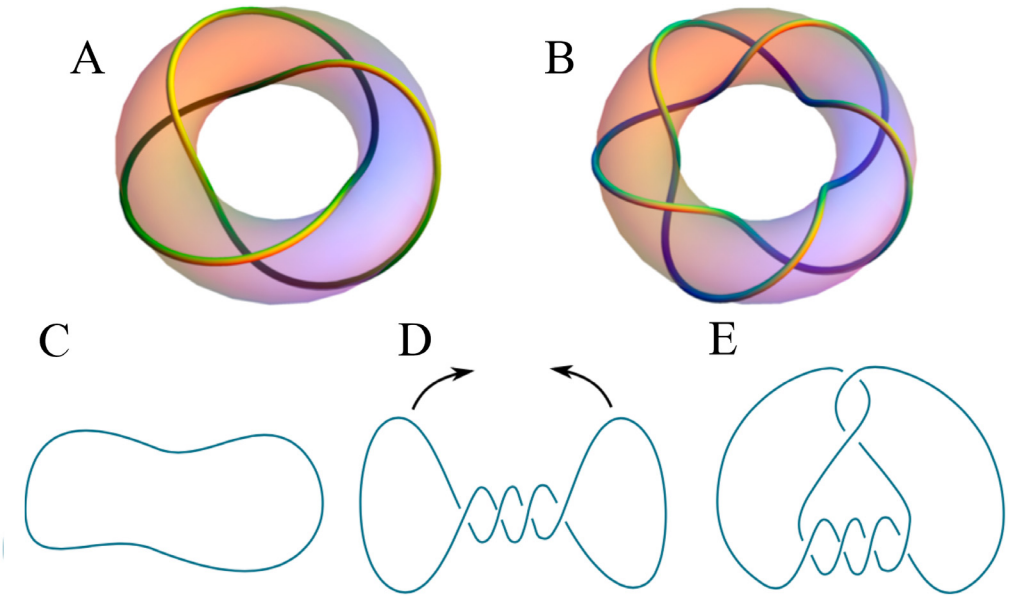

Fig. 4. A–B 3_1 and 5_1 knots are examples of torus knots. **C–E** Twist knots can be formed by taking a circle, twisting it, keeping two loops, and clamping the loops together.

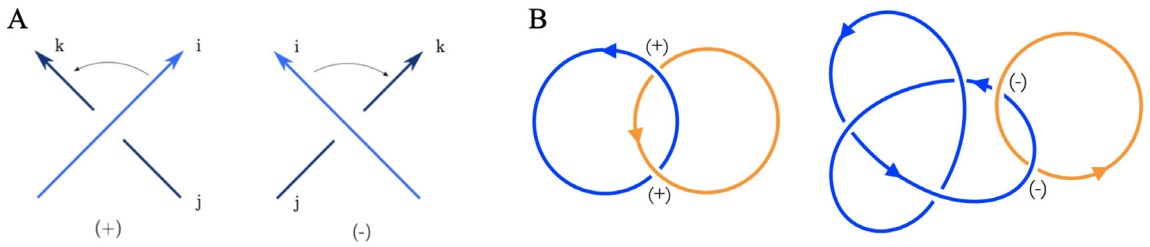

Fig. 5. A The standard convention to assign a sign to crossings in oriented knot projections. The *undercrossing*, i.e., the strand passing below, is denoted by depicting it with a small gap. The convention follows the right-hand rule to define + crossings. **B** Two examples of $Lk(C_1, C_2)$ computed for two different oriented links. The one on the left has $Lk = 1$, the other $Lk = -1$.

By adding an orientation to the strands of knots and links, one can assign a sign to the crossings, following the right-hand rule; see Fig. 5**A**. This procedure enables the definition of a series of topological invariants of knots and links. The simplest among them is the *linking number* of a two-component link formed by oriented knots C_1 and C_2, $Lk(C_1, C_2)$, given by

$$Lk(C_1, C_2) = \frac{1}{2} \sum_{p \in \{C_1 \sqcap C_2\}} \epsilon(p), \tag{1}$$

where $\{C_1 \sqcap C_2\}$ indicates the set of crossings between the two knots (self-crossings are excluded), and $\epsilon(p) = \pm 1$ following the sign of crossing p (Fig. 5**B**). Lk is able to distinguish between Hopf links, 2_1^2, having the same or different orientation between the links, as that changes the sign of the crossings. The linking number is a weak invariant. As can be seen in Fig. 3**C**, both the unlinked pair 0_1^2 and the Whitehead link 5_1^2 have $Lk = 0$.

2.2.4. Knot polynomials, skein relations, the Kauffman bracket

A set of important topological invariants is algebraic in nature and connects a particular knot to a polynomial by assigning different relations to different kinds of crossings in the knot diagram. The key point is that all diagrams corresponding to the same knot type will produce the same polynomial, which is therefore a topological invariant. Research in this direction was spurred by the discovery by Jones in the 1980s of a knot polynomial connecting knot theory with certain aspects of quantum mechanics [3,5,6]. The most adopted polynomial invariants in knot theory are the *Jones* [3,5], *HOMFLYPT* [3,7,8], and *Alexander* [9] polynomials. In the following, we will briefly discuss the Jones polynomials, through the Kauffman bracket, and the Alexander polynomial. We direct the interested reader to the books of Kauffman [6] and Adams [2] for a more in-depth introduction to knot polynomials.

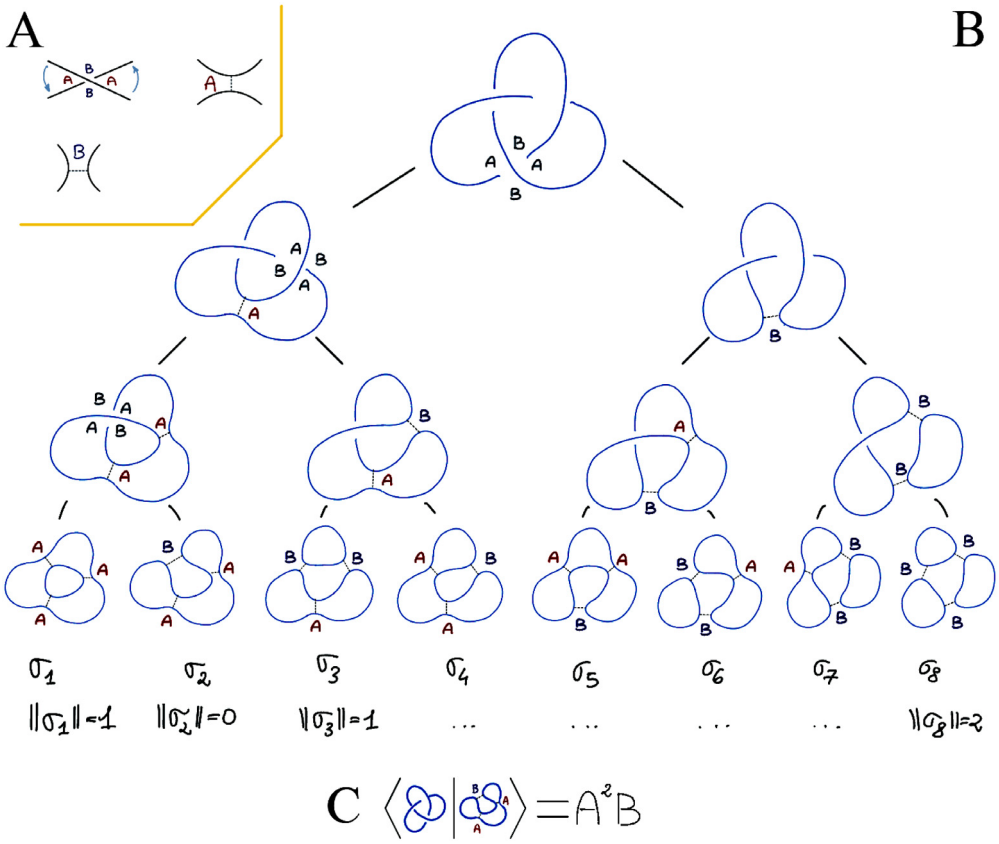

Fig. 6. **A** splicing relations for the Kauffman bracket. **B** The Kauffman bracket can be defined starting from the average of states obtained by splicing the crossings in a projection. The value of $\|\sigma\|$ is reported below each state. **C** An example of the value of $\langle K|\sigma\rangle$ for a specific state in **B**.

Knot polynomials are usually defined through *skein relations*, equations expressing linear relations between different diagrams in which a crossing has been changed. Consider for example the famous Jones polynomial $V_K(t)$. This is a Laurent polynomial—admitting both positive and negative powers—in the variable t that can be defined for any oriented diagram K (e.g., Fig. 5**B**) through the following properties

1. if K is ambient isotopic to K', then $V_K(t) = V_{K'}(t)$;
2. $V_{\bigcirc} = 1$;
3. $t^{-1}V_{\times} - tV_{\times} = \left(\sqrt{t} - \frac{1}{\sqrt{t}}\right) V_{\times}$.

Here the second relation defines the value of V for the unknot, $\bigcirc$, and the third establishes a relation between three oriented diagrams differing by a single crossing. This takes the configuration $\times$ in the first diagram, $\times$ in the second, and $\times$ in the third, while the rest of the diagram remains the same. It can be shown that these rules are sufficient to obtain $V_K(t)$ for any knot or link K through a recursive procedure. While a mathematical demonstration is beyond the scope of this review, here we present a derivation by Kauffman [6] to show how one can build a knot polynomial, the *Kauffman bracket*, and indicate how the Jones polynomial can be obtained from it.

The Kauffman derivation is particularly inspiring for soft-matter physicists, as it defines knot polynomials based on the ensemble average of a quantity over a set of states obtained by removing the crossings in the diagram. To do this, one first defines two possible ways to splice a crossing. In each crossing, the strands divide the plane into 4 quadrants. As shown in Fig. 6**A**, one can divide these quadrants into two A regions and two B regions, with the former defined as those spanned by the over-passing strand if it were rotated anticlockwise, to be on top of the under-passing strand. Following this, we define an A-splice to be one in which the two A regions are joined, and correspondingly a B-splice to be one where the two B regions are joined. Since each crossing can be spliced in two different ways, a diagram with N crossings can be first spliced into 2 diagrams by picking a random crossing and substituting it with an A splice and a B splice respectively. As shown in Fig. 6**B**, this procedure can be repeated until there are no more crossings to be spliced, each time associating the letter A or B with the crossing that has been removed. The procedure results in $M = 2^N$ states $\sigma_i, \ldots, \sigma_M$, each characterized by a different multiplicity of the labels A and B and by the number of loops present in the diagram. From each state, it is

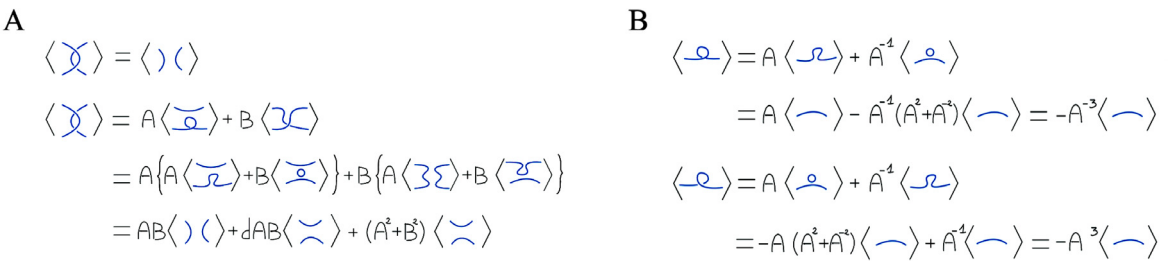

Fig. 7. A Imposing that the Reidemeister type II move does not change the bracket fixes the values of B and d respective to A. The same values make the bracket invariant under type III moves. **B** Computing the Kauffman bracket for a single loop, equivalent to a Reidemeister type I move, breaks the invariance, pointing to the necessity of extending the bracket to make it fully invariant under isotopies.

possible to reconstruct the original diagram by substituting back the crossing corresponding to each label. One can then define the *projection* of a diagram K onto a state σ as $\langle K|\sigma\rangle = A^{\nu(A)}B^{\nu(B)}$, where $\nu(A)$ and $\nu(B)$ are the multiplicity of the labels A and B in σ, as shown in Fig. 6, and the *norm* of a state, $\|\sigma\|$, the number of loops present in the diagram σ minus one, as depicted in Fig. 6**B**. With this notation, the Kauffman bracket can be introduced as

$$\langle K\rangle(A, B, d) = \sum_{i=1}^{M} \langle K|\sigma_i\rangle d^{\|\sigma_i\|}, \tag{2}$$

and the values of A, B, and d are to be determined to guarantee that $\langle K\rangle(A, B, d)$ does not depend on the actual diagram, but only on the topology of the knot K.

The strategy to ensure that $\langle K\rangle(A, B, d)$ is an invariant is to make sure that its value does not change under Reidemeister moves. One can ensure this by introducing a *skein relation*, Eq. (3), connecting the values of A, B and d. One can demonstrate that this is equivalent to our procedure to define the states, Fig. 6**B**, as each split produces a diagram multiplied by A and one multiplied by B. Similarly, Eq. (4) accounts for the fact that each additional loop, that does not introduce new crossings, multiplies the value of a state by d, per our definition of σ. The last equation, Eq. (5), sets the value of the state with a single loop with no crossings,

$$\left\langle \times \right\rangle = A\left\langle \asymp \right\rangle + B\left\langle) (\right\rangle, \tag{3}$$

$$\left\langle \bigcirc \cup K \right\rangle = d\,\langle K\rangle\,, \tag{4}$$

$$\left\langle \bigcirc \right\rangle = 1. \tag{5}$$

One can now impose Eqs (3)–(5) be invariant under Reidemeister moves ensuring, in turn, that the bracket is invariant. As an example, we show in Fig. 7**A** the derivation of the invariance for the Reidemeister type II move. Using Eqs (3)–(4), one can derive a skein relation involving A, B, d, showing that for $\langle K\rangle(A, B, d)$ to be independent under Reidemeister type II moves, one has to fix $B = A^{-1}$ and $d = -A^2 - A^{-2}$. It can be shown that with this choice of B and d, the Kauffman bracket is invariant under type III moves as well.

Having fixed B and d, one can then check whether the bracket $\langle K\rangle(A)$ is invariant under type I moves. As shown in Fig. 7**B**, this is not the case. This shortcoming can be corrected by considering oriented diagrams. This allows one to set a sign for each crossing, following the convention in Fig. 5**A**, and to define the writhe $w(K)$ of the diagram as in Eq. (16) (see also Fig. 13). It is then easy to prove that the writhe of a diagram after a type I move is ± 1 the writhe of the original diagram, depending on the sign of the newly introduced crossing,

$$w\left(\circlearrowright\right) = 1 + w\left(\rightarrow\right), \tag{6}$$

$$w\left(\circlearrowright\right) = -1 + w\left(\rightarrow\right). \tag{7}$$

Putting together the equations in Fig. 7**B** and Eqs (6)–(7), one can demonstrate that the generalized Kauffman bracket

$$X(K) = (-A^3)^{-w(K)}\langle K\rangle, \tag{8}$$

defined for an oriented diagram K, is invariant under ambient isotopies, as it is invariant for all three Reidemeister moves. The Jones polynomial can be obtained from the normalized Kauffman bracket by setting $A = t^{-1/4}$. This in turn provides an algorithmic way to compute the Jones polynomial as an ensemble average.

While the Kauffman bracket, Jones polynomial, and the HOMFLYPT polynomials are particularly good at discriminating between different knots and links, they can be very expensive to calculate. For example, the computational cost of a naive implementation of the Kauffman bracket described in Section 2.2.4 scales like 2^M in the number of crossings M. For this

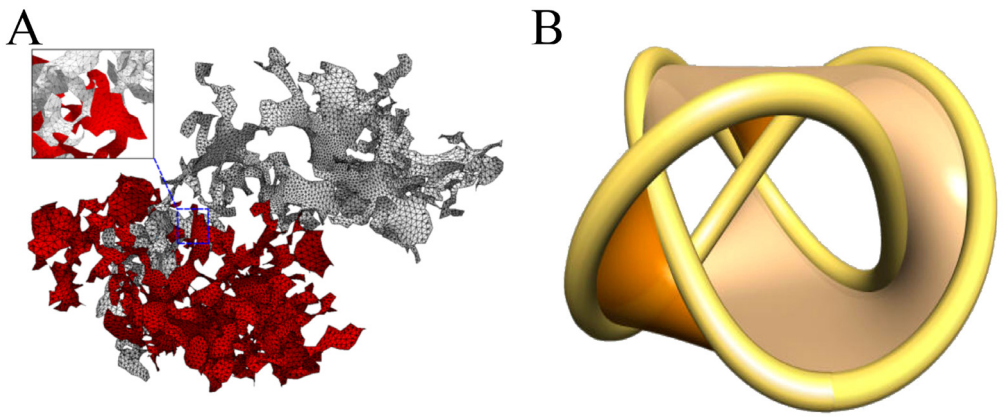

Fig. 8. **A** Minimal surface representation of two unlinked rings **B** SeifertView visualization of a Seifert surface for the trefoil knot rendered as a tube. *Source:* **A** Reproduced from [20].

reason in simulations and analyses where speed is essential, like knot localization [10], it is often convenient to use the Alexander polynomial, which, although less powerful—it can only reliably discriminate knots with less than 8 crossings—can be computed in M^2 steps [9,11]. The algorithm to compute the Alexander polynomial is described in Appendix A. Since the computational costs of computing polynomials scales with the number of crossings, it is often essential to reduce those before computing the polynomial. A common strategy is to reduce the number of vertices in the curve before projecting it through a simplification procedure based on triangular moves (Fig. 1**E**) [10]. The Alexander polynomial is implemented computationally in Kymoknot, a C code to identify and localize knots [10], and Topoly, a Python package to characterize the topology of proteins [12]. The HOMFLYPT, Kauffman, and Jones polynomials are implemented in Knotplot [13], Topoly, in the Mathematica KnotData package, and in Python Sage [14].

All polynomials mentioned so far have the useful property that the polynomial of a composite knot is given by the product of the polynomials of its prime components. This has been exploited in computational studies on composite physical knots to localize their prime components and study their interactions [15–17]. For example, one can identify the prime knotted portion K_1 of a ring hosting three knots $K_1\#K_2\#K_3$ as the smallest arc which upon circularization (Section 3.2.4) has topology K_1 while its complementary arc, the rest of the curve, has topology $K_2\#K_3$ [16].

2.2.5. Minimal surfaces and Seifert surfaces

A recurring theme in knot theory is to look at surfaces whose boundaries are given knots and links. A particularly interesting example of surfaces spanning knots and links is those that admit an orientation, the so-called Seifert surfaces. Seifert surfaces, Fig. 8**B**, can be used to compute several knot invariants. The linking number between two oriented closed curves (i.e., two knots), for example, is given by the signed sum of the intersections that one of them makes with the surface spanned by the other knot [18].

Among surfaces spanning knots, those admitting minimal area are particularly meaningful in applications. The concept of minimal surfaces was formulated in 1760 by Lagrange as the existence of a surface of minimal area for a given boundary. The so-called Plateau problem, named after the Belgian physicist who experimented with soap films, was solved only in 1930 by Douglas [19]. The easiest example of an entity that can have a minimal surface is an orientable, disc-like object with a single connected fixed boundary (e.g., a ring, Fig. 8**A**), but minimal surfaces with more complicated topology exist for both knots and unknots.

More generally, minimal surfaces carry useful physical information, often being the locus of optimal processes of chemical, biological, or dynamical origin. Nowadays, methods that quantify the number of times a curve pierces or threads the minimal surface of another structure, even in the more general case when this is open and not a ring, are available. An important application is presented in detail in Section 4.1.4, where we discuss how minimal surfaces have become a fundamental instrument to understand the physics of melts of non-concatenated and unknotted ring polymers.

From an algorithmic perspective, the minimal surface is found by spanning a triangulated and orientable surface, which is then minimized on each ring separately by displacing the free, off-boundary vertices using different methods [20,21], according to convenience. The most versatile implementation of the minimization is the Surface Evolver software [22] that allows for full control of the different aspects including triangulation, noise, pressure or topology changes on the fly, but requires learning the dedicated language; a basic implementation is available in the Python package Topoly [12]. A tool to visualize Seifert surfaces is provided by SeifertView [23].

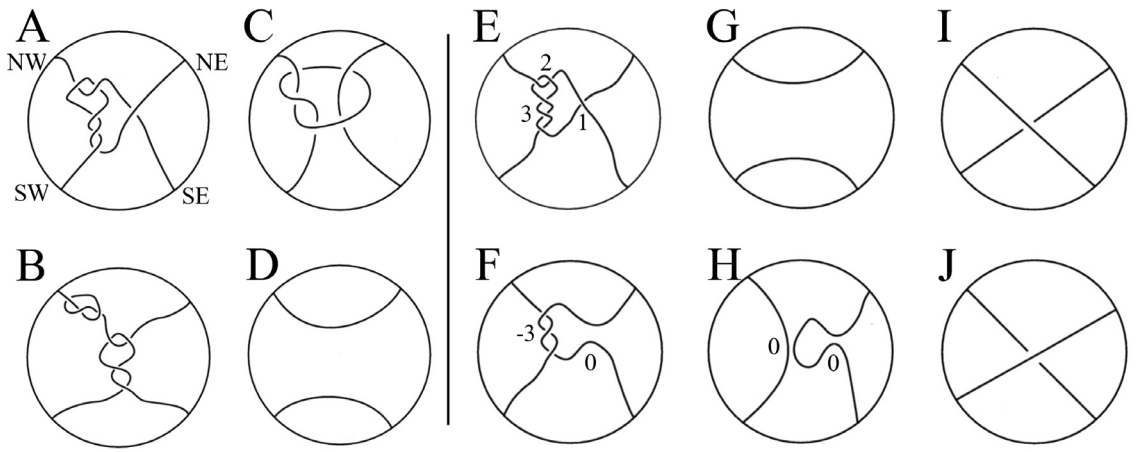

Fig. 9. Tangles. **A** Rational, **B** locally knotted, **C** prime, **D** trivial; Rational Tangle Diagrams: **E** (2, 3, 1), **F** (−3, 0), **G** (0), **H** (0, 0), **I** (+1), **J** (−1). *Source:* Adapted from [25].

2.3. Tangles

In some cases, it is useful to reason about the strand-crossing or twisting operations that can result in a particular knot. This is done through the use of *tangle theory*. Tangles were introduced into knot theory by Conway [24]. One can think of tangle theory as knot theory done inside a unit 3-ball—B^3, which for simplicity can be pictured as a unit sphere—with the ends of the strings fixed to the boundary. Tangles are useful to describe knots, and essential to model the action of enzymes that modify DNA topology through site-specific recombination, see Section 3.3.7. On the unit 3-ball in $\mathbb{R}^3$, select four points on the equator $\{NW; SW; SE; NE\}$. A 2-string tangle in the unit 3-ball is a configuration of two disjoint strings whose endpoints are the four distinguished points $\{NW; SW; SE; NE\}$. Tangles are usually represented by their projections, called tangle diagrams, onto the equatorial disc in the unit 3-ball, as shown in Fig. 9**A–D**. In all figures containing tangles, we assume that the four boundary points $\{NW; SW; SE; NE\}$ are as in Fig. 9**A**, and we suppress these labels. Two tangles in the unit 3-ball are equivalent if there exists an ambient isotopy in the interior of the 3-ball that maps the strings of one tangle into the strings of the other while keeping the boundary sphere fixed. A class of equivalent tangles is called a tangle type. All four of the tangles in Fig. 9**A–D** are pairwise inequivalent. However, if we relax the restriction that the endpoints of the strings remain fixed and allow them to move about on the boundary sphere of the 3-ball during the isotopy, then the tangle of Fig. 9**A** can be transformed into the trivial tangle of Fig. 9**D**. The tangles in Figs. 9**B** and **C** cannot be transformed to the trivial tangle by any sequence of such turning motions of the endpoints on the boundary sphere. The family of tangles that can be converted to the trivial tangle by an ambient isotopy that is allowed to move the endpoints on the boundary sphere is the family of *rational tangles*. Rational tangles form a homologous family of 2-string configurations in B^3, and are formed by a pattern of plectonemic interwinding of pairs of strings, see Section 3.3.6.

There is a classification scheme for rational tangles based on a standard form that is a minimal alternating tangle diagram. The classifying vector for a rational tangle is an integer-entry vector $(a_1, a_2, \ldots, a_n)$ of odd or even length, with all entries, except possibly the last, nonzero and of the same sign, with $|a_1| > 1$. The integers in the classifying vector represent the left-to-right (west-to-east) alternation of vertical and horizontal windings in the standard tangle diagram, always ending with horizontal windings on the east side of the diagram. Horizontal winding is the winding between strings in the top and bottom (north and south) positions; vertical winding is the winding between strings in the left and right (west and east) positions. By convention, positive integers correspond to horizontal plectonemic right-handed supercoils and vertical left-handed plectonemic supercoils; negative integers correspond to horizontal left-handed plectonemic super-coils and vertical right-handed plectonemic supercoils (Fig. 9**E–J**). This sign convention is opposite to that of Conway [24], and was chosen to agree with existing sign conventions used by biologists. Fig. 9**E–J** shows some standard tangle diagrams, which are minimal alternating diagrams. The classifying vector $(a_1, a_2, \ldots, a_n)$ can be converted to an (extended) rational number by means of the continued-fraction calculation

$$\frac{\beta}{\alpha} = \frac{1}{a_{n-1} + \dfrac{1}{a_{n-2} + \cdots}}.$$

Tangles can be used as building blocks for knots and links and to mimic mathematically enzyme action on DNA, as described in Section 3.3.7, if one introduces the geometric operations of tangle addition and tangle closure. Given tangles A and B, one can form the tangle $(A + B)$ as shown in Fig. 10**A**. Equivalently, the tangle sum $(A + B)$ can be viewed as the decomposition of a complicated tangle into two simpler summands. The sum of two rational tangles need not be rational.

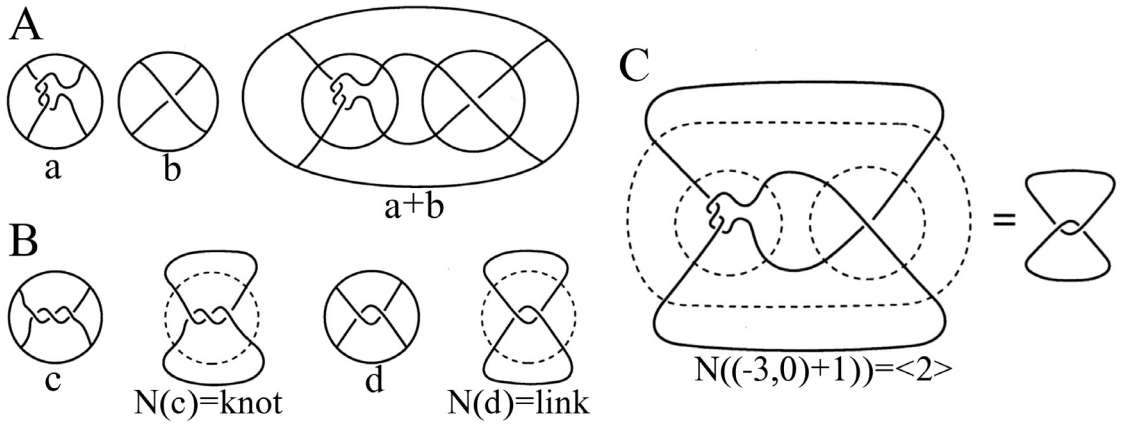

Fig. 10. Tangle operations. **A** Tangle addition, **B** tangle closure, **C** tangle equation $N((-3,0)+(1))=(2)$.
Source: Adapted from [25].

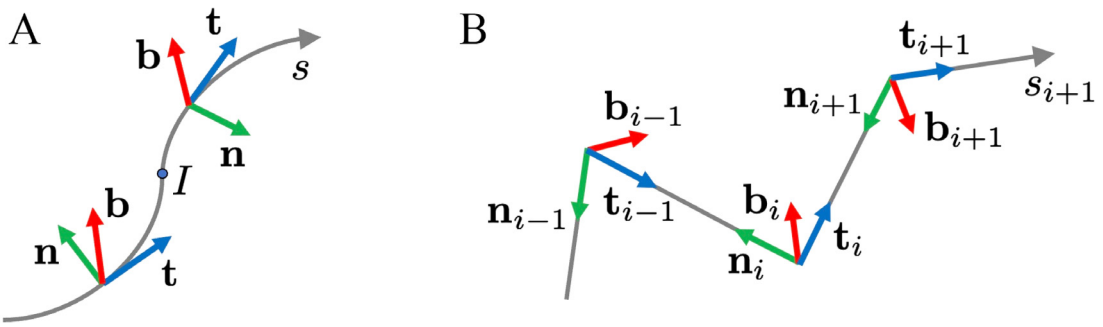

Fig. 11. **A** The Frenet frame on a smooth curve; the point I is a point of inflexion of the curve. **B** Discrete Frenet frames on a polygonal curve.

This is the case for example of the prime tangle in Fig. 9**C**, which can be obtained as $((+3,0)+(-2,0))$. Given any tangle A, one can form the tangle closure, also known as *numerator construction*, $N(A)$ as in Fig. 10**B**. In the closure operation on a 2-string tangle, ends *NW* and *NE* are connected outside the 3-ball, ends *SW* and *SE* are connected outside the 3-ball, and the tangle-defining ball is deleted, producing a knot or a link of two components. Deletion of the tangle-defining 3-ball is the mathematical analogue of the biological action of deproteinization of DNA, described in Section 3.3.7. One can combine the operations of tangle addition and tangle closure to create a tangle equation of the form $N(A+B)=$ knot (link).

2.4. Frenet frame

A space curve C is described by a vector-valued function $\mathbf{r}(s)=(x(s),y(s),z(s))$ that is parametrized by the arc-length $s\in[0,L]$, L being the total length. If C is closed, the curve is periodic in s, of period L. Provided that the curve is sufficiently regular (typically C^3), one can define a local, orthogonal frame of reference given by the Frenet–Serret frame in terms of the unit *tangent* $\mathbf{t}(s)=\frac{d\mathbf{r}(s)}{ds}/|\frac{d\mathbf{r}(s)}{ds}|$, unit *normal* $\mathbf{n}(s)=\frac{d\mathbf{t}(s)}{ds}/|\frac{d\mathbf{t}(s)}{ds}|$, and unit *binormal* $\mathbf{b}(s)=\mathbf{t}(s)\times\mathbf{n}(s)$. The Frenet frame $\{\mathbf{t},\mathbf{n},\mathbf{b}\}$ provides an intrinsic reference frame on C (see Fig. 11, left), allowing us to define two local properties of the curve: the curvature $\kappa(s)=|\frac{d\mathbf{t}(s)}{ds}|$, and the torsion $\tau(s)$ (involving third derivatives); these can be computed via the Frenet–Serret equations

$$\begin{bmatrix}\frac{d\mathbf{t}(s)}{ds}\\ \frac{d\mathbf{n}(s)}{ds}\\ \frac{d\mathbf{b}(s)}{ds}\end{bmatrix}=\begin{bmatrix}0 & \kappa(s) & 0\\ -\kappa(s) & 0 & \tau(s)\\ 0 & -\tau(s) & 0\end{bmatrix}\begin{bmatrix}\mathbf{t}(s)\\ \mathbf{n}(s)\\ \mathbf{b}(s)\end{bmatrix}. \tag{9}$$

Isolated points where, for some $s=s_I$, the curvature is zero, are called inflexion points; at those points the Frenet frame is ill-defined. Once curvature and torsion are prescribed, the Frenet–Serret theorem ensures that the curve is well-defined, and uniquely specified in space.

For coarse-grained models of fibrous materials, such as the Cα representation of polypeptides, one can use the corresponding discrete version of the Frenet frame $\{\mathbf{t}_i,\mathbf{b}_i,\mathbf{n}_i\}$ (see Fig. 11**B**, Section 6 and Appendix B), given for example

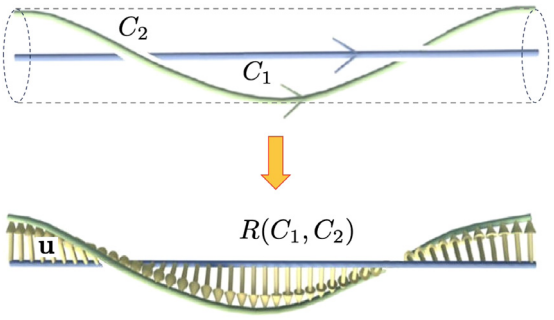

Fig. 12. Construction of a ribbon $R(C_1, C_2)$ from the curves C_1 and C_2; note the rotation of the unit vector $\mathbf{u}$ around C_1 to form a twisted ribbon.

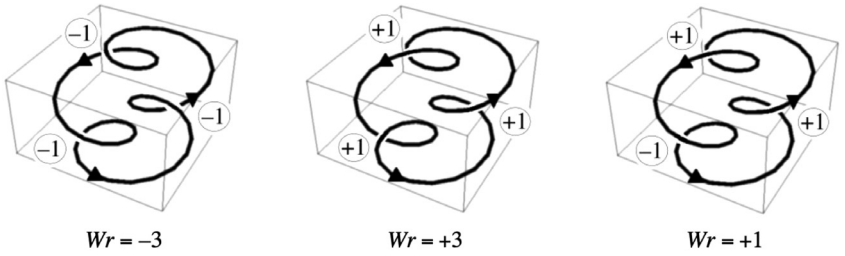

Fig. 13. Different writhe contributions from a single, unknotted loop in space due to the positive and negative coils.

by the polygonal representation of Cα. In this case, the chain[5] geometry is governed by the virtual bond and torsion angles κ_i and τ_i

$$\begin{aligned} \kappa_{i+1,i} \equiv \kappa_i &= \arccos(\mathbf{t}_{i+1} \cdot \mathbf{t}_i), \\ \tau_{i+1,i} \equiv \tau_i &= \text{sign}[(\mathbf{b}_{i-1} \times \mathbf{b}_i) \cdot \mathbf{t}_i] \arccos(\mathbf{b}_{i+1} \cdot \mathbf{b}_i). \end{aligned} \tag{10}$$

Conversely, from the bond and torsion angles of Eqs. (10) one can compute the Frenet frames, and reconstruct the chain using the discrete Frenet equation [26]

$$\begin{pmatrix} \mathbf{n} \\ \mathbf{b} \\ \mathbf{t} \end{pmatrix}_{i+1} = \begin{pmatrix} \cos\kappa\cos\tau & \cos\kappa\sin\tau & -\sin\kappa \\ -\sin\tau & \cos\tau & 0 \\ \sin\kappa\cos\tau & \sin\kappa\sin\tau & \cos\kappa \end{pmatrix}_{i+1,i} \begin{pmatrix} \mathbf{n} \\ \mathbf{b} \\ \mathbf{t} \end{pmatrix}_i . \tag{11}$$

2.5. Linking number and Călugăreanu–White theorem

Eq. (1) allows one to evaluate directly the linking number $Lk = Lk(C_1, C_2)$ of two closed curves C_1, C_2 by crossing sign computation; the expression comes from the solid-angle interpretation [18] of the original integral expression of Gauss (1833), given by

$$Lk = \frac{1}{4\pi} \oint_{C_1} \oint_{C_2} \frac{\mathbf{r}_1(s_1) - \mathbf{r}_2(s_2)}{|\mathbf{r}_1(s_1) - \mathbf{r}_2(s_2)|^3} \cdot \left[\frac{d\mathbf{r}_1(s_1)}{ds_1} \times \frac{d\mathbf{r}_2(s_2)}{ds_2} \right] ds_1\, ds_2 \,, \tag{12}$$

where $\mathbf{r}_1 = \mathbf{r}_1(s_1)$ and $\mathbf{r}_2 = \mathbf{r}_2(s_2)$ denote respectively the parametrization of the curves C_1 and C_2 of arclength s_1 and s_2.

Since the linking number is a topological invariant of the link, its conservation has far-reaching consequences in many contexts and situations. When the two curves define the edges of a single ribbon, as is the case exemplified by double-stranded DNA, the linking number specializes to the self-linking number, a topological invariant of the ribbon. To see this consider the closed curve $C_1 : \mathbf{r_1}(s_1)$ and the tubular neighbourhood of centreline C_1 and radius ϵ. Define a second curve C_2 on the tubular neighbourhood, running all along parallel to C_1, such that $C_2 : \mathbf{r_2}(s_1) \equiv \mathbf{r_1}(s_1) + \epsilon\mathbf{u}(s_1)$, where $\mathbf{u}$ is a unit vector everywhere orthogonal to C_1. The two curves C_1 and C_2 define the mathematical ribbon $R = R(C_1, C_2)$, of width ϵ; see the construction of Fig. 12.

As C_1 and C_2 are two well-defined curves, just separated by ϵ, their Gauss linking number is evidently well-defined. Călugăreanu [27] (see also [28]) demonstrated that by taking the limit $\lim_{\epsilon\to 0} Lk(C_1, C_2)$ we obtain a topological invariant of the ribbon, often referred to as the self-linking number *Sl* of *R*. Let us simplify the notation, and write $C_1(s_1)$ as $C(s)$, and

[5] Following the standard jargon of polymer physics we will often refer to curves as *chains*.

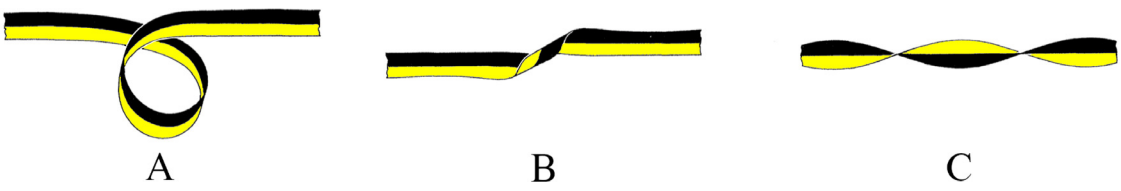

Fig. 14. Contributions to the Călugăreanu–White invariant *Sl* of a ribbon *R* from separate state configurations. **A**: writhe; **B**: localized torsion; **C**: intrinsic twist.
Source: Adapted from [28].

$C_2(s_1)$ as $C^*(s)$ (the push-off of C). An even more important result is that the topological invariant *Sl* admits decomposition in terms of two global geometric quantities, given by the writhing number Wr of the baseline curve C, and the total twist number Tw of the ribbon R, according to the expression

$$Sl(R) = Wr(C) + Tw(R)\ . \tag{13}$$

White [29] was able to express Călugăreanu's derivation in the language of differential forms, thus avoiding the difficulty associated with the possible presence of inflexion points, extending the validity of Eq. (13) to the higher-dimensional case. The writhing number of C is defined by

$$Wr(C) = \frac{1}{4\pi}\oint_C\oint_C \frac{\mathbf{r}(s)-\mathbf{r}(s^*)}{|\mathbf{r}(s)-\mathbf{r}(s^*)|^3}\cdot\left[\frac{d\mathbf{r}(s)}{ds}\times\frac{d\mathbf{r}(s^*)}{ds^*}\right]ds\,ds^*\ , \tag{14}$$

where s^* denotes also a point of C; note the formal similarity with the integral definition of the Gauss linking number (12). Remarkably, the integral Eq. (14) is well-behaved even when $s = s^*$. The writhe of C provides a global geometric measure of the coiling of C in space, and its mathematical properties were explored extensively by Fuller[6] [30]. The evaluation of writhe using Eq. (14) is computationally expensive and in some cases impossible. A more convenient method is based on the exploitation of its algebraic counterpart given in terms of crossing signs; indeed, one can prove [18,28,31] that

$$Wr(C) = \langle \sum_{p\in\{C\sqcap C\}} \epsilon(p)\rangle\ , \tag{15}$$

where angular brackets denote averaging over all direction of sight, $\{C\sqcap C\}$ denotes the set of apparent self-crossings of C, and $\epsilon(p) = \pm 1$ according to the standard sign convention (see Fig. 13). Evidently, to make the definition above computable we can decide to estimate the exact writhe according to a finite set of projections, and experience shows that just three mutually orthogonal directions may suffice for a reliable approximation. Another related quantity, neither topological nor geometric, is the directional writhe of a knot projection. This is defined by summing the signed crossings in a single loop

$$w(C) = \sum_{p\in\{C\sqcap C\}} \epsilon(p)\ . \tag{16}$$

It is not difficult to show that $w(C)$ is invariant under Reidemeister moves of type II and III, while type I move changes $w(C)$ by ± 1 (Section 2.2.4).

The total twist number of R is defined by

$$Tw(R) = \frac{1}{2\pi}\oint_C \left[\mathbf{u}(s)\times\frac{d\mathbf{u}(s)}{ds}\right]\cdot\frac{d\mathbf{r}(s)}{ds}\,ds\ . \tag{17}$$

Tw provides a global geometric measure of the total contorsion and twist of the ribbon in space. It can be shown [28,32] that the total twist number can be decomposed into two contributions T and N, given by

$$Tw(R) = T(C) + N(R) = \frac{1}{2\pi}\oint_C \tau(s)\,ds + \frac{[\Theta]_R}{2\pi}\ , \tag{18}$$

where $T(C)$ denotes the normalized total torsion of C, and $N(R)$ the intrinsic twist of the ribbon. In general, the contribution of $T(C)$ to Tw is rather modest, and to a first approximation it can be neglected. A pictorial representation of these contributions to the self-linking number of a ribbon is shown in Fig. 14. Since self-linking is a topologically conserved quantity, for a given *Sl* writhe and twist can interchange under continuous deformation of the ribbon leaving *Sl* unchanged. This means that a highly twisted ribbon can always reduce Tw by converting twist to writhe through the production of coiling, with the advantage to make the ribbon more compact in space. This mechanism is indeed widely found in nature, for example in DNA to compactify the macromolecule in the cell; see Sections 3.3.6 and 5.

[6] The term *writhe* was indeed introduced by Fuller to denote Eq. (14); it is wrong, however, to refer to Eq. (13) as the "Călugăreanu–White–Fuller theorem", because the full derivation of Eq. (13) was provided by Călugăreanu, and then White, well before Fuller's paper.

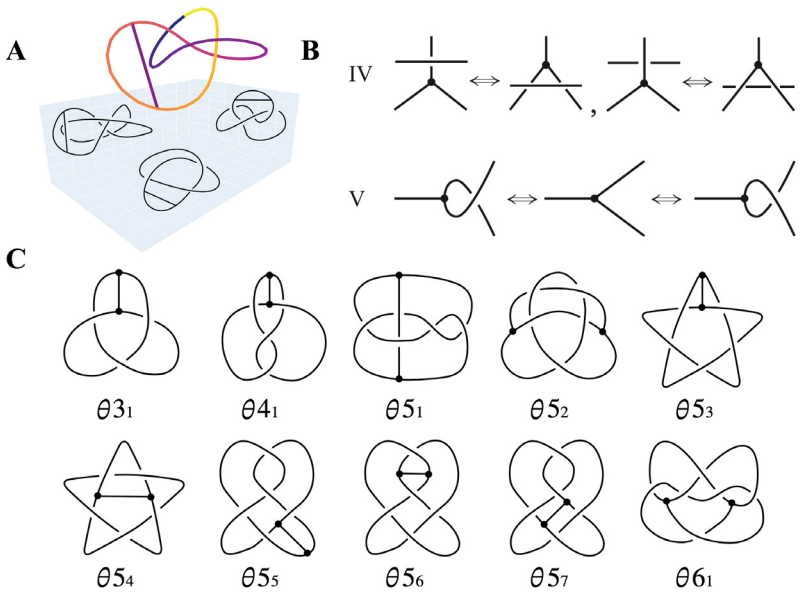

Fig. 15. A An example θ-curve in 3D. **B** The three Reidemeister moves introduced in Fig. 2 can be extended to θ-curves by adding a fourth and fifth move. **C** the first 10 non-trivial θ-curves.
Source: **B**, **C** adapted from Ref. [33].

2.6. Other embeddings: θ-curves

Knots and links are not the only possible form of entanglement. Chemists often work with macromolecules like tadpoles and handcuffs, which consist of both circular and linear sections and correspond therefore to graphs with genus 1, i.e., hosting a loop. A similar situation arises in proteins, where cysteine bridges can connect two side-chains that are far from each other along the protein backbone; see Sections 3 and 6 for details. Recently, these forms of entanglement and their consequences have begun to be studied by extending concepts and tools from knot theory to the more general case of spatial graphs (i.e., graphs embedded in $\mathbb{R}^3$). The simplest family of spatial graphs (other than knots and links), among those that are extensively studied by pure and applied topologists, is represented by θ-curves.

A θ-curve is a graph with two nodes connected by three edges embedded in $\mathbb{R}^3$ (Fig. 15**A**). As in Section 2.2 we consider only piece-wise linear graphs for simplicity. With this assumption, two θ-curves are said to be equivalent if there exists a piece-wise linear ambient isotopy transforming one into the other. As in the case of knots, this allows us to classify all equivalent θ-curves as the same topological object. Prime and composite θ-curves can be defined following a procedure similar to the one used for knots, θ-curves can then be tabulated, and it is possible to work directly on their diagrams thanks to an extension of the Reidemeister moves, (Fig. 15**B**). A table of θ-curves up to 7 crossings is reported in [33]. We show the diagrams of first 10 prime and non-trivial θ-curves in Fig. 15**C**. The trivial θ-curve, $\theta 0_1$, analogous to the unknot, is simply the letter θ. Thanks to the availability of Reidemeister moves, it is possible to follow a strategy similar to the one reported in Section 2.2.4 to define a polynomial that is a topological invariant of θ-curves. A famous example, and the most used, is the Yamada polynomial [34].

2.7. Knots and links in open curves

As discussed in Section 2.2, from a mathematically rigorous point of view, open chains are always unknotted, yet they can nonetheless host *physical knots*, often with very long lives, such as the centuries-old Inca quipus. Their identification and characterization is non-trivial and has been approached in different ways. Here, we will review three of them: *circularization schemes*, *knotoids*, and *intrinsic entanglement measures*. The first approach, circularization, consists in connecting the ends of an open chain in a suitable way (Section 2.7.1), thus mapping it to a circular one whose topological status can be analysed through standard topological invariants (Section 2.2). The second approach is based on a generalization of the Reidemeister moves to open-ended diagrams, which allows one to define a topological equivalence class on open curves, that of *knotoids* (Section 2.7.3). The third approach (Section 2.7.4) is more recent and aims at defining entanglement measures directly on the spatial curves, so that they do not depend on a specific projection or closure. Finally, in Section 2.7.5 we will see how these schemes can be applied to characterize the *topological* state of subportions of a chain.

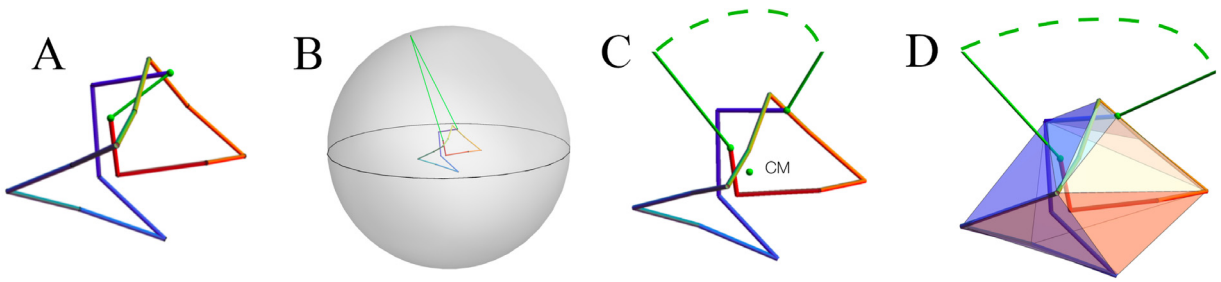

Fig. 16. Closure schemes applied to the same polymer chain. **A** direct bridging, **B** stochastic closure, **C** closure away from the centre of mass (CM) of the polymer chain, **D** minimally-interfering closure scheme. In all panels, the green segments connecting the two termini of the open chain are added to circularize it.
Source: Adapted from [35].

2.7.1. Knot circularization schemes

Circularization schemes for detecting and classifying physical knots require that the termini of the open chain be bridged by a suitably-chosen *auxiliary arc* in such a way that properly defined *topological invariants* (see definitions in Section 2.2) can be computed for the closed ring obtained.

Different closure schemes have been proposed in recent years [35–40] (Fig. 16). The simplest one is known as *direct bridging* and consists in bridging the ends of the chain with a line segment, Fig. 16**A**. This procedure has the merit of being straightforward and immediate in terms of its definition and implementation. However, unless the two ends are relatively nearby each other, the bridging segment may pass through the volume spanned by the rest of the chain, thus adding a potentially large amount of non-native, and hence spurious, entanglement to the closed chain.

An alternative approach, *stochastic closure*, Fig. 16**B**, consists in joining the ends of the chain to randomly chosen points on the surface of a sphere that is sufficiently large to contain the chain. The points on the sphere can then be joined on the spherical surface to return a closed ring [38]. A variant of this method involves joining both chain termini to the same randomly-chosen point on the spherical surface [40]. These schemes based on the so-called closure *at infinity* are inherently stochastic because the entanglement trapped by the closure depends on the randomly picked point(s). One thus needs to choose the latter a number of times so to obtain a probability distribution of knot types, and the dominant one can be taken as the knot state of the open chain. This method is a good complement to direct bridging, in that it works well when the chain termini are exposed, a situation that, for instance, is typical for proteins; see Section 6. However, when the termini are tucked deep inside the volume spanned by the chain, the auxiliary segments, or *rays*, reaching the points on the sphere can add substantial spurious entanglement. The inherently stochastic nature of the method allows one to assign a statistical confidence to the knot state of the open chain. At the same time, the repeated calculation of topological invariants can make the method computationally very demanding when a large ensemble of chains must be profiled. For a trade-off between computational expenditure and a robust determination of the knot state, one can adopt the strategy introduced in [39]. In this method, Fig. 16**C**, the outgoing rays from the termini are directed away from the centre of mass of the chain, minimizing the chances of adding spurious entanglement while using a single closure instance.

Finally, the so called *minimally-interfering closure* (MIC) scheme, Fig. 16**D**, offers a robust and, at the same time, convenient solution to the shortcomings of closures at infinity and direct bridging. In this approach [35], the closure is picked from two alternatives depending on whether the distance between the chain termini, d_{in} is smaller or larger than their summed distance from the convex hull of the chain, d_{out}. If $d_{in} \leq d_{out}$, the *direct bridging* scheme is adopted. Conversely, if $d_{in} \geq d_{out}$, the termini are first joined to their closest points on the convex hull, and these are then joined outside the hull (at infinity, for instance). The adopted closure is thus the one adding the shortest segment(s) running through the convex hull. This intuitively corresponds to minimizing spurious entanglement. It is also computationally effective because all that needs to be done is to evaluate the chosen topological invariant on a *single* closed curve, and not for an ensemble of them as in the other cases. One may verify that, even in the very challenging case of compact chains, the MIC scheme generally returns the same dominant knot state as stochastic closure at infinity, which is more demanding and not necessarily appropriate when termini are buried [35]. The robustness and effectiveness of the MIC scheme are thus ideally suited (Section 3.2.4) for profiling the topological entanglement of large ensembles of open chains [16,41,42].

2.7.2. Mutual entanglement and physical links

The tools developed to detect the presence of physical knots in single polymer chains, Section 2.7.1, can be generalized to explore the *mutual* entanglements occurring in polymer solutions and melts, where multi-chain effects dominate the viscoelastic behaviour (Section 4.1) in the bulk. This leads to the notion of *physical links* between pairs of polymer chains.

For simplicity let us focus on two chains. Similarly to the case of knots, a topologically inspired definition of a physical link can be given by first closing both chains with a method that adds the least amount of spurious entanglement to the system [43]. As illustrated in Fig. 17**A**, this can be achieved by closing each ring away from the centre of mass of the partner ring. After closure, the topological state can be established with standard topological invariants (Section 2.2.3).

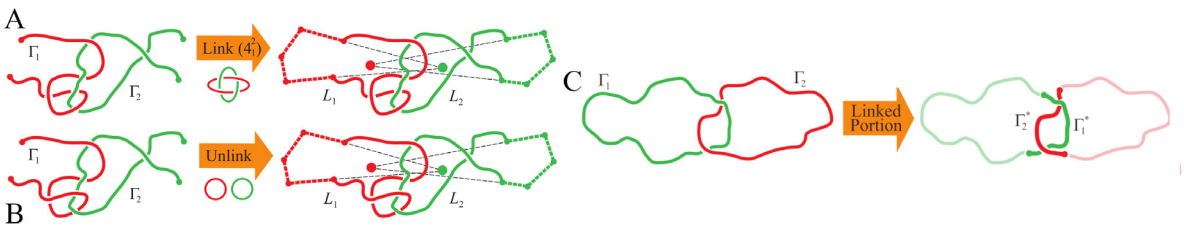

Fig. 17. A, B Detecting physical linking between pairs of open chains. The two curves are circularized by projecting away from their respective centres of masses. Depending on the local entanglement between them, upon circularization they can result to be linked or unlinked, and the topology of the link can be identified. **C** The arc-closing strategy can be used to detect the physically-linked portion in pairs of open or closed chains, too.
Source: Adapted from [43].

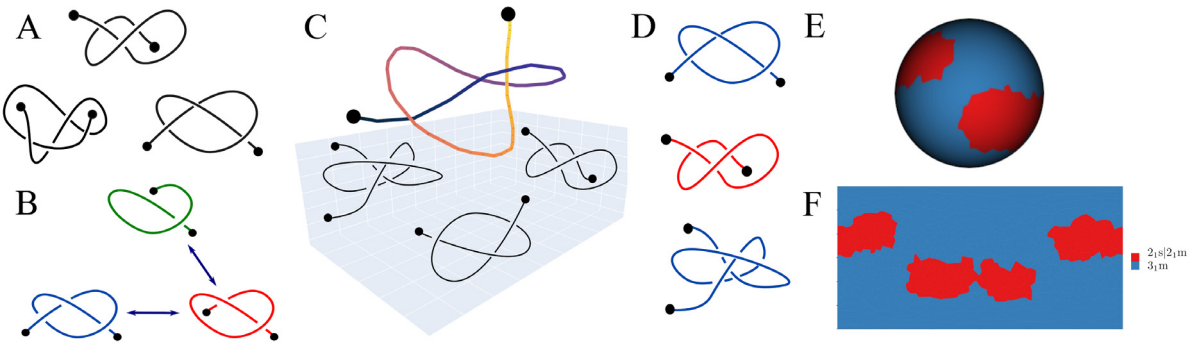

Fig. 18. **A** Knotoid diagrams. **B** A sequence of forbidden moves. **C** An open curve in space together with some of its planar projections. **D** Each planar projection defines a knotoid diagram, whose topological type can be detected using invariants. **E** The knotoid distribution of the curve in panel C is visualized by colouring each point in the surrounding sphere according to the knotoid type obtained by projecting along the corresponding direction. **F** Planar projection of the sphere in **E**. Panels **E** and **F** were obtained using the software Knoto-ID [47].

Analogously to the case of physical knots, the closing arcs construction can be applied to shorter and shorter portions of two chains, thus enabling the search and quantifying the extent of their physically *linked portion* ℓ_{lp} (Fig. 17**B**). The search can be performed not only on physical links but on proper topological links too.

2.7.3. Knotoids

Circularization schemes provide an efficient way of understanding whether an embedded open arc is knotted and determining its global topology, and are particularly useful to localize the knotted portion on a long polymer (Section 3.2.4); however, analysing a closed curve instead of the initial open one inevitably results in some amount of information being lost. This can be particularly problematic when trying simultaneously to characterize geometrical and topological features in open knots. As an example, different geometries of proteins with the same global topology (Section 6) are known to influence their folding behaviour [44]. Recently, new mathematical objects called *knotoids* have been established as a primary tool to characterize the topology of open arcs without relying on artificial closures [45–47]. Mathematically, knotoids are defined as equivalence classes of open ended planar arc diagrams, where the equivalence relation is given by planar isotopies, i.e., local transformations of the plane and the diagram that do not modify its underlying graphical structure, together with the three classical Reidemeister moves, Fig. 18**A**, performed away from the endpoints. Without this latter restriction, Reidemeister moves could be used to untangle any knotoid diagram, thus yielding a trivial theory. Under this definition, moving an endpoint below or under another arc of the diagram, as shown in Fig. 18**B**, changes the underlying knotoid type. These local transformations are known as *forbidden moves*. Forbidden moves are unknotting operations; it can be shown that any knotoid diagram can be transformed into the unknotted one by a finite sequence of forbidden moves and planar isotopies [48].

As in the case of knots, we are interested in distinguishing the topological type of different knotoid diagrams. To this end, several invariants of knots have been extended and generalized to define knotoid invariants, including various versions of polynomials [46,49,50]. The key idea behind the construction of knotoid polynomials is the same as for knot polynomials seen in Section 2.2.4: they are all defined in terms of a set of skein relations. Some of the most effective knotoid polynomials are the bracket polynomial, a straightforward adaptation of the knot definition, whose normalization generalizes the Jones polynomial [49], and the arrow polynomial [51], which is enough to distinguish and tabulate knotoids with low crossing number.

While knotoids were originally defined as equivalence classes of diagrams [49], similarly to the case of knots, it is possible to provide an equivalent characterization as equivalence classes of piece-wise linear embeddings of the unit

interval $[0, 1]$ in the three-dimensional Euclidean space $\mathbb{R}^3$. Formally, this can be done by using the concept of *line isotopies* [49,50,52]. Consider an embedded arc in $\mathbb{R}^3$, whose endpoints lie in the parallel vertical lines, perpendicular to the horizontal plane $\mathbb{R}^2 \times 0$. Two such embedded arcs are *line isotopic* if there is a piece-wise linear ambient isotopy of $\mathbb{R}^3$ transforming one arc into the other, without allowing the arc to pass through the vertical lines, nor the endpoints to leave them. It can be shown that there is a 1 to 1 correspondence between equivalence classes of planar knotoid diagrams and line isotopy classes of embedded arcs. One direction of this bijection is straightforward, and it just requires projecting the curve along the direction given by the vertical lines. Under this projection, the lines are mapped to the endpoints of the diagram. This correspondence can be extended to a bijection between equivalence classes of knotoid diagrams on the sphere S^2 and labelled θ-curves, see e.g., [52].

This three-dimensional interpretation allows thinking about knotoids as the coordinates of an open curve in space, together with a fixed direction of projection. Using knotoids, the topology of an open chain can be characterized by considering all of its different planar projections at once. Each projection defines a knotoid diagram, shown in Fig. 18**C–D**, whose topological type can be detected using knotoid invariants [46]. The resulting distribution of knotoids is then taken as a descriptor of the chain's topology. Visually, the chain can be thought of as lying inside a large enough sphere. Each point on this sphere defines a direction of projection. The distribution of knotoids can then be represented by colouring each point of the sphere according to the knotoid type of the corresponding projected diagram, as shown in Fig. 18**E–F**. Consequently, regions with the same colour contain points sharing the same knotoid type. The coloured sphere is often called the *projection map*. In practice, only a certain number of uniformly sampled points are considered, to obtain an approximate distribution. This can be achieved computationally by using the freely available software Knoto-ID [47]. The above procedure is described in detail in [53]. The knotoid approach provides a more nuanced description of an open curve's structure and topology than any knot closure technique [54], although at a higher computational cost. This approach is thus particularly suitable to characterize entangled proteins, where considerable information can be extracted from a single curve—the folded configuration—while studies of knot localization and diffusion, where thousands of configurations need to be analysed, tend to rely on closure schemes due to their computational efficiency.

A further advantage of this approach comes from the possibility of enriching the knotoid distribution with further structure. As mentioned above, forbidden moves are unknotting operations, and can thus be used to define a notion of topological distance on knotoids. This is called the *forbidden-move* distance, and is given by the minimal number of forbidden moves needed to transform one knotoid into another [48]. The forbidden-move distance can be employed, together with statistical techniques, to define a notion of *dissimilarity* between projection maps of two knotted arcs, and in turn, between the knotted arcs themselves [44]. Such dissimilarity measures can be used to distinguish structures with the same knot type differing by local geometric features of their entanglement. As a concrete application, being able to detect these differences allows identifying and obstructing specific folding pathways for proteins forming open-ended trefoil knots [44].

2.7.4. Intrinsic entanglement measures

More recent efforts consist in finding measures of entanglement that are intrinsic, i.e., that are not associated to a specific closure or projection. A first approach in this direction consists in combining the Jones polynomial definition for knotoids [46] with an approach inspired by the Gauss Integral (Eq. (12)) to define a new measure of entanglement for open curves, the *bracket polynomial of a curve in 3-space* [55]. Intuitively, this is given as an average of bracket polynomials across all knotoid diagrams of the curve obtained by projecting the curve on the sphere S^2. It can be proven that the bracket polynomial is a continuous functions of the spatial coordinates of the curve and that, in the case of polygonal curves, it attains a simple expression based on the spectrum of all the possible knotoids that can be formed by the curve. The lower the number of edges, the simpler the expression, as it becomes impossible to tie the more complex knotoids.

A second approach builds on this first one to define the *Vassiliev measures of complexity of opened and closed curves in 3-space* [56]. Vassiliev invariants, also known as finite type-invariants, are knot invariants that can be extended to curves having a finite number of singular points (i.e., self-intersections). A certain kind of Vassilev invariant can be defined as an extension of the Jones polynomial to such curves. This invariant can be put in relation to the *enhanced Jones polynomial* $J_K(q) = (q + q^{-1})V_K(q)$, with $q = t^{-1/2}$, by substituting $q = e^x/2$ and expanding $J_K(q)$ in powers of x. The coefficients of x^k in this series are the Vassiliev invariants of order k [57]. This expansion is possible both for knots and for knotoids, allowing one to define the kth-order Vassiliev measures of open curves in 3-space by averaging over all possible knotoids projections on S^2, as for the bracket polynomial. Importantly, as demonstrated in [56], the Vassiliev measures are continuous functions of the coordinates of the open curve, and converge to their corresponding Vassiliev invariants as the ends of the curve tend to coincide. Furthermore, it is possible to compute them, and particularly the second-order Vassiliev measure directly from the coordinates of the curve, without having to compute any polynomial. Also in this case, the calculation is simpler for polygonal curves, as it can be expressed over a sum of geometrical probabilities; the shorter the polygonal curve, the lower the number of terms to be considered in the sum.

2.7.5. Slipknots and knot matrices

The ability to assign a topological status to open chains, either through circularization or by the knotoid approach, allows one not only to assign a knot type to the whole chain, but also to its subportions. This can be used for example to localize the *knotted portion* of a chain i.e., the shortest portion of it that—upon closure—hosts the same kind of knot as

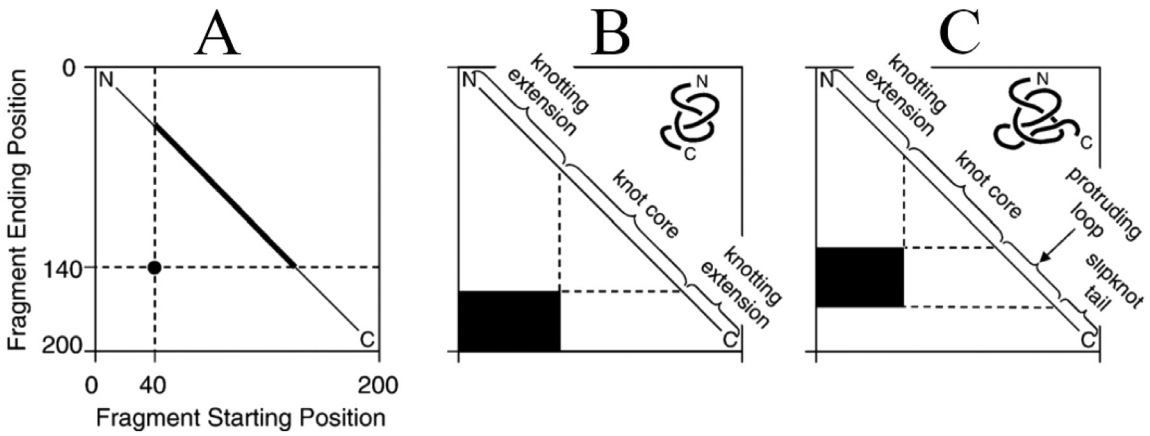

Fig. 19. Knot matrix for visualizing knots and slipknots in proteins. **A**: Each point in the lower left region corresponds to a fragment or partial structure (bold line segment) within the whole chain. The bottom left corner corresponds to the complete chain. **B**: The knot matrix is shown for a hypothetical knotted filament. The coloured region comprises the partial structures that would be judged to be knotted. The lengths of the sides reveal how deep is the knot. **C** The knot matrix is shown for a hypothetical slipknotted filament. The complete chain would be judged to be unknotted in the mathematical sense.
Source: Adapted from [58].

the whole chain [10]. More generally, the possibility to map the local geometrical properties of a portion of the chain to a knot type allows one to identify the portion of the chain whose topology is not that of the whole chain. This includes *slipknots*, portions that appear locally knotted only to become untied when one considers a longer section of the chain. This information can be condensed in the so-called *fingerprint* or *knot matrix*, whose elements a_{ij} contain the topology of the chain segment comprised between beads i and j of the chain (Fig. 19). This instrument is particularly useful in characterizing the entanglement of proteins, see Section 6. Slipknots can be identified using a knot fingerprint: they correspond to regions representing non-trivial knots and separated from the corner of a fingerprint matrix [59].

2.8. Topology in field theory

Physical quantities are often defined throughout space, as continuous entities. This is the case, for example, of electromagnetic and gravitational fields and, if one disregards their microscopic constituents, of fluids. In this case, the dynamical variable is no longer a finite localized object, such as a particle or a polymer filament discussed previously, but a field. The nature of the field depends on the intrinsic nature of the physical object. For example, it could be a vector describing a magnetic field or the velocity of a fluid. In liquid crystals, the field is the extrapolation of the direction of microscopic anisotropic particles that can be described with a director, similar to a vector but without an arrow. In this case we talk about director fields instead of vector fields. More generally, different fields can map the position of scalars, vectors, tensors, or other target spaces. Furthermore, the approach of field theory can also be used to describe objects such as polymers, despite their discrete nature. The most general and unified perspective of topology arising in matter thus comes when we take the more formal framework of field theory, as it is able to describe topological objects including, but not limited to, those of soft matter.

Despite the fact that, at first glance, knots and field defects might appear to be completely different objects, their common ground is that they are topological objects that depend on global properties of the system, rather than on local properties and interactions. For both types of object one can define topological invariants and equivalence classes that characterize the physical properties of the object in question. In fields, particularly useful classification tools come from homotopy theory.

Topology in field theory has been particularly studied in high-energy and quantum physics and at the end of the 1980's led to the discovery of a direct connection between knots and the more general formalism of field theory. In work that led to him being awarded the Fields medal [60], Witten showed that Jones polynomials, used to characterize knots, arise naturally in quantum field theory and found an intrinsically three-dimensional definition for them. This overcame the problem of all traditional definitions of topological knot invariants through polynomials that are built on the projection of the knot in a 2D space, then requiring a proof that the result is independent of the particular projection.

Below we discuss topology in field theory and emergent topological structures in fields that behave as discrete objects, including string-like objects that can be tied into knots and links. Such structures appear in liquid crystals, in other complex fluids, and in the more theoretical descriptions of polymer physics.

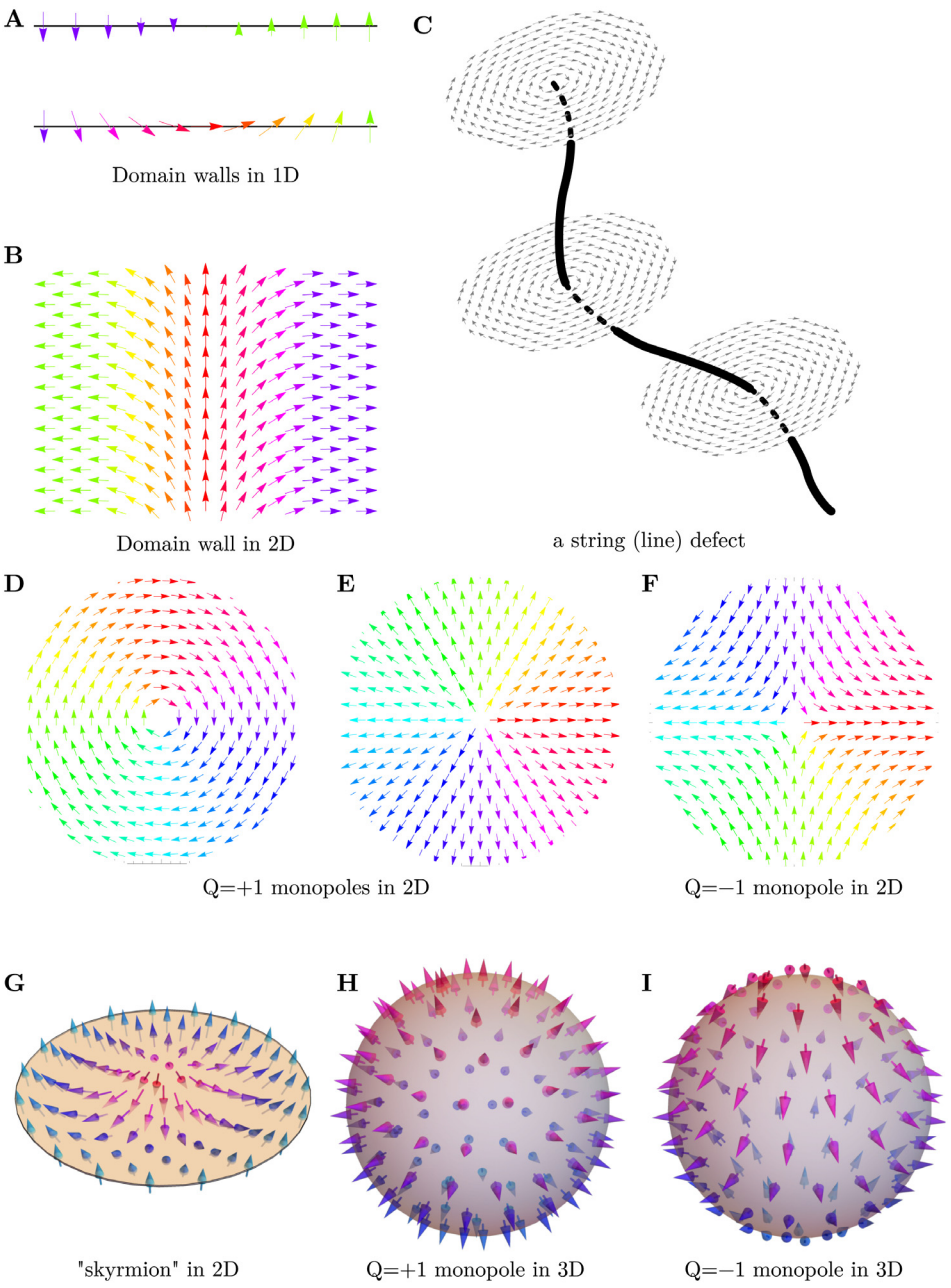

Fig. 20. Defects of a vector field. **A** Two realizations of a domain wall in 1D: (top): vectors depart from the ground state (the preferred magnitude); (bottom): vectors obey the ground state, at expense of gradients (elastic energy). **B** A wall in two dimensions between oppositely oriented domains. **C** A line defect in a 3D space has codimension 2; perpendicular to the defect line is a two-dimensional space. **D,E** Two different realizations of a monopole (point defect) in two dimensions with the winding number $Q = +1$. **F** A monopole with the opposite winding number, $Q = -1$. **G** A 2D skyrmion, a type of topological soliton with the field allowed three-dimensional values. **H,I** Monopoles in 3D with opposite topological charge.

2.8.1. Topological structures in the continuum

Topological properties of field structures depend directly on the degenerate space of global and/or local minima of its energy functional (the ground state manifold; in quantum mechanics these are also called vacuum states), each corresponding to a different uniform field arrangement. Without prescribed boundary conditions, the ground state is usually a field configuration that is uniform in space, since field gradients typically cost energy.[7] When boundary

[7] A notable exception are chiral nematics, where the ground state prefers helical order.

conditions are prescribed, a solution that cannot be continuously deformed into the uniform ground state without violating the boundary conditions is broadly designated as a *topological defect*, and is usually associated with higher energy cost compared to the ground state. On a chosen domain, for example over an infinite domain with the boundary conditions at infinity, states that cannot be continuously converted into each other belong to distinct topological classes, and can be classified by topological invariants. The advantage of using topology to classify field configurations is that this classification is universal and independent of the local details of the field.

Topologically nontrivial behaviour occurs when the ground state manifold cannot be shrunk continuously to a point; in other words, when it contains holes, allowing for the possibility that a region may have to deviate from the ground state even if its boundary has minimum energy. If the target space of the field, the field variable, itself has this property, then instead of just deviating from the ground state according to the energy functional, it may not be possible to find a continuous solution at all for some boundary conditions without the field variable remaining undefined in some places. Let us take, for example, a field described by normalized vectors. The space of normalized vectors is the surface of a unit sphere: states inside and outside, including the zero vector, are not allowed. Having these *holes* in the domain, where normalized vectors cannot be assigned, allows nematic defects to be regarded as discrete physical objects based on the locations where the underlying material changes its state. These are topological defects in a specific sense, as they refer to local objects—points, curves, surfaces—whereas the field, as a whole, does not possess a nontrivial topology; further, topological invariants can be assigned to defects and they can be studied individually.

These localized objects (especially defect lines) being (locally) stabilized by the topological properties of the ground state manifold, can be knotted, linked, and manipulated in other ways (see Sections 3.5.2 and 7.3), within the restrictions imposed by the field equations and the boundary conditions. Around the defects, gradients of the field and the associated energy usually diverge too. Whenever relevant, we will refer to such defects as *singular defects* to distinguish them from topologically nontrivial structures where the field is well defined everywhere, which will be called *topological solitons*. Formally, the topology of such a field can be understood by studying the domain obtained as the complement of the defects. In traditional knot theory, this involves studying the knot complement, but in field theory, the properties of the ground state manifold itself add to the topological structure of the singular defects. This makes a connection between the topology of fields and the topology of discrete objects, described in the first part of this section, and allows a treatment not unlike that seen in systems of particles and polymers.

Often, the physics of a system can be expressed either with a topologically trivial field variable, or a topologically nontrivial lower-dimensional field variable, usually chosen to match the ground state manifold, excluding the higher-energy states. A simple example of this is a complex-valued light field which can reach any value including zero, compared to its complex phase, which is undefined at the zeroes, so that locations of zero light intensity are identified as singular defects of the phase. Topological defects and solitons can be of different dimensionality; see Fig. 20 for a few examples of topological defects in a vector field in one, two, and three dimensions. They may be infinitely extended in some spatial directions such as in *domain walls*, extending to infinity in all but one direction, or *string*-like objects, infinite in one direction; or they may be localized in all directions, as in *monopoles*.

Field configurations with non-trivial topologies are induced and stabilized by the boundary conditions imposed on the fields. In a model in which various ground states exist, enforcing a condition such that the field reaches a different ground state in different parts of the boundary[8] may have the effect of forcing the solution to be in one of many nontrivial topological classes. In these cases, relaxation to one of the uniform, i.e., topologically trivial, ground states is impossible because one would need to violate the boundary conditions. As an example consider a vector field confined to a box, which has two ground states with the same energy but different field values, say, $\pm v$. Topologically trivial ground states are the ones in which the field is uniform and takes on the same value, say $+v$, everywhere in the box. Suppose now that we impose boundary conditions such that the field takes on the value $+v$ on the right wall of the box and $-v$ on the left wall. These boundary conditions are incompatible with either uniform ground state, and any acceptable solution will be space-dependent and interpolate between the two values, as in Fig. 20**B** (*Domain Wall*). As we will see later, this solution has a nontrivial topology, and it exhibits a topological defect, i.e., a region where the field departs from the ground state somewhere in the middle of the box. This defect cannot relax to either uniform ground state by any local dynamics, because this would imply a violation of the boundary conditions: the defect is stable due to its non-trivial topology. This is sometimes referred to as *topological protection*. Another example is that of a string-like defect, a line defect, or a vortex, in which a vector field is constrained to point in different directions at the boundary, see Fig. 20**C**. In this case, one detects the non-trivial topology by going around a circle at the boundary and measuring the rotation of the vector field.

In the examples above, the solutions are characterized globally, but the same approaches can be applied locally on individual singular defects, for example, referring to normalized vectors, by focusing on a subset of the whole space surrounding the defect. In the example of the vortex, the defect can be identified by going around its core, i.e., the region where the field is not in the ground state, even if it is not at the outer boundary, and measuring winding numbers or other relevant topological invariants. For any field configuration one can define a conserved quantity, characteristic of its global topology, and independent of the local dynamics, called *topological charge* [61] (see the discussion below for a formal definition). These topological invariants are known under different names, such as winding number, depending

[8] The boundary conditions may be given at infinity, if the field is defined on infinite space, or it may be the physical boundary in the case of a confined system.

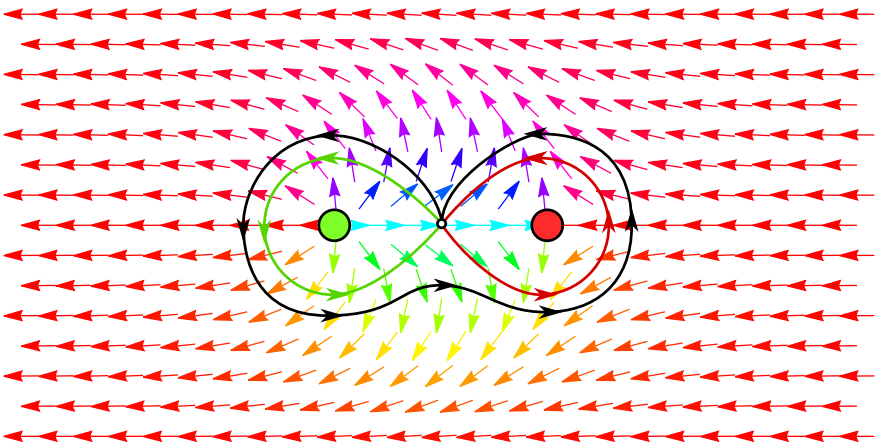

Fig. 21. Defect and anti-defect pair in 2D. Two monopoles of charge $+1$ (green dot) and -1 (red dot) respectively, are detected by computing the winding number along the green and red path. The black path that encircles both gives rise to a total topological charge $Q = 0$, demonstrating additivity.

on the dimensionality of the space and the field in question. A general field configuration can combine several localized defects that possess individual charges; the total charge is conserved under local changes, even if they involve merging or splitting of defects. The charges are additive, so the topological charge can be understood to count the net number of defects or solitons, similarly to electric charge. However, addition must be understood in a generalized way, if the associated homotopy group of the ground state manifold is not isomorphic to integers, such as in the case of liquid crystals.

For example, for a vector field, in a given field configuration one could have a defect of charge $+1$ and a defect of charge -1 but the total topological charge of the configuration is zero as it is possible to reorient the vectors locally in order to have a configuration with no defect in the end. Another way to see this is that far away from the local defects the field configuration is the same as one in the absence of any defect. Fig. 21 shows the example of such a case for two monopoles of charges $+1$ and -1 in two dimensions. In general one can talk about pair production or annihilation of defects. In physical systems this is behaviour encountered, for example, in the dynamics of liquid crystals and in turbulent fluids or superfluids.

Before giving a more formal introduction to the mathematics describing topological defects, let us look in more detail at a simple example in which topological features arise: a vector field in two space dimensions. Consider the case of a two-component vector field $\boldsymbol{\phi} \equiv (\phi_1(x, y), \phi_2(x, y))$ in two space dimensions, with a potential energy density given by

$$V(\boldsymbol{\phi}) = \tfrac{1}{2}\lambda \left(|\boldsymbol{\phi}|^2 - v^2\right)^2 \tag{19}$$

where v and $\lambda > 0$ are constants. This potential describes, for example, the magnetization vector in a two-dimensional ferromagnet or nematic director in a two-dimensional liquid crystalline system. The energy is minimized by field configurations that satisfy

$$|\boldsymbol{\phi}|^2 = v^2. \tag{20}$$

Eq. (20) states that the minimal energy configurations form a circle of radius v in field space. In addition to the potential, there is normally also an energy contribution from the field gradients. The global ground states of the system with zero gradient are uniform field configurations in which $\boldsymbol{\phi}(x, y)$ has length v and points in the same direction at all points (x, y) in 2D space. This configuration corresponds to picking a specific point on the circle of ground states in field space.

Suppose now we want to describe a more general field configuration, which is not one of the uniform ground states, but has the property that any non-zero energy density is confined in a finite region of space. This requires that, as $r = \sqrt{x^2 + y^2} \to \infty$, such a configuration must tend to one of the ground states, described by a point on the circle of radius v in field space. However, one can reach different limiting orientations — different points on the circle — as one approaches infinity from different directions in coordinate space. More precisely, if one thinks of spatial infinity as a circle of radius R in the limit $R \to \infty$, such field configurations are classified by maps from this very large circle in physical space to the minimal-energy circle in field space. We denote this map by a function γ, which associates each point of the large circle at infinity, i.e., each direction in physical space, with a point on the circle of radius v in field space, i.e., a direction of the vector field

$$\gamma : \text{circle at spatial infinity} \to \text{minimal-energy circle in field space.} \tag{21}$$

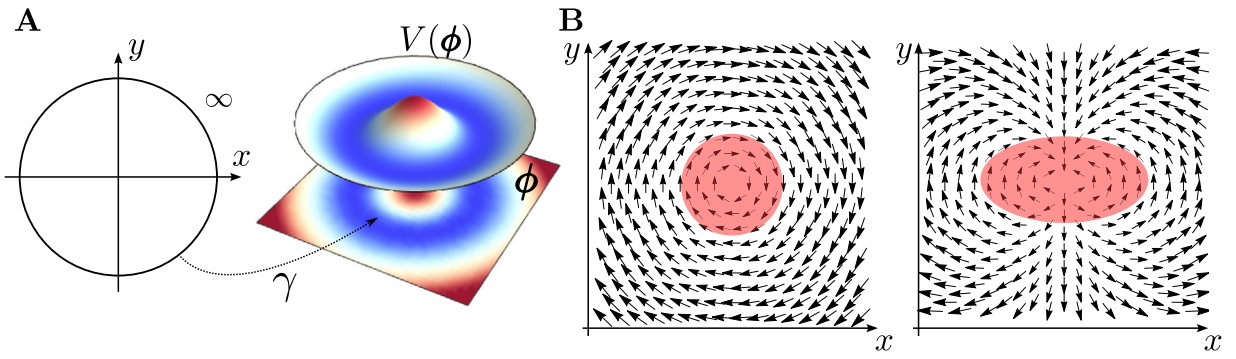

Fig. 22. A The function γ maps the circle at spatial infinity in coordinate space (x, y) to the minimal energy circle in field configuration space (ϕ_1, ϕ_2). The potential profile is that of Eq. (19). **B** Field configurations with winding number 1 (left) and 2 (right). The red shadow indicates the region of physical space where the field deviates significantly from its ground state, which can be identified with the location of the defect.

The map and potential are represented in Fig. 22**A**. The large circle at infinity can be thought of as the place where one assigns the boundary conditions to the problem; for confined systems, it is replaced by a closed curve at the boundary. As long as the boundary of space has effectively the topology of a circle, this distinction is unimportant.

The map γ may fall into different classes, distinguished by their winding number. This is an integer w that counts how many times the map γ spans the circle of ground states as one goes around the spatial boundary circle once. For example, for a global ground state, as we go around the spatial boundary circle the field does not move from its position on the ground state circle in field space, i.e., there is no winding, $w = 0$. To have a configuration with winding number $w = 1$, the vector field orientation must change by a full 2π (e.g., anticlockwise) as one goes around the spatial boundary circle. Negative winding is also possible, if the vector field goes around the ground state circle by 2π in the opposite direction. Some examples of field configurations with different winding numbers are illustrated in Fig. 22**B**.

Let us now describe in more detail a configuration with non-zero winding in our example of the two-dimensional vector field. For this, it is useful to write the field ϕ in terms of radial and angular field variables $\rho(x, y)$ and $\psi(x, y)$,

$$(\phi_1, \phi_2) = (\rho \cos\psi\,, \rho \sin\psi\,)$$

and also to use polar coordinates for space, $(x_1, x_2) = (r\cos\theta, r\sin\theta)$. A field configuration winding w times at spatial infinity has the following property,

$$r \to +\infty : \qquad \rho(r, \theta) \to v, \quad \psi(r, \theta) \to w\theta. \tag{22}$$

where ρ is the magnitude of the field and v is its ground state value. The condition above implies that, at spatial infinity, the angular field variable changes by $2\pi w$ as the angular spatial variable θ describes a full circle, while $\rho = v$ stays fixed. In this case the map γ is explicitly given by

$$\gamma(\theta) = w\theta \tag{23}$$

and it describes the phase of the field as a function of the angular direction in space.

Eq. (22) can be taken as a boundary condition for the local, dynamical field equations, referring not necessarily to time evolution, but to any equations that prescribe the behaviour of the field. This boundary condition selects solutions with fixed winding w. Any such solution must contain a defect, i.e., a region where the field is either singular or its absolute value departs from its ground state, e.g., $|\phi| = 0 \neq v$. This region corresponds to the core of the defect. Whether it is singular or not depends on the details of the field dynamics.[9] In the example above, spatial infinity can be replaced by the actual boundary of space for confined systems or, more generally, by a circle surrounding the defect if one wants to consider local winding number. The value of the winding number w associated with a defect can be expressed formally by integrating a local expression along a closed loop $\gamma(\theta)$ parameterized by $\theta \in [0, 2\pi)$, enclosing the defect

$$w = \frac{1}{2\pi}\int_0^{2\pi} (\boldsymbol{\gamma}' \cdot \nabla\psi) d\theta \tag{24}$$

where $\boldsymbol{\gamma}'$ is the tangent vector to γ at θ. If the curve γ is at the spatial boundary, or if it encloses all the defects that are present, then one obtains the total winding number, i.e., the quantity with a well-defined topological meaning. Concatenating two curves starting from the same basepoint gives a sum of the individual winding numbers; see Fig. 21 for examples of curves that enclose one or all defects in the system. To make a parallel with knots, this is the analogue of the Gauss linking number.

[9] We are referring to generalized dynamics (meaning any relation holding for the field and its derivatives).

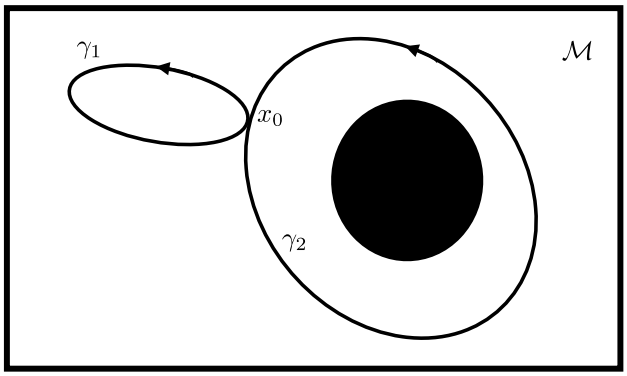

Fig. 23. A sketch of space $\mathcal{M}$ with non-trivial π_1 (the black region is not part of $\mathcal{M}$): the loop γ_1 is contractible, the loop γ_2 is not. The two loops share the same basepoint x_0, which enables one to compose them, by traversing one then the other, giving the group structure on $\pi_1(\mathcal{M})$.

The total winding number does not depend on the detailed form of the function γ, but is a property only of its *homotopy class* [62]. Two maps are said to be in the same homotopy class if they can be continuously deformed into one another. For example, if we replace Eq. (23) by the function $\gamma(\theta) = w\,\theta^2/2\pi$, this would lead to the same winding number. In other words, the topology of a given field configuration is characterized by the homotopy class of the function that maps the spatial boundary, i.e., spatial infinity, to the space of minimal energy configurations of the field variable.

If we consider a space $\mathcal{M}$ as the set of field configurations that minimize the energy, often called the *ground state manifold*, for example, the circle of radius v in the previous example, the set of homotopy classes of functions that map the circle at the spatial boundary to $\mathcal{M}$ is denoted by $\pi_1(\mathcal{M})$. Its elements are topological invariants of $\mathcal{M}$.

The example above describes a point-like defect in two spatial dimensions, but other topological invariants exist; they can be introduced to generalize the discussion to d space dimensions and to defects extended in p directions — strings, membranes, etc — see Fig. 20. A defect that extends in p directions in a d-dimensional space is said to have *codimension* $d - p$: this is the number of directions transverse to the defect. For example, a completely localized object, a point, has $p = 0$ (codimension d), a string-like object has $p = 1$ (codimension $d - 1$), and so on.

A field configuration with a non-zero energy density localized in p directions approaches an element of $\mathcal{M}$ at spatial infinity in the remaining $d - p$ transverse directions. Such a localized feature can be surrounded by a large sphere of dimension $n = d - p - 1$. The inequivalent boundary conditions can then be classified by functions from a large n-dimensional sphere S^n to the ground state manifold $\mathcal{M}$

$$\gamma : S^n \to \mathcal{M}, \quad n = d - p - 1. \tag{25}$$

Such maps describe closed n-dimensional surfaces[10] in $\mathcal{M}$. Two maps γ_1 and γ_2 are said to belong to the same *homotopy class* if the corresponding surfaces can be continuously deformed one into another. The set of homotopy classes of n-dimensional surfaces forms a group[11] which is called the *n−th homotopy group of* $\mathcal{M}$, $\pi_n(\mathcal{M})$. All closed surfaces on the ground state manifold $\mathcal{M}$ that can be continuously contracted into a point are equivalent to the uniform field. Thus, non-trivial topological field configurations are allowed only if $\mathcal{M}$ contains non-contractible closed surfaces. This is illustrated in Fig. 23 for the case $n = 1$, where the n-dimensional surfaces are closed loops. This leads to the statement that in d space dimensions, topological defects of dimension p are classified by the elements of $\pi_{d-p-1}(\mathcal{M})$.

The example we discussed above of the vector field in two dimensions, Eq. (19), corresponds to the case $d = 2$, $p = 0$, $n = d - p - 1 = 1$. In this example, the ground state manifold is the circle $\mathcal{M} = S^1$, and it admits non-contractible loops that wind w times around it, for any integer w. The relevant homotopy group is $\pi_1(S^1) = \mathbb{Z}$, since the winding could happen either clockwise or anticlockwise. It is the codimension $d - p$ that determines which homotopy group can be used: for example, particles in $d = 2$ and strings in $d = 3$ are classified by the same homotopy group, namely $\pi_1(\mathcal{M})$.

The topological classification we gave above indicates which defects may occur in a theory. However, this classification can miss important and interesting properties of field-theory solutions. For instance, in a given theory, there may be different asymptotic field configurations — boundary conditions — all with the same topological characteristics. Which of these should be used when trying to find a topological defect solution? This can lead to situations in which there exist different defect solutions, all having the same topological charge, see e.g., [63,64]. Furthermore, whether these defects actually exist and form in a given situation depend on the details of the physical system in question, which cannot be answered using topology alone; these issues depend also on local features such as the nature of interactions. Similarly,

[10] To be precise, the definition involves *based* maps, i.e., such that the corresponding surfaces all have in common a point (base) $x_0 \in \mathcal{M}$.

[11] The group operation between two classes is defined by the concatenation of two representative surfaces in each class. It can be shown that the homotopy class of the resulting surface does not depend on the choice of representatives, and therefore it is a well defined operation between two homotopy classes.

whether a given defect is stable or unstable depends on local interactions, as, for example, topology does not forbid a defect to decay into objects which, individually, have lower topological charge, as long as the total topological charge is conserved. If a defect with a higher topological charge has more energy than the sum of two smaller charges with the same sum, all one can say is that the defect with *lowest* topological charge is stable.[12]

Below we discuss some examples, starting with the lowest codimension $d - p$. Although the corresponding field theories apply to disparate physical systems — liquid crystals, superfluids, particle physics, cosmology — the underlying mathematical structure is universal. Many topological defects arising in physics can be related to the breaking of a global symmetry by the ground state.

Domain walls. These are codimension-1 objects. This case is important but somewhat special, because the "sphere" that surrounds the defect at spatial infinity is disconnected. For example, in $d = 1$, spatial infinity is the set of two points $\pm\infty$. In terms of homotopy groups, the relevant maps are those from $S^0 = \{-1, +1\}$ to $\mathcal{M}$. The set of homotopy classes of these maps is called $\pi_0(\mathcal{M})$, and it classifies the disconnected components of $\mathcal{M}$. Models with non-vanishing $\pi_0(\mathcal{M})$ have localized lumps of energy called kinks.

For $d > 1$, domain walls are infinitely extended in $p = d - 1$ directions and localized in one, which we will call z. Each domain wall separates space into different disconnected components. These generally occur in systems with broken discrete symmetries. A typical example is a real scalar $\phi(\mathbf{x})$ with a $\mathbb{Z}_2$-symmetry $\phi \to -\phi$, such as the one described by the potential energy density

$$V = \frac{\lambda}{2}\left(\phi^2 - v^2\right)^2. \tag{26}$$

The $\mathbb{Z}_2$ symmetry is broken in the ground state: the potential is minimized when $\phi^2 = v^2$ and $\mathcal{M} = \{v, -v\}$. Therefore, $\pi_0(\mathcal{M})$ is composed of two elements (if we choose $1 \in S^0$ to be mapped to $+v$): one is trivial, corresponding to $\phi \to v$ as $z \to \pm\infty$ (same ground state at both infinities); the non-trivial element is associated with configurations such that

$$\lim_{z\to+\infty} \phi(x_i, z) = v, \quad \lim_{z\to-\infty} \phi(x_i, z) = -v \qquad i = 1 \ldots d-1. \tag{27}$$

A solution of the field equations satisfying these boundary conditions cannot decay into either homogeneous vacuum solutions $\phi = \pm v$. The region of space where the field differs from the ground state is called a *defect*. One can define the topological charge

$$Q = [\phi(+\infty) - \phi(-\infty)]/2v.$$

Exchanging v and $-v$ in Eq. (27) changes the sign of $Q \to -Q$. In this example $Q = 0, \pm 1$.

This kind of situation extends to models with any finite number, or an infinite discrete number of ground states, e.g., periodic potentials, for which $\pi_0(\mathcal{M}) = \mathbb{Z}$. Domain walls are found, for example, in cholesteric liquid crystals under an applied magnetic field [65].

Lines, strings and vortices. These are codimension-2 defects, classified by $\pi_1(\mathcal{M})$. They are string-like objects in $d = 3$ spatial dimensions, and particle-like configurations in $d = 2$. This class includes disclinations in liquid crystals, vortices of superfluid helium and type-II superconductors, cosmic strings of cosmology and high energy physics, etc. According to the general classification, these topological defects may arise when $\pi_1(\mathcal{M})$ is non-trivial. This is, for example, the case of a two-component real vector field $\boldsymbol{\phi}$, as in Eq. (19). In this case, the potential is invariant under the group $G = O(2)$ of 2-dimensional rotations in field space. This symmetry is completely broken by a choice of a ground state belonging to the continuous family $|\boldsymbol{\phi}| = v$. The ground state manifold is the circle S^1. As we saw above, vortices are classified by an integer, the winding number, which counts how many times the field at the spatial boundary, or at infinity, winds around the ground state manifold. This yields $\pi_1(S^1) = \mathbb{Z}$, allowing integer valued w.

If, instead of a vector, one has a director field, as is the case for two-dimensional nematic liquid crystals, the ground state manifold is the unit circle S^1 with opposite points identified, denoted by $S^1/\mathbb{Z}_2$. Vortex-like defects — also called disclinations — with half-integer or integer winding number are topologically allowed, as observed by Frank [66], and illustrated in Fig. 24. In liquid crystals, it is customary to work with the normalized director, $\boldsymbol{n} = (\cos\psi, \sin\psi)$, which distinguishes localized singular defects, where the angle is not defined. The winding measured around a closed loop can be realized in different ways, as long as the total winding of the encircled defects is the same.

In three-dimensional nematics, one can also observe codimension-2 line defects: disclination lines. The field space is now $S^2/\mathbb{Z}_2$, i.e., the sphere S^2 with antipodal points identified, also known as the real projective plane $\mathbf{RP}^2$, or equivalently as the Grassmannian $Gr(1, 3)$ [68]. Although $\pi_1(S^2)$ is trivial, as all loops on the two-sphere are contractible, $\mathbf{RP}^2$ contains non-contractible loops: these are loops connecting the antipodes, such as the north and south pole, shown in Fig. 25**A**. Moreover, loops going from the north pole to the south pole and back, as in Fig. 25**B**, *are* contractible. Therefore, $\pi_1(\mathbf{RP}^2) = \mathbb{Z}_2$ contains only two equivalence classes, one of which is the trivial one. This implies that there is only one topologically non-trivial local profile, a single type of disclination line. Along a loop encircling a line defect, the director is non-orientable and we find a $\mathbf{n} \to -\mathbf{n}$ sign discontinuity along the loop. This topological fact is often not of primary importance compared to energetic considerations. Line defects are often seen to have either a $+1/2$ or $-1/2$ profile, even though a $+1/2$ profile can change to a $-1/2$ profile smoothly through a twist deformation; see Fig. 25**C**.

[12] This gives rise to strong cosmological constraints for high-energy theories that tend to produce too many stable defects in the early universe. This fact was one of the driving motivations for the original proposal of cosmological inflation.

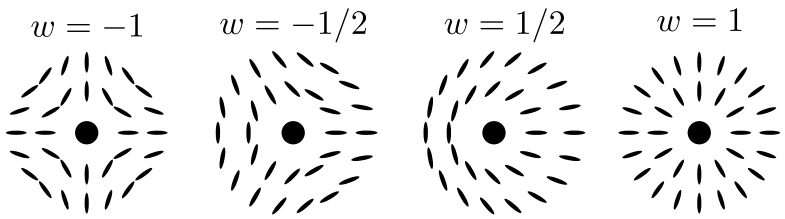

Fig. 24. Defect profiles in two-dimensional nematics and their winding number w. The defects are singular, with the director undefined in the middle.

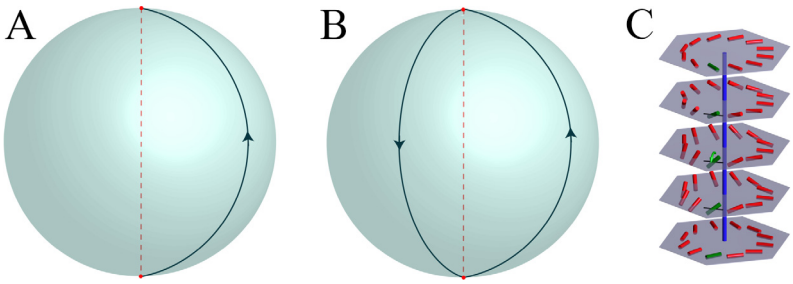

Fig. 25. **A** The curve joining the north and south poles is not a loop on the sphere, whereas it is a non-contractible loop on the sphere with antipodal points identified. **B** The loop that goes from the north pole to the south pole and back can be shrunk to a single point. **C** In three dimensions, all half-integer defect lines are topologically equivalent. By rotating the director around a perpendicular in-plane axis, a disclination with a $-1/2$ profile (bottom) is transformed into one with a $+1/2$ profile (top).
Source: **C** reproduced from Ref. [67].

Monopoles and point defects. These are codimension-3 objects, which are particle-like configurations in $d = 3$. They are classified by $\pi_2(\mathcal{M})$. A representative example can be found in unit vector fields in three dimensions, which describe, for example, magnetization in ferromagnetic systems, or, up to a sign, the director of nematic liquid crystals. For systems with a 3-component vector field, the topological charge associated with the field can be calculated by evaluating the expression

$$q = \frac{1}{4\pi} \int_{S^2} \nabla \times \mathbf{A} \cdot d\mathbf{S} \tag{28}$$

on the sphere S^2 enclosing the defect with dS_i an oriented surface element; note the connection to Gauss' law. This is valid if the enclosing sphere does not intersect the defect region, meaning the field on the sphere lies on the ground state manifold and can thus be normalized to a unit vector field $\mathbf{n}$. The auxiliary field $\mathbf{A}$ is a vector potential defined by $A_i = (e_1)_j \partial_i (e_2)_j$, where $(\mathbf{e}_1, \mathbf{e}_2, \mathbf{n})$ form a right-handed frame field. $\mathbf{A}$ is defined up to a gauge transformation rotating the frame around the vector $\mathbf{n}$, which allows mixing of $\mathbf{e}_1$ and $\mathbf{e}_2$, but this does not alter the value of $\nabla \times \mathbf{A}$, given by $(\nabla \times A)_i = \epsilon_{ijk}\epsilon_{abc} n^a (\partial_j n^b)(\partial_k n^c)$,[13] which depends only on $\mathbf{n}$.

In high-energy physics, point defects are called *monopoles* and arise, for instance, from the breaking of an internal symmetry group $SU(2)$, the group of complex 2×2 unitary matrices, down to $U(1)$, the group of complex phase rotations. In this case the ground state manifold is topologically equivalent to S^2, and since $\pi_2(S^2) = \mathbb{Z}$, their topological charge takes on integer values. See Fig. 20**H,I** for examples of monopoles of different charges and field configurations.

In nematic liquid crystals, the second homotopy group is the same as for vector fields, $\pi_2(\mathbf{RP}^2) = \mathbb{Z}$, so nematic monopoles, usually referred to as point defects or hedgehogs, can also arise. However, there is a caveat: the expression for $\nabla \times \mathbf{A}$ is odd in powers of n, so it reverses under the nematic symmetry. This means that, strictly, point defects in nematics have an ambiguous sign of their topological charge. In the presence of line defects, one cannot assign vector directions to the director field without introducing sign discontinuities. Ambiguity of relative signs of defects leads to a weaker form of the conservation law, conserving only parity of the total topological charge. Instead, the monopoles in Fig. 20**H,I**, ignoring the arrow directions, are known as radial and hyperbolic hedgehog, respectively, based on the general shape of their director field. Topological charge can also be assigned to closed defect loops as a whole, as they can also be enclosed in a sphere.

An example of a point defect occurs in a homeotropic nematic droplet [69,70]. The interaction of the nematic with the interfacing medium can be arranged to strongly prefer homeotropic anchoring, that is, at the boundary the director $\mathbf{n}$ prefers to be orthogonal to the bounding surface. Consequently, on the surface of a spherical droplet, the director field

[13] $\epsilon_{\alpha\beta\gamma}$ is the Levi-Civita tensor.

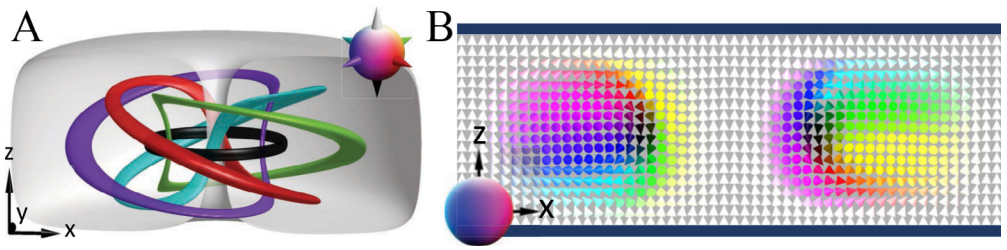

Fig. 26. Three-dimensional texture of a $\nu = 1$ hopfion. **A** pre-images, locations of constant field direction, are linked with each other. **B** Cross section shows variation of field direction with no singularities.
Source: reproduced from [78].

points radially (inwards or outwards are equivalent descriptions). This topologically requires the existence of a point defect at the droplet centre, with a radial hedgehog profile, Fig. 20**H,I**, or a topologically equivalent structure, such as a small disclination ring. Hyperbolic point defects, on the other hand, can be found next to spherical inclusions with homeotropic boundary anchoring [71].

More generally, one can introduce other topological properties of $d = 3$ nematics, namely those characterized by homotopy classes of maps from tori, rather than spheres, to the ground state manifold [72]. An example is a closed defect line, a disclination loop, which is classified by maps from the two-torus $\mathbf{T}^2$ to $\mathbf{RP}^2$. This corresponds to encircling the defect with a tubular, rather than spherical, domain, and is a natural description of closed disclination loops.

Topological solitons. There are also field configurations without singular defects that are topologically distinct from the homogeneous uniform-field configuration. The field assumes allowed values from the ground state manifold within the entire sample, with no singularities. For a theoretical treatment, we can assume that it fills the entire space, $\mathbb{R}^3$, or its one-point compactification S^3, but in physical samples, field equations practically restrict the relevant structure to bounded regions within a greater sample. These are also often referred to simply as topological solitons, and can behave like quasi-particles moving within the surrounding uniform field. In materials science, such structures are studied in magnetic systems, where many different versions have been observed [73], and in chiral liquid crystals [74].

One variant of such structures are the so called *baby skyrmions*,[14] which are two-dimensional solitons; see Fig. 20**G**. They can be seen in chiral ferromagnets [73] and chiral nematic liquid crystals [75]. Topologically, the baby skyrmion field on the S^2 compactification of the 2D Euclidean plane is equivalent to the field on a sphere enclosing a point defect, so the expression for the skyrmion charge is the same; Eq. (28). Baby skyrmions in liquid-crystal systems are typically stabilized using the chirality of the cholesteric interaction.

Hopf solitons are the final type of topological soliton, mathematically associated with the homotopy group $\pi_3(S^2) = \mathbb{Z}$ and the Hopf fibration; see Fig. 26. Given a non-singular unit vector field $\mathbf{n}$ in three dimensions, with uniform boundary conditions at infinity, the Hopf charge is defined as the gauge invariant expression

$$\nu = \frac{1}{(8\pi)^2} \int_{\mathbb{R}^3} \mathbf{A} \cdot \nabla \times \mathbf{A} \, \mathrm{d}V, \tag{29}$$

with $\mathbf{A}$ defined as in Eq. (28). The Hopf charge applied to unit vector fields is equal to the linking number between field preimages, the regions of space where the orientational order points in a chosen direction; see Section 3.5.4. Hopf solitons can be found in confined and frustrated cholesteric systems, where linking and knotting of preimages of the director field is readily observable [75–77].

2.8.2. Fluid helicity and linking number decomposition in fluid mechanics

The topological invariance of Eq. (29) for any vector field $\mathbf{A}$ in $\mathbb{R}^3$ was recognized by Whitehead as early as in 1947 [79], but the result remained very little known. If we take $\mathbf{A}$, subject to the Coulomb condition $\nabla \cdot \mathbf{A} = 0$, as the vector potential of a magnetic field $\mathbf{B} = \nabla \times \mathbf{A}$, we can identify the integral Eq. (29) with its three-dimensional counterpart given by the magnetic helicity, defined by

$$H = \int_{\mathcal{D}} \mathbf{A} \cdot \mathbf{B} \, \mathrm{d}V \ . \tag{30}$$

Here $\mathcal{D} \subseteq \mathbb{R}^3$ is taken to be the domain of the magnetic field. In the context of ideal magnetohydrodynamics — no resistive effects present — assuming that there is no flux of $\mathbf{B}$ through the boundary of $\mathcal{D}$, Woltjer [80] demonstrated that H is conserved under the continuous action of a fluid flow. Hence, by combining Whitehead's realization with Woltjer's

[14] In the particle-physics community, the term *skyrmion* is associated with the codimension-3 topological defects (particle-like) in three dimensions, which are used to describe baryons in the low-energy chiral Lagrangian description of hadrons. The term *baby skyrmions* is used to refer to the two-dimensional structures.

observation, we conclude that H is also a topological invariant of an ideal fluid. An explicit proof of this came only in 1969 with the work of Moffatt [81], who relied on an alternative form of Eq. (30), so-called kinetic helicity, given by replacing **A** and **B** with the velocity **u** and the vorticity $\boldsymbol{\omega} = \nabla \times \mathbf{u}$ of Euler's equations. The proof that kinetic helicity is a conserved quantity of ideal fluid mechanics was given by Moreau [82]. Since helicity, kinetic or magnetic, is one of the few conserved quantities of ideal fluid mechanics and magnetohydrodynamics, it clearly plays a central role in the analysis of fluid flows where magnetic or vortical structures are present. Considering fields localized in linked flux tubes, and using the Biot–Savart law that relates the source field $\boldsymbol{\omega}$ or **B** with its induced field **u** or **A**, Moffatt was able to prove that the helicity integral above could be written in terms of the Gauss' linking number integral, Eq. (12), thus establishing a deep connection between ideal fluid mechanics and topology. An extension to knotted flux tubes was given by Berger and Fields [83], which was followed by the work of Moffatt and Ricca [28], who provided a rigorous derivation of the helicity for an isolated, knotted flux tube in terms of self-linking, through the standard decomposition in terms of writhe and total twist.

The helicity of n vortex or magnetic knots can thus be expressed in terms of their relative flux Φ_i ($i = 1, \ldots, n$) and topological complexity, by reducing the integral formulation of helicity — often difficult to compute — to the directly computable algebraic sum of linking numbers, given by

$$H = \int_V \mathbf{A} \cdot \mathbf{B}\, \mathrm{d}V = \sum_i \Phi_i^2 Sl_i + \sum_{i \neq j} \Phi_i \Phi_j Lk_{ij} \qquad (i, j = 1, \ldots, n)\,, \tag{31}$$

where $Sl_i = Wr_i + Tw_i$ denotes the Călugăreanu–White self-linking number of the ith knot, and Lk_{ij} the Gauss linking number between the knot i and j. Eq. (31) provides a remarkable simplification of the helicity computation, avoiding the cumbersome and often impossible analytical integration of the constituent field lines. Following Witten's approach [60] by interpreting Eq. (30) as an Abelian action, Liu and Ricca [84,85] were able to derive appropriately adapted Jones and HOMFLYPT polynomials from the helicity of fluid knots, thus deepening and extending further the topological foundation of ideal fluid mechanics and providing additional tools to investigate the topological complexity of fluid flows. All this work is now finding many applications in various physical contexts [86], from the analysis of superfluid vortex tangles to the study of defects in condensed matter physics, and from the diagnostics of vortex flows in classical turbulence to the energetics of magnetic fields in the solar corona and astrophysics.

2.9. Path-integral formulation for polymers

Path integrals first emerged in the quantum mechanics of particles as a direct consequence of wave–particle duality. Currently, they are employed to describe many different phenomena, not only in physics, including the diffusion of particles subjected to Brownian motion and, particularly relevant here, fluctuating polymers (polymers as physical objects will be introduced in Section 3.1.1, here we are interested mainly in the field-theoretical formalism). In the latter cases the path-integral formalism is used as a tool for performing the statistical sum over the particle trajectories and the polymer paths. It is thus based on principles that are completely different from quantum interference.

If molecular details are disregarded and coarse grained, a conformation of a polymer chain of length L with ends fixed at two points $\boldsymbol{r}_0$ and $\boldsymbol{r}_N$ may be described by the Gaussian model (Section 3.1.1) with N monomers and mean bond length b such that $Nb = L$. The distribution of the length of all bonds formed by two contiguous monomers $\boldsymbol{r}_i, \boldsymbol{r}_{i-1}$, with $i = 1, \ldots, N$, is proportional to $\exp\left[-\frac{3}{2b^2}\sum_{i=1}^{N}(\boldsymbol{r}_i - \boldsymbol{r}_{i-1})^2\right]$. In the continuous limit $N \to \infty$, $b \to 0$ and $Nb = L$, the Gaussian chain passing through the points $r_0, \ldots, r_N$ is replaced by a continuous path $\boldsymbol{r}(s)$ parameterized by the arc-length $0 \leq s \leq L$. Of course, $\boldsymbol{r}(0) = \boldsymbol{r}_0$ and $\boldsymbol{r}(L) = \boldsymbol{r}_N$. The bond distribution becomes[15] $\exp\left[-\frac{3}{2b}\int_0^L ds \left|\frac{d\boldsymbol{r}(s)}{ds}\right|^2\right]$. The argument of the exponential in the last expression coincides with the kinetic energy term of a particle with the time t substituted by the arc-length s and the coefficient $3/b$ playing the role of the particle mass m. Due to the thermal fluctuations, the path $\boldsymbol{r}(s)$ of the continuous chain is subjected to random changes, so that any curve connecting the points $\boldsymbol{r}_0$ and $\boldsymbol{r}_N$ is an allowed conformation. The value of an observable $\mathcal{O}$ like the mean-square end-to-end distance (Eq. (39)) or the mean-square gyration radius (Eq. (40)) is only dependent on the conformation of the chain, i.e., on its path $\boldsymbol{r}(s)$. As a consequence, the average $\langle\mathcal{O}\rangle$ over all polymer conformations may be expressed in the form of a path integral

$$\langle\mathcal{O}\rangle = \frac{1}{Z(L)} \sum_{\text{all paths from } \boldsymbol{r}_0}^{\text{to } \boldsymbol{r}_N} \mathcal{O}(\boldsymbol{r}(s)) \exp\left[-\beta H\right]. \tag{32}$$

Here $Z(L) = \sum_{\text{all paths from } \boldsymbol{r}_0}^{\text{to } \boldsymbol{r}_N} \exp\left[-\beta H\right]$ is the partition function and H is the total energy of the system

$$H = \int_0^L ds H(\boldsymbol{p}(s), \boldsymbol{r}(s)) \tag{33}$$

[15] Here and in the rest of this section we follow the convention of putting the differential immediately after the integral sign, as this is frequently adopted in the path-integral description of polymers.

where $H(\boldsymbol{p}(s), \boldsymbol{r}(s))$ is the energy density, while $\boldsymbol{p}(s) = \frac{d\boldsymbol{r}(s)}{ds}$. $H(\boldsymbol{p}(s), \boldsymbol{r}(s))$ contains the analogue of the kinetic energy mentioned above plus a potential $U = U(\boldsymbol{r}(s), \boldsymbol{r}(s'))$ that describes the interaction between two points $\boldsymbol{r}(s)$ and $\boldsymbol{r}(s')$ of the continuous chain. An important example of potentials is the one for excluded volume forces

$$U_{ex.\ vol.}(\boldsymbol{r}(s), \boldsymbol{r}(s')) = v_0 \int_0^L ds \int_o^L ds' \delta(\boldsymbol{r}(s) - \boldsymbol{r}(s')), \tag{34}$$

where $\delta(\boldsymbol{r})$ is the Dirac delta function and v_0 is the excluded volume parameter. The functional form Eq. (34) accounts for a polymer in a solution with a so-called *good* solvent, namely the monomers "prefer" to be surrounded by solvent molecules rather than by other monomers [87] and, in this configuration, monomer–monomer interactions are effectively short-range and strictly repulsive.

Eq. (32) summarizes the statistical model of a polymer chain based on the continuous theory of Edwards [88–90]. The passage from paths to fields has proven very useful. This is based on the simple consideration that a polymer conformation can be described not only in terms of paths, but also using the monomer density in space $\rho(\boldsymbol{r}) = \int_0^L ds\, \delta(\boldsymbol{r} - \boldsymbol{r}(s))$, where $\boldsymbol{r}$ is any point of the space. $\rho(\boldsymbol{r})$ corresponds to the density of a uniform distribution of monomers concentrated along the polymer's backbone $\boldsymbol{r}(s)$. Next, it is required that $\rho(\boldsymbol{r}) = \psi^*(\boldsymbol{r})\psi(\boldsymbol{r})$, with ψ^*, ψ being a couple of complex fields constrained by the consistency condition $\psi^*(\boldsymbol{r})\psi(\boldsymbol{r}) = \int_0^L ds\, \delta(\boldsymbol{r} - \boldsymbol{r}(s))$. The monomer density $\rho = \psi^*\psi$ plays the role of the order parameter, i.e., it is one of the observables whose values depend on the phase in which the system is. For example, polymers in solvents admit two phases, expanded and collapsed, in which the monomer density is profoundly different. The forces are treated as noise with a suitably chosen distribution such that, after averaging the expectation values over the noise, the interactions among the monomers described by the potential U are reproduced. The advantage of this procedure is that we do not have to deal with a large number of monomers interacting via a generally complicated potential. In this way, each monomer is immersed in a noise background and, apart from this common background, there is no coupling with the other monomers. The passage from paths to densities and fields for such a system becomes straightforward. The price to be paid for this simplification are some technicalities that are needed to calculate the averages over the noise using analytical methods. In particular, a single pair of complex fields ψ^*, ψ is no longer sufficient and n replicas $\vec{\psi} = (\psi_1, \ldots, \psi_n)$, $\vec{\psi}^* = (\psi_1^*, \ldots, \psi_n^*)$ of these fields should be considered. The physical case is recovered in the limit $n = 0$ (zero replicas).

With the help of the sketched strategy the Edwards' model discussed above may be mapped onto a field theory consisting of a Ginzburg–Landau model whose energy is $H = \int d^3r \left[|\nabla \vec{\psi}|^2 + \frac{m}{2} |\vec{\psi}|^2 + V(|\vec{\psi}|^2) \right]$. The product $\vec{\psi}^* \cdot \vec{\psi} = |\vec{\psi}|^2$ is the scalar product of two vectors. The first energy term $|\nabla \vec{\psi}|^2$ takes into account the spatial fluctuations of the monomer density. The second term is a mass term in the language of field theory. Intuitively, if the "mass" m approaches zero, there is no energy cost in changing the monomer density at any point in the space. In this way, monomers become very mobile and able to interact often with any other monomer. Monomers in such a system are highly correlated: when $m = 0$, the so-called correlation length $\xi \propto m^{-1}$ becomes infinitely long and the system undergoes a second-order phase transition. In polymers, m is small when the filaments are long, so that polymers become critical systems in the limit $L \longrightarrow \infty$. The third term is a potential which is polynomial in the powers of ρ. $V(|\vec{\psi}|^2)$ is responsible for the energy due to the monomer–monomer interactions. A quartic term $V(|\vec{\psi}|^2) = \int d^3r\, d^3r'\, U(\boldsymbol{r}, \boldsymbol{r}')\, |\vec{\psi}(\boldsymbol{r})|^2\, |\vec{\psi}(\boldsymbol{r}')|^2$ is needed to consider interactions between two monomers. This is sufficient to capture the behaviour of long polymers in a good solvent (Eq. (34)). For polymers in a solution with a *bad* solvent [87], monomers tend to minimize the contact surface with the solvent molecules and, in doing so, they assume a compact conformation with high monomer density in the interior. In this situation monomer–monomer interactions include also an effective attractive term that complements the barely repulsive one (34): in the corresponding field theory, it is then necessary to add a sextic term that describes the interaction when any three monomers come into contact with each other.

2.9.1. Knots and links in the path-integral formulation for polymers

Analytic microscopic models employing field theories have proven successful in understanding the statistical properties of long polymer chains [91,92], including those of RNA [93] and proteins [94]. Polymer field theories have been applied to polymer dynamics too, see e.g., [95]. The Landau–Ginzburg-type Hamiltonian H accounts for various physical contributions such as bending energy, (in)extensibility, and monomer–monomer interactions; for details we refer the reader to the book of de Gennes [96]. In the framework of path integrals [92], this machinery allows for the construction of probability distributions for a polymer's spatial arrangement via statistically weighted summations over all allowed configurations.

So far, the achieved results, many of them summarized in [91] and [97], mainly concern open polymer chains and polymer rings whose topological state is not fixed. The mapping from the polymer problem to Ginzburg–Landau field theory can be generalized to polymer rings with unspecified topology and to systems containing any number of chains. Rings of unspecified topology are not physical owing to steric interactions between monomers, which forbid the crossing of polymer strands, a necessary condition for modifying the topology of the system. Thus, while the paths of a fluctuating open chain correspond to random or self-avoiding walks, those of a closed ring are subject to the additional condition that topology should be preserved, i.e., whether it is knotted and/or concatenated with other rings, as well as the type of the formed knot and/or link. The fact that two polymer strands cannot cross induces topological constraints on these

configurations: e.g., if the ends of a polymer chain are joined together, it matters whether the obtained conformation is self-knotted or not.

In the literature one often encounters the opinion that analytical models of knots and links are mathematically intractable and that it is difficult to treat topological constraints in field theories of polymers. In the following, we will briefly review such difficulties and the attempts to overcome them. A first problem arises owing to the fact that, in contrast to the usual constraints confining the system to particular geometries and whose treatment is well known in the path integral formalism, topological constraints are global in nature. While monomers may move freely, the topological state constrains the system as a whole, meaning that each part of the polymer should retain the memory of the position of all the other parts. Conceptually, this problem was solved by Edwards decades ago [88]. Following Edwards, the path integral summation for computing the average of an observable $\mathcal{O}$ of a polymer system containing K rings $C_1, C_2, \ldots, C_K$ subjected to topological conditions, meaning that they are knotted or linked together, may be represented as follows

$$\langle \mathcal{O} \rangle = \sum_{\substack{\{\mathbf{r}_a(s_a)\} \\ a=1,\ldots,K}} \mathcal{O}\left(\{\mathbf{r}_a(s_a)\}\right) \sqrt{\frac{\Lambda}{\pi}} e^{-\Lambda[I(\{\mathbf{r}_a(s_a)\})-\mu]^2} e^{-H(\{\mathbf{r}_a(s_a)\})/kT}\,, \tag{35}$$

where the sum over the set of paths $\{\mathbf{r}_a(s_a)\} = \{\mathbf{r}_1(s_1), \ldots, \mathbf{r}_K(s_K)\}$ of $C_1, \ldots, C_K$ is performed using path-integral techniques. Here, H is the polymer Hamiltonian and I is the topological invariant used to characterize the topology of the system (definitions and examples of topological invariants are reviewed in Section 2.2). Both H and I depend on the configuration of the strand(s), i.e., on $\{\mathbf{r}_a(s_a)\}$. For present purposes, we consider numerical invariants I that take real values. From Eq. (35), the topological constraint $I - \mu = 0$ implies that a topological state of the system is selected such that I takes the particular value μ (a real constant). $\Lambda \gg 1$ characterizes how strongly this topological constraint is imposed, in particular exact topological constraints are recovered in the limit $\Lambda \longrightarrow +\infty$:

$$\delta(I-\mu) = \lim_{\Lambda\to+\infty} \sqrt{\frac{\Lambda}{\pi}} e^{-\Lambda(I-\mu)^2}\,. \tag{36}$$

The δ-function, $\delta(I-\mu)$, ensures that only the path conformations obeying $I = \mu$ are counted in the summation over all paths. It is worth mentioning that no existing topological invariant can capture the topology of a system of knotted and/or concatenated rings unambiguously. In the setting of Eq. (35), this implies that the impenetrability of paths is not perfectly captured, so that crossings are partially allowed. For this reason, it is important to consider sufficiently powerful topological invariants, or a set of these, so that the topology be fixed as uniquely as possible.

A second, relevant problem is due to the intrinsic complexity of the topological invariants. Already the simplest of them, namely the Gauss linking number of Eq. (12), looks like a complicated potential. This difficulty may be overcome by moving to field theory. In field theory, the interactions are mediated by particles and the potentials are very simple, at most polynomials in the fields. In the case of topological constraints, the monomers are subjected to interactions that prevent the crossing of the polymer line, thus avoiding changes in the topological state of the system of rings. It turns out that these interactions of topological origin are mediated by magnetic fields $\mathbf{B}_a(\mathbf{x}, s)$ generated by fictitious currents $\mathbf{J}_a(\mathbf{x}, s)$ flowing along the loops C_a. The most general form of these currents is

$$\mathbf{J}_a(\mathbf{X}, s) = \frac{d\mathbf{r}_a(s)}{ds}\delta(\mathbf{x} - \mathbf{r}_a(s))\,. \tag{37}$$

The trick consists in considering the $\mathbf{J}_a$'s as general field conformations not depending on the paths $\mathbf{r}_a(s)$ and imposing the condition Eq. (37) using a set of Lagrange multipliers $\mathbf{c}_a(\mathbf{x}, s)$. Up to now, this connection to magnetic fields has been proved in the case of certain numerical invariants that can be extracted from the perturbative expansion of topological field theories. Such numerical invariants are naturally written in terms of the magnetic fields $\mathbf{B}_a$. Also the $\mathbf{B}_a$'s do not depend on the paths $\mathbf{r}_a(s)$ because they satisfy the condition $\nabla \times \mathbf{B}_a = \mathbf{J}_a$ and the currents $\mathbf{J}_a$ are path independent due to the use of Lagrange multipliers mentioned before. The residual terms containing the polymer paths $\mathbf{r}_a(s)$ in the Lagrange multiplier sector can be easily integrated out. The result is that the previously introduced Landau–Ginzburg model is gauged, i.e., the energy of the system becomes of the form[16]

$$H = \sum_{a=1}^{K} \int d^3r \left[|(\nabla - i\mathbf{c}_a)\psi_a|^2 + \frac{m}{2}|\psi_a|^2 + i\mathbf{c}_a \cdot (\nabla \times \mathbf{B}_a) + V(|\psi_1|^2, \ldots, |\psi_K|^2) \right]. \tag{38}$$

Finally, the topological invariant $I(\{B_a\})$ becomes a polynomial interaction for the magnetic field $\mathbf{B}_a$.

Summarizing, interactions of topological origin can be treated by introducing fictitious currents flowing along loops and the related magnetic fields. A physical interpretation of these magnetic fields has been provided in [98] in the case of two linked rings with two points of each ring attached to two different surfaces located at a distance H from each other. In this particular, yet physically relevant, situation, it is possible to decompose the energy H into two terms H_s and H_c. In the first term, the magnetic fields are responsible for long-range interactions. Clearly, a long-range component of the forces is necessary to keep the topological state, because this is a global feature of the system which requires a coordination

[16] We write the differential d^3r instead of dV to avoid confusion between the volume and the potential V.

of monomers that are far apart. However, also a short-range component should be present in order to prevent the local crossing of polymer lines, a condition that is sufficient to change the topology. Indeed, the second term H_c describes short-range interactions that are similar to the excluded volume interactions, but may be either repulsive or attractive.

In conclusion, it is possible to formulate the problem of knotted and linked rings as a field theory containing polynomial interactions using a large class of topological invariants to fix their topological state [99]. A few results using analytical techniques have already been obtained, mainly confined to the case of two concatenated polymer rings forming a link whose topological relations are taken into account using the Gauss linking number as an invariant. Renormalization group analysis combined with the effective loop expansion shows for this system that its scaling behaviour is changed by the entropic interactions associated with topology. In particular, when polymer rings are very long and the monomer density is almost constant, attractive interactions prevail and screen the excluded volume interactions in a good solvent in agreement with experimental results. This and other results can be found with more details in Ref. [98] and references therein.

A few problems remain. First, it is not known how to map the sum over paths of Eq. (35) in the case of most topological invariants I. Moreover, the constraint $\delta(I-\mu)$ over the path summation becomes a constraint over field summation and it is not easy to deal with such an insertion of a δ-function term inside a field path integral apart from the already mentioned case of two concatenated polymer rings.

3. Physical realizations of topological objects

The abstract topological objects introduced and discussed in Section 2 emerge naturally across various substrates from the microscopic to the macroscopic scale. Their inherent nature remains unaffected by the material in which they appear, serving as a unifying thread that connects seemingly disparate areas of investigation. Yet there is a connection between the mathematical properties of these topological objects and the physical properties of their realizations. Objects, such as knots, links, field defects, and solitons provide a discrete set of equivalence classes over the continuum of geometrical conformations of a system, separated by free energy barriers that are in general high enough to be considered unsurmountable or, in the case of physical knots and links, by particularly long relaxation time-scales. Their study thus offers several possibilities to characterize and affect the behaviour of a soft matter or biological system; possibilities that are fundamentally the same irrespective of the particular system under consideration.

First, one can look at the microscopic creation mechanisms of objects with different topological classes, probabilities of their emergence, and use them to characterize the properties of the system. This is done for example with knots in DNA and proteins (Sections 3.2.2, 3.2.8), entanglement and links (Sections 3.3.3, 3.3.5, 3.3.6) and defects and solitons in liquid crystals (Section 3.5.1). The emergence of different topological objects can also be used to test the limits of our current theories and improve upon them, like in protein folding (Section 3.2.8) or vortex dynamics (Section 3.5.5). Secondly, one can consider the case in which a topological class has been fixed, thus limiting the conformational space accessible by the system, and look at its consequences, both physical and biological (see Sections 3.2.3 and 3.3.1 for polymers, 3.3.6 for DNA, Sections 3.5.2 and 3.5.4 for liquid crystals and 3.5.5 in the case of fluid flows). Thirdly, the ability to control the topology of a system can be used to actively control its physical properties: for example the toughness of a fibre through knotting (Section 3.4) the lattice self-assembly of colloids embedded in a liquid crystal (Section 3.5.2), and the optical properties of liquid crystals themselves (Sections 3.1.4, 3.5). Finally, the ways in which the topology of a system can be modified are of intrinsic interest, not only for possible applications, but in particular when they have been implemented by nature, as in the case of enzymes modifying the topology of circular DNAs (Section 3.3.7).

This section is dedicated to describing the connections between topology and physics described above in a number of cases of interest for soft matter. We consider four different substrates of key importance for bio- and soft matter: polymers, DNA, proteins, and liquid crystals. Their essential physical and chemical characteristics are described in Section 3.1. We present topological objects in order of complexity, discussing their emergence and consequences in a number of different physical systems. To simplify the presentation, we consider polymeric systems first and complex fluids last. We choose to do so because, while knots and links appear in both cases, in complex fluids they emerge as configurations of the field or its defects; thus, one needs to understand the behaviour of fields and defects first.

Section 3.2 covers the emergence and consequences of knots in generic polymeric systems, DNA and proteins. We discuss how knots can be used to probe the properties of DNA (Section 3.2.2) and proteins (Section 3.2.8), their consequences in circular polymers (Section 3.2.3), the mechanisms through which they emerge spontaneously in linear polymers (Section 3.2.4), how they can be tied through nano-manipulation techniques (Section 3.2.5), the phenomenon of topological friction (Section 3.2.7) and the mechanics of knots in fibres (Section 3.4). The emergence and consequences of knots in proteins are discussed in detail in Section 6. Section 3.3 looks at the consequences of circularization and linking in multi-chains systems. The consequences of circularization on the visco-elastic properties of a melt of unlinked rings are introduced in Section 3.3.1 and their relation to chromosome organization in Section 3.3.2. These phenomena are discussed in more depth in Section 4 and Section 5 respectively. Section 3.3.3 reports on topological effects in active polymers, and their connection to complex fluids. Proper links in which two or more chains become interlocked are introduced in Section 3.3.4 in the context of proteins and Section 3.3.5 in relation to olympic networks and kinetoplast DNA. The consequences of the Călugăreanu–White (CW) theorem for dsDNA are discussed in Section 3.3.6. Topological knots and links on some physical substrate can be modified if enough energy is poured into the system to cut the thread. In

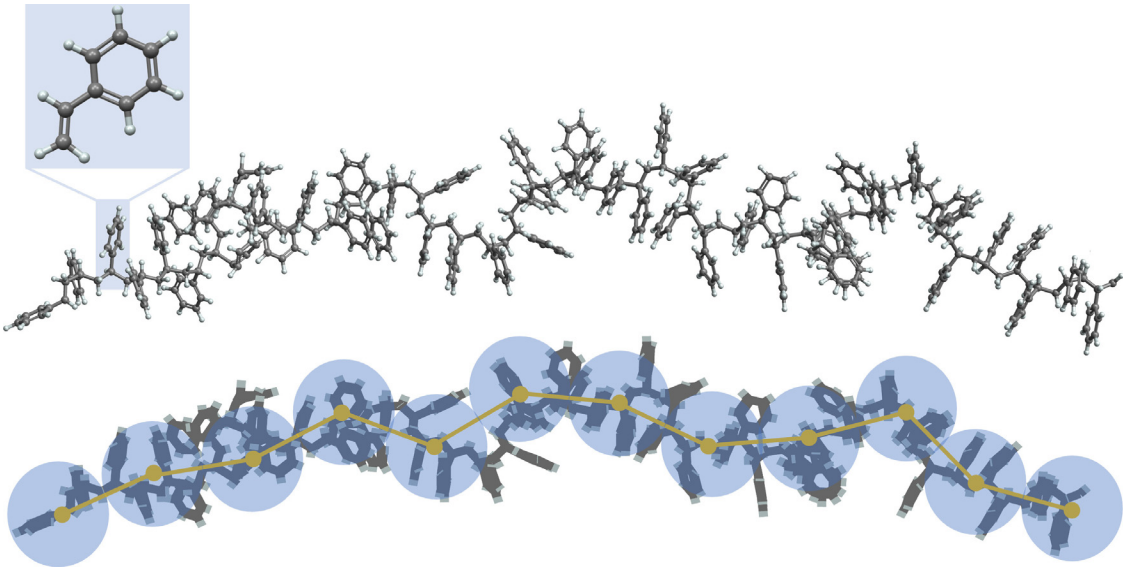

Fig. 27. (Top) The common synthetic polymer polystyrene is made of identical units of styrene, a simple compound containing carbon bound to a benzene ring and another carbon (inset). In the polymerization process, the single units join, one after the other, leading to giant molecules; here, a fragment of polystyrene of 50 styrene units is shown. (Bottom) The physical properties of polystyrene, as well as of any other polymer, can be understood based on a *coarse-grained* representation of it as a string (orange line) of beads connected one after the other by flexible joints. The length of each joint in the string is equal to the so called Kuhn length ℓ_K of the polymer [87]. On length-scales above ℓ_K, polymer behaviour does not depend on atomistic details and obeys *universal* laws, thus the same physical model describing the simple polymer polystyrene can be applied to more complex polymers like DNA.

DNA, this happens through the specific and regulated action of a class of enzymes, topoisomerases, which are fundamental for the regulation of our genes. Due to the importance of this subject in connecting mathematics and biology we dedicate Section 3.3.7 to topological enzymology. On the other hand, a filament can be broken mechanically, if sufficient stress is applied to it: we discuss the interplay between filament material properties and its topology — and how to exploit it — in Section 3.4. Section 3.5 is dedicated to topological structures in fields, offering an overview of topological objects in liquid crystals and complex fluids and connecting them to their equivalents in more general physical fields. In Section 3.5.2, we present an overview of knots and links tied from disclination lines in nematic liquid crystals, and how they can be stabilized. Liquid crystals can also have a twist density; that is the case of cholesterics, which enlarges the family of topological objects that can emerge. Those are introduced in Section 3.5.3. Chiral liquid crystals can also host solitons with highly complex topologies, like linked fields, hopfions, which are discussed in Section 3.5.4. These structures can be formed in fields in general; some fascinating occurrences are discussed in Section 3.5.5. The topics of this subsection are covered in detail in Section 7.

Here and in the following sections, we conform to the nomenclature adopted by the soft-matter community, although we try to clarify it. Therefore, we use the word *knot* to refer both to topological knots, as defined in Section 2.2, and to physical knots, identified with the knotted portion defined in Section 2.7. In the same way, we use *topological constraints* in relation to melts of polymers to indicate steric constraints between linear chains that can be thought of as transient links between them, using the terminology adopted by the polymer-physics community. The precise meaning of each term should be clear from the context. We mention here that although this nomenclature is mathematically imprecise, the connection between transient, but long-lived, geometrical properties and topology is motivating a rich research in low-level topology, partially described in Section 2.7.

3.1. Description of physical systems

3.1.1. Polymers: basic concepts

Polymers [87,100,101] consist of macromolecular strings of covalently bonded repeating chemical units or monomers. While, typically, the *backbone* of any polymer chain may feature a common chemical structure, often this is complemented by *side chains* influencing the physico-chemical properties of the entire macromolecule. These side chains can be all of the same type, resulting in a *homopolymer* like polystyrene, or be composed of different chemical groups, giving a so-called *heteropolymer*, as in the cases of biopolymers like proteins, RNA, and DNA. The process of *polymerization* (exemplified by polystyrene in Fig. 27), i.e., the chemical synthesis giving rise to any — artificial or present in nature — polymer chain is the basis of the formation of *macro*molecules, which exceed in length — by orders of magnitude — the typical size of

their single constituents. A notable example is the cm-long DNA filament of a single human chromosome in comparison to the sub-nm spacing of a single base pair (Section 5).

It was recognized decades ago [87,100,101] that the capability of forming large macromolecules is the basis of most of the fundamental physical properties attributed to polymer chains. Long polymer chains are, in particular, easily bendable due to torsional isomerism and/or thermal fluctuations such that a single polymer made of N monomers is described in terms of an exponentially large, $\mathcal{O}(e^N)$, ensemble of accessible spatial conformations. Therefore, the theoretical description of the physical properties of polymers becomes a statistical-mechanics problem [101].

Based on these considerations [87,100,101], polymer conformations of N chemical bonds are quantitatively characterized in terms of the mean-square end-to-end distance

$$\langle R^2 \rangle \equiv \langle (\mathbf{r}_N - \mathbf{r}_0)^2 \rangle \,, \tag{39}$$

or the mean-square gyration radius, applicable also for polymer architectures that have more than just two ends or no ends at all,

$$\langle R_g^2 \rangle \equiv \left\langle \frac{1}{N+1} \sum_{i=0}^{N} (\mathbf{r}_i - \mathbf{r}_{\rm com})^2 \right\rangle \,, \tag{40}$$

where $\mathbf{r}_{\rm com} \equiv \frac{1}{N+1} \sum_{i=0}^{N} \mathbf{r}_i$ is the centre of mass of the polymer and $\mathbf{r}_i$ are the positions of the monomers, and where the brackets in the r.h.s. of Eqs. (39) and (40) denote the average over the entire ensemble of thermodynamically-accessible polymer conformations.

Upon introducing the mean bond length b and the polymer contour length $L = Nb$, by neglecting all forms of interactions between non-bonded monomers and by limiting the discussion (to fix the ideas and unless otherwise said) to *linear* chains, it is seen that polymers with torsional isomerism can be described to a first approximation (Fig. 27) by the *freely-jointed chain* model [87] and follow Gaussian-like statistics,

$$\langle R^2 \rangle = 6 \langle R_g^2 \rangle = \ell_K^2 \frac{N}{N_K} = \ell_K L \,, \tag{41}$$

where ℓ_K is the so-called *Kuhn length* and $N_K \equiv \ell_K / b$ is the number of monomers per Kuhn segment. For thermally-fluctuating chains, an alternative recurring description of polymer conformations is in terms of the so called *worm-like chain* model [87], where:

$$\langle R^2 \rangle = 2 \ell_p^2 \left(\frac{L}{\ell_p} + e^{-L/\ell_p} - 1 \right) . \tag{42}$$

Eq. (42) interpolates between the small-scale, stiff-fibre regime, $\langle R^2 \rangle \simeq L^2$, $L \ll \ell_p$, and the large-scale, flexible-fibre regime, $\langle R^2 \rangle \simeq 2 \ell_p L$, $L \gg \ell_p$, with the two regimes separated by the characteristic *persistence length*, ℓ_p, of the chain.[17] Both ℓ_K and ℓ_p are a measure of chain flexibility (Fig. 27): in particular, in the long chain limit where $L \gg \ell_p$, Eq. (42) becomes equivalent[18] to Eq. (41) with $\ell_K = 2\ell_p$. The worm-like chain model (and the related concept of persistence length) is, however, considered a much better model for DNA and used as *the* reference description in the literature (Section 3.1.2).

For long polymers with non-bonded interactions amongst monomers, the scaling relationship Eq. (41) between chain size and number of monomer generalizes as

$$\langle R^2 \rangle \sim \langle R_g^2 \rangle \sim b^2 N^{2\nu} \,, \tag{43}$$

where the exponent ν (1/2 for ideal Gaussian statistics, Eq. (41)) depends on the *universality class* of interactions [87] between monomers of the polymer chain[19]. In the case that the non-bonded interaction cannot be neglected, field-theoretical approaches (Section 2.9) have proven very successful to predict the behaviour of Eq. (43). In particular, it was shown by de Gennes [102] that long polymers are in the same universality class as magnetic systems; therefore, they can be described by the n-component Landau–Ginzburg field theory (Section 2.9) in the limit where the number of components of the field, n, goes to 0. It is thus possible to determine the scaling properties of polymers with the usual tools provided by the renormalization-group formalism, which is especially suitable to study systems near a critical point where a second-order phase transition occurs. Since polymers are normally very long and the critical point occurs in the case of infinite polymer length, polymer systems may be considered equivalent to critical systems [102]; in turn, very

[17] The persistence length ℓ_p corresponds to the length-scale above which the polymer can be bent without significant energy penalty; a fully flexible chain has $\ell_p \sim \mathcal{O}(b)$ while a semi-flexible polymer has $\ell_p \gg b$.

[18] Such equivalence between the two models implies that — whenever non-bonded interactions can be ignored and in the long-chain limit — all linear polymers become equivalent to a freely-jointed chain with $L/\ell_K = N/N_K$ statistical Kuhn segments and are, therefore, described by the same universal physical law Eq. (41).

[19] These considerations also extend to cases in which the architecture of the polymer chain plays an important role: for instance, whether polymer constituents are arranged into purely linear strings or if, upon synthesis, the two ends are brought close to each other and *permanently* joined into a circular molecule, a *ring* polymer, influences dramatically both chain structure and dynamics (Section 3.2, 3.3 and 4).

long polymers are said to be in the *scaling regime*. One of the main advantages of field theory is that it takes into account the corrections to the critical exponents due to thermal fluctuations, whereas such corrections are neglected in models based on simpler scaling arguments. In this manner, the scaling exponent ν (Eq. (43)) or the critical behaviour of the osmotic pressure that governs the degree of interpenetration of two polymers when the monomer density increases have been computed.

In general, the results that have been obtained — for example the prediction of the scaling exponent $\nu = 0.588\ldots > 1/2$ [96] for three-dimensional self-avoiding polymers — are in excellent agreement with experiments and have confirmed that long polymers are indeed universal systems, in the sense that their scaling properties near criticality are independent of the chemical composition of the monomer. From the perspective of numerical simulations, this universal nature allows us to employ simple and numerically efficient models to study polymeric systems, rather than a detailed and expensive atomistic description. These approaches have proven crucial in tackling the challenge posed by the scaling limit. In particular, this entails considering macromolecules as large as possible and proving the power-law nature of scaling relations by spanning orders of magnitude in the system size. The field of polymer simulation techniques is huge and will not be covered here; nevertheless, we highlight that the vast majority of the results that will be reported in the rest of the review have been achieved within this framework and could not have been achieved otherwise. The polymer models considered are either on- or off-lattice; in the latter case, they are usually called *bead–spring* models. Here, monomers are identified by the coordinates of their centre of mass (*beads*) and interact via some potential energy that depends on their mutual distance. Bonds are enforced by harmonic[20] interactions (*springs*). If the macromolecule is semi-flexible, a bending potential energy may be included [104]. These basic elements are enough to reproduce the scaling properties of polymeric systems. In the context of the study of the topological properties, particular care should be taken in the choice of the numerical model: if bonds are allowed to stretch, strand crossing may occur as artefact. This naturally changes the topology and may be a critical issue, depending on the system under consideration. If the topology must be conserved, a good practice is to check the topological state *a posteriori*, using the methods reviewed in Sections 2.2.4, 2.5 and 2.7.

3.1.2. DNA

Deoxyribonucleic acid, DNA, is one of the most intriguing topological objects in nature. Most people know DNA to be the way genetic information is stored, reproduced, and transmitted by cells. But importantly, thanks to the ease with which DNA can be designed via cloning, the convenient synthesis of long ($\sim$1000–100 000 base pairs or, in short, bp) DNA molecules through bacteria cultures and high specificity via Watson–Crick pairing, DNA has become a prototype for the study of topological properties of linear, circular as well as branched polymers and, in general, complex fluids [105].

At the atomic scale, a DNA molecule comprises monomers called nucleotides. These are formed of a hydrophilic part made of a sugar molecule attached to a phosphate group, and a hydrophobic part made of a nitrogen-containing base, which can be of 4 types: adenine, thymine, cytosine, and guanine (Fig. 28**A,B**). Nucleotides connect to each other to form filaments of single-stranded DNA, ssDNA. Two ssDNA filaments with complementary base sequences that fulfil the Watson–Crick pairing rules [106], can *anneal* with each other to form a double-stranded DNA molecule, dsDNA (Fig. 28**A**). Under physiological conditions, hydrated dsDNA forms a right-handed helix with a pitch of about 10.5 bases, called B-form DNA [107,108]. Although other forms exist — in particular the right-handed A-DNA helix and the left-handed Z-DNA helix — B-DNA is the most common and will be implicitly assumed herein.

From the physical and chemical point of view, dsDNA is a negatively charged biopolymer made of repeating units (Fig. 28**C**). It possesses large torsional and bending (see Eq. (42)) persistence lengths, measured to be around $C = 109$ nm and $\ell_p = 50$ nm, respectively [107,110] compared with its width, around 2 nm in the hydrated form [106]. In comparison, the bending stiffness of ssDNA is much smaller, around 2 nm [111]. For a review of single-molecule measurements on DNA, see Ref. [112].

It is instructive to explain why the equilibrium structure of dsDNA is that of a double helix [106]. This self-assembly is preferred over other geometries owing to the hydrophobicity of the nitrogenous bases. Due to this, the bases tend to minimize contacts with water molecules, which are instead favoured to contact the hydrophilic backbone. The rather planar structure of the bases (Fig. 28**B**) implies that they can be tucked inward thereby exposing the sugar–phosphate backbone. A final piece of the puzzle is that the distance between two phosphate groups along the backbone (0.6 nm for B-DNA) is longer than the distance between bases (0.33 nm for B-DNA). The net result is that DNA twists itself into a helix to eliminate the space between the bases. An alternative way to visualize this is to imagine bricks stacked in a spiral staircase in such a way to have a fixed distance between the top rightmost corners of consecutive bricks [107].

The helical nature of dsDNa has many profound implications for its physical and biological properties, particularly when one considers circular dsDNA molecules, called *plasmids*, or chromosomes (Section 5). In circular dsDNA, the two single strands can be considered as the edges of a single ribbon, meaning that their behaviour is constrained by the Călugăreanu–White theorem (Sections 2.5, 3.3.6). In chromosomes, the double-helical structure makes dsDNA prone to form topological links, especially during replication. This was identified by Delbrück as the *insurmountable entanglement problem*, which was resolved by the discovery of topoisomerase by Wang [113] (Section 3.3.7).

In nature, DNA molecules are hugely heterogeneous and display a variety of topological states: linear in eukaryotes, circular and supercoiled in bacteria, or even knotted in viruses [114] (Section 3.2.2). They also come in a large variety

[20] Perhaps the most popular model employs the finite extensible nonlinear elastic (FENE) potential [103].

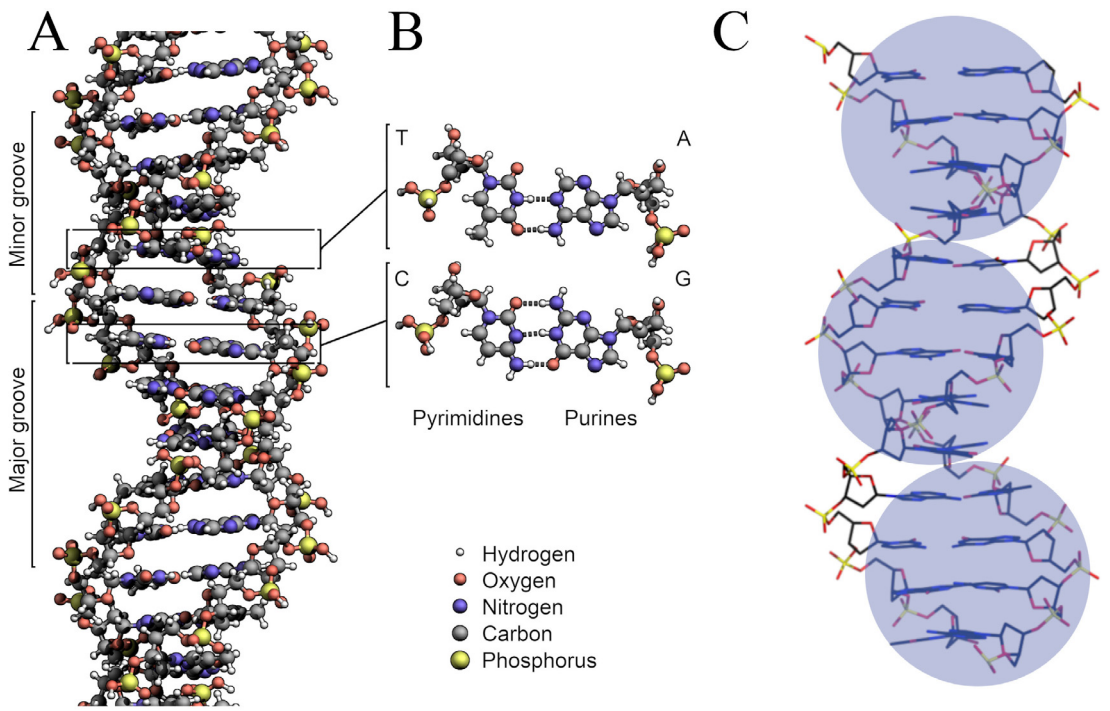

Fig. 28. DNA: From chemical details to universal physical properties. **A** Full-atom representation of a double-stranded DNA (dsDNA) molecule made of two intertwined single-stranded DNA molecules (ssDNA). **B** Details of the canonical Watson–Crick pairing. **C** Representation of a dsDNA molecule, that, similarly to Fig. 27 bottom, can be *coarse-grained* into strings of mutually impenetrable beads.
Source: **A–C** adapted from Wikipedia [109].

of contour lengths, from the 2 metres ($\sim 10^9$ base pairs) of the human genome, to short μm-long ($\sim 10^3$ base pairs) bacterial plasmids and viral genomes. They also come with different sequences, reflecting random changes and natural adaptation of individual species. However, the physical properties of DNA as a polymer, beyond hundreds of nucleotides, are largely independent of the fine details of the DNA sequences and atomistic details of the structure (Fig. 28**C**). This is where the physics concept of *universality* kicks in; largely irrespectively of the sequence, any long enough DNA molecule typically displays similar behaviour, such as radius of gyration, topological entanglements, etc. We review in more detail the properties and organization of DNA as a biopolymer in Section 5.

From a practical experimental perspective, so-called *polymeric* DNA, DNA that has been isolated from its cellular or viral environment and studied in free solution, constitutes an ideal system, affordable and well controlled. Polymeric DNA primarily comes as λ-DNA (48.5 kbp or $\sim$16 μm) or T4 DNA (166 kbp or $\sim$55 μm) from bacteriophage virus genomes, but also from bacterial plasmids, ranging from 2 to 150 kbp. The former are the two longest DNA molecules commercially available. An interesting feature of λ-DNA is that it has "sticky" complementary single-stranded overhangs at each end; they naturally form transient circles or concatenamers, which can be irreversibly closed after ligation [115,116]. DNA breakage can be easily catalysed by restriction enzymes [117], and other topological operations such as knotting, linking and torsional relaxation can be mediated by commercially available topoisomerase proteins [105,118]. This renders DNA somewhat special with respect to other synthetic polymers: in addition to obeying universal physical laws, it can be manipulated by a powerful protein toolkit, provided by nature, that allows one to easily alter its topology. Overall, DNA is an ideal system to study topologically complex polymers.

Finally, many different computational models of dsDNA exist [119,120]; however, most of the numerical investigations of dsDNA that will be discussed in the rest of the review and particularly in Section 3 are based on bead–spring models (Section 3.1.1). In this context, a bead corresponds to a dsDNA segment of a few nucleotides that fixes the level of coarse-graining of the model. In general, the bead's diameter corresponds to the width of the hydrated dsDNA filament. A Kratky–Porod bending energy term is included to reproduce the stiffness of dsDNA. Depending on the salt concentration of interest, screened electrostatic interactions may be applied to account for the charged nature of DNA. Within the framework of bead–spring models, supercoiling (Section 3.3.6) can be considered through the inclusion of a torsional potential that introduces a twist in the chain or through suitably arranged anisotropic interactions, as in Ref. [121]. Chromatin (Section 5.3.2) may be modelled in the same spirit. As in the case of conventional polymers, the use of simple models hinges on universal properties in the scaling limit. Systems that are either of biophysical interest or that can be employed to study topological properties, such as λ-DNA, large plasmids, or chromosome regions, are usually long enough

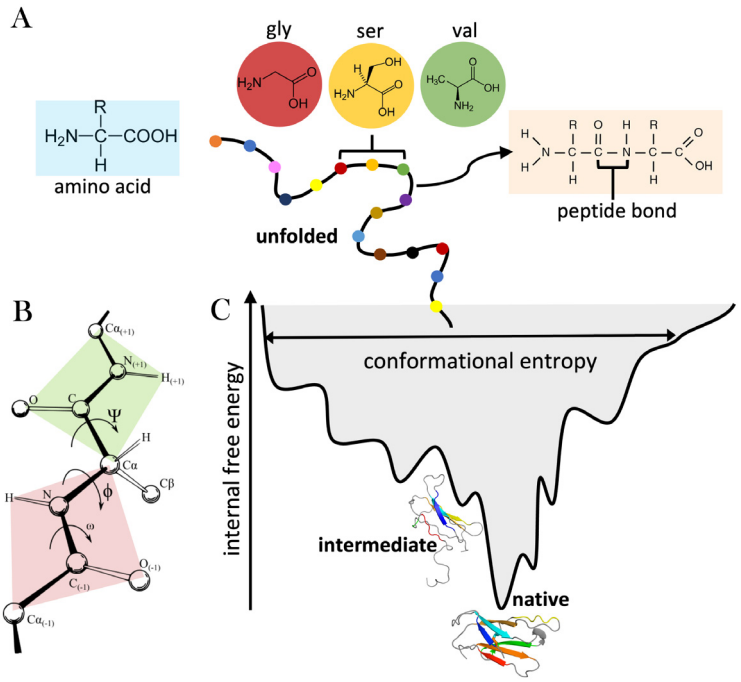

Fig. 29. **A** An amino acid contains a basic amino group, an acid carboxylic group, a hydrogen atom and an R-group, or side-chain group, which are all attached to a central carbon atom, the alpha carbon, C_α. The 20 naturally occurring amino acids differ by the side chain *R*. The sequence of amino acids forming a polypeptide chain constitute a protein's primary sequence. The peptide bond connects the nitrogen atom from the amino group of one amino acid to the carbon atom from the carboxyl group of the next. **B** Geometry of the polypeptide chain indicating the torsional angles ψ and ϕ and the amide plane. **C** A pictorial representation of a funnel-shaped free-energy landscape where the vertical axis represents the internal free energy of a single chain while the conformational entropy is represented by the funnel width.

to fit in the scaling limit. As highlighted in Sections 3.2.4, 4.2.3 and 3.3.6 more sophisticated or detailed models, which are more computationally demanding, can be employed when the level of detail is crucial to achieve a better match with experimental data or to understand effects intimately related with the structure of the double helix. For example, to study the coupling between twist and bending in dsDNA, an effect arising from the asymmetry between the minor and major grooves [122], it is necessary to employ a model that accounts for the groove asymmetry [123,124].

3.1.3. Proteins

Proteins are the building blocks and functional units of all biological systems. A living organism may contain as many as 100 000 different proteins that perform crucial roles in virtually all biochemical processes vital for life, such as catalytic activity, molecular recognition, signal transmission, and mechanical support, to mention just a few.

Proteins are biopolymers constituted by a sequence of amino acids forming a polypeptide chain (Fig. 29**A**). Naturally occurring amino acids can broadly be classified as hydrophilic or hydrophobic according to the structure and chemical properties of the side chains. While the former include strongly polar and/or electrically charged groups, the latter are neutral and relatively non-polar. Although the physical properties of long dsDNA chains are largely independent of their sequence, this is not the case for proteins, where the sequence plays a fundamental role in determining their physical, chemical and biological properties.

Amino acids are linked together by a rigid amide bond, which, in the context of proteins, is termed a peptide bond (Fig. 29**A**). The peptide bond and its four adjacent bonds are coplanar. Each amide plane can rotate around the C_α–C and the C_α–N bonds. The angles describing the two rotations are the torsional angles ψ and ϕ, respectively (Fig. 29**B**). Some ψ-ϕ combinations are highly unfavourable owing to steric clashes of backbone atoms. Other more favourable combinations allow the formation of hydrogen-bond interactions that stabilize the structural arrangement of the polypeptide chain into elements of secondary structure, the most common being the alpha helix and the beta sheet. The packing of the secondary structural elements leads to the tertiary structure, a compact three-dimensional structure that often coincides with the biologically active native state. In some cases, a functional protein consists of more than one polypeptide chain organized into a quaternary structure. A well-known example is that of haemoglobin, a tetramer formed by four polypeptide chains.

The tertiary and quaternary structures are sometimes stabilized by a special type of covalent bond termed a disulfide bond, which is formed between the thiol groups (-SH) of two cysteine amino acids. Unlike peptide bonds, disulfide bonds can be formed reversibly, but this depends upon the redox conditions. Other sources of energetic stabilization at the level of tertiary and quaternary structure include (i) salt bridges, established between the ionizable side chains of amino

acids, aspartic acid, glutamic acid, arginine, lysine, and also histidine, and (ii) hydrophobic interactions between non-polar amino acids that lead to a tightly packed protein core, where the formation of weak van der Waals interactions between the side-chain groups is highly optimized. Despite all these sources of energetic stability, the native state of proteins is frequently only thermodynamically marginally stable with regard to the unfolded state.

Once synthesized by the ribosome, most globular proteins self-assemble into their native structure through the process of protein folding. While several aspects of protein folding remain to be understood, a general theoretical framework, the free-energy landscape theory of protein folding, was developed in the 1990s based on statistical-mechanics models of polymers, the theory of spin glasses, and computer simulations of simple lattice models [125]. The free-energy landscape helps to represent protein conformational states. The landscape can be represented as a multidimensional surface where the vertical axis indicates the *internal* free energy of a single chain and the multiple remaining axes represent the conformational coordinates, e.g., the set of torsional angles associated with a polypeptide chain, $\phi_1, \psi_1, \phi_2, \psi_2, \ldots$, see Fig. 29**C**. The internal free energy of one single chain accounts for hydrogen bonds, salt bridges, hydrophobic interactions, solvation free energies, torsion angle energies, etc., *except* for the conformational entropy, i.e., the number of conformations with a given internal free energy. It is a free energy, and not simply the total energy, because the solvation terms typically involve entropic contributions due to water ordering. A point in the free energy landscape represents a protein conformation, and geometrically close conformations stand close to each other. In this theoretical framework folding is viewed as a succession of random conformational transitions starting from an arbitrary unfolded conformation. In its search for the native state the polypeptide chain will lower its internal free energy by shielding the hydrophobic residues in the core, and by increasing its content of intramolecular hydrogen bonds, number of salt bridges, disulfide bonds, etc., while it becomes progressively more compact. The funnel shape of the free energy landscape reflects the concomitant decrease in the chain's internal free energy and conformational entropy that occurs during folding (Fig. 29**B**).

A possible alternative way to understand protein structure and dynamics is through a soliton; or more precisely, the soliton solutions of a generalized discrete nonlinear Schrödinger equation. A soliton is a topological, stable object that emerges when nonlinear interactions in a physical system combine its elementary constituents, such as individual atoms, into a localized collective excitation that is stable against small perturbations. As explained in Section 2.8, a soliton can provide a methodical approach to describe both structural and dynamical self-organization in a physical system. In order for these collective modes to emerge, suitable key variables must be determined — in this case the Frenet angles described in Fig. B.79 — and, through the symmetries of the system and the separation of scales, the dynamics of such key variables can become simple and be described by a self-consistent effective theory. This theory can reveal qualitatively new features including structural self-organization and emerging topological order. This topological approach is described in detail in Appendix B, where it is discussed in relation to protein folding.

Experimental as well as numerical techniques to study protein topology are reported in Sections 6.10.1 and 6.10.2.

3.1.4. Achiral and chiral nematic liquid crystals

The preceding subsections dealt with the topological structure of extended anisometric flexible entities — polymers that are long enough compared to the persistence length and proteins consisting of well-defined and more or less freely jointed units — which can form fascinating topological structures such as knots and entanglements by themselves. Instead, in materials composed of small building blocks, topologically non-trivial constraints appear at the mesoscopic scale and originate from the spatial arrangements of a large number of these building blocks. This is the case of nematic liquid crystals, where complex topologies arise based on the position and relative orientation of small, anisometric rigid bodies. These can either be small-molecular-mass, nm-size rodlike molecules that constitute thermotropic liquid crystals or μm-size colloidal particles such as the fd virus, which resembles a semi-flexible needle, or gibbsite platelets. When packed together, these particles locally align, and exhibit optically birefringent behaviour, so much can be learned about nematic liquid crystals by viewing them between crossed polarizers. The best-known signature polarizing optical microscopy pattern of this kind, called a schlieren texture (schlieren being German for streaks), reveals the internal symmetry of the material. It features many dark brushes, each radiating from a certain special point in the micrograph in a fan-like manner and fused with the brush from a nearby special point. An example of such an image is shown in Fig. 30. Some of the points have four brushes, while others only have two, and we know that dark brushes signify alignment of the molecules in such a way that matches the optical axis to one of the polarizers.

By interpreting schlieren textures, it becomes clear that nematics can be described by a director field $\mathbf{n}$, a normalized vector representing the average molecular orientations in a small volume of the material, and that the orientations $\mathbf{n}$ and $-\mathbf{n}$ are equivalent; this equivalence is referred to as nematic symmetry. The director varies across distances much larger than the size of the building blocks; in thermotropic liquid crystals often across micrometres. The special points in the textures are topological defects of the director field — regions where alignment of units is ill-defined — and can also be seen in bright field microscopy, owing to light scattering; see Section 2.8. In many samples where the nematic liquid crystal is trapped between parallel glass plates, no special care is required to introduce such defects; in fact, effort must be taken to avoid them. Defects may spontaneously move away from or towards each other, driven by forces stemming from the spatial variation of the director field. This demonstrates the presence of elastic behaviour despite the material being a liquid: so called nematic elasticity. At defects, the liquid crystal avoids excessive spatial gradients of $\mathbf{n}$ by melting so that the orientationally ordered phase is locally replaced by a disordered, isotropic phase. Those defects that approach each other may eventually annihilate, rendering the director field less distorted.

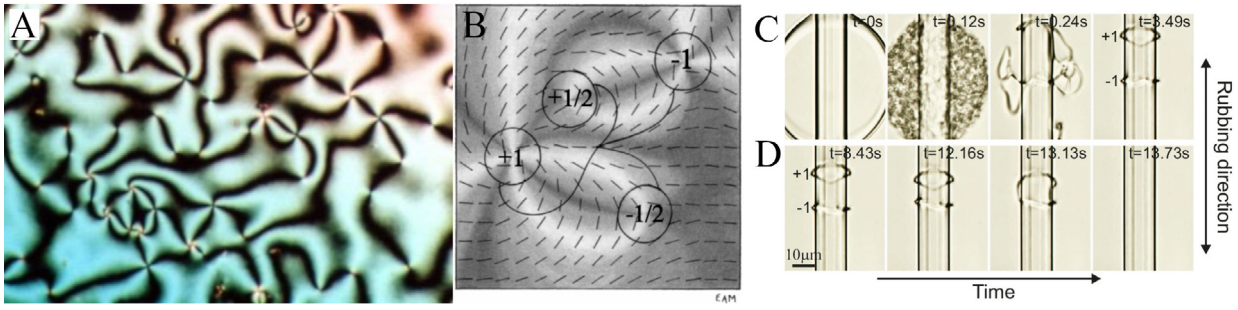

Fig. 30. **A** Schlieren texture of a nematic liquid crystal. **B** Around each point defect the magnitude of the charge is equal to the number of dark brushes divided by four. **C–D** A bright field image of creation and annihilation of line defects around a fibre (vertical cylinder) in a nematic liquid crystal after heating it with a laser (the difference in refraction index seen as a circular outline in the first panel) and then letting it cool. The defect lines are visible due to light scattering on the orientationally disordered defect core.
Source: **A** reproduced from Wikipedia [130]; **B** adapted from [72]; **C–D** reproduced from [131].

In general, nematic liquid crystals include arrangements of point defects, disclination lines or loops that can be ascribed different topological invariants and conservation rules [61,126–128], as described in Section 2.8. Defects can also be manipulated effectively with external optical and electric fields, and by boundary conditions. Features on the micrometre scale can be quite stable as they resist thermal fluctuations and are of interest for soft photonic applications, owing to strong spatial variations of birefringence, the dependence of the refractive index on the polarization of the incident light [129].

A nematic liquid crystal can be thought of as a collection of anisotropic molecules or units, with some net alignment measured, for example, by the Maier–Saupe order parameter [132]. If the degree of order is approximately constant away from defects, and the alignment of the liquid crystal is concentrated along a single direction, the uniaxial state, then we can describe the liquid-crystal order using the unit magnitude director field $\mathbf{n}$, $\mathbf{n}\cdot\mathbf{n}=1$. The symmetry of the nematic phase means that this alignment is unoriented, so that the director field $\mathbf{n}$ is equivalent to $-\mathbf{n}$. The lowest-order terms in an expression for the elastic energy of the liquid crystal will be comprised of functions of the gradient tensor $\nabla\mathbf{n}$ that are invariant under rotations as well as the nematic symmetry $\mathbf{n}\to-\mathbf{n}$. These terms yield the Frank free energy [66,132]

$$F=\int\left\{\frac{K_1}{2}(\nabla\cdot\mathbf{n})^2+\frac{K_2}{2}(\mathbf{n}\cdot\nabla\times\mathbf{n}+q_0)^2+\frac{K_3}{2}\left[(\mathbf{n}\cdot\nabla)\mathbf{n}\right]^2+K_{24}\nabla\cdot\left[(\nabla\cdot\mathbf{n})\mathbf{n}-(\mathbf{n}\cdot\nabla)\mathbf{n}\right]\right\}\mathrm{d}V, \tag{44}$$

comprising splay, $(\nabla\cdot\mathbf{n})^2$, twist, $(\mathbf{n}\cdot\nabla\times\mathbf{n}+q_0)^2$, bend, $[(\mathbf{n}\cdot\nabla)\mathbf{n}]^2$ and saddle-splay distortions, respectively; the first three shown in Fig. 31, each with their own elastic constants. The elastic constants may vary dramatically in magnitude; for example in lyotropic liquid crystals the twist constant K_2 can be an order of magnitude smaller than the other elastic constants. Using Gauss' theorem the saddle-splay contribution to the energy may be rewritten as a boundary term, and can be neglected if the boundary conditions are fixed and there are no defects. In theoretical work it is common to take the one-elastic-constant approximation, setting all the elastic constants to be equal. In this case the Frank free energy with $q_0=0$ becomes equal to the energy of a continuum ferromagnet,

$$F=\int\frac{K}{2}|\nabla\mathbf{n}|^2\mathrm{d}V, \tag{45}$$

where $|\nabla\mathbf{n}|^2=\sum_{i,j}(\partial_i n_j)^2$ [132]. For a magnet the local magnetic moment $\mathbf{m}$ is an internal quantum variable, whereas in the liquid crystal $\mathbf{n}$ is the direction in space along which the molecules are aligned.

If the constant q_0 is non-zero, then the Frank free energy describes a chiral nematic, also called a cholesteric, and no longer has a reflection symmetry. The ground state in this case has a helical structure rotating around the local pitch axis, here the z direction, given by

$$\mathbf{n}=(\cos q_0 z,\sin q_0 z,0). \tag{46}$$

Cholesterics have a natural length-scale $p=2\pi/q_0$, the pitch, which leads to a huge number of metastable topological structures.

Continuum theories of nematic and cholesteric liquid crystals come in two main flavours: director fields and Q-tensors. We will focus on the director field approach, which is a better tool for analytical approaches and understanding topology. However, the director field also has limitations when it comes to numerics. Its fixed magnitude means that it cannot easily accommodate defects, or serve as an order parameter for the liquid-crystalline–isotropic phase transition. Moreover, a liquid-crystal system can have more complex alignments than simply uniaxial, for example the blue phases (Section 7.1). For numerical modelling of nematic and cholesteric liquid crystals, the tensor-based approach is usually used [133], where the Q-tensor holds the information of the quadrupolar moment of molecular orientational distribution with the principal eigenvector coinciding with the director and the eigenvalue corresponding to the degree of order.

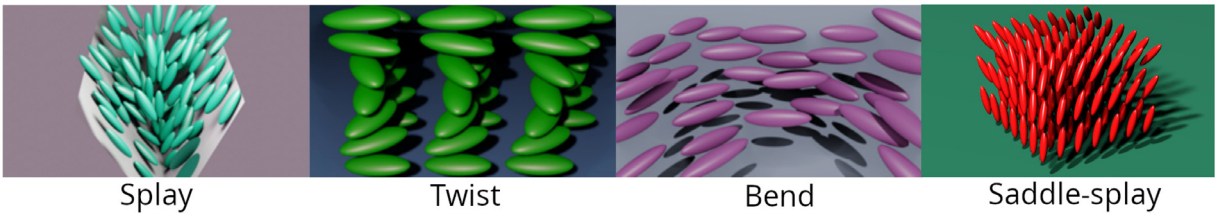

Fig. 31. Splay, twist, bend and saddle-splay distortions of a nematic liquid crystal.

For a general introduction to these topics we refer the interested reader to the books by Chaikin and Lubensky [132] and Kleman and Lavrentovich [61]. For a more formal approach to defect topology in nematics through homotopy theory, see reviews by Mermin [62], and Alexander et al. [72].

3.2. Knots in polymeric systems

Knotted filaments are common at all scales: from climbing ropes, shoelaces, and earphones in everyday life, to knotted polymers, biopolymers, and fibres at the micro- and nano-scale. In some cases, these knots are tied intentionally, in others they emerge spontaneously. In most instances, the type of knots that can be formed is influenced by physical factors such as the filament rigidity, thickness etc. and, once tied, its presence in turn affects the filament properties and its spatial organisation. Thus, researchers have focused on three questions. First, what is the probability of obtaining knotted or unknotted chains, and what are the relative frequencies of different kinds of knots when polymers are circularized in equilibrium? These quantities, the *knotting probability*, *unknotting probability* and *knot spectrum* can be related to physical properties of the system. Second, if one considers a polymer with a fixed topology, how does this affect the polymer's physical characteristics? Third, how can knots be tied and untied from polymers? What is their size, and how do they move along the polymer backbone? Initially, these questions were investigated only for circular polymers. Recently, thanks to advances in experimental, mathematical and computational techniques, the scope has been broadened to include physical knots in linear polymers. In this subsection, we present a series of significant results that highlight this connection in different systems. We discuss how knots emerge in them, and how they can be used to infer or affect the physical properties of these systems.

3.2.1. Emergence of knots in polymers: the Frish–Wasserman–Delbrück conjecture

In the 1960s, Frish and Wasserman [134] and Delbrück [135] conjectured that sufficiently long DNA — and sufficiently long polymers in general — would certainly be knotted. This conjecture had important repercussions both for polymer physics, since if knots are ubiquitous they should be accounted for in models, and for biology, as the presence of knots affects DNA biological functions. The modelling of topological constraints was started a few years later with the seminal work of Edwards [89]. Nevertheless, this proved to be a difficult and still open task (Section 2.9.1), and most results have been obtained numerically. The first numerical study of the Frish–Wasserman–Delbrück (FWD) conjecture was published by Vologodskii et al. [9]. The authors generated closed rings on a lattice through a Monte Carlo approach and analysed their topology using the Alexander polynomial described in Appendix A, showing that the probability of finding a knot in a closed chain indeed increases with the chain's size.

Experimentally, the first observation of knots in DNA, to the best of our knowledge, dates back to the 1970s for single-stranded rings [136] and to the early 1980s for double-stranded DNAs from bacteriophage capsids [137,138]. These early studies were limited to the observation of the knots via electron microscopy, to their resolution via enzymes (Section 3.3.7) and to some qualitative physical characterization; e.g., differences, with respect to reference systems, were observed in the viscosity of the suspension or in the sedimentation speed.

The FWD conjecture was rigorously established in 1988 for a discrete model of ring polymers with N monomers on a lattice where it was shown that the probability of their being unknotted, $P_{\emptyset}(N)$, goes to zero exponentially fast with N [139]. The proof proceeds as follows: denoting by p_N and $p_N^{\emptyset}$ respectively the number of N-step polygons on the cubic lattice and the number of the subset of the unknotted ones, one first shows that $p_N = e^{\kappa\, N+o(N)}$ and $p_N^{\emptyset} = e^{\kappa_{\emptyset}\, N+o(N)}$. Since the unknotting probability is given by the ratio

$$P_{\emptyset}(N) = \frac{p_N^{\emptyset}}{p_N} = \frac{e^{\kappa_{\emptyset}\, N+o(N)}}{e^{\kappa\, N+o(N)}}, \tag{47}$$

to prove the exponential decay of $P_{\emptyset}(N)$ it is sufficient to show that $\kappa_{\emptyset} < \kappa_0$. This is however the hardest part of the theorem, whose proof relies on an extension of Kesten's pattern theorem of self-avoiding walks to polygons and to the choice of a special pattern made by a knotted arc that is so strongly tightened as to forbid other parts of the polygon to interfere with it; for details see [139]. From an extension of the above arguments, one can also show that sufficiently long polygons not only are knotted with high probability, but they are also badly knotted, i.e., they accommodate a positive

density of prime knots [37]. Similar results have also been proved for off-lattice models of polymer rings such as Gaussian random polygons [140] and equilateral random polygons [141]. A more difficult question to handle rigorously concerns the *knot spectrum*, i.e., the probability $P_K(N)$ of observing knotted N-monomer rings with knot type K. This can be expressed in terms of the cardinality $p_K(N)$ of the set of rings of contour length $N\sigma$ and knot type K, compared to the number of all rings $p(N)$. With the exception of the unknot, shown before, no rigorous results are available and most of our knowledge relies on numerical simulations. However, an expression for the knotting probability of composite knots can be obtained by leveraging the fact that prime knots are weakly localized (Section 3.2.3), implying that for N sufficiently large each prime component behaves as a point-like decoration that can be placed everywhere along the backbone of an unknotted ring [142]. If we further assume that prime components do not reciprocally interfere for large N, a property that has been recently discussed in [16], this argument gives

$$p_K(N) \sim N^{\pi_K} p_{\emptyset}(N), \tag{48}$$

where π_K is the number of prime components in the knot decomposition of K.

3.2.2. Using knots to probe the properties of circularized polymers and DNA

Circular DNA is abundant in bacteria and eukaryotes — for instance, in mitochondria — and can be present in knotted and linked forms both *in vitro* [143], and *in vivo* [144]. There is a field of research, *topological enzymology*, Section 3.3.7, that focuses on using DNA knotting as a read-out to understand the action of certain enzymes, such as recombinases and integrases [145].

Comparing the relative abundance of knots in different models and in experiments can provide information on the physical properties of a system. A typical example is provided by the study on the knotting probability of viral dsDNA molecules under different ionic concentrations, carried out by Rybenkov et al. in 1993 [146]. The dsDNA strands were first randomly circularized at different ionic strengths and then analysed through gel electrophoresis, an experimental technique that consists in pushing the negatively charged DNA through a porous gel, typically agarose, using an electric field. Because of the porous structure, more compact molecules will travel faster and thus farther along the gel. In knotted molecules, part of the contour is sequestered by the knot, resulting in a smaller gyration radius; the more complex the knot, the smaller the size, allowing one to effectively separate molecules based on their topology (Section 3.2.2).

The knotting probability was found to decrease as the ionic strength of the solution decreased. This result was interpreted as reflecting the fact that DNA is a polyelectrolyte and responds to the decrease of the salt concentration by displaying an effectively larger diameter due to longer electrostatic repulsion. In other words, at lower ionic strength, DNA–DNA repulsion is less screened by the ions in solution and the DNA behaves as being effectively stiffer, in turn displaying a smaller knotting probability [146]. This effect was explained by simulating dsDNA rings made of cylinders with diameter d and with a bending energy term chosen to reproduce the Kuhn length of DNA [146]. By fitting the experimental data on the knotting probability at different salt conditions with the results from the simulations and with d as free parameter, the authors could interpret d as an effective diameter of the dsDNA at a given ionic strength. This is an example in which a measure of the topological properties of dsDNA rings in solution, the knotting probability, has been used to estimate a physical property of the molecule, its effective diameter as a function of the salt condition. This first computational approach was further developed to take into account the details of the screened Coulomb interaction [147], where the authors considered a lattice model of circular polyelectrolyte rings with a Yukawa potential representing the ion–ion interaction in Debye-Hückel theory. The knotting probability estimated via Monte Carlo simulations was in good agreement with the experimental findings [146].

An important factor affecting the emergence of knots in polymeric chains is confinement, which has attracted a lot of interest from the polymer community in the last decades. In the 1960s, soon after the discovery of the DNA double helix, Delbrück and Vinograd [135,148] realized that long filaments of DNA, typically tens of μm long, can be stored in tiny volumes, e.g., in viral capsids $\sim$100 nm in size, bacteria $\sim$1 μm, and cell nuclei $\sim$10 μm. Successive studies have revealed that these confined DNA molecules can be knotted in viruses [114,137,138,149,150], bacteria [151,152], and yeast [144], although apparently not in human chromosomes [153]. Studying the knot spectrum can thus provide information about the organization of DNA packaging *in vivo*.

One remarkable example in this respect is the case of DNA inside viral bacteriophage capsids. While viruses are small, $\sim$100 nm, their genome can still span tens of thousands of base pairs. Because of this, viruses are one of the entities with the most topologically complex genomes. In a series of seminal papers, Arsuaga, Trigueros, and colleagues revealed that the DNA stored in viral capsids is not only heavily knotted when circularized [150] but also displays some bias towards torus knots, which was at first attributed to the writhe of the DNA [114]. Subsequently, coarse-grained simulations from Marenduzzo and colleagues provided evidence that the spectrum of knots in viruses could instead be explained by chiral interactions between DNA molecules tightly packed inside the capsid [154]. At the typical densities experienced inside capsids, the double-helical nature of dsDNA cannot be ignored as it causes nearby strands to almost perfectly align to reduce the electrostatic interaction between their phosphate backbones. Taking into account this effect in simulations led to almost spool-like configurations that qualitatively reproduce the experimentally observed knot spectrum, including the paucity of 4_1 knots and the relative abundance of 5_1 torus knots over 5_2 twist knots.

3.2.3. Circular chains with fixed topology

An important question is how the presence of a knot influences the properties of a polymer. Indeed, this question applies to unknotted rings as well, as the simple act of circularization, by preventing the formation of non-trivial knots, restricts the accessible conformations of the ring, and thus affects its physical properties. For example, a sufficiently long trivial knot exhibits an effective swelling, signalled by an increase in the radius of gyration. The amount of swelling induced by freezing the topological state of the ring appears similar (see [155] and related computer simulations [156]) to that induced by simple excluded-volume interactions in self-avoiding walks, with the same scaling exponent ν (Eq. (43)) relating the chain's mean gyration radius and number of monomers, $\nu = 0.588\ldots$ [96].

While the theoretical treatment of this form of constraint is still an open problem [157,158], considerable progress has been made following the independent introduction by Grosberg et al. [159] and Stasiak and co-workers [160] of a simple topological invariant, the ratio $p = L/D$ between the length of the ring L and the maximum diameter D to which the curve can be inflated while avoiding self-intersections and keeping L fixed. The unique conformation thus obtained for each knot is called the *ideal knot* and p is a proxy of knot complexity. First, it has been shown that the average crossing number of ideal knots directly correlates with the distance travelled by real DNA knots in gel electrophoresis [161]. Second, by connecting the parameter p to the idea of the primitive path (Section 4.1.2) of the "polymer in the lattice of obstacles", Grosberg et al. [159] were able to construct a Flory-type theory for knotted polymer rings. Using it, they estimated the entropic contribution to the free energy of a ring polymer with *quenched* knotted topology and predicted that — upon suitable changes of the conditions of the solvent surrounding the polymer (e.g., from good to bad solvent; Section 2.9) surrounding the polymer — knots make polymers more resilient to both swelling and compaction. At the same time the theory predicts the significant increase of knot complexity upon random chain closure and polymer compression, as well as the size scaling as a function of p.

A related question concerns the size of the knot ℓ_{kn}, i.e., the contour length of the shortest portion of the ring containing the knot[21] This can be identified using the approaches discussed in Sections 3.2.4 and 2.7. Numerical estimates have shown that in good solvent ℓ_{kn} grows sublinearly with N [39,162]. This *weak localization* property of prime knots implies that, for N sufficiency large, the knot behaves as a point-like decoration, and does not affect the leading scaling terms of various physical quantities, which behave as those of unknotted rings. For a discussion of these results see [163,164] and the references therein. Knot localization — also called knot segregation — in swollen chains is also predicted by the mean-field theory of Grosberg et al. [159].

Other consequences of the closure of a linear chain are more subtle and emerge when one considers the effects of hydrodynamic interactions in polymer dynamics, see Section 4.2.

3.2.4. Spontaneous knotting in linear polymers

Having connected the probability of knots in circular rings to their properties, the next question addressed by the researchers was how self-entangled motifs can form, develop, and eventually disappear in linear polymers with fluctuating ends. The investigation of these issues requires the extension of the topologically rigorous definition of a knot in closed curves to the more phenomenological concept of *physical knot* to include the layman's understanding of the word: *the portion of a thread that is entangled*. We discussed how this can be done either through circularization schemes, by introducing the concept of knotoids, or through intrinsic entanglement measures in Sections 2.7.1, 2.7.3 and 2.7.4 respectively.

The presence and mechanisms of formation of physical knots have been mostly investigated by numerical simulations of coarse-grained model of polymer chains, in particular, by performing either Monte Carlo or large-scale molecular dynamic simulations on flexible homopolymers and on models of dsDNA[22] both in and out of equilibrium and with different solvent conditions [162,166–168]. It was found that physical knots in a linear chain can spontaneously form, giving rise to long-lived metastable states that can diffuse along the polymer backbone and eventually disappear at its ends [162,168–172]. Moreover, almost invariably, the onset of a physical knot is a two-step process in which an initially looped subregion of the chain is threaded either by one of the ends or by a backfolded portion of the chain. These two mechanisms were first pointed out in the context of protein folding [173].

Final validation should come from experimental investigation of the knot pathways; however, as we discuss below, spontaneous knotting is difficult, albeit not impossible, to observe in experiments. Intuitively, direct observations are extreme occurrences, as knotting events are rare and knot formation time is short; moreover, the spatial resolution required to resolve the threading process is in practical terms out of reach. However, the few direct observations suggest that knots form close to the chain ends, thus following a mechanism compatible with the numerical results. Spontaneous knots can thus be detected both in simulations and experiments and results can be directly compared. Notably, one can quantify the abundance of knots and relate it (as observed in Section 3.2.2) to the physical properties of the polymeric substrate that hosts them.

The simplest representative quantity that can be extended from circular to linear polymers is the equilibrium *knotting probability*, P_{kn}, namely the probability that a certain linear chain hosts a *physical knot* (see Section 2.7), a quantity that

[21] Specifically, this is the shortest portion of the chain whose topology coincides with that of the whole chain, Section 2.7.5.

[22] These kinds of simulation usually consider a generic bead-and-spring polymer model [103] with Finite Extensible Non-linear Elastic (FENE) bonds [165], a Kratky–Porod term for chain flexibility, and simple pairwise non-bonded interactions.

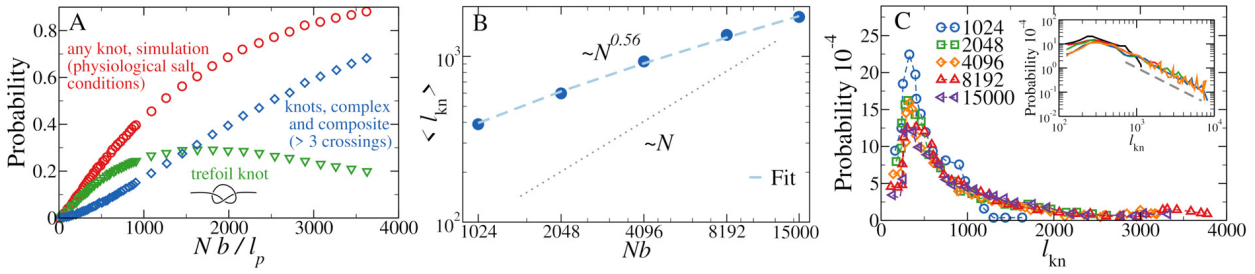

Fig. 32. **A** Knotting probability P_{kn} of model linear DNA polymer chains in bulk as a function of the reduced contour length Nb/l_p. Symbols are for the probability of occurrence of (red) any knot type, (green) the simplest trefoil (3_1) knot, (blue) knots of more complex topology than the trefoil knot. Notice the monotonic dependence of knot complexity with the contour length of the chain. **B** Average knot length, $\langle \ell_{\mathrm{kn}} \rangle$ as a function of the total contour length of the chain $L = Nb$. Note the sub-linear increase of $\langle \ell_{\mathrm{kn}} \rangle$. **C** Probability distribution function, $P(\ell_{\mathrm{kn}})$, for the knotted portion ℓ_{kn} in chains of total contour length L, from $L = 1024$ to $L = 15000$. lin–lin (main panel) and log–log (inset) representations. The log–log representation in the inset highlights the long-tail behaviour of $P(\ell_{\mathrm{kn}})$ (dashed line).
Source: **A** reproduced from [166]; **B–C** reproduced from [162]

can be measured in simulations as well as in experiments. Numerical studies allow us to characterize the dependence of P_{kn} on different parameters [162,166–168]. Most notably, the knotting probability was found to increase upon increasing the length of the chain (Fig. 32**A**).

Numerical DNA models can be compared with experiments. From the experimental perspective, *polymeric* DNA, i.e., DNA isolated from its cellular or viral environment and studied in free solution, constitutes an ideal system, affordable and well controlled, as explained in Section 3.1.2. Furthermore, experimental measures performed at high ionic strengths (∼4M) λ and T4 DNA should, with 30% to 60% probability, contain knots [166,174].

Experiments with individual knotted DNA molecules can be divided into two classes. Nanopore translocation experiments measure the blockade of ionic current through a nanoscale pore as DNA molecules translocate, and use spikes in the blockade current to identify knots; Section 4.2.3. Fluorescence optical microscopy experiments can visualize individual stained DNA molecules, and various techniques, primarily nanochannel confinement and microfluidic flows — Section 4.2.3 — can be used to stretch them such that knots appear as regions of higher brightness. These techniques allow for detection and, possibly, location of the knot along the chain but are not able to resolve the internal knot structure. In general, from the experimental perspective, results from these different classes need to be considered separately, as the experimental conditions are different.

Nanopore experiments, in principle, sample an equilibrium population of DNA molecules in high-salt buffer (although that equilibrium may be disturbed during the translocation process) [175,176]. The observed probabilities were found to be consistent with equilibrium predictions for several different molecular weights.

The spontaneous formation of knots has generally not been observed in single-molecule fluorescence experiments, with a few exceptions. A study [177] claims that 10% of λ-concatemers, stretched with optical tweezers, contained bright spots consistent with knots; however, their buffer conditions make for a difficult comparison with other experimental results. Two independent studies used nano-channel elongation for genomic mapping of *E. coli* DNA [178] and partially denatured yeast DNA [179] and found knots in their DNA. These mapping techniques rely on a linear correspondence between spatial and genomic position along the DNA, which is obfuscated by the presence of knots. *E. coli* DNA showed knots in less than 7% of the examined molecules, while in yeast DNA 7 knots in 134 molecules were reported; 5.2%. To our knowledge, these are the only experimental fluorescence microscopy studies where spontaneously knotted DNA has been observed.

The identification of the knotted portion implies the estimation of its size ℓ_{kn}, i.e., the amount of chain involved in its formation, and of the contour distance of its middle point from the closest end of the chain, the *depth* of the physical knot. From a simulation perspective, the knotted portion can be determined, for example, via systematic chain pruning.[23] Such an analysis can be performed on large data sets, such as those obtained from molecular dynamics or Monte Carlo simulations, using publicly available algorithmic tools [10]. Moreover, the *average* size of a given type of knot (most studies focused on the trefoil, 3_1, knot) increases *sublinearly* with chain length (Fig. 32**B**), implying a weak localization for asymptotically long chains [39]. Finally, the most probable value of ℓ_{kn} does not depend on the chain length [16,169,172]. These results reflect a peculiarity of the probability distribution function $P(\ell_{\mathrm{kn}})$: the distribution has a single peak, whose location is little sensitive to chain size (Fig. 32**C**, main panel) but, at the same time, displays a fat tail (Fig. 32**C**, inset). The tail contributes significantly to the average of ℓ_{kn} and makes it dependent on the chain contour length [162]. Experimental evaluation of ℓ_{kn} is not trivial but can be done reliably. Studies that definitively observe trefoil knots state they have a contour length of 200 to 600 nm, which is comparable to the mode of the size distribution predicted in [166].

[23] The identification of the knotted portion is generally robust for different pruning or search strategies, although there can be exceptions, as in the case of highly confined chains [41].

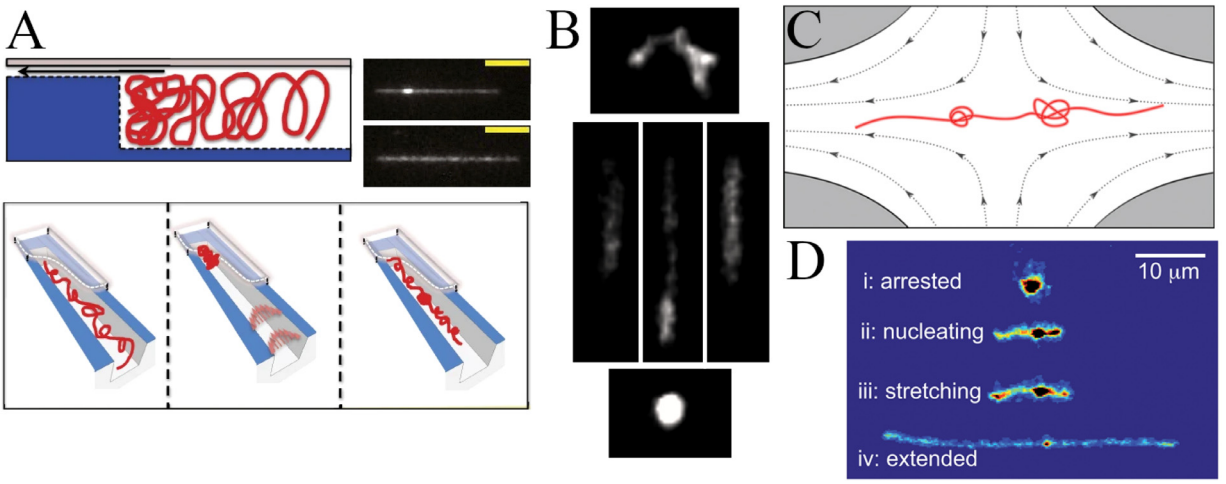

Fig. 33. A Diagram from Amin et al. showing knot formation by compressing a molecule into a nanofluidic barrier. Inset shows knotted and unknotted molecules from Ma and Dorfman entangled with the same method, scale bar is 5 μm. **B** Snapshots from a video from Tang et al. showing the contraction of a molecule after the application of an alternating electric field. **C** Schematic from Klotz et al. showing the stretching of a knotted DNA molecule in a divergent electric field in a microfluidic device. **D** Images from Renner and Doyle showing a molecule entangled through an electrohydrodynamic instability before nucleating and being stretched, leaving a knot in the molecule's interior.
Source: **A** adapted from [181,182]; **B** reproduced from [170]; **C** reproduced from [183]; **D** reproduced from [184].

Why are knots observed so much more frequently in nanopore experiments than in fluorescence studies? Typically, nanopore experiments use much higher salt concentrations, up to 4M, in order to improve the electrical sensitivity of their measurements, whereas fluorescence experiments require lower salt concentrations, typically 0.01 to 0.1M, such that the fluorescent dye remains bound to the molecules. This is consistent with the observations reported in Section 3.2.2 regarding the relation between chain excluded volume and knotting probability. In this instance, experiments and simulations quantitatively disagree. Simulations [174] predict that, at 0.01M, only ∼5% of T4 of DNA should be knotted. Nevertheless, a significantly large number of T4 molecules have been stretched without any observation of knots; better DNA models should thus be employed in this limit.

3.2.5. Induced knotting in polymeric DNA

Nano-manipulation techniques can induce knotting in genomic DNA molecules by exploiting three main mechanisms. The first route is direct manipulation: optical tweezers were used in a pioneering experiment to tie knots in DNA [177]. However, the feat has not been replicated in 20 years[24], possibly due to the low yield, labour-intensive nature of the experiment. The first high-throughput mechanism used to form knots in DNA is compression against a nanofluidic barrier, also known as a *knot factory* [181]. When the compression is released, the molecules expand back to their equilibrium length with a knot localized in the interior of the molecule. The second high-throughput mechanism involves a hydrodynamic instability induced by an alternating electric field, typically in the form of a 10 Hz, 1 kV/cm square wave, applied across a microfluidic channel, which can cause molecules to collapse into tight globules [170].

The nanofluidic knot factory was introduced as a proof of concept [185] with experimental details cited as a manuscript "to be published"'. This prophecy was fulfilled 13 years later [181] (Fig. 33**A**) and the technique was used in several studies [182,186,187]. It was found that the probability of forming a knot increases with the duration and magnitude of the compression; the knot factory was further explicitly simulated [188] using molecular dynamics, showing similar qualitative features. The electrohydrodynamic instability was first observed in 2011 [170] (Fig. 33**B,C,D**). The authors noticed bright regions in the molecules' interiors and used a divergent electric field, mimicking extensional flow in a planar microchannel, to stretch the molecules and show a bright knot trapped in the interior.

The knots produced through these stochastic methods are typically quite large, estimated between at 1 and 5 μm in contour length: Metzler et al. [185] reported a knot containing over 2 μm of contour, Reifenberger and Dorfman [178] a peak contour of 1.5 μm, Klotz et al. [189] 2–5 μm and Ma and Dorfman between 6 and 34 μm [182,186]. Notice that here knots are under tension and hence are intuitively more localized than in untensioned chains, that appear to have a larger size than spontaneous ones (Section 3.2.4). A possible explanation is that they are likely much more complex than a trefoil. One may hypothesize that, since experiments have different stretching conditions, the same knot topologies may have different contour lengths between experiments. It is implicitly assumed that the size of the knots is proportional to their topological complexity, as indicated for knotted rings by electrophoretic experiments [107] and simulations [190]. However, this may be violated if the knots contain non-essential entanglements (Section 2.2.1) or slipknots (Section 2.7.5).

[24] The same feat had been performed a few years earlier by another group with much stiffer actin filaments [180].

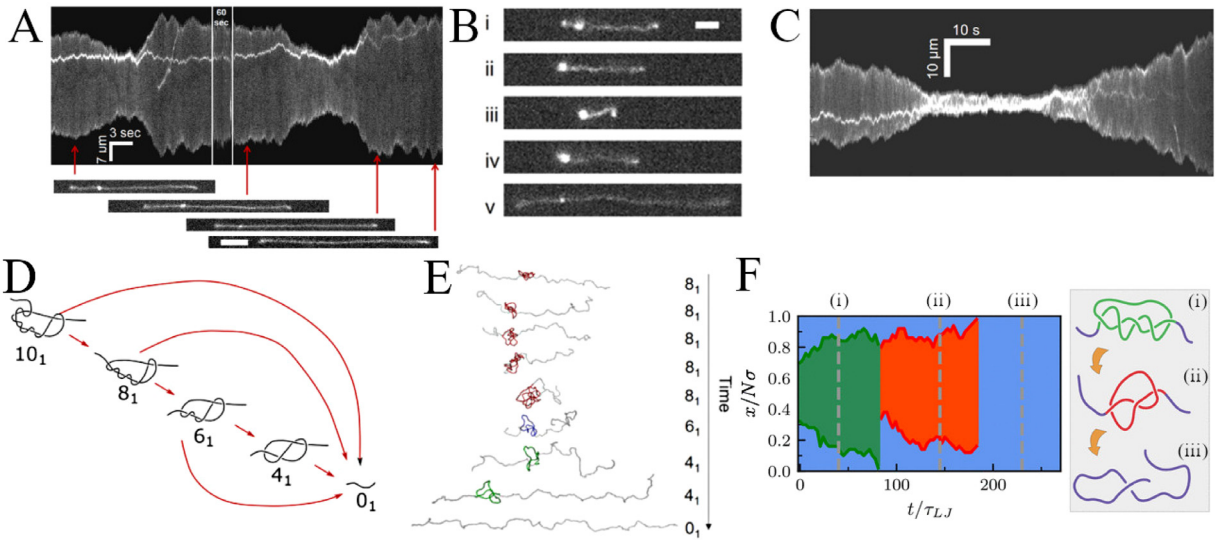

Fig. 34. **A** kymograph and molecule snapshots from Narsimhan et al. showing a stretched knotted DNA molecule going through four topologies as it unties in three stages, stretching slightly more as DNA is liberated from the knot. **B** Snapshots from Soh et al. showing a knotted molecule contracting as the knot reaches the end, before re-stretching with a smaller knot. **C** Kymograph from Soh et al. showing a molecule undergoing a stretch–coil–stretch transition as it partially unties, with the coiled untying stage lasting about 30 s. **D** Diagram from Narsimhan et al. showing potential pathways for a 10_1 twist knot to untie, either in a single stage to the unknot, or through increasingly simpler twist knots, each of which can untie to the unknot. **E** Molecular-dynamics simulation from Soh et al. showing the configurations of an initially 8_1 knotted polymer untying through a series of simpler twist knots, undergoing the contraction observed in the previous figure. **F** Simulated kymograph from Caraglio et al. showing a 5_1 knot untying into a trefoil which unties into an unknot.
Source: **A**, **D** reproduced from [194]; **B**,**C**,**E** reproduced from [195]; **F** reproduced from [196].

The presence of non-essential entanglements in stretched knots may imply (i) rapid stress relaxation as knotted chains are stretched, which has not been observed, (ii) in the case of a widely-sampled knot size distribution, larger variance, highlighting wild fluctuations in apparent size, which has also not been observed. Thus, it is likely that these stochastic knot formation mechanisms increase not just the probability of knot formation, but also the size and complexity. Indeed, simulations from Dai and Doyle [191] which grow a chain in a confining cavity to create complex knots, find that knot probability and knot complexity are strongly correlated and display a universal relation. An earlier study from Mansfield and Douglas [192] showed that lattice polymers that collapse due to a quench to poor solvent conditions (Section 2.9) form knots that are often too complex to be categorized, highlighting a limitation of many knot-detection algorithms. Those based on the use of Alexander polynomials for example can reliably distinguish only knots up to 8 crossings (Appendix A).

In modelling the knot factory [188] and the electrohydrodynamic collapse mechanism [193], it was observed that knots typically become much more complex than trefoils. It was hypothesized that the coupling of the fluid and polymer motion — *jostling* — during the electrohydrodynamic collapse instability would promote knot formation. Simulations [193] support the jostling description, and find that the mechanism can produce knots that occupy up to 60% of the chain's contour length; Section 4.2.3.

3.2.6. Untying events in polymeric DNA

Even when a knot has reached the end of the chain, it can modify the conformation and the dynamics of the polymer substrate by untying. This was first observed in [185], reporting a 14% increase in the molecule's extension after the untying event. The primary experimental investigations into the untying process are found in [194,197,198]. The divergent field used to elongate the molecules in the experiments allowed knots to be driven towards the end, increasing the yield of this process. The two key features of the observations were that complex knots may partially untie into smaller or simpler knots and take several steps to vanish entirely, and that there is a coupling between the untying process and the molecule's elastic response such that the molecule tends to contract during untying, sometimes to the point of reversing the coil–stretch transition (Fig. 34**A, B, C**; Section 4.2). It was observed that multi-stage events are more likely than single stage; the highest reported was a 5-stage event. Multi-stage untying events may be used to place a lower bound on the topological complexity of the initial knot: for example, a trefoil or figure-eight knot in their simplest forms, without non-essential crossings, cannot untie in more than one step.

These knot-untying observations suggest several interesting lines of investigation. What pathways can a complex knot take towards the unknot, to what extent are certain pathways preferred, and how can we characterize the topology of an untying knot? Untying pathways have been investigated computationally for several classes of knots. Alternating torus knots such as 5_1 have been investigated [196] (Fig. 34**F**) but must follow a specific pathway (5_1, 3_1, 0_1), whereas twist

knots such as 8_1 with an unknotting number of 1 can either untie through a complex pathway (8_1, 6_1, 4_1, 0_1), or in a single step, depending on whether the chain end passes through a twist or a clasp, a process that is stochastic and that does not depend on initial conditions [198,199] (Fig. 34**D,E**). One prediction is that a single prime knot such as 8_{19} can undergo a partial untying event into a composite pair of knots. Finally, the various forms of minimally interfering closure (Section 2.7) used to define the Alexander polynomial of open chains are not well-defined during untying, nor is the specific topology of a knot. A probabilistic closure scheme may be used to track the change of one knot to another, but invariants suited to open chains such as the second Vassiliev invariant [56] or a modified Jones polynomial [55] (Section 2.7.4) and an extension of knot theory beyond closed curves, such as knotoids (Section 2.7.3) may be needed for understanding this process.

3.2.7. Topological friction

Perhaps the most intriguing physical phenomenon that has emerged from the study of localized physical knots is the so-called *topological* friction, which has been invoked to account for the dynamical differences between non-entangled and self-entangled chains in various settings. Some manifestations of topological friction have been argued to be relevant in the ejection of knotted DNA filaments from viral capsids [154,200,201] and there is an ongoing debate on its relevance to the degradation of proteins by proteasome [202–206] (Section 6). This friction has also been exploited at the macroscale to engineer novel, tough fibres inspired by spider webs, discussed in Section 3.4. However, single-molecule microfluidic experiments bring about this effect most vividly. Applying an extensional field to DNA globules after electrohydrodynamic entanglement, Renner and Doyle [184] and Soh et al. [207] observed that self-entanglement increased the critical strain required to stretch a molecule by an order of magnitude, and that stretching was slower once it was initiated. Switching off the field, the opposite is true: knotted molecules relax back to the coiled configuration faster than unentangled ones. This was interpreted as a topological constraint leading to a nucleation barrier that had to be surpassed, with topological friction slowing down the stretching process. From an atomistic perspective, this behaviour can be understood by considering the effects of the electrostatic interactions between DNA segments. As the molecule is stretched, the knot is pulled tight and electrostatic repulsion between the monomers participating in it strengthens, thus resisting further knot tightening and slowing down the stretching. In the reverse process, electrostatic repulsion rapidly swells the knot and accelerates relaxation back to equilibrium. A common thread between all the systems mentioned is the fact that the filament is pulled or under tension: simulations show that, in general, tension affects the tightness of the knot [208] and hence the effective friction that accompanies its motion [209]. However, the concept of a topological friction appears also in equilibrium, as knotted molecules show reduced diffusivity; Section 4.2.3.

3.2.8. Knots in proteins

The accepted picture of protein folding (Section 3.1.3) largely resembles that of a polymer in a poor solvent, the latter pulling the molecule towards a compact conformation through hydrophobic collapse. With this picture in mind, the possibility that proteins might form knots as anything but a mishap was for a long time ruled out. While it is reasonable to expect long polymers at equilibrium might possibly be knotted, each copy of a given protein has to reach its specific, well-defined native structure to be functional. The formation of knots was perceived as incompatible with the folding process, on the one hand, and with the regular native conformation, on the other. Surprisingly, however, for some proteins the native state indeed embeds a knot, or even more complex topologies such as θ-curves, as a result of chain branching allowed by cysteine residues and their capacity to form covalent disulfide bonds.

The first protein structure featuring a knot was reported in 1977: the native structure of a carbonic anhydrase contained a loop through which the C terminus protruded by a few residues, thus forming a knot [210]. This knotted structure was again identified by Mansfield in 1994 in the first in-depth investigation of crystallographic structures deposited in the Protein Data Bank [38] that highlighted how protein backbones are significantly less knotted than compact homopolymers in equilibrium. Mansfield also emphasized that the knot in carbonic anhydrase is *loosely formed*, it being sufficient to remove only four residues from one terminus to untangle the chain. In current terminology, such a protein knot is classified as shallow. In a shallow-knotted protein, the knotted portion (Sections 2.7.5, 3.2.3, 3.2.4), the minimal segment of the polypeptide chain that contains the knot, is close along the contour to one of the chain termini. Alternatively, one can say that in a shallow knot, one of the knot tails — the segment extending from the knotted portion to the protein terminus — is short, less than 10 residues. Conversely, for a protein knot to be classified as deep, at least 10 residues must be removed from one of the termini to unknot the chain, i.e., at least one of the knot tails must contain 10 or more residues. In 2000 the existence of a deeply knotted protein was reported by Taylor [211], and in the following years the number of knotted proteins known, including deeply knotted ones, has increased greatly. The deepest knot in proteins reported so far was found in Tp0624 in *Treponema pallidum* (PDB id: 5jir) [212], and its knot tails have more than 120 amino acids.

An interesting variation amongst tangled protein conformations is that of the slipknot (Section 2.7.5 and Fig. 19), originally identified by Yeates and co-workers [58]. As we saw in Section 2.7.5, a slipknot is a topologically trivial configuration that involves a loop formed by a piece of a protein's backbone pulled through another such loop; a slipknot gets untied when pulled by its termini. The techniques introduced in Section 2.7 allow detecting slipknots similarly to knots in open chains, by assigning a knot type to each subportion of the chain and constructing a fingerprint matrix; Fig. 35.

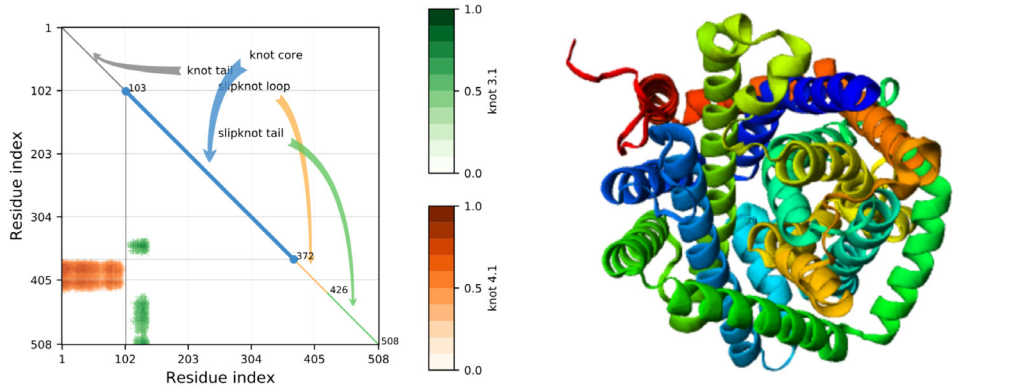

		Knot core range	Knot core length	Knot tails range	Slipknot tails range	Slipknot loops range	N-end length	C-end length	Type
view details	$+3_1$	142-337	196	338-508	1-105	106-141	105	170	slipknot
view details	4_1	103-372	270	1-102	426-508	373-425	102	83	slipknot

Fig. 35. Knot fingerprint (top left) for the carnitine transporter from *Proteus mirabilis* (PDB ID: 2WSW), and its other characteristics provided by the KnotProt database [54]. The colour of a point at position (x, y) in the matrix corresponds to the type of knot that is formed by the chain fragment from residue x to residue y. In particular, the colour of the lower left corner of the matrix encodes the knot type formed by the whole protein chain. From the matrix one can see that although 2WSW is unknotted, it contains two slipknots: the fragment 103–372 forms a 4_1 knot, while the fragments 142–337 form a 3_1 knot.

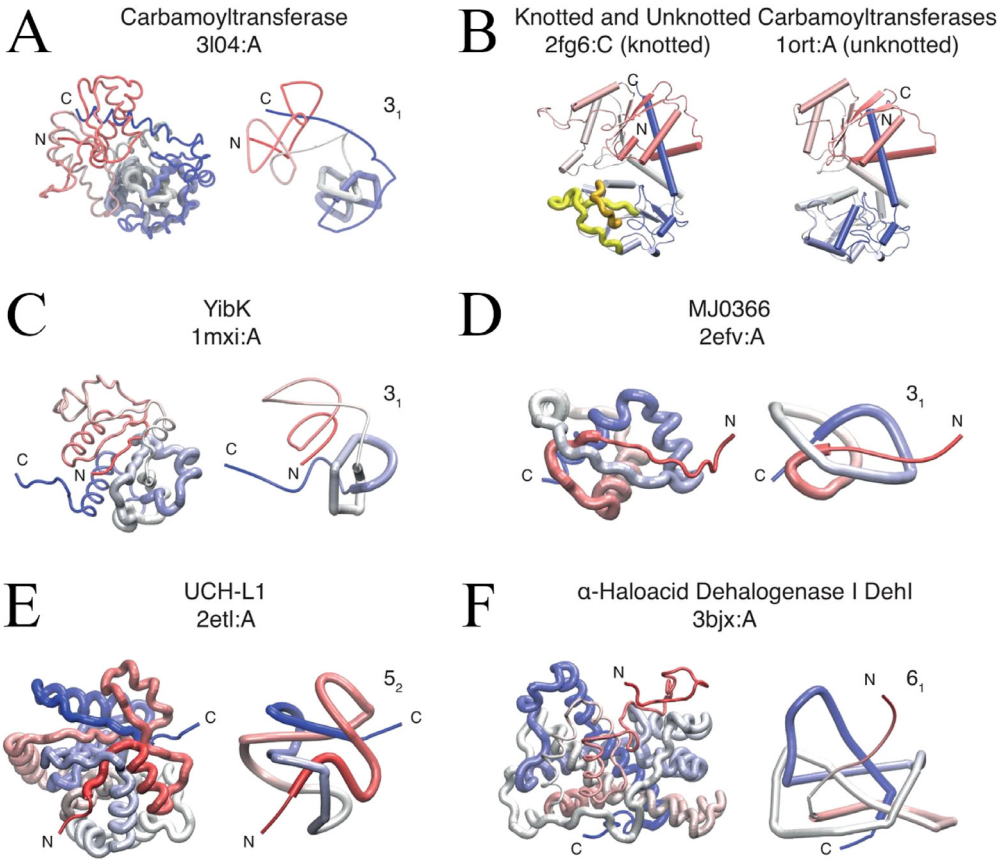

Fig. 36. Knotted proteins. In panels **A**, **C–F**, a smoothed structural representation is used to highlight the knot. Panel **B** presents a knotted/unknotted pair of carbamoyltransferases. A virtual excision of either or both of the highlighted loops, coloured yellow and orange, unties the knotted variant. *Source:* Adapted from [213]

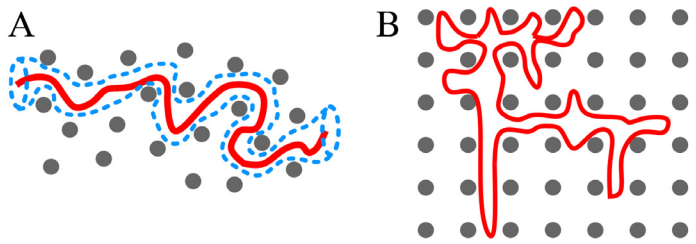

Fig. 37. The two prevalent microscopic interpretations for linear **A** and ring **B** polymers in melt conditions. In both panels, the *probe* chain is in red while the other chains are represented by grey dots that constitute the physical network of topological constraints (entanglements). In panel **A**, the blue dotted line represents the tube-like region to which entanglements confine the probe chain. For rings, panel **B**, which lack free ends, the notion of a confining tube is lost and a new theoretical framework is required (Section 4).

As of 2023, about 1% of the 200 000 experimentally determined structures deposited in the Protein Data Bank (PDB) contain a knot or a slipknot. The vast majority of knotted proteins are enzymes [214] and their active site is usually embedded in the knotted core. There are at least 15 enzymatic families in which knotted members are found [212]. Some of them have been extensively studied experimentally and theoretically, via computer simulation (Fig. 36). This is the case of the tRNA/rRNA methyltransferases (members of the SPOUT family) and ubiquitin C-terminal hydrolases. Among knotted proteins, there are also representatives of DNA-binding families. The smallest knotted protein known today, MJ0366, is a DNA-binding protein featuring a shallow trefoil knot. Because of its small size, approximately 100 amino acids, it has been extensively studied in computer simulations.

The most complex knot found so far in proteins, the stevedore, or 6_1 knot, was identified in two Group I dehalogenases. One of them, DehI (PDB id: 3bjx) [215,216], is a deeply knotted protein, it being necessary to remove 20 amino acids from the C-terminal end to untie it. The protein consists of two regions, each containing approximately 130 amino acids, which share about 20% sequence similarity [215]. Neither of these two regions is knotted separately, and it is likely that DehI's structure is the result of a tandem sequence duplication event [216]. The second most complicated knot encountered in proteins to date is the 5_2 knot. This type of knot has been found exclusively in members of the ubiquitin C-terminal hydrolase family. The simplest type of knot, the trefoil or 3_1 knot, is the most abundant among knotted proteins [214]. The trefoil knot is not exclusive to enzymes and can be found in several DNA-binding proteins as well as in transmembrane proteins, e.g., Ca^{2+}/cation (CaCA) antiporters [212].

We dedicate Section 6 to the discussion of the possible role of knots in proteins.

3.3. Entanglements in polymeric systems

As in the case of single chains, many structural and dynamical phenomena in multi-chain polymeric systems can be traced back to, and therefore understood via, the fact that polymer chains, in general, cannot cross. In the case of dense solutions or melts of linear polymers, these *topological* constraints — which arise due to the mutual repulsion between distinct polymer chains — are *transient*, although long-lived (Section 3.3.1). When instead one considers ring polymers, they possess a *hard* topological constraint, unchangeable without cutting open one or more rings. This affects the behaviour of the system both in the case in which the rings are unconcatenated, Section 3.3.1 (also a notable model for chromosome organization, Section 3.3.2), and/or far from equilibrium (Section 3.3.3), and in the case in which they are concatenated, forming a catenane or olympic network (Section 3.3.5), as can happen to DNA under the action of the type II topoisomerase enzyme. The action of these enzymes is the subject of topological enzymology, discussed in Section 3.3.7. Other particular instances regarding the mutual entanglement between two polymer chains are the case when they form a ribbon, and one obtains the conditions of the Călugăreanu–White theorem (Section 2.5) which has important implications for double-stranded DNA (Section 3.3.6), and the naturally occurring intertwining between certain classes of protein molecules (Section 3.3.4).

3.3.1. Topological constraints in melts

In a typical melt, i.e., a polymer system at very high density, topological constraints or *entanglements* between chains arise from dense-packing conditions and manifest their presence in the form of characteristic chain–chain interactions. A general consequence of these interactions is that any inter-chain crossing is effectively prevented, therefore polymers can move only by flowing *past* each other (Fig. 37). On the other hand, there are other consequences that are far less general and may change depending on the specific architecture of the polymers. Melts of linear chains, as opposed to melts of unknotted and non-concatenated ring polymers, are particularly notable in this respect, especially regarding their linear viscoelastic behaviour under shear flow.

Linear chains in a melt are highly interpenetrating. As a consequence the self-exclusion interaction in any single chain is, with respect to dilute conditions, screened [100] by an equivalent excluded-volume effect due to the spatial overlap with different chains: therefore, linear polymers follow Gaussian statistics, i.e., the mean spatial size of a chain

of N monomers is $\langle R\rangle \sim bN^{1/2}$ (Eq. (43) with $\nu = 1/2$). As for the dynamics, the physical network of entanglements (schematized as grey dots in Fig. 37A) constrains single-chain diffusion mainly along the one-dimensional centre-line (the *primitive path*, Section 4.1.2) of an effective tube-like region [87,90] (Fig. 37**A**). Then, each chain gains a new conformation owing to its chain ends that move across the terminal sections of the tube: the resulting motion — reminiscent of how snakes move — has been termed *reptation*. With a characteristic time-scale $\tau_{\text{rept}} \sim N^3$, the reptation model is the basis for the microscopic theory of linear viscoelasticity (Section 4.1.1); in particular it explains the emergence of a distinct plateau modulus analogous to that observed in natural polymer networks such as rubber [87].

Unlike linear chains, unknotted and non-concatenated rings in a melt are much less interpenetrating. The distinct behaviour originates from the unlinkedness constraint that, having to be maintained on the entire scale of each chain, induces an effective, strong [157,217], repulsion between the rings: this interaction, that has no counterpart in equivalent linear melts, is of topological origin because it comes entirely from the topological ring state. As a consequence of it, rings display (Fig. 37**B**) non-Gaussian mean spatial size $\langle R\rangle \sim bN^{1/3}$ (Eq. (43) with $\nu = 1/3$) and segregate from each other [218–221]. As for the dynamics, by virtue of their lack of free ends, we expect to observe substantial differences from linear chain behaviour. Ring dynamics and its effects on melt viscoelasticity remain controversial (Section 4.1.3). Experiments with purified high-molar-mass ring polymers, computer simulations and theoretical modelling [222–229] seemed to conclude that rings move faster than their linear counterparts (for the same polymer length N) and stress relaxation shows no rubber-like plateau. However, recent developments [230,231] hint at the opposite, i.e., that, for very long rings, a plateau might emerge as the consequence of rings mutually threading (Section 4.1.4) — and hence dynamically affecting — each other. All these are, in many ways, surprising features: their physical consequences have motivated an ongoing line of research concerning the viscoelastic properties of polymer melts (Section 4.1).

3.3.2. Topological origin of chromosome territories and the analogy with ring polymer melts

One of the most remarkable and unexpected findings in the physics of ring polymers is that they display segregation above the characteristic entanglement length-scales. This feature provides us with a conceptual model to understand a very different, yet physically related system, that of chromosomes packaged inside the nuclei of eukaryotic cells [232].

Fluorescence *in situ* microscopy has shown that cm-long DNA chromosomes are tightly packed within sub-μm regions of the cell nucleus, also known as chromosome territories [233]. Theoretical arguments corroborated by computer simulations have suggested [234] that territories emerge as a consequence of a purely polymer-physics phenomenon: the inevitable slow (reptation) dynamics of very large polymer chains in entangled solutions (Section 4.1.1). This slow dynamics prevents full relaxation of the polymer conformations and topology associated with the initial chromosome conformation soon after the cell is divided. During cell division, chromosomes assume a tight cylindrical shape, which computer simulations have estimated to take up to 500 years to relax fully to equilibrium (Section 5.3.5). Thus, the mitotic (during cell division) state of chromosomes, typically unknotted and non-concatenated with other chromosomes, is to some extent retained throughout the whole cell cycle because the associated relaxation time-scale surpasses by orders of magnitude the average life-span of a single cell. As a consequence, although chromosomes are *linear* polymers, their internal structure resembles [232,234] that of melts of unknotted and non-concatenated ring polymers (Section 4.1.3), whereby large chunks of genomic regions tend to segregate into territories. Already by 1993 [235] it was imagined that such peculiar segregation or *crumpling* of interphase chromosomes would be desirable: the absence of geometrical constraints like knots and links implies that the local chromosome structure and dynamics are less impacted, less harmed, by mechanical stress.

3.3.3. Topological signatures far from equilibrium: entanglements in active polymers

Non-equilibrium phenomena in bio-polymer systems, driven by the action of chemically powered molecular motors, have been observed in many biophysical systems, including actomyosin networks, microtubule arrays [236], the cytoskeleton [237], and chromatin [238]. In the last few years there has been an increasing interest in mesoscopic models of such *active* filaments, characterized by a level of detail between the precise atomistic description of molecular motors and the mean-field level of active nematics (Sections 7.5 and 7.6). These models, generically dubbed *active polymers*, are especially fit for reproducing the organization of filamentous bacteria, parasites, and worms, but have also been applied in other contexts. We direct the reader to a recent review [239] for an overview. We focus on the emergent topological phenomena observed in systems of active linear and ring polymers, remarking that *active* is not used here as a synonym of *self-propelled* and, thus, different activity models will be considered.

Active polymer models have been used to obtain microscopic insight into the organization of self-propelled filaments in active nematics (Section 7.5), allowing the explicit incorporation of filament semiflexibility [240] (Fig. 38**A**). Energy, injected into the system through self-propulsion, generally excites bend deformations and reduces the apparent filament bend modulus. The emergent characteristics of the active nematic depend on activity and flexibility only through this activity-renormalized bend modulus; this prediction has been also verified experimentally [241]. It has been shown that, if motor concentration is high enough, an initially nematic arrangement of filaments is unstable and evolves into a highly dynamic structure formed by polar domains with persistent defect formation and annihilation. The scaling of domain sizes is universal and depends on the motors' strength and number [242].

In the context of chromatin modelling, the idea of incorporating the effect of molecular motors has been gaining traction. Active polymer models have been employed to reproduce the collective motion observed in chromatin [244]

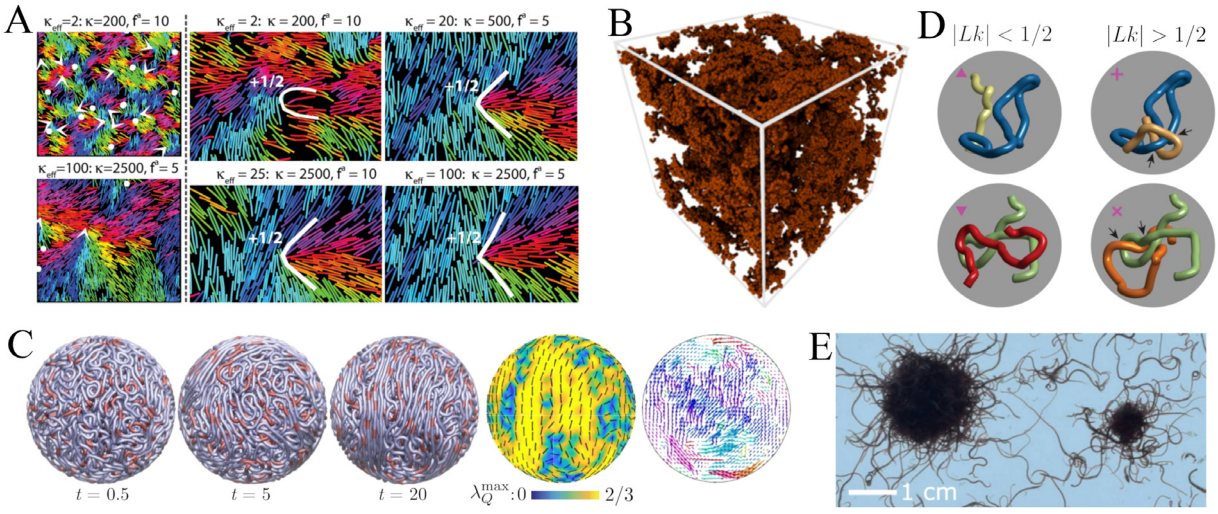

Fig. 38. **A** Active nematic emergent properties depend on the activity parameter and the filament bending modulus; filament beads are coloured according to the orientations of the local tangent vector. **B** Spontaneous aggregation of active regions in an active ring melt. **C** Active chain under confinement reproduces chromatin coherent motion. From left to right: fibre configurations at different times $t = 0.5$, 5, 20, red segments showing instantaneous dipole locations; nematic structure of the fibre on the surface of the confining sphere, colours showing the maximum eigenvalue λ_{max} of the nematic order tensor and black segments showing the corresponding nematic director; chromatin displacement maps in a plane across the spherical domain, colour-coded according to the direction of displacement. **D** Topological analysis enables the classification of tangle structure between worms: contact (left column) and linking interactions (right column), distinguished by the linking number. **E** Aggregation and phase separation of *T. tubifex*.
Source: **A** reproduced from [240]; **B** reproduced from [243]; **C** reproduced from [244]; **D** reproduced from [245]; **E** reproduced from [246].

(Fig. 38**C**) as well as the large-scale fingerprints of chromatin organization [247], through the interplay between motor activity and cross-links. Active polymer models could be a natural fit for complementing *coloured* models (Section 3.3.2), in a possible next step in chromatin modelling.

Including non-equilibrium fluctuations in chromatin organization, within the ring-melt analogy (Section 3.3.2), was the motivation behind the investigation of melts of partially active rings [243,248]. Such melts turn out to reach dynamical arrest, achieving a *topological glass* state[25] [243]. Such an arrested state is caused by the increase of threadings (Section 4.1.4) between neighbouring rings, which traps them and slows down the entire system (Fig. 38**B**). This active topological glass also features the onset of micro-phase separation, similar to what has been observed in chromatin, that here eventually leads to vitrification [248]. Dynamical arrest is also achieved in another active ring polymer model [251], this time at the single-ring level; this shows that the effect of circularization in presence of activity is non-trivial.

A last relevant topic concerns the viscoelastic properties of active filamentous suspensions. Active polymers display entanglement properties that deviate greatly from the passive case. For example, the motion of an active *probe* linear chain in a passive linear melt can be treated analytically [252] as an effective enhanced reptation. Upon increasing activity, the dynamics initially retains the signature scaling of the tube model until activity overrules entanglement and the chain behaves qualitatively as isolated [253]. This latter feature distinguishes active chains from active colloids, which cluster at high activity. On the other hand, an aggregation mechanism in relatively dilute systems has been observed in many different species of worms. Such aggregates, called *blobs*, have been postulated to be of topological origin, caused by entanglements [246] (Fig. 38**E**). A description of these blobs in terms of tangles has recently been proposed [245], with a companion numerical model that suggests that the aggregation is driven, essentially, by the activity pattern of the worms' heads (Fig. 38**C**). A similar topological phenomenon has also been observed for short active polymers under confinement. In this latter case no activity pattern was encoded; instead hydrodynamic interactions, neglected in the previous case, were included [95]. It would thus be interesting to elucidate which are the minimal ingredients driving filament tangling. Aggregation has also interesting repercussions for the properties of the resulting material [254]. How blob response to mechanical stress is connected with traditional rheological properties [255] has yet to be elucidated, but is of key importance for the design of soft robotic systems[256].

[25] A *topological glass* is a hypothetical condition of a ring melt characterized by the fact that the melt relaxation time is no longer a power law of N but becomes $\sim \mathcal{O}(e^N)$. This state is supposed to be maintained by the network of ring–ring threadings that forms a percolating cluster across the whole melt. Some (indirect) evidence of the existence of a topological glass is given by numerical simulations for pinned [249] and, as highlighted here, active [243] ring melts, i.e., systems maintained artificially out of equilibrium. In more ordinary thermal systems, the state can be difficult to observe due to the prohibitively large size of rings required [250].

3.3.4. Mutual entanglement in proteins

In most cases, proteins do not act as single, isolated, entities but form higher-order complexes where two or more protein molecules share the same region in space. Important examples are the class of domain-swapped dimers, such as the 1LGP and 3DIE dimers where the two molecules intertwine in space in a rather complicated fashion. If one is interested in measuring the mutual entanglement of the two chains, a natural generalization of the notion of open knots is the concept of linking between two open chains (Section 2.7.2); this can be defined by first circularizing the two chains and then computing linking invariants such as the two-variable Alexander polynomial, the HOMFLYPT polynomial or the simpler Gaussian linking number (Section 2.5). As for physical knots, the closure can be performed in many ways, each with its own advantages and drawbacks (Sections 2.7.1 and 2.7.2). In Ref. [257], the entanglement complexity of 110 non-redundant domain-swapped dimers was computed by first closing the dimers at infinity and then computing the Gauss integral, G, of the two resulting loops (Section 2.5). The result is that $\sim$15% of the domain-swapped dimers have a significant degree of mutual entanglement ($|G| > 1$) with a preference for negative *G*s (the sign depends on the orientation of the curve; for proteins, the natural N-C direction is assumed). The suppression of intertwining observed in long dimers is at odds with what is expected in dense suspensions of long random chains, suggesting a natural selection mechanism that suppresses random interwinding between chains.

Although the Gaussian integral between two open curves is not a topological invariant, it still provides a number that quantifies the degree of intertwining between curves. By computing the integral in Eq. (14) for open curves, one can demonstrate that the resulting Gauss integral is equal to the average, over all possible projections, of half the algebraic sum of the inter-crossings, in the projection of the two curves, analogously to Eq. (15) [55]. Moreover, the description of a protein's native state in terms of secondary structures such as helices, beta-sheets, and loops suggests that good and spatially more detailed descriptors of protein self-entanglement may be obtained by computing Gaussian integrals $G(\gamma_i, \gamma_j)$ between pairs of subchains (γ_i, γ_j) properly extracted by the same protein's backbone. For instance, one can compute the $G(\gamma_i, \gamma_j)$ between any looped portion of a protein — a looped subchain is a portion that has its first and last residue forming a contact — and any other subchain, either looped or non-looped. If the contacts defining the looped subregion are chemically very strong, such as cysteine pairs or disulfide bridges, this procedure allows the detection of lassos [258] and links [259] within the protein's backbone (Fig. 66). Focusing on well-defined looped regions is computationally efficient and can be applied to analyse folding trajectories. Such a strategy enabled the finding that entanglement is the primary cause of the emergence of long-lived misfolded states in a relevant subset of *E. coli* proteins [260,261]. Because entangled conformations can lead to long-lived metastable states only if structural perturbations are small relative to the native state, they allow misfolded proteins to remain, overall, very similar to the native structure; this, in turn, allows the protein to stay soluble and evade the proteostasis network — the cellular machinery that degrades misfolded proteins — with reduced function, with repercussions for the whole cellular network. For example, enzyme activity can be compromised by these long-lived, poorly-functioning entangled misfolded states, possibly caused by synonymous mutations [261]. However, if all contacts of the native structure are considered in the definition of the sub-loops γ_i, a large variety of entangled motifs can be detected [262]; further, its maximum value $|G(\gamma_i, \gamma_j)|$, computed over the set of sub-regions, correlates, for a large class of proteins, with the protein's folding rates[263]. This suggests that mechanisms such as that found in *E. coli* proteins may be more common than expected.

3.3.5. Olympic networks and kinetoplast DNA

An example of a fascinating and markedly unique type of topologically complex genome is so-called *kinetoplast* DNA, or kDNA. Its structure resembles that of a quasi-two-dimensional *olympic* network, a physical network where the connections are due to topological interlinking rather than chemical cross-linking [102]. kDNA is found in the mitochondrion of unicellular organisms of the class Kinetoplastida, such as Trypanosomes. As early as 1968, Simpson isolated this structure from parasites and using transmission electron microscopy (TEM) realized that it was a genome like no other: it is made up of about 5000 small (mini) DNA circles (1–2.5 kb) and a few large (maxi) DNA circles (up to 30 kb) linked together to form an extended structure [264]. Chen and colleagues were able to characterize in more detail the topology of this extraordinary network [265]. They extracted kDNA from the parasite *Crithidia fasciculata* and performed careful digestion experiments where a random fraction of minicircles was cut once. Then, by gel electrophoresis, they quantified how many catenated dimers, trimers, etc. were generated. The relative amount of each versus the amount of linearized circles yielded a characteristic curve that is compatible with a 2D hexagonal network structure, akin to chain-mail armour [265] (Fig. 39**C**).

This picture of kDNA as a regular lattice of links may be overly simplistic given the apparent complexity seen with electron and atomic force microscopy. In certain organisms, there is evidence that maxicircles are themselves catenated, and that a dense loop of redundantly linked minicircles is present at the edge of kDNAs. The topology of the kinetoplast network is not only of purely intellectual interest. Because kDNA is found only in parasites, a drug that disrupts kDNA replication and assembly may cure the infected host. For instance, ethidium bromide and berenil, two DNA-binding molecules, are known to interfere with correct kDNA catenation, although their precise mode of action is not yet fully understood [266].

Diao et al. [270] modelled kDNA as a 2D lattice of perfect circles under confinement and found a critical percolation transition density. Inspired by this work, Michieletto et al. [271] modelled kDNA as an ensemble of quasi-phantom semi-flexible rings and studied their behaviour using molecular-dynamics simulations. By comparing their simulations to Chen's

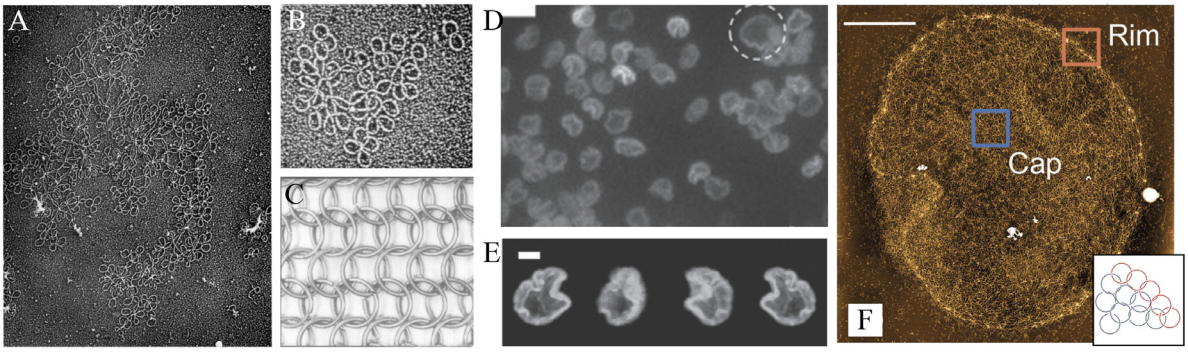

Fig. 39. A–B Transmission electron microscopy images of kDNA from *Leishmania tarentolae*. **C** The kDNA network structure represented as mediaeval chain-mail. **D–E** Confocal images showing the *shower cap* buckled conformation assumed by kDNA in the bulk. **F** AFM image of *C. fasciculata* kDNA. Scale bars are 2 μm in **G** and **H** and 10 μm in **F**.
Source: **A–B** reproduced from [267]; **C** reproduced from [265] ; **D–E** reproduced from [268]; **F** reproduced from [269].

experiments [265] using simulated *digestion* (Fig. 39**D–E**) they found that kDNA appears to be poised very close to the transition between a gas of unlinked rings and a percolating network of linked rings [271]. This has been interpreted as being evolutionarily advantageous in biological terms, since being close to the percolation transition offers a compromise between integrity of the structure and efficiency of disassembly during replication [271]. More recently, the groups of Klotz and Doyle have investigated the conformational properties of kDNA in solution [268], showing that it assumes a buckled *shower-cap*-like shape (Fig. 39**F–G**).

Research into kDNA is a promising future direction for researchers interested in topology and biophysics. It is humbling, and at the same time fascinating, to realize that decades after their conceptualization [102], olympic hydrogels and networks made of synthetic polymers have rarely been achieved or scaled up in the lab; meanwhile nature has been making them for millions of years inside parasites. Moreover, topological materials made of interlinked rings such as polycatenanes [272], and both 2D and 3D olympic networks, may offer a new way to assemble materials via topology, potentially displaying highly nonlinear material properties [273,274]. Recent work has raised the possibility that the two-dimensional kDNA sheet may be ultrasoft, with an in-plane Young modulus 10^6 times smaller than lipid bilayers [269]; additionally, these types of topological polymers provide fresh challenges for the polymer physics community, particularly with regard to the discovery of "non-conventional" scaling laws [275–277]. Future research into the formation, assembly and disassembly of kDNA may thus lead us to the design of surfaces, sheets or textiles made of linked rings. A major effort in this field will be to relate the material properties to the topologies of these materials so as to achieve bottom-up designability.

3.3.6. Supercoiled DNA and the Călugăreanu–White theorem

In circular dsDNAs, at each turn of the double helix the two DNA strands that run in opposite directions become linked exactly once. As discussed in Section 2.5, this can be best seen by visualizing circular dsDNA as a ribbon where the two edges represent the two strands. When a full turn is introduced, the ribbon can be cut along the centre line to produce two singly-linked rings. A natural consequence of this is that we can define an equilibrium linking number Lk_0 between the two DNA strands of a circular DNA molecule as the number of turns in the molecule, $Lk_0 = N/p$, with N the length of the molecule in base pairs (bp) and p its pitch. The ratio N/p typically will not be an integer value. Therefore, when DNA forms a simple circle, its ends require additional twisting to align. Although this twisting is generally negligible over thousands of base pairs, a DNA molecule joined into a circle with the minimum torsional stress will have a linking number that is the closest integer to N/p. For the B-DNA form, $p \simeq 10.5$ bp/turn, entailing that a DNA molecule 10 500 bp long will twist on itself $Lk_0 \simeq 1000$ times to achieve the most energetically favourable conformation. Thermal fluctuations and biological processes can alter this number. If DNA molecules 10.5 kbp long are randomly circularized in solution, the closed chains will not all display 1000 turns due to thermal fluctuations. However, closed chains with 1000 turns will be formed most frequently, followed by closed chains with more and fewer turns in a well-defined distribution whose width is determined by, among other parameters, the length of the chain and the temperature [107]. It is thus typical to refer to the DNA linking number *deficit* $\Delta Lk = Lk - Lk_0$ and, in turn, to define the *supercoiling* degree as the normalized linking-number deficit $\sigma = \Delta Lk/Lk_0$, how much over- ($\Delta Lk > 0$) or under-twisted ($\Delta Lk < 0$), a DNA molecule is with respect to its equilibrium value. Typical values of supercoiling in bacteria are negative: the DNA is underwound, taking values between $\sigma \simeq -0.02$ and -0.06 [107]. Molecules with the same ΔLk are called topoisomers (from the Greek *topos*, space; *isos*, equal and *meros*, part) since they are molecules that have the same (supercoiled) topology.

As we will see, the value of σ is closely connected to some biological processes, such as DNA transcription or replication [278], that affect the geometry of DNA and may thus interplay with DNA supercoiling [279,280] (Section 5). In general, the relationship between DNA mechanics and supercoiling found robust mathematical modelling, for example,

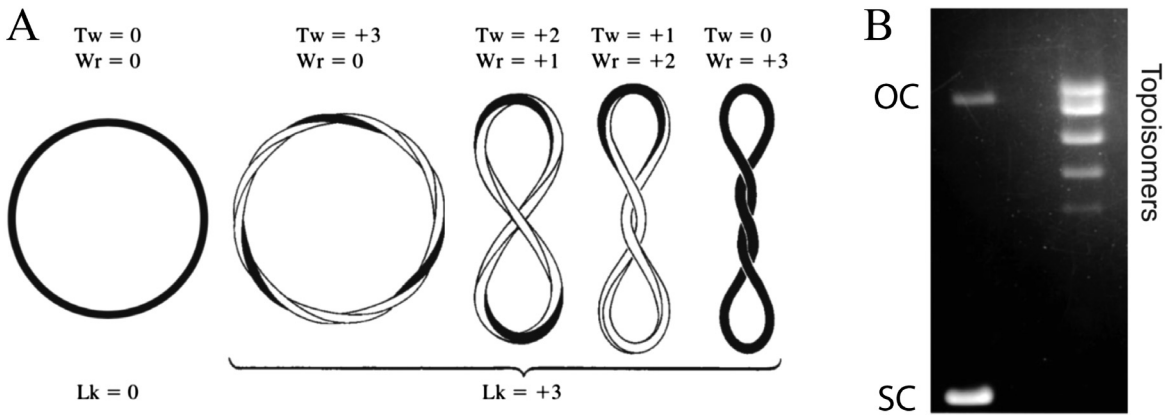

Fig. 40. **A** Cartoon of a rubber cylinder of square cross-section, where one face is painted black, to illustrate the Călugăreanu–White theorem [31]. **B** Image of a gel electrophoresis experiment. The bands on the left represent relaxed open circular (OC) and supercoiled circular (SC) DNA extracted from bacteria. The bands on the right are a result of treating the DNA on the left with Topoisomerase I, which relaxes the linking number deficit to thermal equilibrium.
Source: Figures adapted from [107,108].

in the problem of twisted elastic rings and related instability addressed via Kirchhoff models for elastic rods; see Goriely et al. (2006) [281] and references therein.

As explained in Section 3.3.5, it is possible to measure the linking of the many rings in kDNA using digestion experiments; however, how can one measure the topological properties of a single DNA molecule and, in particular, its supercoiling? A widely used method is gel electrophoresis, (Section 3.2.2), which can be used to determine the linking number (deficit) of the DNA strands, because there is an intimate relationship between the supercoiled topology of DNA and its 3D conformations. While circular DNA molecules cannot change their ΔLk, the CW theorem (Section 2.5) tells us that they can convert twist to writhe to minimize the free energy for a given ΔLk (Fig. 40**A**). As a consequence, the supercoiled DNA rings can writhe onto themselves, thereby assuming, on average, more collapsed conformations than ones with smaller ΔLk. Because the number of apparent crossings is directly related to the degree of collapse of DNA [160], molecules with more apparent crossings will be more collapsed and thus travel farther in the gel pushed by the electric field. This is typically seen in native DNA plasmids, circular dsDNA, extracted from bacteria: when run through an electrophoresis gel they separate into two bands, the faster-moving being supercoiled DNA while the slower is *nicked* DNA. The latter is produced when one of the strands in a dsDNA ring is broken; in such a scenario, the torsional constraint on the twist is relaxed and the need to obey the CW theorem is removed. A further consequence of supercoiling is the appearance of supercoiled-induced structures, often referred to as *plectonemes*, which are windings of the double helix onto itself, similar to over-twisted telephone cords; one can appreciate the twisted DNA in the outer part of Fig. 58. While plasmids can assume a range of ΔLk in cells, these different topoisomers appear collapsed onto the same band on this gel, Fig. 40**B**, because the pores in the gel are usually too large to allow for fine separation of molecules with slightly different sizes. When treated using a topoisomerase, the linking deficit is relaxed to, or near, thermal equilibrium. This generates a Gaussian distribution of topoisomers with mean Lk_0 and variance such that the free-energy difference of the conformations in the distribution is of order k_BT. A typical gel showing this distribution is shown in Fig. 40**B**.

3.3.7. *Knots, links and their regulation in vivo: topological enzymology*

Naturally occurring enzymes such as topoisomerases manipulate DNA in topologically interesting and non-trivial ways. The actions of these enzymes include passing one strand of DNA through another via transient enzyme-bridged breaks in one of the strands — a move performed by type II Topoisomerase — and breaking a pair of strands and recombining them to different ends — a move performed by DNA recombinase (Fig. 41**A**).

The precise arrangement of the strands involved in these operations is not obvious, as they may be twisted in a way to entrap writhe or crossings by the proteins. An interesting use of mathematical topology was the development of a topological approach to enzymology, applied to the study of how enzymes and proteins work, by Cozzarelli in the 1980s [282]. This is an experimental protocol that exploits knot theory in an effort to understand the action of certain enzymes on DNA. One reacts DNA plasmids with purified enzymes *in vitro*; the enzymes act on the DNA, causing changes in both the geometry, supercoiling, and in the topology, knotting and linking, of the molecules [282,283]. These enzyme-caused changes are experimental observables, using gel electrophoresis to fractionate the reaction products (Fig. 40), and transmission electron microscopy to visualize directly DNA knots and links (Fig. 41**A–D**). This experimental technique calls for the building of knot-theoretic models for enzyme action, in which one wishes to extract information about enzyme binding and twisting mechanisms from the observed changes in the DNA molecules. One such model is the *Tangle Model for Enzyme Mechanism* [145,284–287].

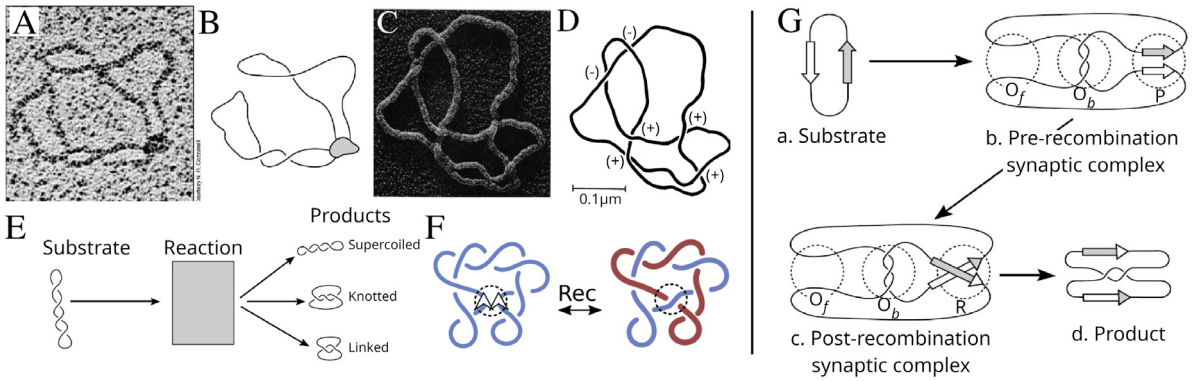

Fig. 41. A–B The *synaptic complex* of Tn3 resolvase, a recombination enzyme, capturing the resolvase protein during the action of changing DNA topology. **C–D** Transmission electron micrograph of a DNA knot produced by Tn3 resolvase. **E** *Topological enzymology* approach: treating the recombinase protein as a *black box* that takes in supercoiled DNA and outputs DNA knots or links. **F** An example of a recombination move that transforms a supercoiled plasmid into two linked DNA plasmids. **G** A more generic framework to treat recombination operations and leading to the tangle equations.
Source: **A,B,G** adapted from [25]; **C,D** reproduced from [282].

Let us focus on the example of site-specific recombination. A recombination site is a short, 10–15 base pair, oriented segment of duplex DNA whose base-pair sequence is recognized by the recombinase. Site-specific recombination can occur when a pair of sites — on the same or on different DNA molecules — become juxtaposed and aligned while bound to the recombinase [288–290]. This stage of the reaction is called *synapsis* and we call this intermediate protein–DNA complex, formed by the part of the substrate that is bound to the enzyme, together with the enzyme itself, the *synaptosome*. We call the entire DNA molecule(s) involved in synapsis, including the parts of the DNA molecule(s) not bound to the enzyme, together with the enzyme itself, the *synaptic complex*. The electron micrograph in Fig. 41**A–B** shows a synaptic complex formed by the recombination enzyme Tn3 resolvase when reacted with unknotted circular duplex DNA. The synaptosome is the black mass attached to the DNA circle, with the unbound DNA in the synaptic complex forming twisted loops in the exterior of the synaptosome, and the pair of recombination sites bound to the *3-ball* enzyme forming a (protein, DNA) 2-string tangle (Section 2.3). After forming the synaptosome, a single recombination event occurs: the enzyme makes two double-stranded breaks at the sites and recombines the ends by exchanging them in an enzyme-specific manner. The synaptosome can then dissociate, and the DNA is released by the enzyme. We call the pre-recombination unbound DNA molecule(s) the substrate and the post-recombination unbound DNA molecule(s) the product.

In addition to changing the genetic sequence of the substrate DNA molecule, site-specific recombination usually alters the topology of the substrate, changing types of knots, links and supercoiling in the circular molecules (Fig. 41**E**). At each recombination site, the base-pair sequence is in general not palindromic, and hence induces a local orientation on the substrate DNA circle. If these induced orientations from a pair of sites on a singular circular molecule agree, this site configuration is called direct repeats, or head-to-tail; if the induced orientations disagree, the site configuration is called inverted repeats, or head-to-head. If the substrate is a single DNA circle with a single pair of directly repeated sites, the recombination product is a pair of DNA circles and can form a DNA link, or catenane (Fig. 41**F**).

Fig. 41**G** describes the tangle model for site-specific recombination in more general terms. A single recombination event on a pair of directly repeated sites on unknotted substrate yields 4 unknown 2-string tangles: O_f (the outside free tangle, consisting of the DNA outside of the protein), O_b (the outside bound tangle, describing the binding of the protein to the DNA), P (the parental tangle, describing the DNA recombination sites just before recombination), and R (the recombinant tangle describing the recombined sites). The tangle structure of the DNA bound to the protein is described by two tangle sums: (O_b+P) just before recombination, and (O_b+R) just after recombination. For any tangle T, the notation $N(T)$ denotes the numerator construction on the tangle (Section 2.3), where one connects the two upper ends of the tangle strands with each other and the two lower ends of the tangle with each other, producing either a knot or a 2-component link when the tangle defining ball is omitted. A single recombination event on a single circular substrate molecule produces two recombination tangle equations in four unknowns

$$N(O_f + (O_b + P)) = S, \tag{49}$$

$$N(O_f + (O_b + R)) = K_1\,. \tag{50}$$

Both right-hand sides of Eqs. (49)–(50) are known by means of electron microscopy or atomic force microscopy, for instance the former (substrate, S) could be the unknot while the latter (the knotted product, K_1) a Hopf link (Fig. 41**G**). Thus one can conclude that O_f is the trivial tangle, and one can also argue that P is also the trivial tangle [25,145]; so in practice there are only 2 variables to be found, O_b and R. Since there are two unknowns, we use experimental information

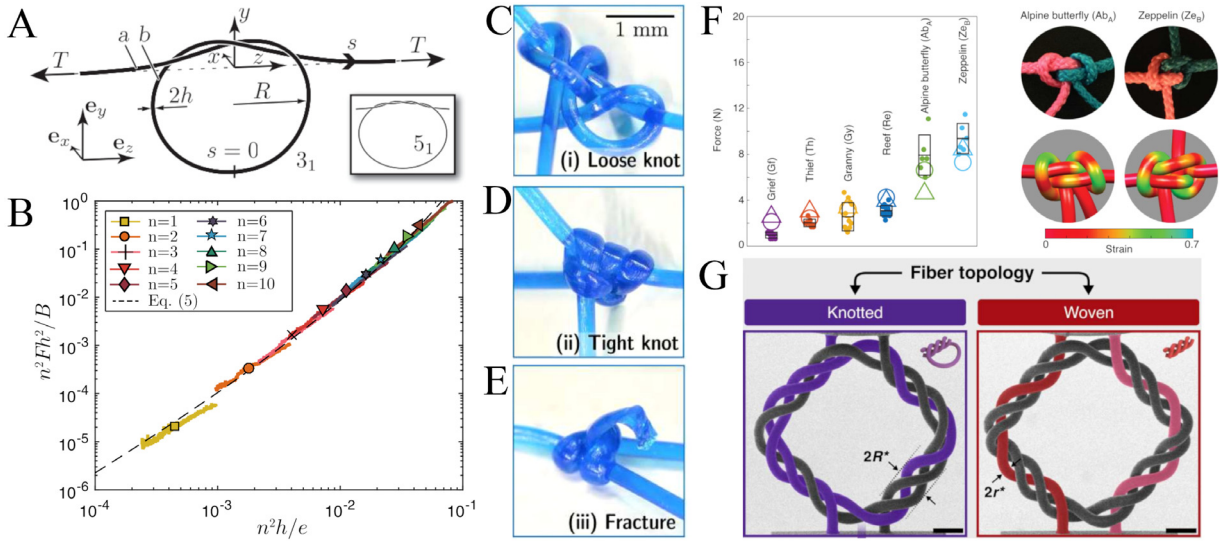

Fig. 42. **A** Geometry of an open trefoil knot under tension. Inset: open cinquefoil knot. **B** experimental traction curves as a function of the nondimensional end-to-end shortening; the dashed line is Eq. (5) of [294]. **C–E** Photographs of representative knots tied with different values of pre-tension: **C** loose knot **D** tight knot and **E** fracture of the last throw. **F** (left) Experiments measuring the maximum load before untying of two commercial fibres: averages (horizontal lines) over individual experiments (small filled circles) agree quantitatively with the relative strength predicted from simulations (large empty circles or large empty triangles); black boxes indicate standard deviations of the individual experiments; (right) simulations of complex bends show good shape agreement with tight configurations of bends in nylon ropes, with colours indicating the nonuniform strain distributions. **G** SEM images with colour shading overlaid onto a single fibre in the knotted (left) and woven (right) hierarchical rhombuses, each with two vertically connected fibres; an overhand knot is formed by each of the two fibres in the knotted rhombus, vertical fibres in the woven rhombus are coloured red and pink.
Source: **A** reproduced from [295]; **B** reproduced from [294]; **C–E** reproduced from [296]; **F** reproduced from [297]; **G** reproduced from [298].

from two iterated rounds of recombination, producing a second product equation

$$N(O_f + (O_b + R + R)) = K_2\,. \tag{51}$$

These tangle equations can be solved for the unknown tangles using the topological techniques of Dehn surgery on branched cyclic covering spaces, described in detail in Ref. [145].

3.4. Mechanics and elasticity of knots

Knots have been known since the dawn of humanity and are employed in the most diverse settings, including surgery, construction, sailing, climbing and engineering. It is common knowledge in those settings that the presence of a knot decreases the tensile strength of a fibre [1], i.e., knotted fibres break at a lower value of the applied stress. It is also commonly known that the fibre is weakest just outside the entrance of the knot. Despite this, the mechanical properties of knotted and tangled fibres — the elastic and plastic response of the fibre to an uniaxial deformation — were not explored for a long time. Only at the beginning of the 21st century were simple uniaxial elongation experiments performed systematically, in which the knotted fibre is pulled in opposite direction from its free ends until it breaks. This can be done with any filament: fishing line or spaghetti at the macro-scale [291,292], actin, knotted and pulled with optical tweezers, at the micro-scale [180] or even at the molecular level [293]. With a combination of experiments and numerical simulations, it was proposed to pinpoint the *fault* point of a knot at the point of greatest curvature [291] that corresponds to the point of highest stress; such a point was observed to be invariably located at the knot entrance. Further, the greater the curvature, the greater is the reduction in tensile strength (more precisely, the lower is the tensile load required for crack formation) as, in real fibres, stress due to bending adds to that due to the load. It was also observed that the knot strength is correlated with its complexity; however, this result was later challenged by successive experiments on knotted fishing lines, where the authors found the exact opposite trend [292]. This discrepancy has been ascribed to the different materials constituting the filaments used in the experiments, which favour different deformation patterns.

Friction was left out from these first attempts; however it has to play a role in determining the strength of a knot, at least in macroscopic filaments. Friction at contact points hinders the tightening of the knot under load. On the other hand, depending on the material, it may become the dominant cause of a failure, as the filament breaks rather than slide further against itself. In general, predicting the mechanics of knots is a challenging endeavour, due to the complex interplay of elasticity, friction and bending. In particular, the problem of describing knot tightening has been attempted via statistical mechanics [299], purely geometrical [300] or perfectly flexible models [301]. However, a considerable advance

was achieved with elastic theories of overhand knots — knots that can be tied starting from a 3_1 — which, through a perturbative [295] or a scaling [294] approach, were able to predict the shape of the knot and the traction force as a function of the end-to-end shortening (Fig. 42**A**,**B**). The latter quantity gives an indication of the strength of the knotted fibre. Recent work on surgical knots has elucidated the influence of the interplay between friction and elasticity on knot strength, showing also that knots with multiple throws, i.e., more complex knots, are, at least for this class of knots, stronger than simple knots [296] (Fig. 42**C**-**E**).

Aside from simple or overhand knots, the mechanical response of oriented 2-tangles (Section 2.3) has been investigated. For these simple tangles a purely topological classification can be brought forward, showing that their strength can be predicted based on the number of crossings N, the twist fluctuation τ and the so-called edge circulation Γ [297]. The quantity τ is related to internal torques of the fibres that can favour or disfavour untangling; Γ is connected to friction and it increases if pairs of edges of the knot diagrams, belonging to different strings and sharing a face, are pulled in opposite directions and thus have to slide against each other. This triplet of observables correlates strongly with the tangle strength, measured in experiments as the maximum load before untangling (Fig. 42**F**). Intriguingly, this description may be extended to complex fluids and liquid-crystal structures (Section 7): as noticed in [297], tangled vortices in complex fluids (Section 3.5.5) and defect loops in liquid crystals (Section 3.5) may permit similar statistical descriptions through reduction to topological crossing diagrams.

Knots have also emerged recently as an enhancing factor for a material property of engineering interest: toughness. Toughness is usually defined as the ability of a material to absorb energy and deform plastically without breaking; in other words, it aims to quantify the structural resistance of a material, its ability to absorb damage and its reliability under stress [302]. A high-toughness material is very desirable for applications where failure would be disastrous. A clever way to increase toughness, inspired by nature [303,304], is the introduction of a *hidden length*, a portion of the filament sequestered, through some mechanism, from the contour. Consider a macroscopic linear filament of contour length ℓ whose ends are grafted onto two separate surfaces: the aim of this filament is to provide a connection, e.g., an electric wire. If the surfaces are pulled apart, the filament can be extended without any energy penalty up to the length ℓ: as such, no work is done and no energy is dissipated up to the distance ℓ. Suppose that a part of the filament is folded and is kept in its folded state by some mechanism, e.g., by weak sacrificial bonds. Now the folded fibre can be extended freely only up to $\ell_0 \ll \ell$; work has to be done in order to elongate it further. Thus, under a load, the folded filament is able to elongate much more than its reduced original length ℓ_0, emulating a plastic deformation and dissipating energy without breaking.

A knot provides a way to realize such a hidden length, as shown in [305], as it dissipates energy during sliding through friction. The experimental proof of concept [305] of such a system produced the world's toughest fibre, increasing the toughness modulus of a commercial Endumax macroscopic fibre from 44 J/g up to 1070 J/g. These results [305] surpass the benchmark of Kevlar ($\approx$ 80 J/g) and even spider silk, the toughest natural fibre, the record being 390 J/g [306]. This concept [305] raises the interesting question of whether the presence of knots in some natural materials could result from an evolutionary pressure to improve their toughness and robustness; furthermore, it was very recently proven to be transferable to more complex designs, such as hierarchical intertwined materials, for which a knotted pattern was shown to be much more deformable and tough than a simply woven design [298] (Fig. 42**G**). Thus, a knot makes a filament weaker and, at the same time, increases its toughness. This is not a contradiction: indeed, a classical materials-design problem is that strength and toughness tend to be mutually exclusive; strong materials are brittle while tough materials are highly deformable [307]. Knots are no exception: however, topology may inspire further design ideas to improve deformability in strong, brittle materials.

3.5. Topological structures in the continuum

In continuum descriptions of media, the core object is the field, describing the spatial variations of the dynamical variables, such as molecular orientations, velocities, currents and electromagnetic fields. Superficially, this differs from the description of loops, knots, links, and other topological objects that appear in DNA, proteins and other polymers. However, while a field itself is continuous, topology ensures that fields can bear defects of different dimensionalities: points, surfaces, and curves that behave as discrete objects that can be knotted or linked, and can analysed using the tools from knot theory, albeit with additional restrictions provided by the surrounding field. Defects can thus be dealt with on the level of continuum models. Additionally, solitons are possible, which are not localized to idealized points or curves, but nevertheless possess quantized topological invariants and are as such protected from transitioning into another state without crossing an energy barrier.

Examples of topological defects in fields and the underlying mathematical rules were outlined in Section 2.8.1. In this section, we present the most iconic realizations of topological objects in continuous media, in achiral and chiral nematics, plasma and superfluids. More in-depth topics are discussed in Section 7.

3.5.1. Defect creation in nematic liquid crystals

In the bulk of a nematic liquid crystal, far from any constraining boundaries, the orientational order will tend to a uniform defect-free state due to elastic energy minimization, but out of equilibrium, it can contain many defects, which give it the name *nematic*, meaning thread-like. These defects undergo a coarsening dynamics, reducing in complexity,

combining, annihilating, typically following a power-law evolution of typical defect density and length-scale [308,309]. A typical way of creating initial defects is by cooling down from the isotropic (disordered) state. This coarsening can be studied statistically, and reflects some properties of the material. To create defects that persist in equilibrium, and hold desired topological properties, designed in advance, such as entangled loops and knots, one can engineer the boundary conditions to enforce a particular configuration. This is outlined in Sections 3.5.2 and 7.3. Systems with broken chiral symmetry that prefer spatially nonuniform orientational order, and can thus support stable defects in equilibrium, are discussed in Sections 3.5.3, 3.5.4 and 7.1.

In active nematics, closely related to active polymers introduced in Section 3.3.3, there is an internal energy production that can counteract the coarsening by driving shear flows that can extend and split existing line defects and create new defects by pair creation, all the while preserving the overall total topological invariants. This is called *topological turbulence*, and is a focus of recent studies [310,311]. Topics related to active nematic systems are discussed in Section 7.5.

3.5.2. Topological colloids and knots in liquid crystals

Nematic liquid crystals offer a realization of knots through defects in the director field. The objects of interest are line defects: disclination lines, which can follow different curves in space. If a line defect in a nematic forms a loop, then more subtle topological features come into play [72,312–314]. In the bulk, they are only transient structures occurring after a phase transition, but they can be stabilized by introducing inclusions that enforce homeotropic boundary conditions, e.g., the fibre in Fig. 30**C–D**.

It is natural to ask in what way knotting or linking of these lines can be achieved. Early experimental observations of knotted defects in liquid crystals were Hopf links made of oily streak disclinations in cholesteric liquid crystals [315]. In the 1990s, attention turned to confinement configurations where the liquid crystal surrounds a small particle such as a water droplet [316] or a colloidal particle [317] that induces, through suitable anchoring, a topologically non-trivial director structure around it. The most recognizable example of a stable loop defect is the Saturn-ring configuration [318] (Fig. 43), which forms around a spherical inclusion in a liquid-crystal host and is prepared such that the liquid crystal aligns along the normal direction at the particle interface. The defect is required in the liquid crystal to counteract the *effective defect* present due to the colloidal particle. The liquid-crystalline matrix can mediate interactions between several inclusions, which are fundamentally different from those known in isotropic fluids [319]. These results set the stage for a revival in the field, largely prompted by the study of an array of colloids within a nematic host [320]. The defects were first considered as the epitome of the deformed director configuration and perhaps even the fabric that binds colloidal inclusions into an ordered lattice. By micromanipulating them using laser tweezers, rings of disclination lines in such a system can be opened and reconnected so as to create knotted structures identical to those in Fig. 3 [127,313,321]. The extent of these knots of disclination lines is determined by the size of inclusions and can extend over distances of a few tens of μm. An even more impressive phenomenology is seen around colloidal inclusions of non-spherical topology [322] and non-orientable inclusions such as a Möbius strip [323]. Knotted structures are also observed in chiral nematics confined to cavities [324].

Topological features in nematics rely heavily on well-defined boundary conditions imposed on the director field by the confining walls, and on interfaces with solid inclusions or surrounding liquid. Most commonly, the sample is sandwiched between two parallel plates with fixed spacing: a liquid-crystal Hele-Shaw cell. The plates must be treated in order to align the director in the chosen direction. For rod-like calamitic liquid crystals, perpendicular, also called homeotropic, alignment is achieved by coating the surfaces with substances with long perpendicular chains, and uniform planar alignment is achieved by rubbing a polymer-coated surface. When planar alignment on top and bottom are oriented in perpendicular directions, this is a twisted nematic cell. Similar approaches are used to induce homeotropic alignment on silica microspheres.

By confinement in a twisted nematic cell, and using a lattice of spherical microparticles, defects in liquid crystals can be stabilized in different forms. The simplest structures are particles accompanied by point defects, or encircled by Saturn-ring defects, forming chains or rhombic 2D lattices, respectively [325] (Fig. 43**A,B**). More interesting are the cases where the line defects (disclinations) with winding number $-1/2$, discussed in Section 2.8.1, assume the shapes of more complex curves. Using just spheres with homeotropic anchoring, one can, with suitable confinement, create different two-dimensional [326] or three-dimensional [327,328] lattices that support almost arbitrarily long persistent closed defect loops — disclinations — that can be knotted or linked (Fig. 43**C–D**).

Around particles with homeotropic surface anchoring, nematic disclinations are topologically required to close into loops that may be knotted. The line field around the loop gives it a local structure that has its own topological rules. The resulting knots are best described as *framed knots*, as in addition to the curve in space, they require a local coordinate frame at each point that encodes the behaviour of the surrounding field. For example, if the disclination line has a constant $-1/2$ winding number, only self-linking numbers of multiples of $1/3$ can exist in a closed loop, to preserve the continuity of the surrounding field with the three-fold symmetry. The simplest nontrivial example of such self-linking is found around a pair of colloidal particles (Fig. 43**E**) . A global topological conservation law connects the total topological charge of the colloidal inclusions, the self-linking number of disclination loops, and linking numbers between different constituent loops [313]

$$\sum_i \frac{3}{2} Sl_i + \sum_{ij} Lk_{ij} = q - n \mod 2, \tag{52}$$

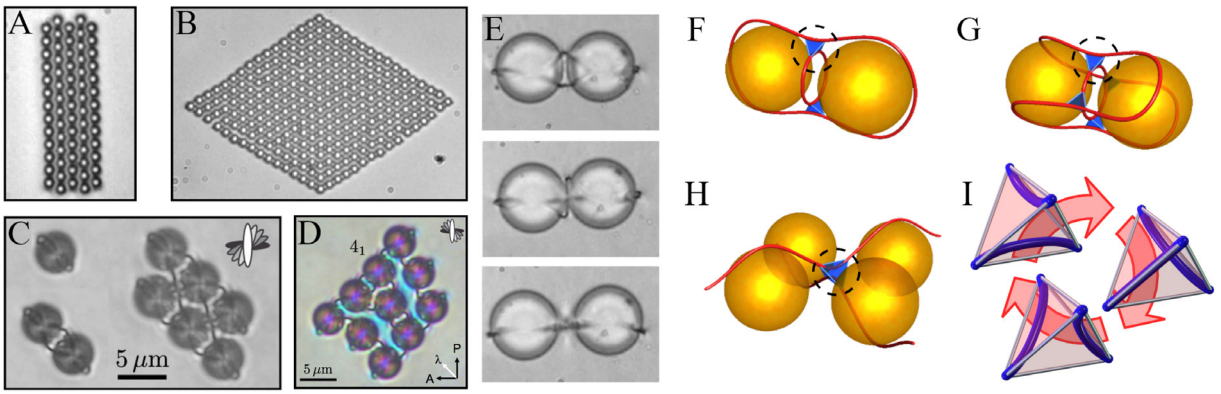

Fig. 43. A–D Nematic colloids based on silica microparticles with homeotropic anchoring, assembled with different topological defects: **A** dipolar structure (point defects), **B** quadrupolar structure (Saturn-ring defects), **C** disclination lines entangling multiple colloidal particles, **D** knotted disclination lines, forming a figure-eight knot. **E–I** Rewiring of disclinations. **E** Entangled colloidal dimer in three conformations. **F** A schematic view, showing two tetrahedral rewiring sites in a homogeneous cell. **G, H** Similar tetrahedral rewiring sites in a π-twisted and $\pi/2$-twisted nematic cell, respectively. **I** Three ways of connecting disclination lines in each tetrahedral site.
Source: **A** reproduced from [71]; **B** reproduced from [325]; **C–D** reproduced from [329]; **E** reproduced from [313]

which shares an algebraic form with helicity, defined by Eq. (31). q and n are the total topological charge of the linked disclinations and their number. The ambiguity modulo 2 stems from the $\mathbb{Z}_2$ nature of the fundamental group $\pi_1(\mathbf{RP}^2)$, acting on the second homotopy group $\pi_2(\mathbf{RP}^2)$ of the real projective plane (Section 2.8.1); bringing a point defect continuously across an arbitrarily positioned sign discontinuity changes the sign of the topological charge. Using the Călugăreanu–White theorem, self-linking is directly coupled to the writhe (Section 2.5), and thus to the three-dimensional shape of the disclination line, providing a way to control the shape through topology. Additionally, the abstract rewiring moves, coming from knot theory, correspond to rotations of local tetrahedral chunks of director field [313] (Fig. 43**F–I**).

This mechanism comes to full fruition on a two-dimensional lattice of particles (Fig. 43D), where the top projection, seen under the microscope, corresponds to a planar knot diagram (Section 2.2.1). The spaces between the particles represent crossings of the type shown in Fig. 43**H**, which can be reconfigured between the crossing and two smoothings using optical tweezers [127], in a procedure akin to the splicing of crossings used to define the Kauffman bracket (Section 2.2.4). This rewiring of disclinations allows targeted design of any conceivable knot based on its planar diagrams and using a rectangular lattice of microspheres of sufficient size. The Jones polynomial of a knot also relates to the knot diagram seen under the microscope [329]. While the global topology of the disclinations may form any knot, the physical properties of the resulting entangled lattice of defects depend more on the local properties of each tangle, as the disclination is elastically bound to the particles, and only interacts locally.

Topologically nontrivial surfaces, such as tori and higher genus surfaces, i.e., surfaces obtained by taking the connected sum of multiple tori [322], as well as micro-fabricated knots and links [330], can be used to design systems particularly suited for self-assembled and switchable structures that reap all the benefits of topologically protected states (Section 2.8.1). This versatility is especially promising in soft micro-photonics [129].

If disclination loop cross sections are not restricted to constant cross sections, the self-linking rules generalize to a non-commutative, quaternionic algebra [313]. Such disclinations can be stabilized by confinement of chiral nematics, or seen as transient structures in active nematics. An interesting parallel with quantum logic gates has recently been demonstrated [331]. For knotted disclination loops, connections between the global topology of the nematic field and invariants such as the knot determinant and Goeritz matrix, have been demonstrated [314,332].

3.5.3. Chiral, or contact, topology in cholesterics

The twisted structure of cholesterics, or chiral nematics, is a consequence of the presence of a constant term in the Frank free energy,

$$\mathbf{n} \cdot \nabla \times \mathbf{n} = -q_0,$$

that induces a preference for a non-zero value of the twist density; here $p = 2\pi/q_0$ being the cholesteric pitch. This characteristic length-scale, coupled with the complex interplay of geometry, elasticity, and boundary conditions, leads to a huge variety of metastable structures in cholesterics, including many of the phenomena discussed elsewhere in this text, such as knots, skyrmions and other solitons. On one level, the topology of cholesterics is just the topology of nematics — both systems are described by director fields — but cholesterics typically exhibit more complex topological structures. Oily streaks, for example, where the pitch is much smaller than the system size, exhibit networks of disclination lines that can be described by Hamilton's quaternion algebra [333]. For systems where $p \sim L$, the system size, this approach is no longer applicable. Many recent experiments exploring topological structures in cholesterics probe this regime, and

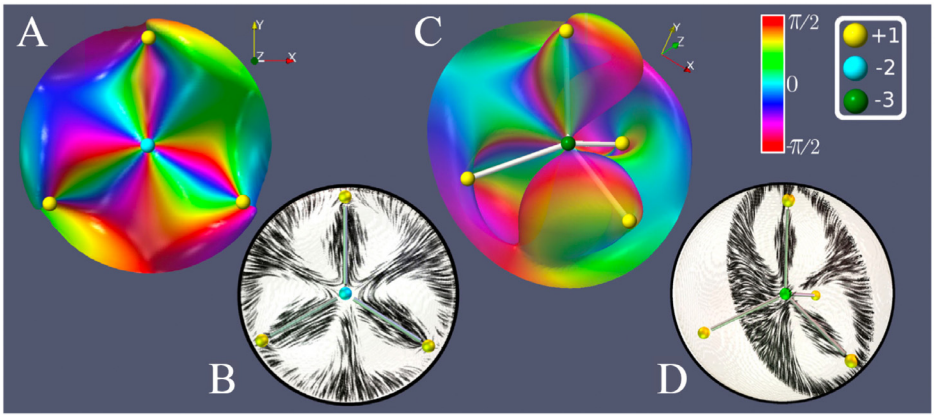

Fig. 44. Point defect constellations in cholesteric droplets. The defects are shown by small spheres inside the droplets; the colour of the sphere indicates the charge (shown top right). The coloured surfaces in **A** and **C** are the loci of $n_z = 0$, with the colour indicating the angle (n_x, n_y) relative to the x-axis. **B** and **D** show the director field configurations on slices through the droplets. These structures are described in terms of contact topology and the ADE classification of singularities.
Source: **B**, **D** adapted from [335].

whether topological methods can be used to understand these systems is important, particularly for the design of robust soft devices.

Recently, an alternative perspective has been developed, using methods and ideas of contact topology to understand cholesterics [334]. In this theory, the key topological role is played by the twist density, $\mathbf{n} \cdot \nabla \times \mathbf{n}$. In the contact-topology perspective one studies the interplay between the twist density and topological properties of the liquid-crystal configuration. Since topology is inherently scale free and the twist density has dimensions of 1/length, in contact topology one cares only about the sign of the twist, or if it is zero. If $\mathbf{n} \cdot \nabla \times \mathbf{n} \neq 0$ everywhere, then it is single-signed, and we say that the texture is chiral. One of the essential properties of chiral textures is that they are non-integrable everywhere, i.e., not representable as a potential field. In mathematics, such structures are more formally defined as contact structures. Contact topology studies the topology of such structures, and provides a wealth of new techniques that may be brought to bear on cholesteric materials.

A simple example of this is the behaviour of a hedgehog defect inside a cholesteric. Starting with the standard hedgehog director field $\mathbf{n} = (x, y, z)/\sqrt{x^2 + y^2 + z^2}$, which has zero twist, one can attempt to perturb it to make it chiral, i.e., having a single sign of twist, to become more compatible with the cholesteric energy. It is, however, a celebrated theorem of Thurston's that such a chiral perturbation does not exist [335]. As a consequence, any hedgehog defect in a cholesteric must have a region of reversed handedness; indeed experiments demonstrate that near cholesteric point defects the twist reverses in sign in some small region [336]. More recently, experiments and theory have explored cholesteric droplets with normal anchoring [335,337,338]; some examples are shown in Fig. 44. Such a system has a natural dimensionless parameter $N = R/p$, where R is the radius of the droplet and p is the pitch. When N is small, one can observe something close to the hedgehog; as N increases the defect moves to the edge of the droplet, to suppress the region of wrong-handedness. As N is increased further, however, the defect returns to the centre, now a hyperbolic point defect, which *can* be made chiral, becoming the focal point of a constellation of point defects, which can be understood using the ADE classification of singularities given by Arnold [335].

Another application of contact topology is to use it to classify chiral textures. We start with an analogy. Consider a three-component director field in a 2D domain, with boundary conditions $\mathbf{n} = (0, 0, 1)$ (Fig. 20**G**). The topological classification of such textures is given by an integer, the skyrmion charge. We can augment this classification by further demanding that the textures be chiral — so the twist density does not vanish — and consider two textures distinct if they cannot be connected by a path of chiral textures. A simple example here is a cholesteric between two parallel plates of separation h, with boundary conditions $\mathbf{n} = (1, 0, 0)$ on both top and bottom plates. One may then consider the twisted textures $\mathbf{n} = (\cos w\pi z/h, \sin w\pi z/h, 0)$, with w an integer winding number, the layer number. As a nematic texture, w is topologically equivalent to $w + 2$. Using contact topology however, one can show that w and $w + 2$ are topologically *distinct* when considered as chiral textures; any path between them must pass through a configuration where the twist vanishes at some point in the material [334]. We therefore establish a chiral topological barrier to changing the layer number, which can explain the complex and frustrated structures seen, for example, as a consequence of the Helfrich–Hurault layer instability (Fig. 45), which has received renewed recent interest [339]. More generally, imposing the chiral condition leads to a variety of similar results. For example, layering transitions in cylindrically-confined chromonic liquid crystals [340] and the structure of line defects in cholesterics [341], can both be understood from this perspective.

So far the applications of contact topology have been rudimentary; it remains to be seen if it can bring fresh ideas into exotic topological structures in cholesteric liquid crystals such as knots and Hopf solitons [75,76,314,342,343]. More

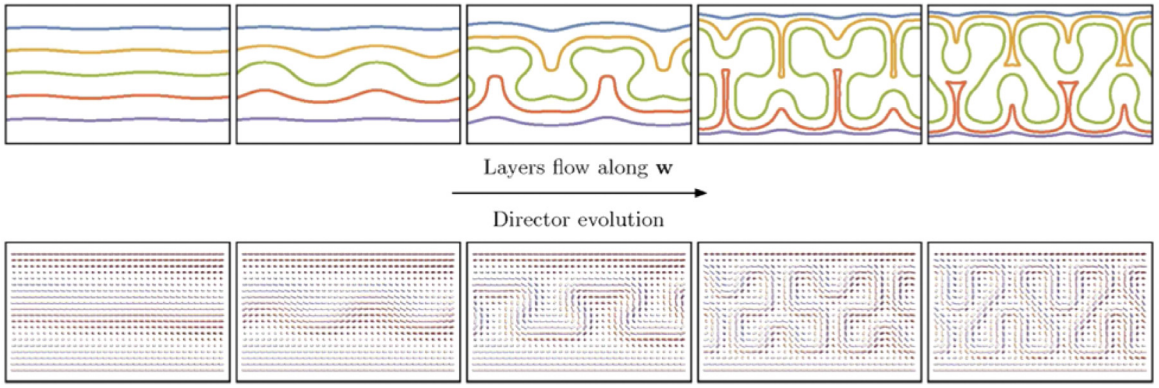

Fig. 45. The Helfrich–Hurault instability leads to layer undulations; contact topology proves the existence of an energy barrier preventing relaxation to the lowest energy uniformly twisted state. See [334] for more details on the definition and time evolution of cholesteric layers.
Source: Adapted from [334]

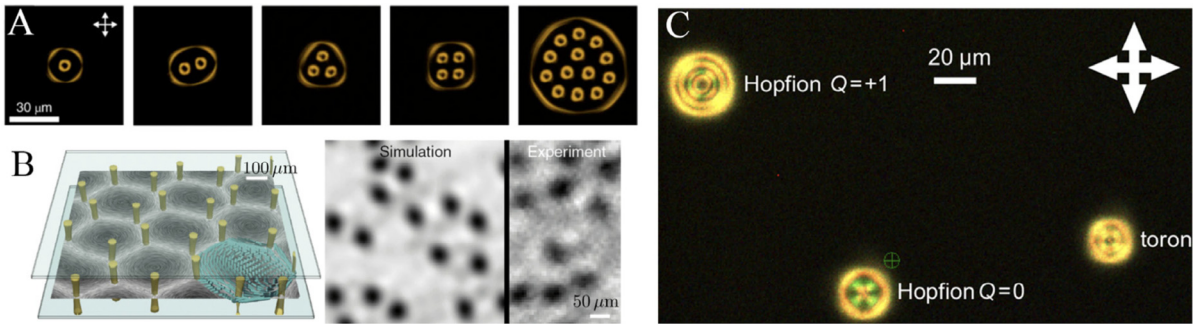

Fig. 46. Topological solitons in confined chiral nematics. **A** Skyrmions in a thin chiral nematic cell behave as free-floating quasi-particles and can be caught in *skyrmion bags*, a different kind of solitonic structure. **B** A hexagonal lattice of half skyrmions in a 135 nm thin cell filled with a chiral nematic in the blue phase III state, and a comparison of simulated and measured transmission micrographs. The scale bar corresponds to 50 nm. **C** Experimental realization of hopfions in a thin cell of a chiral nematic.
Source: **A** reproduced from [346]; **B** reproduced from [349]; **C** reproduced from [75].

broadly, the mathematics of contact topology has ties to string theory, Floer homology and three-manifold topology, and could be used to explore the interplay of chirality and topology in other materials.

3.5.4. Topological solitons in chiral nematics

Recent works show that solitonic field structures with highly nontrivial topology can be made, manipulated, and assembled, even at a level of performing as effective particles. Generally, solitonic structures exhibit a knotted or linked director field; the object that is linked in this case is not an easily visible physical disclination line, but the set of locations in space, where the director points in the same direction. The topological formalism behind these solitons is described in more detail in Section 2.8.1.

Such solitonic structures are observed in chiral nematics: when a chiral nematic is confined in a thin cell that forces a homeotropic alignment on both boundaries, the conflict between the unfavourable uniform director enforced by the boundary conditions and the elastic tendency towards a helical organization leads to a frustrated environment. With careful selection of the ratio between the cell thickness and the intrinsic helical pitch, an environment can be created that stays in a uniform field configuration, but solitons can be induced by external electric fields or with focused laser light. Solitons move freely and scatter light, acting as optical elements when self-assembled. Many different but related structures have been observed, depending on the exact experimental parameters, and different soliton types may also be created in the same sample, such as torons, hopfions, skyrmions, merons and bubble domains [75,344–346]. Fig. 46 shows a few examples of baby skyrmions [346–349] and hopfions [75–77] (see also Fig. 26), as realized in an experimental setting. Examples of blue phases are given in Section 7. Topological protection ensures that these continuous fields exhibit stable particle-like excitations that remain separate and persist in a deterministic form. Such manifestations of topological concepts in continuous media are not limited to liquid crystals, as we explore below and in Section 7.

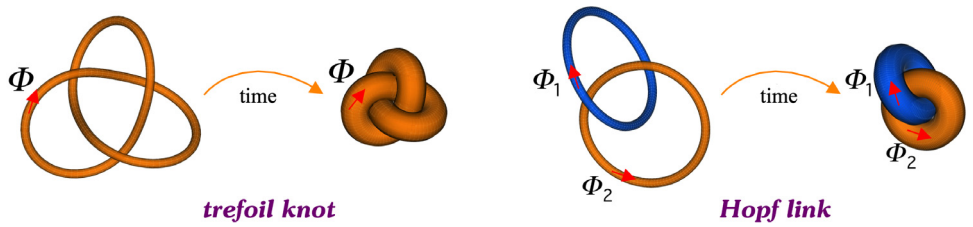

Fig. 47. Relaxation of a trefoil knot and a Hopf link to their tight configurations, under the ideal conservation of magnetic volume V and flux Φ.

3.5.5. Topological fluid mechanics

The topological interpretation of helicity in terms of linking numbers through its direct computation by Eq. (31) contributed to the development of modern topological fluid mechanics [86,350,351]. The search for knotted flows in dynamical systems has led to the mathematical proof of the existence of knotted solutions to the Euler equations [352], and mathematical questions related to integrability and soliton formation have been re-interpreted in terms of existence and transport of topological properties. From a physical viewpoint questions relating energy to topology have become one of the central topics of current research.

Energy groundstates and ideal knots. Fundamental results on energy lower bounds for topologically complex magnetic fields in terms of linking and crossing numbers stimulated the search for ground-state energy spectra. The magnetic relaxation of tubular knots and links made of bundles of field lines subject to volume- and flux-preserving diffeomorphisms can be explained considering the relaxation of a magnetic trefoil knot under the action of the Lorentz force. Since this force shortens the field lines, under conservation of magnetic volume V, the tubular knot bundle will gradually increase the cross-section, and because of flux conservation the average magnetic field will gradually decrease its intensity. Hence, the magnetic energy $M = M(t)$ will decrease as the knot becomes gradually tighter. The process stops when parts of the inflated tube come into contact (Fig. 47), reaching in the end the tight configuration of an ideal knot [353] (Section 3.2.3). The minimum energy state is achieved when the topology of the system prevents further relaxation.

Lower bounds to magnetic energy are found by inequalities between energy, helicity and crossing number of the form [354–356]

$$M(t) \geq q|H| \,, \qquad M(t) \geq \left(\frac{2}{\pi}\right)^{1/3} \frac{\Phi^2 \bar{C}(t)}{V^{1/3}} \,, \tag{53}$$

where q is a positive constant function of the field configuration, and $\bar{C} \geq c_{\min}$ (topological crossing number) is the average crossing number. This problem has revealed interesting connections with other aspects of theoretical physics [357]. By combining analytical methods with numerical optimization techniques, developed for instance by Cantarella and collaborators [358], the ground-state energy spectra of hundreds of knots and links have been determined [359], providing insight into related problems in mathematical vortex dynamics and high-energy physics [360].

Braided structures in solar physics and particle transport. Since in highly conducting plasmas magnetic helicity is approximately conserved, topological techniques have proven particularly useful to estimate energy contents in solar activity and astrophysical flows. Various methods have been developed for this purpose [361]. One significant development is to replace the standard helicity for closed volumes with the relative helicity for open volumes [83], while retaining its topological meaning and gauge invariance. This new form of helicity is computed with respect to some reference field, and has the advantage to account for the helicity flux across boundaries. Another key ingredient comes from modelling coronal loops by representing magnetic fields as open braids (Fig. 48B). By mapping the photospheric regions where the footpoints of the coronal loops are located to the horizontal planes $z = 0$ and $z = 1$ of a straight braid, we can make use of the potential

$$\mathcal{A} = \int_{z=0}^{z=1} \mathbf{A} \cdot \mathrm{d}\mathbf{l} \tag{54}$$

to provide, under an appropriate gauge, topological information on the braid pattern in terms of the average crossing number of field-line pairs [362,363], and by applying braid theory techniques to coronal plasma loops, it is possible to determine accurate estimates of the free energy of the magnetic field [364].

Upon close interaction, magnetic field lines may also reconnect and change topology, due to the presence of intense currents and plasma resistivity ($\eta \neq 0$). In this case one can prove that the magnetic energy $M = 1/(2\mu_0) \int |\mathbf{B}|^2 \mathrm{d}V$, μ_0 being the magnetic permeability in the vacuum, is dissipated at a rate bounded from below by the helicity change, according to

$$\left(\frac{\mathrm{d}H}{\mathrm{d}t}\right)^2 \leq 8\mu_0 \eta M \frac{\mathrm{d}M}{\mathrm{d}t} \,. \tag{55}$$

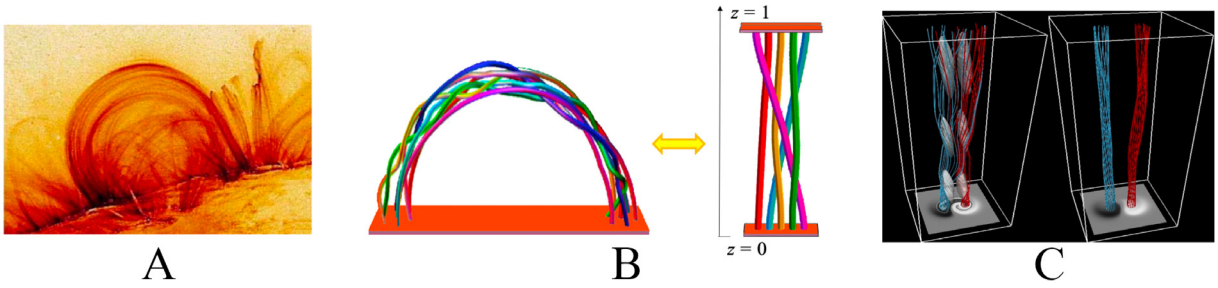

Fig. 48. **A** Plasma loops in the solar corona (TRACE mission, November 6, 1999, 2 UT). **B** Numerical rendering of a braid of magnetic fields, and straight braid representation. **C** Numerical simulation of the energy relaxation of braided magnetic field lines).
Source: **C** reproduced from [363].

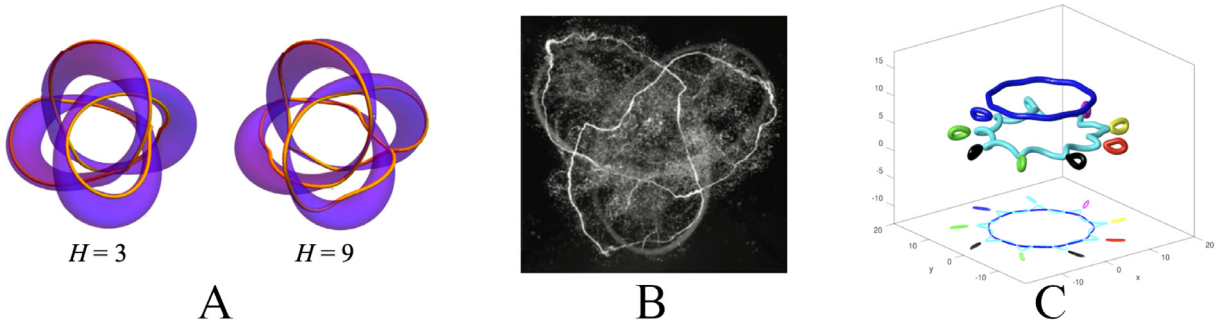

Fig. 49. **A** Figure-of-8 knot fibrations by tuning magnetic helicity. **B** Production of a trefoil knot vortex filament in water. **C** Numerical simulation of the topological decay of an initial torus knot $T(2, 9)$ defect to loops and ringlets, under the Gross–Pitaevskii equation in a Bose–Einstein condensate.
Source: **A** reproduced from [373]; **B** reproduced from [376]; **C** reproduced from [377].

This approach led Hornig and collaborators [365] to investigate different scenarios of energy relaxation by relating topological entropy with heat production.

Braid theory has also offered new insight into the problem of optimal mixing of fluid flows and the chaotic behaviour of particle transport and passive scalars [366]. By interpreting the central axis of a straight mathematical braid as the time axis of a dynamical system, one can design and implement a braid protocol to optimize the efficient mixing of fluid particles by the mechanical action of stirrers, or by the induced motion of vortices [367]. Relating Lyapunov exponents to topological entropy [368], it is possible to determine new measures of particle transport, and envisage new techniques for the control of pollutants in the ocean and the atmosphere.

Knotted fields in electromagnetism. Another strand of research concerns the design of knotted fields as solutions to Maxwell's equations [369]. This approach originates with the work of Kamchatnov [370] and Rañada [371], who showed that the Maxwell equations in free space (vacuum) admit an underlying, rich topological structure given by a complex scalar field, that determines linked solutions (the so-called hopfions) to Maxwell's equations. These solutions are typically classified by a Hopf index. Because of the dual representation of electric and magnetic field encoded in Maxwell's equations, several authors obtained hopfions of linked electric and magnetic lines of force by a systematic construction [372–375] (Fig. 49A), an approach that is currently exploited for technological applications in geometric optics, as well as other physical contexts.

Vortex knots in fluids and condensates. From a mathematical viewpoint, torus-knot solutions to the Euler equations were first obtained by Kida [378] for thin vortex filaments. These solutions, written in terms of complete elliptic integrals, were also derived as linear perturbations from the circular vortex ring by Keener and Ricca [379,380], and have been investigated numerically in the context of superfluid flows [381]. Under viscous dissipation vortex filaments interact and exchange strands by a reconnection mechanism that is reminiscent of polymer recombination. Since reconnections are ubiquitous in real fluids, they often involve energy transfer and dissipation, with possible exchange of writhe and twist helicity. One of the first numerical experiments to investigate these aspects was performed in 1991 [382]. The first laboratory production of knotted and linked vortices in water was carried out in 2013 [376] (Fig. 49B), and it allowed detailed evaluations of writhe and centreline helicity, as well as careful measurements of energy transfer across scales. Several direct numerical simulations of similar processes under the full Navier–Stokes equations followed, with remarkable visualizations and diagnostics of the process of topological restructuring of vortex line bundles during reconnection [383,384].

Geometric and topological analyses of the evolution of complex vortex tangles and knots have been carried out in superfluid helium and Bose–Einstein condensates [385–387] (Fig. 49**C**). Further work has revealed interesting connections between defect dynamics in condensates and the evolution of minimal Seifert surfaces of maximal energy bounded by defects [377]. The recent discovery of the formation of complex knot topologies in superfluid turbulence [388] has stimulated the implementation of more sophisticated tools such as the adapted knot polynomials of Liu and Ricca [84–86]. The hope is to be able to determine direct relations between the observed unlinking simplification and topological decay of complex vortex knots and links and the observed energy dissipation and entropy production typical of turbulent regimes.

4. Topological constraints and viscoelasticity of polymeric materials: from linear to nonlinear rheology

Historically, one of the main motivations behind the study of the physical properties of polymeric materials was the need to provide a *microscopic* foundation for the problem of the *macroscopic* elasticity of rubber [87]. Natural rubber is formed of a dense mixture — a solution — of polymer chains, the stochastic motion of each of which is temporarily impeded by the others. Understanding the physical consequences of such impediments, which we will refer to as *entanglements* or, in the context of linear chains, *topological constraints*, on the elastic response of dense polymer solutions is a central goal of rheology.

To fix ideas and to set a common language, we consider the situation where the polymeric sample is sheared between two flat rigid surfaces [87]. The effect of the applied shear is given by the stress tensor σ_{ij} and the obtained distortion is represented by the strain tensor γ_{ij}. Within the *linear response* approximation, there are two extreme regimes. In the *elastic regime* holds $\sigma_{ij} \propto \gamma_{ij}$, usually referred to as the stress–strain relation, well known from elasticity theory [132]. On the other extreme one finds the *viscous regime*, where $\sigma_{ij} \propto \dot{\gamma}_{ij}$, characteristic of Newtonian fluids. For homogeneous systems, both the strain and the stress tensors become scalar quantities. Polymer solutions and melts follow a *viscoelastic regime* that is intermediate between these two extremes, where both σ and γ are time-dependent quantities. This can be conveniently represented by the convolution relation

$$\sigma(t) = \int_{-\infty}^{t} dt' \, G\left(t - t'\right) \dot{\gamma}(t') \,, \tag{56}$$

where $G(t)$ is the *shear modulus*; in the linear response limit, it is often called stress relaxation modulus. Eq. (56) reduces to the elastic regime when $G(t)$ is constant, $G(t) = G_0$, and to the viscous regime when $G(t) = \eta\delta(t)$ where η is the viscosity and $\delta(t)$ is the Dirac δ function. A popular model representing this intermediate viscoelastic behaviour is the so-called Maxwell model [87], where $G(t) = G_0 e^{-t/\tau}$, which reduces to an elastic response in the $t \ll \tau$ limit and to a viscous response with $\eta = G_0\tau$ in the opposite limit $t \gg \tau$. In practice, most modern experimental apparatuses apply a shear deformation in an oscillatory, periodic manner [87]. Thus, in oscillatory linear rheology one works in the frequency, instead of time, domain: the Fourier transform of the shear modulus is split into the *storage* (or elastic) modulus $\hat{G}'(\omega)$ and the *loss* (or viscous) modulus $\hat{G}''(\omega)$, which quantify how much of the external energy input is stored in the material or dissipated via friction, respectively. A perfect viscous (respectively, elastic) medium is characterized by $\hat{G}'(\omega) = 0$ (resp., $\hat{G}''(\omega) = 0$), while viscoelastic polymeric materials and polymer liquids have simultaneously $\hat{G}'(\omega)$ and $\hat{G}''(\omega) \neq 0$.

The time dependence of the shear modulus $G(t)$, which accounts for various (micro- or meso-scopic) possible time-scales, encodes the response to the applied strain and is a characteristic property of the material. In principle, the derivation of $G(t)$ from first statistical-mechanics principles requires a comprehension of the interactions between the macromolecular constituents of the material. In practice, the exact molecular details of these interactions may be disregarded and modern theories of viscoelasticity are based on coarse toy models for polymers, such as bead–spring models [87,90]. Yet, even assuming these simplifications, providing a theoretical interpretation of the rheological response remains hard, particularly in the case of high-weight polymeric liquids whose long-time behaviour reflects the role of entanglements (topological constraints) between distinct chains [87,90].

It is difficult to figure out *a priori* how the entanglements enter into the game. We clarify this by the following examples. As for the occurrence of knots and links (Section 3.2) in single linear chains, entanglements in linear dense solutions are also intrinsically *transient* or, in other words, the microscopic topological state of a linear polymer can change over time. This is the situation commonly described in textbooks [87,90]. On the other hand, we have already observed (Section 3.3.1) that joining the two ends of a linear polymer together to form a ring is the simplest way to quench, permanently, the polymer architecture into a state which differs from the linear one.

In Section 4.1 we consider and contrast the corresponding behaviours of polymer melts for the two architectures of linear chains and ring polymers, these being the simplest and arguably the most important examples where topological constraints play a key role. In particular, we present in detail analytical predictions of the corresponding shear modulus $G(t)$ from microscopic first principles. Then, in Section 4.2 we extend the discussion beyond the linear viscoelastic response theory. In particular, we focus on the interplay between topology and hydrodynamic behaviour of single polymer chains subject to elongation flows.

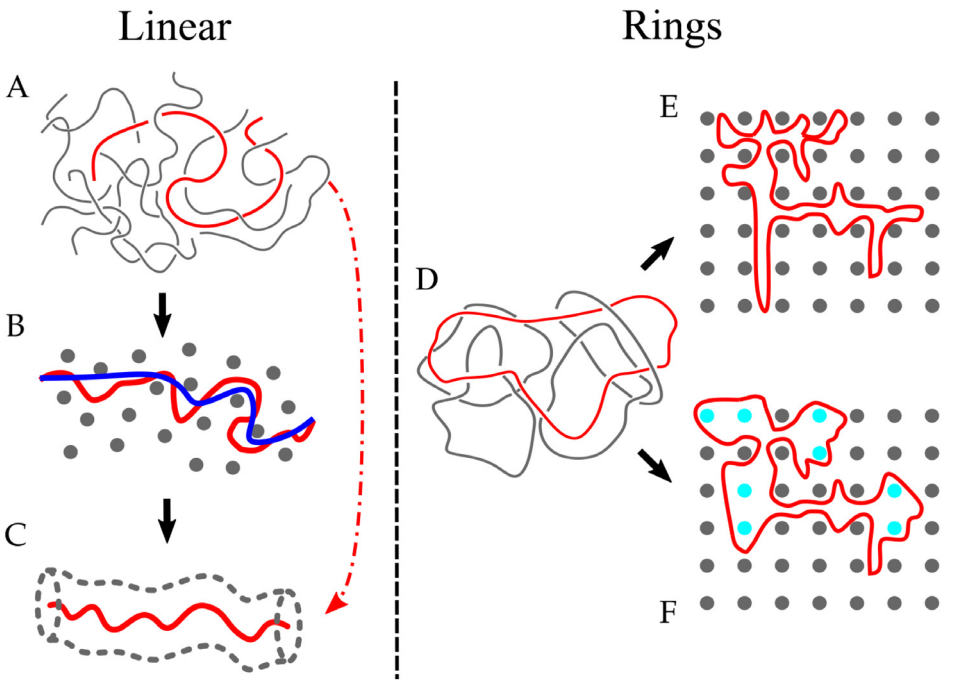

Fig. 50. Entanglement effects in melts of linear (left) and ring (right) polymer chains. **A** Schematic view of an entangled polymer melt. The thermal fluctuations of the red strand are reduced due to a caging effect from nearby chains. **B** The primitive path (blue) of the red chain is the shortest path between the chain ends that can be reached from the initial conformation without crossing any of the fixed obstacles. **C** Tube model: in a single-chain picture, entanglements are represented by an effective potential localizing thermal fluctuations. The challenge is to predict the parameters of the tube model from the molecular structure. The concept of *primitive path analysis* (Section 4.1.2) allows us to derive systematically the parameters of the tube model by passing from **A** over **B** to **C**. **D** Schematic view of an entangled ring melt. Rings are not linked, thus they can only avoid or thread each other. **E** If threadings are neglected, a ring optimizes its conformational entropy by double-folding in an array of fixed obstacles. **F** Threadings, represented here as cyan dots, increase the red ring conformational entropy by opening up once double-folded loops and blocking their gliding. *Source:* **A**–**C** adapted from [389]; **D**–**F** adapted from [222].

4.1. Linear viscoelasticity of polymer melts

As in classical liquids, polymeric materials and polymer liquids at melt conditions are such that the single chains composing the sample are tightly packed close to each other [87,90]: albeit, unique to polymers, spatial overlap between distinct polymers is such that each chain shares the volume spanned by its own size with other chains. Under these conditions, polymers can only flow *past* each other but not *through* each other or, in other words, the motion of each chain is — similarly to tightly knotted shoelaces — *topologically* restricted by (*entangled* with) the surrounding chains. In Section 4.1.1 we recapitulate the fundamental physics and viscoelasticity of melts of linear polymers, the simplest polymer architecture one can deal with, and establish their microscopic foundation by introducing primitive path analysis 4.1.2. In Section 4.1.3 we describe melts of unknotted and non-concatenated ring polymers, which feature many intriguing properties, absent in linear melts and still not fully understood, ascribable to their unique topological state. In Section 4.1.4 we discuss the phenomenology of topological interactions in ring melts in terms of the geometry of *minimal surfaces*, introduced in Section 2.2.5.

4.1.1. Melts of linear polymers

As first noticed by Flory [100], in melts the self-exclusion interaction between monomers of any chain is *screened* by an equivalent excluded volume interaction due to the spatial overlap (Fig. 50**A**) between different chains. This compensation mechanism — usually referred to as the *Flory theorem* [87] — leads to polymers following Gaussian statistics or, in other words, the mean-square end-to-end distance ($\langle R^2\rangle$, Eq. (39)) and the mean-square gyration radius ($\langle R_g^2\rangle$, Eq. (40)) are described by the same expressions appearing in Eq. (41) i.e.,

$$\langle R^2\rangle = 6\langle R_g^2\rangle = \ell_K^2 \frac{N}{N_K} = \ell_K L\,, \tag{57}$$

where (see definitions in Section 3.1.1) N, $L = Nb$, ℓ_K and $N_K = \ell_K/b$ are, respectively, the chain's total number of monomers, total contour length (b is the mean bond length), Kuhn length and number of monomers per Kuhn length.

For the dynamics of *unconstrained* polymers (i.e., polymers in dilute conditions), there are two reference time-scales, the Rouse time $\tau_{\text{Rouse}} \propto N^2$ and the Zimm time $\tau_{\text{Zimm}} \propto N^{3/2}$, the difference being that the Zimm time accounts for

hydrodynamic interactions, unlike its Rouse counterpart, and it agrees with experimental findings in dilute polymer solutions [90]. Instead, in a melt of *entangled* polymers (Fig. 50**A**) each chain is temporarily trapped by the topological constraints induced by the surrounding chains (the dots in panel **B** of Fig. 50) into a tube-like region (Fig. 50**C**). Hence, each chain of the melt undergoes *reptation*, a distinctive type of diffusive motion — very different from (and much slower than; see below) the conventional motion involved in both the Rouse and Zimm dynamics previously alluded to — performed along the one-dimensional centre-line (the so-called *primitive path*, Section 4.1.2) of the tube [90,390]. As discussed in Section 3.3.1, the memory of the initial polymer conformation is progressively erased whenever the chain ends reach the extremities of the tube and hence become free to explore new regions of space. Therefore, it is essential for the chain to possess free ends, which is of course always the case for linear chains; on the contrary, it is not at all the case for ring polymers. We will come back to this point in Section 4.1.3.

The tube is characterized by two parameters, which depend on the physical details of the polymer chains: the entanglement length N_e (which provides a measure of the number of monomers between two entanglement "points", see Section 4.1.2) and the tube diameter d_T. The two quantities are not independent, they are related to each other by the expression [389]

$$d_T = \ell_K \sqrt{\frac{N_e}{N_K}}\,, \tag{58}$$

i.e., the tube diameter is defined by the spatial extent that each contour segment $\simeq N_e$ can wiggle unconstrained. From Eq. (58) it follows that Eq. (57) can be recast in entanglement units as

$$\langle R^2 \rangle = 6\,\langle R_g^2 \rangle = d_T^2 \frac{N}{N_e}\,. \tag{59}$$

Only polymers with $N > N_e$ are properly constrained inside their own tubes and reach the reptation regime. Consequently, under these conditions, the chain relaxation time is given by the de Gennes–Edwards [90,102] power-law expression[26]

$$\tau_{\text{rept}}(N) = \tau_e \left(\frac{N}{N_e}\right)^3\,, \tag{60}$$

where the *entanglement time* τ_e is the characteristic time-scale associated with the local fluctuations of the chain on length-scales of $\mathcal{O}(d_T)$. Overall, the memory of the initial tube (Fig. 50**B,C**) persists for time-scales up to τ_{rept} that, being evidently much longer than the Rouse or Zimm time-scales, is the dominant time-scale of long linear polymers in melt conditions.

The tube theory represents the fundamental theoretical framework [87,90,102] for computing the shear modulus $G(t)$ that governs linear melt decay to equilibrium after strain (Eq. (56)). In particular, at typical times $\tau_e \lesssim t \lesssim \tau_{\text{rept}}$ in the reptation regime, $G(t)$ exhibits the characteristic rubber-like[27] *plateau modulus*

$$G_e \equiv \frac{k_B T\,\rho}{N_e}\,, \tag{61}$$

where ρ is the monomer number density of the melt, and Eq. (61) describes the collective contribution to melt relaxation coming from all chain strands of single contour length $\simeq N_e$. Later than its longest relaxation time $\tau_{\text{rept}}(N)$ (Eq. (60)) $G(t)$ decays exponentially, reflecting the escape of the chain from its original tube

$$G(t) \simeq G_e\, e^{-t/\tau_{\text{rept}}(N)} = \frac{k_B T\,\rho}{N_e}\, e^{-t/\tau_{\text{rept}}(N)}\,. \tag{62}$$

The complete quantitative description of $G(t)$ has been complemented by contour-length fluctuations (CLF[28]) and thermal constraint release (TCR[29]) or, equivalently, dynamic tube dilution (DTD) and constraint release Rouse (CRR) [90,391–393]. An additional contribution is due to the longitudinal modes, which represent the redistribution of monomers along the tube after deformation and occur at short times near the onset of the entanglement plateau. The complete state-of-the-art [394] expression for $G(t)$ is

$$G(t) = G_e \left[\frac{4}{5}\mu(t) R(t) + \frac{1}{5Z}\sum_{p=1}^{Z-1} \exp\left(-\frac{p^2 t}{\tau_{\text{rept}}}\right) + \frac{1}{Z}\sum_{p=Z}^{N} \exp\left(-\frac{2p^2 t}{\tau_{\text{rept}}}\right)\right] \tag{63}$$

[26] The expression Eq. (60) is simply the time to diffuse, in one-dimension, the distance of about the chain length, with a diffusion coefficient inversely proportional to N (Rouse model [87]).

[27] The plateau marks the time-scales at which the material response is elastic-like; it is called *rubber-like* because a plateau response is typical of natural polymer networks such as rubber [87].

[28] CLF occur because, due to the intrinsic flexibility of each polymer chain, the tube length itself is not fixed at one value but fluctuates as the relative polymer conformation fluctuates too.

[29] TCR occur because the molecules surrounding the chain are also mobile and so are able to release or renew the topological constraints responsible.

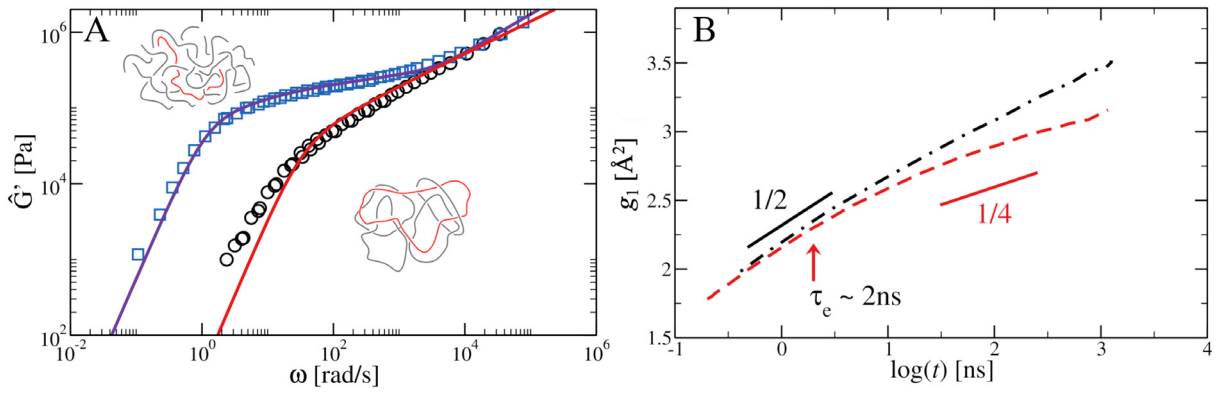

Fig. 51. **A** Linear viscoelastic master curves of storage modulus $\hat{G}'(\omega)$ for linear (blue) and ring (black) polystyrenes of the same molar mass (185 000 g/mol, $Z \approx 11$ entanglements) at reference temperature $T_{\text{ref}} = 150°\text{C}$. **B** Atomistic molecular-dynamics simulation data of the segmental (monomer) mean-square displacement (g_1, Eq. (64)) as a function of time for poly(ethylene oxide) linear (red) and ring (black) polymers with molar mass of 20 000 g/mol (about same $Z \approx 10$) at $T = 140°\text{C}$. The arrow marks the position of the entanglement time τ_e, defined in Eq. (60).
Source: **A** reproduced from [396]; **B** reproduced from [229].

where $\mu(t)$ is the unrelaxed stress-carrying fraction of initial tube, $R(t)$ the relaxation function due to TCR, $Z \equiv N/N_e$ the number of entanglements per chain and p a relaxation mode. For a given polymer, Eq. (63) features three control parameters, G_e, N_e and τ_e, which can be determined experimentally.[30] This model is now included in the freely available software Reptate [395].

A few additional correlation functions prove useful in the description of these phenomena

$$g_1(t) = \left\langle \left(\mathbf{r}_i(t+t') - \mathbf{r}_i(t')\right)^2 \right\rangle, \tag{64}$$

$$g_2(t) = \left\langle \left(\mathbf{r}_i(t+t') - \mathbf{r}_{\text{com}}(t+t') - \mathbf{r}_i(t') + \mathbf{r}_{\text{com}}(t')\right)^2 \right\rangle, \tag{65}$$

$$g_3(t) = \left\langle \left(\mathbf{r}_{\text{com}}(t+t') - \mathbf{r}_{\text{com}}(t')\right)^2 \right\rangle. \tag{66}$$

Here, $g_1(t)$ is the monomer mean-square displacement as a function of time, $g_2(t)$ is the same quantity but with respect to the coordinates of the centre of mass of the corresponding chain, and $g_3(t)$ is the mean-square displacement of the chain centre of mass. In particular, the emergence of the plateau modulus G_e, Eq. (61), for $t \gtrsim \tau_e$ is marked by $g_1(t) \sim t^{1/4}$ because of a Rouse-like subdiffusion of monomers along a random-walk-like path of the tube [225,397]. Fig. 51**A** depicts the measured (blue symbols) storage modulus $\hat{G}'(\omega)$ of an entangled linear polystyrene melt, along with the quantitative prediction based on the Fourier transform of Eq. (63) (the line through the blue symbols), while g_1 for entangled linear poly(ethylene oxide) is shown by the red line in Fig. 51**B**.

Together, Eqs. (58)–(63) describe well experimental and/or simulation results for the viscoelasticity of linear melts. Yet, the theory outlined so far is not completely satisfactory because it relies on the one single, material-dependent [398,399] parameter N_e that, up to this point, has been defined by physical intuition (see Eq. (58)) rather than through a "formal" approach. In fact its microscopic foundation is rooted in so-called *primitive path analysis*, for which we provide a detailed account in Section 4.1.2.

4.1.2. Microscopic foundations of the tube model: Primitive path analysis (PPA)

As discussed in Section 4.1.1, modern theories of polymer dynamics and rheology [90] describe the universal aspects of the viscoelastic behaviour based on the concept (Fig. 50**B**) that molecular entanglements confine linear filaments to a one-dimensional, diffusive dynamics — reptation [390] — in tube-like regions in space [88]. There are about 40 years of literature comparing experimental and simulation data to increasingly refined theories based on this concept [400]. In contrast, direct access to the statistics and dynamics of the tube or of the confining cage of neighbouring chains has for a long time proved elusive.

In a thought experiment [402,403], the random-walk-like tube axis can be identified with the shortest *primitive* paths (PP) between the two ends of the original chains into which their contours can be contracted without crossing fixed obstacles or each other (Fig. 50). Primitive-path analysis (PPA) algorithms [389,404–406] implement this idea for the analysis of computer-generated conformations of atomistic or coarse-grained models of entangled polymer systems. PPA has become a standard tool in computational polymer physics. In what follows, we focus mostly on to what extent PPA lives up to its triple claim: (i) to provide insight into polymer entanglement on a molecular scale, (ii) to establish the

[30] However, the exact description of constraint release remains to some degree debatable.

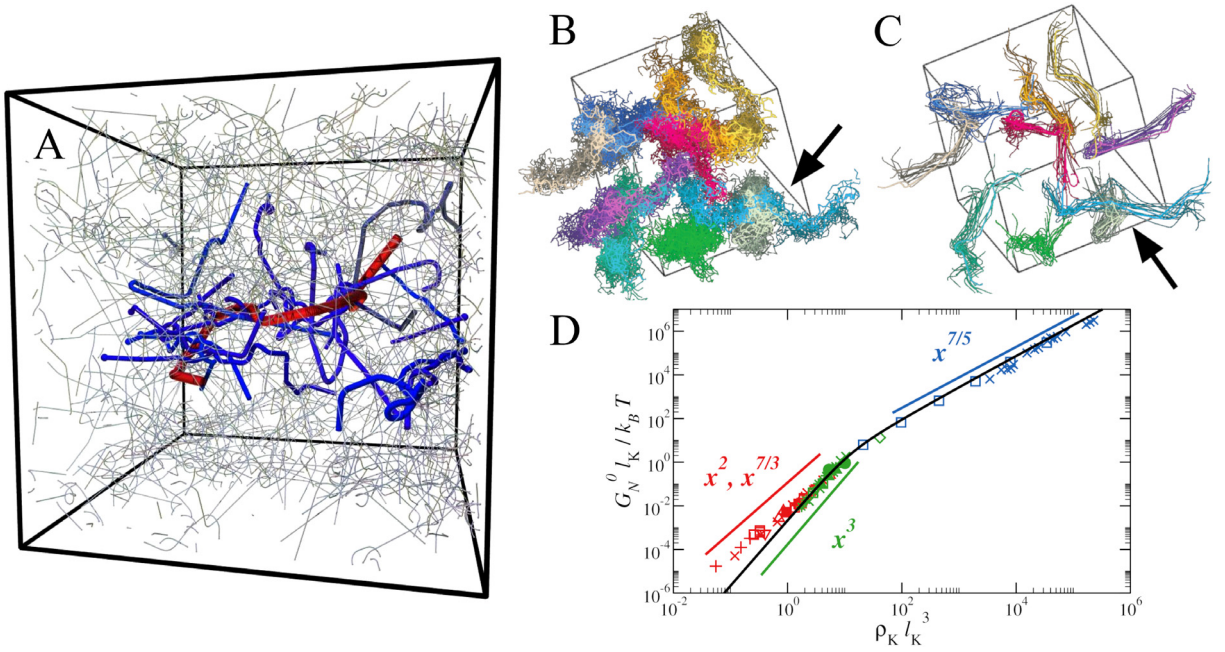

Fig. 52. **A** Result of the primitive path analysis of a Kremer–Grest [165] melt of $M = 200$ chains of $N = 350$ beads. The red primitive path of the chain in the centre is in direct contact with the primitive paths of a large number of other chains shown in blue. Other primitive paths are shown as thin lines. **B, C** Superposition of chain conformations **B** and of the corresponding PP conformations **C** for a long MD trajectory of $M = 500$ Kremer–Grest chains with $N = 500$ beads. We have used a graphical representation where older conformations fade away. Arrows highlight the constraint release event near the centre of the blue chain at the bottom right corner. **D** Dimensionless plateau moduli, $G_e \ell_K^3/k_BT$, as a function of the Kuhn number, $\rho_K \ell_K^3$: Experimental data versus scaling predictions $G_e \propto \left(\rho_K \ell_K^3\right)^\alpha$ and PPA results. Symbols indicate experimental data (+, ×) and PPA results (□) for (i) tightly entangled solutions (blue), (ii) loosely entangled melts (green) and (iii) loosely entangled θ-solutions (red). The black line shows the mean-field prediction for the result of the PPA. The prediction is typically accurate, failing for θ-solutions (red symbols), see [401] for details.
Source: **A** adapted from [389]; **D** reproduced from [401].

microscopic foundation of the tube model and (iii) to endow a highly successful phenomenological model with predictive power for structure–property relations.

Starting with the first point, the mesh of primitive paths revealed by PPA for an equilibrated melt of bead–spring model polymers (Fig. 52**A**) is in excellent agreement with physical intuition underlying the tube model [402,403]. Individual primitive paths consist of straight segments of strongly fluctuating length and more or less sharp turns at entanglement points between two paths. Furthermore, a given chain is constrained by contacts with a large number of primitive paths representing chains sharing the same volume in space. Figs. 52**B** and **C** illustrate that the primitive paths preserve the large-scale structure of the original chain conformations without following the local fluctuations below the entanglement scale. Qualitatively, PPA confirms many theoretically expected aspects of the dynamics of topologically constrained chains: for example, Figs. 52**B** and **C** show evidence for the initiation of the configurational relaxation at the PP ends as well as for occasional constraint release events in the central part of the PP, highlighted in the figure by two arrows.

The original PPA algorithm [389] can be implemented with the help of a standard molecular-dynamics code. In the PPA *force field* the intra-chain interactions are replaced by harmonic bonds between neighbouring beads. In the course of an energy minimization with fixed chain ends, the bond springs pull the chains taut, while the inter-chain excluded volume interactions ensure that different chains do not cut through each other. The numerically much more efficient *Z*-code [404] uses a stochastic sequence of geometrical operations to shorten primitive paths, which are treated as infinitely thin, tensionless lines rather than finite-diameter multibead chains. Other PPA algorithms [401,405–407] follow similar recipes. Part of the differences are motivated by algorithmic convenience, but there are also physical arguments as to whether one should either minimize the mean-square bond length [389,408] or the mean bond length [405].

The second claim of PPA is to establish the microscopic foundation of the tube model. The microscopic structure of the original polymer liquid is best discussed in terms of the Kuhn length and the relative number of monomers of the chains (respectively, ℓ_K and N_K, see Eq. (57)) and the number density of Kuhn segments, $\rho_K \equiv \rho/N_K$. A mesh of primitive paths as shown in Fig. 52**A** is characterized by a number of different length-scales [389,401]. All algorithms provide an estimate of the mean bond and contour lengths, $Nb_{pp} \equiv \langle L_{pp} \rangle$ of the PP, which are considerably reduced compared to their counterparts for the original chains. The PP contour length density can be converted into a mesh size, ξ_{pp}. In the long-chain limit, the PP Kuhn length, $a_{pp} = \langle R^2(L) \rangle / L_{pp} = \ell_K L / L_{pp}$ (see Eqs(39) and (57)) is straightforward to calculate

and increases by the same factor by which the contour length shrinks, $a_{pp}/l_K = L/L_{pp}$. The *Z* [404] or the CReTA [406] codes also provide direct access to the PP contour distance, l_e, between kinks. Corrections due to finite chain length and stiffness are discussed in Refs. [398,409].

This raises the question: which, if any, of these length-scales is related to the standard *rheological* entanglement length, $N_e^{\text{rheo}} = (\rho\, k_B T)/G_e$, derived from the entanglement (plateau) modulus, Eq. (61)? The tube model [90] identifies the entanglement length with the number of monomers per Kuhn length of the primitive path, $N_e \equiv a_{pp}/b_{pp}$. An analogy to classical rubber elasticity theory [410] explains the relation to the *topological* entanglement length [406], $N_e^{\text{topo}} \equiv l_e/b_{pp}$, which plays a role similar to the average strand length in a classical phantom network [87].

The question of whether PPA endows the phenomenological tube model with predictive power can be investigated in two ways. Firstly, given N_e inferred via PPA and a careful estimate [165,398] of the monomeric friction coefficient, ζ, for Kremer–Grest type model polymers, the tube model makes quantitative predictions that can be directly tested against simulation data. Recent results [398] for $g_l(t)$ ($l = 1, 2, 3$, see Eqs. (64)–(66)) not only exhibit the expected power-law exponents [165] but are also in excellent agreement with the prefactors predicted [411] by the tube model. Similarly, there is excellent agreement between the predicted and observed plateau [412] and stress relaxation moduli, $G(t)$ [413].

Furthermore, there is a wide spectrum of entangled polymer liquids that are fully characterized by the dimensionless Kuhn number, $\rho_K \ell_K^3$. These systems comprise semi-dilute θ-solutions of synthetic polymers, the corresponding dense melts above the glass-transition or crystallization temperature, and solutions of semi-flexible (bio)polymers such as f-actin or suspensions of rodlike viruses. Combined [401], they cover a wide range of loosely and tightly entangled polymer liquids, with the available experimental data for G_e varying over eight orders of magnitude in SI units and 12 orders of magnitude in reduced units (Fig. 52**D**, symbols + and ×); the agreement with corresponding PPA results (Fig. 52**D**, symbols □) is striking. In particular, PPA faithfully reproduces scaling relations between the entanglement length and the microscopic structure of different classes of entangled polymer liquids, which are also shown in Fig. 52**D**. This establishes the microscopic foundation of the tube model, since it shows that the phenomenological entanglement length can be inferred from a sample's microscopic topological state using a procedure that is directly inspired by the very ideas underlying the tube model.

Finally, thinking along the lines of PPA also helps to understand better the observed scaling relations. A suitable starting point is the theory [414,415] for the contour distance between entanglement points, $l_e(\ell_K, \xi)$, of tightly entangled chains, i.e., for the limit where thermal fluctuations are irrelevant on the entanglement scale and where PPA has essentially no effect on the chain conformations. Applying this theory to estimate $l_e(a_{pp}, \xi_{pp})$ for the PP mesh [401] shown in Fig. 52**A** yields a pair of equations for the entanglement length, whose self-consistent solution is shown as a black line in Fig. 52**D** and which reduces to the successful [416,417] packing argument for loosely entangled polymer melts.

To conclude, the combination of PPA and the tube model allows one to make quantitative predictions for dynamic observables based on the analysis of the microscopic structure of a sample. Predictions for averages like $G(t)$ and $g_{1/2/3}(t)$ are borne out with remarkable precision. It remains to be seen whether predictions for the motion or confinement of individual chains or entanglements are in equally good agreement with detailed observations [418–421] for persistent contacts between time- or ensemble-averaged mean paths or the correlated motion of beads on different chains.

4.1.3. Melts of non-concatenated and unknotted ring polymers

As in linear melts, *excluded-volume* interactions in ring melts tend to remain screened. However, the other kinds of constraints of chain circularization, unknottedness and non-concatenation produce effective, novel interactions — of exquisite topological origin, as anticipated in Sections 3.2.3 and 3.3.1 — between distinct rings that are not screened and whose effects manifest themselves as systematic deviations from the Gaussian behaviour seen in equivalent (i.e., of the same contour length) melts of linear chains. Although the *ring-melt* problem has been keeping researchers busy for decades, a proper theory is still lacking because the mathematics required to take account, in a rigorous manner, of the topologically constrained conformations is fundamentally intractable; the reader may have sensed part of it in Section 2.

Scaling arguments [218–221] supported by computer simulations [422,423] suggest that the *same* entanglement length (N_e) and tube diameter (d_T) from equivalent *linear* melts are relevant for ring melts; for instance, ring gyration radii from different systems are described by a universal master curve after rescaling as a function of N/N_e [424]. At the same time, and always in comparison to linear systems, reaching the ring asymptotic scaling behaviour requires a much wider crossover ($N \gtrsim 14N_e$ [425]). Beyond these scales, the non-concatenation constraint produces an effective repulsion that forces the chains to minimize their mutual overlap (Fig. 50**D**); the consequence is that, contrary to linear chains, rings obey non-Gaussian, crumpled statistics with scaling exponent $\nu = 1/3 < 1/2$ (Eq. (43)), i.e., the ring mean-square gyration radius[31] is given by the expression (compare with Eq. (59) for linear melts)

$$\langle R_g^2 \rangle \simeq d_T^2 \left(\frac{N}{N_e} \right)^{2/3} . \tag{67}$$

The exponent $\nu = 1/3$ implies *territoriality* — connected to replication and entropic segregation in prokaryotes (Section 5.2) and large-scale chromosome conformation in eukaryotes (Section 5.3) — of the distinct ring polymers, and

[31] Since rings have no ends, we measure their size only through the gyration radius (Eq. (40)).

an asymptotically constant number of chains sharing the volume of one chain [423]. This contrasts with linear polymers where each chain shares the volume with a number $N^{1/2}$ of other chains [87].

The validity of Eq. (67) and the corresponding $\nu = 1/3$ is corroborated by the following two models for rings' conformations. Similarly to the *Gedankenexperiment* for linear chains, in the lattice-tree (LT) model [218,219] each ring protrudes (Fig. 50**E**) through an effective array of step size $= d_T$ of point-like, impenetrable obstacles rationalizing the reduction of the ring's threadable surface exposed to the surrounding chains. As such, every ring almost double folds into a branched or *tree-like* conformation. This idea was implemented in a numerical *bottom-up* procedure [423] for constructing *by hand* putative ring melt structures virtually indistinguishable from those obtained by computationally expensive, brute-force molecular-dynamics simulations. On the other hand, the LT model deliberately ignores the possibility that nearby rings may pierce or *thread* each other (cyan dots in Fig. 50**F**). Although their presence could be rare [426] or hard to detect [424,427], the effects of these threadings, particularly for ring dynamics, should not be underestimated; see discussion below and in Section 4.1.4. Another very popular and accurate model is the so called *fractal loopy globule* (FLG) [228] model. The FLG model is largely based on the packing conjecture by Kavassalis and Noolandi originally formulated for linear chains [417]: namely, that the number of distinct chain filaments occupying an entanglement volume is a constant independent of the polymer species. According to the FLG hypothesis, the overlap parameter between distinct rings remains at the same constant value for all contour lengths $\gtrsim N_e$; ring conformations above N_e are then *self-similar* with the scaling exponent $\nu = 1/3$ that is practically postulated.

The consequent ring structure in the FLG model, built of loops on loops, is still randomly branched, where the loops (which are not necessarily double-folded [228]) are viewed as the branches. On this fundamental point, the main difference between the FLG and the LT models is in what one assumes to be the branching statistics that gives rise to the structure of the mean tree backbone or, also, tree *primitive path* (PP)[32]. In particular, in the LT model the tree backbone, governing the stretching and branching of the ring, is *defined* as a properly weighted average of all possible path lengths in the tree structure (see [227] for details), while in the FLG model the PP of the ring is *measured* [228] by using a method analogous, but not identical, to the PP for linear chains (Section 4.1.2). From the dynamical point of view, in the LT model ring motion on time-scales above the entanglement time τ_e is a combination of loop retraction and mass transfer along the branched chain PP [227,428]. Instead, in the FLG model, the scaling is more complicated and is explained by introducing the concept of *tube dilation* [228], meaning that the constraints' release imposed by the surrounding segments, due to their motion, increases progressively the mean distance between the constraints themselves. This can be modelled in terms of a time-dependent entanglement length $N_e(t)$. Therefore, if the ring segment is $\lesssim N_e(t)$, its PP is straight and the linear size of the segment scales linearly with the length; instead, if the segment is $\gtrsim N_e(t)$, its linear size scales with the exponent $\nu = 1/3$ equal to that of the whole ring.

Both the LT model and the FLG model predict [227,228,428] that the total relaxation time of the rings is given by the power law

$$\tau_{\text{ring}}(N) \simeq \tau_e \left(\frac{N}{N_e}\right)^x , \tag{68}$$

for the same entanglement length (N_e) and time (τ_e) of equivalent linear chains (Section 4.1.1) and where the exponent $x = 5/2 = 2.5$ or $= 23/9 \approx 2.56$ for the LT model[33] or $x = 7/3 \approx 2.33$ for the FLG model. These exponents are, notably, close to each other and, most importantly, the relaxation time Eq. (68) is shorter than the corresponding reptation time Eq. (60) for linear chains, i.e., rings move faster than their linear counterparts. Together, the theoretical prediction Eq. (68), computer simulations, and experiments with purified high-molar-mass ring polymers [222–229] converge to the description of *self-similar* stress relaxation with *no* equivalent of a rubber-like plateau modulus as seen for linear melts, Eq. (61). Instead, the shear modulus, Eq. (56), takes the particular functional form

$$G(t) \simeq G_e \left(\frac{t}{\tau_e}\right)^{-1/x} \exp\left(-\frac{t}{\tau_{\text{ring}}(N)}\right) , \tag{69}$$

where x is the same exponent as in Eq. (68). The experimental storage modulus $\hat{G}'(\omega)$ for an entangled ring polystyrene is shown in Fig. 51**A** (black symbols); it confirms the absence of the plateau and, interestingly, compares favourably to the Fourier-transform of Eq. (69) (red line) with the exponent $x = 7/3$ of the FLG model [228]. Correspondingly, the segmental MSD of entangled ring poly(ethylene oxide) polymers (Fig. 51**B**; black symbols) demonstrates that rings typically tend to move faster than their linear counterparts (with same polymer mass, as predicted by Eq. (68)) at time-scales longer than the entanglement time τ_e.

Although Eq. (69) recapitulates well both experimental and simulation data for ring melts, recent, both experimental and simulation, works [230,231] for unprecedentedly large rings shows deviations from the power-law behaviour and a crossover to a plateau once again, which the authors explain in terms of ring–ring interactions inducing inter-ring *caging*.

[32] Similarly to the PP for melts of linear chains (Section 4.1.2), we adopt the term PP here in the sense of the shortest end-to-end path of the chain to which its contour can be contracted without crossing other chains. However, since rings have no ends, the equivalence between tree backbone and tree PP remains unclear.

[33] The value depends on the model adopted for the description of the branched PP conformations [227].

Thus, there is new experimental evidences calling for the possibility that at much larger molecular weights, well above 15 entanglements, a plateau may appear in ring polymers. Although these results need further confirmation, they challenge the community to consider this important direction.

In order to understand what might be the reasons for these puzzling discrepancies, a closer look at the experimental details should prove illuminating. Behind all the previous studies supporting Eq. (69), it is the use of *liquid chromatography at the critical condition* (LCCC), a mixed mode of separation mechanisms compensating entropic size exclusion and enthalpic interaction of polymers with the porous packing materials, which has yielded highly purified non-concatenated ring polymers, essentially free of linear contaminants [222,429–431]. The technique has reached an impressive level of accuracy, demonstrating in particular that, while the FLG model does an excellent job in describing accurately the power-law response over about three decades, it underpredicts the terminal regime of $\hat{G}'(\omega)$. This discrepancy, now confirmed by independent experimental studies [432], can be traced back [432,433] to linear contaminants remaining undetected by LCCC and/or ring–ring penetrations. On the one hand, adding a tiny fraction of linear chains to a ring matrix of the same molar mass has a dramatic impact[34] on its dynamics because of the threading of rings by the unlinked chains [222,225,396,422,432,434–436]; in solution, this mechanism is responsible for substantial topological slowing-down of rings and the eventual formation of a conjectured topological glass [243,249,250,437,438] (see footnote 25 in Section 3.3.3). On the other hand, atomistic molecular-dynamics simulations of polyethylene oxide (PEO) rings [433] indicate that mutual ring interpenetration (reviewed in Section 4.1.4 in the context of the rings' *minimal surfaces*) may contribute to the slow dynamics as well [433] by means of threading events (Fig. 50**F**). The new study [230] employs instead cyclic poly(phthalaldehyde) (cPPA), a metastable polymer that rapidly depolymerizes from free ends at room temperatures; in that context, linear chains rapidly decompose and do not contaminate the ring sample. Despite the reliable absence of such contaminants, the measured stress relaxation modulus for the largest rings is non-power-law, and this appears confirmed also by accompanying molecular-dynamics simulations of bead–spring rings. Whether this is the beginning of new physics remains however to be elucidated: in particular, the question whether the power-law behaviour of stress relaxation holds or breaks at some point for very long rings will be definitively answered only by more systematic experimental as well as computational efforts.

Besides ring–linear and ring–ring threading, another important feature of unlinked rings is their interlocking or knotting induced by an external deformation field. Recent investigations by means of experiments and simulations have shown that this phenomenon has consequences in enhancing extensional stress and is quite distinct from generic threading [439–441]. Knots may affect the conformations of rings, making them more compact [442] and, as in the case of linear chains with knots (Section 3.2.4), they affect their dynamics and, hence, their rheology [195].

4.1.4. Minimal surfaces and threadings in ring polymer melts

As we have stressed in Sections 4.1.1 and 4.1.3, the nature of entanglements is quite distinct in linear and ring melts. New concepts and tools to characterize the conformations and the entanglements are needed, in particular a less ambiguous definition of threadings (Fig. 50**F**) between different rings or other topologically nontrivial polymers, as well as the quantitative assessment of their role.

In this respect, *minimal surfaces* (MS, Section 2.2.5), spanned on the ring polymer contour, are an example of such a tool [20,21]. For example, MS have been used to estimate the non-concatenation costs in semi-dilute ring solutions [21,443], and have helped to understand the compact conformations of rings [20]. MS have been of key importance in resolving delicate controversies in the theoretical description of ring polymer melts. As briefly reviewed in Section 4.1.3, the LT model assumes that a ring would adopt a double-folded, tree-like conformation in the lattice of topological obstacles. However, no definitive evidence for the tree-like structure had been found and it is difficult to define trees for simulated crumpled rings. This was resolved in [20] by demonstrating that the MS of rings in melt show the area $A \sim N$, as must hold for tree-like conformations.

With MS one can directly and non-invasively measure mutual ring threadings (Fig. 53**A**) as piercings of a ring through the minimal surface of another ring (Fig. 53**B**), that are neglected for strictly tree-like conformations [20]. Threadings, observed before indirectly [444] or invasively [433,435], have been suspected of slowing down the ring dynamics [219,432], eventually leading to a conjectured topological glass (see also footnote 25 in Section 3.3.3) for large rings [243,249,437,438]. MS allow for quantification of the threadings' depth, by measuring the lengths of the threading segments from one surface piercing to another. The sum of all threading segments of one ring found on one side of the MS of another ring — the so-called *separation length* L_{sep} (Fig. 53**C**) — correlates with the time it takes for the two rings to separate completely from each other by thermal Brownian motion [20]; the larger the separation length the longer it takes for the two rings to disentangle completely from each other. Similar conclusions were drawn from threadings defined through piercings of (minimal) surfaces spanned on primitive paths [433]. Hence, threadings in equilibrium do exist, affect the dynamics and ring-melt constructions based on trees [423] do not reproduce well local conformation openings by threadings as shown by comparing the magnetic radius [424] and also the threading statistics [427]. In particular, the latter work shows that threading quantities based on MS construction, such as separation length distribution, are independent of the underlying polymer model, giving further credence to the physical relevance of the MS.

[34] To have an idea (see [396] and references therein), a blend with 20% linear has the identical plateau modulus of the pure linear melt whereas its viscosity exceeds that of the linear by about 100% because of the constraint release effects of the threading linear on the ring.

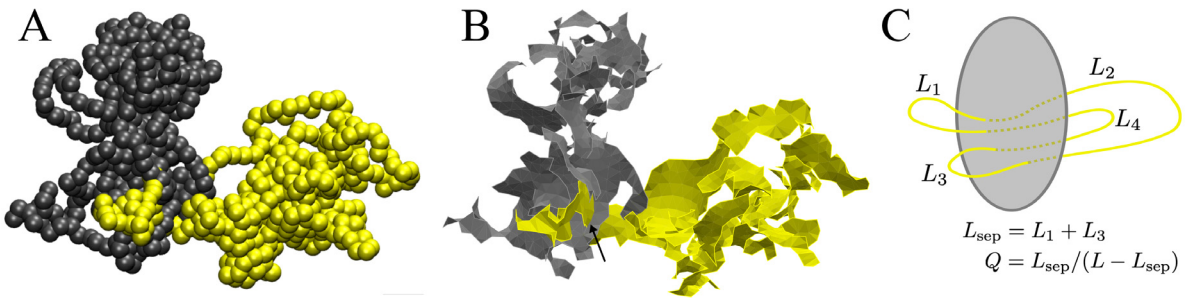

Fig. 53. **A** Snapshot of two threading rings from a melt. **B** Corresponding minimal surfaces spanned on the rings. The threading is marked with an arrow. **C** Schematic threading picture with a definition of the separation length $L_{\rm sep}$ and the threading ratio Q of the contour lengths on the two sides of the surface of the threaded ring. The threading ratio is a universal quantity independent of the polymer model, showing that trees with annealed branching are under-threaded in comparison to properly equilibrated rings [427].

Threading constraints apply to a wider class of polymeric topological materials. MS analysis and threading detection has been used to discover *lasso* conformations [258] in proteins (Fig. 71**F**), to investigate threading-induced dynamical transition in tadpole-shaped polymer solutions [445], diffusion properties of ring-linear blends [446] and supercoiled plasmids [121] and to explain viscosity-thickening of ring melt under nonequilibrium conditions [243,440].

The versatility of the MS method promises further applications, while many fundamental questions remain open. One of the main aims should be the unified understanding of the threading effects and the development of a physical quantity — analogous to the entanglement length N_e of linear melts — governing the dynamics of topological polymers. So far, threadings have been characterized by pairwise quantities, such as the above-mentioned $L_{\rm sep}$, which gives some insight, but there is room for extensions. For example, local surface orientations, threading directions and threading localization on the surface together with multi-ring threading properties can reveal the structure and hierarchy of threading constraints and thereby provide microscopic understanding of the resulting dynamic consequences [243,249,437,438]. The connection between squared magnetic radius and minimal surface area is not clearly formulated, with some differences reported [121, 424]. Knotted boundaries support minimal surfaces that are connected only to a subset of the boundary [447] and their scaling properties for random knotted polymers are yet to be discovered. Last but not least the scaling $A \sim R^2 \sim N^y$, with $y = 2\nu$ for $\nu > 1/2$ and $y = 1$ for $\nu \leq 1/2$ for random unknots under different conditions should be investigated in detail. Although the scaling is intuitive, because R, the ring gyration radius, is the only length-scale of the system, the fractal nature of the boundary might create a correction to the exponent. Numerical evidence supporting $y = 1$ for rings with $\nu = 1/2$ has been provided [21], but for self-avoiding rings $y > 2\nu$ has recently been measured [448].

4.2. Topological signatures of polymer chains in single-molecule microfluidics

In this section, we discuss how topological features can be probed in single-molecule microfluidic experiments. Their main advantage is the absence of inter-molecular effects: this, *per se*, brings out most vividly some of the characteristic features of a non-trivial topology. Nonetheless, some of the phenomena discussed below are also relevant for dense systems, and the interested reader is referred to a recent study of shear thinning in ring melts, combining simulations, experiments and modelling based on the concept of blobs in shear and tension [449]. In the context of the present review, there are two broad classes of topologically non-trivial polymers that have been investigated in microfluidic devices: linear polymers (knotted and unknotted) and ring polymers (usually unknotted). We will follow the same sequence as in Section 3, with unknotted rings followed by knotted open filaments. We discuss how microfluidic setups, and their computational analogues, can highlight effects that are purely topological, using either elongational flows or electric fields.

4.2.1. Microfluidics for single-molecule studies of polymers and DNA

Microfluidics has proved to be a very versatile platform, allowing one to investigate a plethora of different systems in a reliable and controlled way [450]. In the context of the single-molecule experimental study of topologically non trivial polymers, microfluidics can provide confined environments in which DNA molecules are constrained to the focal plane of a microscope and can be translated and deformed with hydrodynamic flows or electric fields. Microfluidics thus provides a flexible framework in which many different systems can be studied. In addition to rings and knotted chains, the same setup can be used to study catenated networks [451]; for non-charged polymers, the electric field can be substituted with a suitable elongational flow [452]. Thus, in principle, any complex architecture or any type of filament can be studied. Experiments also offer a setting akin to real-world processes, like plastic extrusion grafting, where, at the same time, one can control and directly measure the properties of the sample.

The primary microfluidic system that has been used to study knotted DNA consists of perpendicular 2-μm channels meeting in a "T" or a "+" with hyperbolic corners, with voltages applied across the channels to create a divergent electric field with a fixed point at the centre (Fig. 54**A**). Alternatively, the same stagnation point can be created with a planar

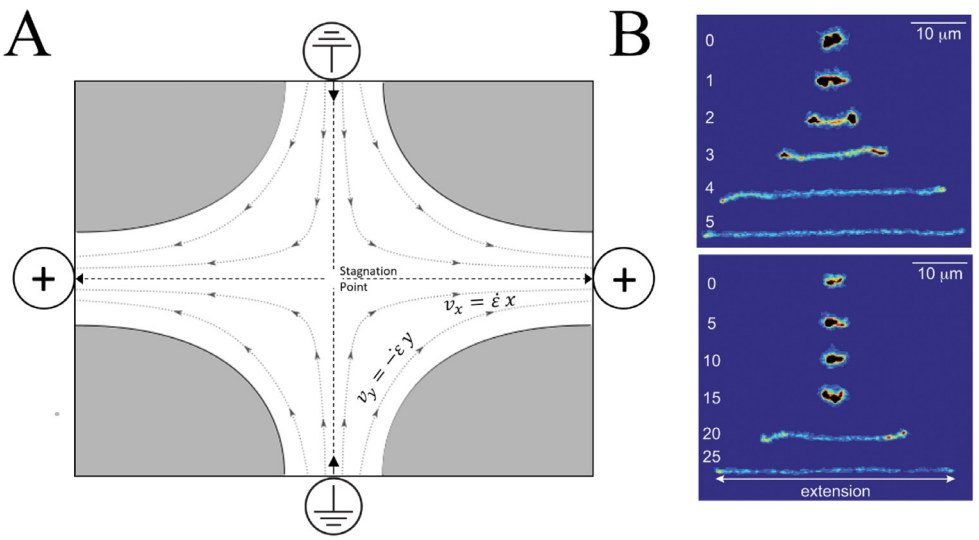

Fig. 54. **A** Microfluidic device used to generate extensional fields to stretch DNA. The out-of-plane height of the device is typically 2 μm. Arrowed curves show the trajectory of negatively charged test particles. **B** Images showing unentangled (top) and entangled (bottom) DNA being stretched in such a device. Significantly more strain is required to stretch the entangled molecule.
Source: **B** reproduced from [184].

extensional flow field; in both cases, it can be maintained for hundreds of seconds [453]. The velocity of a charged test particle in this field increases linearly with position along one planar axis and decreases linearly with position towards zero along the other planar axis, giving it the same velocity profile as extensional or elongational flow at first order. This can be appreciated comparing the extensional curves of linear polymers in both cases [453,454]. We refer to these as elongational fields. A molecule at the zero or stagnation point will experience an outward force on both ends of the molecule, and will stretch.

There are several salient features of a molecule's behaviour in such a field. The field strength, either flow or electric, is characterized by the dimensionless Weissenberg number $\mathrm{Wi} = \dot{\gamma}\tau$ ($\mathrm{Wi} = \dot{\varepsilon}\tau$, see Eq. (70) and definitions below), expressed as the product of the shear $\dot{\gamma}$ or elongation $\dot{\varepsilon}$ strain rate with the polymer's longest relaxation time τ [455]. One usually takes τ as the longest relaxation time τ_{RZ} — see definitions in Section 4.1.1 — we will define the strain rates more precisely below. The Weissenberg number, comparing the advection rate with the typical time-scale of the system, indicates how much a macromolecule is affected by the external flow. In the setup of interest, the result is the elongation of the polymer. Single-molecule microfluidic experiments pertain to the realm of *nonlinear* rheology: they study elongated macromolecules under tension, observe the elastic recovery after extension and extract information on the relaxation dynamics and on the relaxation time-scales at different elongation rates. Below $\mathrm{Wi} \simeq 1$, the filament is not stretched faster than it can relax and remains coiled, above $\mathrm{Wi} \simeq 1$ a coil–stretch transition occurs and the molecule approaches full extension as Wi increases. The coil–stretch transition is a phase transition in that changes in the system as measured by the chain extension stall as energy is input in the form of accumulated strain, and after a critical strain has been surpassed a molecule will stretch.

We introduce here, for convenience, the description of the flow pattern imposed in experiments and in simulations: the flow is described by the streaming velocity field $\mathbf{u}(\mathbf{r})$ of the pure solvent, where $\mathbf{r} = (x, y, z)$ is the position vector expressed in Cartesian coordinates. Simple shear flow (SSF), also called Couette flow, and planar extensional flow (PEF) — the two most common flow patterns employed in simulations and experiments — are described by the velocity gradient tensor $\nabla\mathbf{u}$, i.e., the Jacobian matrix of the velocity field, as

$$\text{a) } \nabla\mathbf{u} = \begin{bmatrix} 0 & \dot{\gamma} & 0 \\ 0 & 0 & 0 \\ 0 & 0 & 0 \end{bmatrix} \quad \text{for SSF} \qquad \text{b) } \nabla\mathbf{u} = \begin{bmatrix} \dot{\varepsilon} & 0 & 0 \\ 0 & -\dot{\varepsilon} & 0 \\ 0 & 0 & 0 \end{bmatrix} \quad \text{for PEF,} \tag{70}$$

introducing the shear and strain or elongation rates $\dot{\gamma} \equiv \mathrm{d}\gamma/\mathrm{d}t$ and $\dot{\varepsilon} \equiv \mathrm{d}\varepsilon/\mathrm{d}t$ respectively. In the former case, following the usual naming convention, a velocity profile $(u_x, u_y, u_z) = (\dot{\gamma}y, 0, 0)$ results: the solvent is pulled in the *flow* direction x with a velocity proportional to the coordinate along the *gradient* direction y, without any effect along the *vorticity* direction z. In the latter case, the velocity profile reads as $(u_x, u_y, u_z) = (\dot{\varepsilon}x, -\dot{\varepsilon}y, 0)$, defining the *extension* axis x and a *compression* axis y, once again leaving the solvent unaffected along the *neutral* axis z.

4.2.2. Rings in microfluidic flows

Ring polymers under flow have been recently the subject of research, as the development of suitable microfluidic devices allows for high-precision control of the location of the polymer in the flow field [456]. Utilizing this device, Li

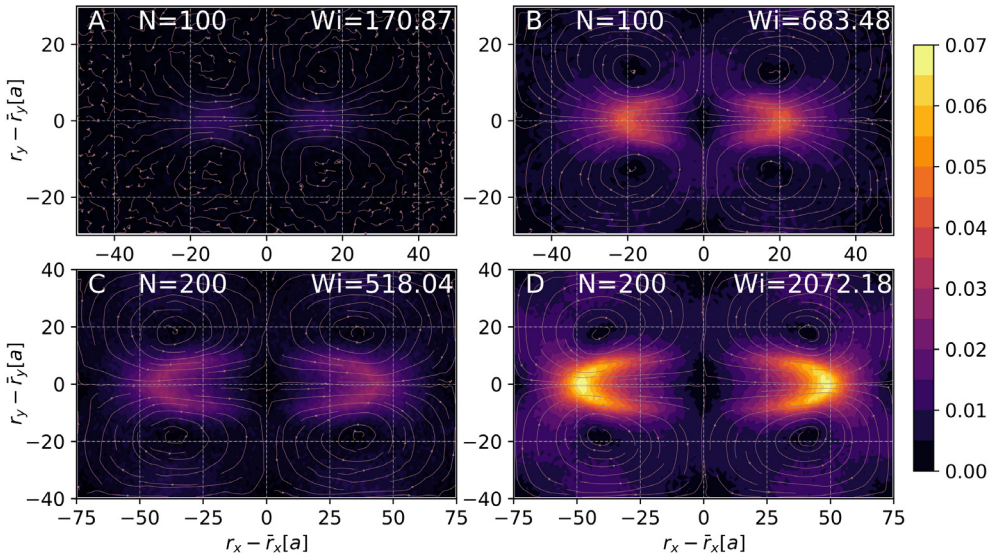

Fig. 55. Solvent backflow for sheared rings. The figure shows the solvent flow fields in the flow-vorticity plane around the centre of mass $\mathbf{r}_{com}$ of an 0_1 ring under shear rate $\dot{\gamma}$, as indicated in the plots, obtained by employing MPCD simulations [459]. Here, m is the mass of the solvent particle, a is the size of the MPCD collision cell and k_BT is the thermal energy. The colour map encodes velocity magnitudes in units of $[\sqrt{k_BT/m}]$. Left to right: Increasing shear rates $\dot{\gamma} = 0.02, 0.08$ $[(k_BT)^{0.5}m^{-0.5}a^{-1}]$. Direct comparison between equal shear rates shows backflow is significantly more pronounced at $N = 200$.
Source: Adapted from [459].

et al. [453] investigated the stretching characteristics of circular chains in elongational flows in comparison to linear ones. They found that circular DNA has a smaller relaxation time in equilibrium than linear DNA and that, although both display a coil–stretch transition, circular molecules begin to stretch at higher strain rates, due to the longer relaxation time.

Furthermore, there is less *molecular individualism* (a concept dating back to de Gennes [457]) observed for rings compared to linear chains regarding the pathways to stretching: essentially, identical linear chains subjected to elongational flow may display completely different behaviour and, in particular, vastly different elongation pathways, while identical rings behave typically more similarly to each other. This phenomenon is due to the out-of-equilibrium nature of the setup and to the diversity of initial configurations attainable by the polymers: rings show more similar pathways to stretching because of the low diversity of the initial states in comparison to linear chains. Information on ring conformations has been obtained in subsequent work by Hsiao et al. [458] who looked not only at the ring's behaviour along the extension axis but also along the compression and the neutral directions, accompanying their experiments by computer simulations. The most striking characteristic was the swelling of the ring also in the neutral direction, a characteristic absent for linear polymer chains.

From the perspective of numerical simulations, rings in microfluidic channels provide an excellent example of numerical data complementing experiments almost perfectly. In particular, Multiparticle Collision Dynamics (MPCD) [460,461] is an efficient and accurate computational method to simulate in-shear and transport flows, further allowing for switching on-and-off the hydrodynamic interactions by suitable modifications of the solvent and solvent–monomer collision rules. Liebetreu et al. [462] employed MPCD to investigate the behaviour of knotted and circular polymers in SSF. They established that vorticity swelling is caused by solvent reflected on the horseshoe regions that escapes along the vorticity axis, colliding with the ring there, see Fig. 55, and it disappears both in the absence of hydrodynamic interactions and in the case of linear chains. When a trefoil knot is present in the rings, vorticity swelling leads to a release of tension for moderately sized chains ($N \approx 100$ monomers) and a subsequent opening of the knot, accompanied by enhanced tumbling motion, i.e., a sudden folding and exchange of the front and the back of the ring in the flow direction.

The vorticity-swelling phenomenon is unique to rings and it provides proof of coupling between hydrodynamics and topology present only for macromolecules with no ends. Its validity was independently confirmed in subsequent work by Young et al. [463]. Experimental evidence for ring-polymer vorticity swelling under shear was offered in the work of Tu et al. [464], which also established the existence of tumbling and of significant differences in the distribution of fractional chain extensions for circular and linear molecules under shear. The effects of ring architecture coupled with hydrodynamics become more spectacular for longer chains, as established in recent work by Liebetreu and Likos [459]. Here, it was found that not only is vorticity-swelling present but *gradient*-swelling also occurs, as shown in Fig. 56. The phenomenon is due to an overall stretching of the molecule under shear for a window of values of the Weissenberg number, which is accompanied by a stabilization of the expanding ring, and a strong suppression of tumbling during that dynamical regime. This phenomenon, termed *hydrodynamic inflation* is, once more, specific to rings. Tumbling resumes after the end of the inflation phase, when the ring has become fully stretched.

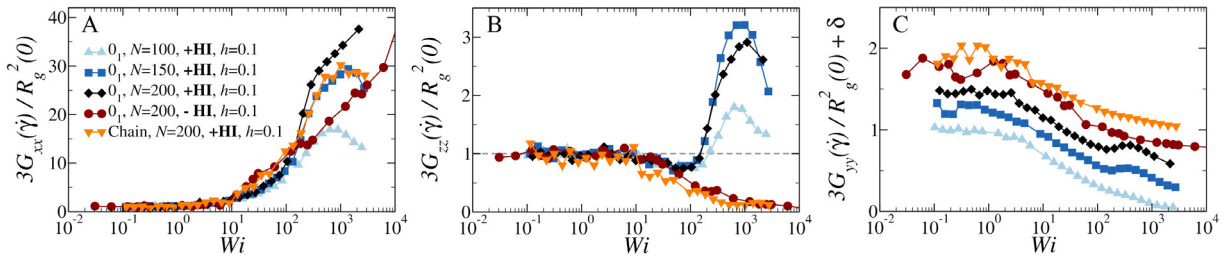

Fig. 56. Diagonal gyration tensor elements $G_{\alpha\alpha}(\dot\gamma) = 1/N \sum (r_\alpha - r_{com,\alpha}) \cdot (r_\alpha - r_{com,\alpha})$ for a set of rings, normalized over their equilibrium value $R_g^2(0)/3$, against the Weissenberg number Wi. **A** G_{xx} (flow direction) increases with Wi to some maximum and then drops as rings align into flow-vorticity plane and experience less strain; saturation was not yet reached for the $N = 200$-ring without HI. For chains, G_{xx} increases with shear rate and eventually saturates. **B** G_{zz} (vorticity direction) decreases to a minimum and then shoots up at values of Wi that anticipate the inflation anomaly observed in panel (c). For chains and rings without HIs, G_{zz} decreases continuously. **C** G_{yy} (gradient direction) initially decreases with shear rate. For $N = 150$ and $N = 200$, an inflation anomaly is observed, which is hardly visible for $N = 100$. G_{yy} for chains and rings without HI decreases monotonically with shear rate. To highlight the anomaly, shifts δ have been applied along the vertical axis ($\delta = 0.25$ w.r.t. the preceding set). *Source:* Adapted from [459].

We conclude this section highlighting that it is also possible to study the effect of compression on rings using an electrohydrodynamic instability. Soh et al. [465] experimentally applied electric fields on DNA rings that were shown to induce self-entanglements. The emergence of deep self-entanglements in rings was shown to slow down the relaxation to equilibrium with respect to their linear counterparts. Characteristic types of such self-entanglements as well as a partial characterization of the same by using tools from knot and link theories have been analysed by employing athermal, macroscopic chains that have been exposed to mechanical agitation [466].

4.2.3. Dynamics of knotted DNA

How does a knot behave under flow and how does a knotted chain respond to external flow fields as a whole? In Section 3.2.5, we introduced two techniques for systematically knotting polymeric DNA molecules, using microfluidic or nanofluidic devices. Here, we discuss these experimental techniques in more detail and summarize what has been learned through using them about the physics of knotted polymers.

Applying an extensional field to DNA globules after electrohydrodynamic entanglement, Renner and Doyle [184] observed that self-entanglement increased the critical strain required to stretch a molecule by a factor of ∼10, and that the stretching was slower once initiated. Polymers stretched under extensional flow, or an analogous electric field, have a complex tension profile, such that the tension is strongest near the centre of the molecule and falls off quadratically towards the ends of the chain, where it vanishes. A knot in an extensionally-stretched polymer feels a non-uniform tension profile as well as a motive force, hydrodynamic or electrostatic, towards the end of the molecule. As such, uniform Brownian diffusion of knots is not expected; simulations by Renner and Doyle [171] predicted that knots would diffuse close to the centre of the chain until they reach a critical length-scale beyond which they translate towards a chain end in a deterministic fashion. Subsequent experiments by Klotz et al. [197] observed this diffusion near the chain centre and directed motion of knots towards the chain ends. However, the motion of the knot along the contour, as observed from the experimental data, is more erratic than in simulations; it was also observed that a sudden increase of the extensional field strength, which increases both the chain tension and the knot's motive force, can halt the motion of knots (Fig. 57**B**), counter to simulated predictions. This is interpreted as evidence of intramolecular friction within the knot leading to jamming, as predicted by Narsimhan et al. [467], which can be seen as another manifestation of topological friction, Section 3.2.7. The mobility of knots was observed to decrease with increasing Weissenberg number; although it is not a measure of diffusivity, this contradicts earlier observations by Bao et al. [177], who measured the diffusivity of knots in molecules tied and stretched with optical tweezers (Fig. 57**A**). They measured a decreasing diffusivity with increasing knot complexity, but observed no dependence on the chain tension as it varied by a factor of ∼20. The discrepancy may be due to the viscoelastic buffer used by Bao et al., which made the molecule artificially rigid and gave it an effective width much larger than the corrugated double-helix backbone of the DNA, thought to be the source of intra-chain friction (Section 3.2.7). Atomistic simulations of the interaction between the exteriors of double helices may provide additional insight to resolve this discrepancy.

Nanochannel confinement provides a uniform stretching suitable for the study of knot diffusion Fig. 57**C**. Ma et al. [182] explored knot diffusion in nanochannel confinement and observed that knots move along their polymers' contour lengths sub-diffusively, suggesting a self-reptation mechanism (Section 4.1.1). The presence of a knot also affects the diffusion coefficient of the molecule itself; the presence of topological friction between the knot and the channel wall can decrease the diffusivity of a polymer, but the effective shortening of a knotted molecule reduces its drag profile and increases its diffusivity. A subsequent study measured the diffusion coefficient of knotted molecules along a nanochannel [186], finding that knots decrease the diffusivity of nano-confined polymers. As discovered by Renner and Doyle, the stretching as well as the subsequent relaxation of a molecule are affected by the presence of a knot; thus, knots affect the elasticity

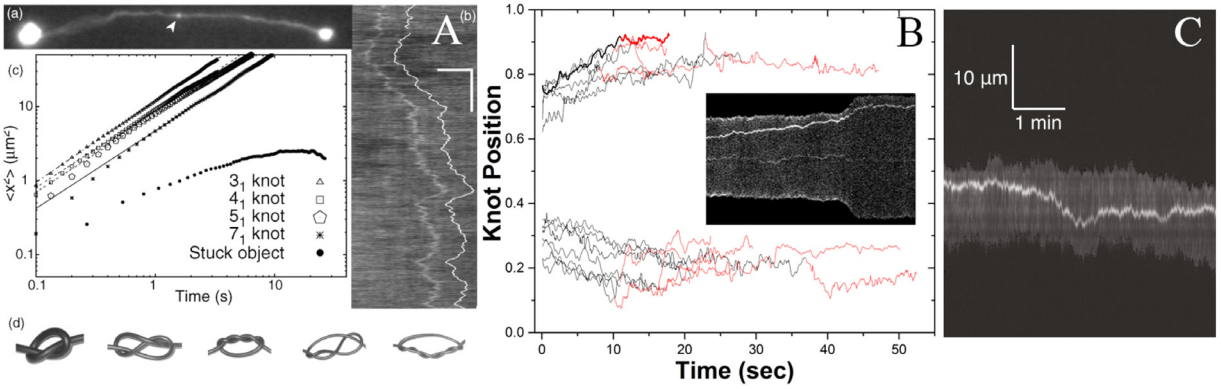

Fig. 57. **A** Experimental micrograph, kymograph, and mean-squared displacement data for knots tied with optical tweezers in stretched DNA from Bao et al., showing diffusive knot motion. **B** Knot trajectories from Klotz et al. showing directed motion towards the nearest end of the molecule which is halted when the chain tension is increased. Inset kymograph shows a molecule with a directed knot near the end and a diffusive knot near the middle, both of which halt under tension. **C** Kymograph from Ma and Dorfman showing the diffusion of a knot in a nanochannel-confined molecule that is itself diffusing.
Source: **A** reproduced from [177]; **B** reproduced from [197]; **C** reproduced from [182]

of a molecule. Soh et al. [207] measured the relaxation times and steady-state extension of T4 DNA molecules with and without knots at various Weissenberg numbers. Knotted molecules had a shorter extension compared to their unknotted counterparts, and the difference was greater than could be explained by sequestration of contour within the knot. This was more pronounced at low Wi, where the coil–stretch transition was observed at a higher strain rate than expected. It was also observed that the relaxation time of a stretched knotted molecule decreased as the apparent size of a knot at maximum Wi increased. This was interpreted in terms of an effective Weissenberg number, in which the effective shortening of the molecule due to the knot decreases its relaxation time via the molecular-weight dependence of the relaxation time, which scales as N^2 and $N^{1.8}$ in the Rouse and Zimm models respectively, lowering the effective Weissenberg number for a given strain rate. One may posit that knots have their own intrinsic time-scale separate from that of the molecule, but experiments on knot expansion during chain relaxation by Klotz et al. [189] show that a knot expands locally over the same time-scale over which the chain contracts globally.

Another consistent observation is the localization of knots. Whether the DNA is linearized by optical tweezers (Fig. 57**A**), nanochannel confinement (Fig. 57**B**), or elongational flow (Fig. 57**C**), the knot is observed to occupy a diffraction-limited spot of intensity. With modern equipment, a typical diffraction limit for YOYO-1 emission (515 nm) is 183 nm, comparable to the pixel size of current microscope cameras, although in practice the resolution may be coarser. While the localization may be considered an effect of the elongation, Klotz et al. [189] showed that even when the elongational field is de-activated and the polymer relaxes towards a coiled configuration, the spatial extent of the knot remains consistent with a diffraction-limited peak as its intensity grows, until the knot can no longer be resolved from the linear strands outside it. It was also observed that in molecules with two knots of significantly different fluorescence intensity, the spatial extent of each knot was the same. The theoretical basis for the localization is that of knot metastability, initially proposed by Grosberg and Rabin [169] and expanded upon with more detailed simulations [172,468]. A polymer with a knot loses configurational entropy as the unknotted configurations are restricted and the contour within the knot experiences confinement by the other segments forming the knot. The looser a knot is, the more the polymer experiences an entropy reduction. Thus, when a knot is formed, it may entropically self-tighten to minimize the amount of restricted contour in the knot. This predicts that knots have a *tight* equilibrium size, and that they should only untie by diffusing towards the chain ends, rather than by globally expanding to encompass the whole polymer. There has not been a comparison of this model with existing experiments, although free-energy parameters calculated for trefoil knots were used to inform the model used by Amin et al. [181]. The notable exception to the observation of localized knots was in a nanopore experiment by Sharma et al. [176], showing *global* knots interpreted as large loops extending from tight knots.

Nanopore translocation experiments have provided additional insight into the dynamics of knots, typically in more extreme conditions in terms of confinement and strain rates than fluorescence experiments. As a knotted DNA molecule translocates a nanoscale pore, one may ask how the knot responds, particularly if the equilibrium size of the knot is larger than the pore. Sharma et al. [469] present four possibilities: the knot can slide towards the back of the molecule, can jam at or in the pore and halt the translocation, can tighten until it can fit through the pore, or can isomorphically deform through the local disruption of base pairing. Data presented by Plesa et al. [175] are consistent with knots in closed circular molecules sliding towards the back, the observed distribution of knots during circular DNA translocation being consistent with sliding. Sharma et al. [469] disagree with this assertion, and argue that their measured ratio of the fraction of knotted molecules in circular and linear DNA is inconsistent with sliding, which would disfavour the detection of knots in linear molecules, and that isomorphic deformation is the dominant mechanism. In a nanopore experiment

with linked circular molecules extracted from kinetoplast DNA, Rheaume and Klotz [470] found that the translocation time of molecular Hopf links is consistent with a slowdown due to the linkage, albeit with less precision than the knot translocation studies.

DNA molecules with two knots may be used to study their interaction. Metzler et al. [185] reported a doubly-knotted molecule, and Amin et al. [181] showed that the probability of forming two knots can exceed that of a single knot if a molecule is sufficiently compressed, and that the observed distribution of pairs of knots on elongated DNA could be understood by hard-sphere repulsion between the two knots in the compressed state. Several computational studies [15,471] indicate that there should be an attraction between knots on a stretched chain, understood through a free-energy minimum that occurs when two knots overlap each other to minimize the total entangled contour. Klotz et al. [183] presented observations of long-range attractive interactions between pairs of knots in elongationally stretched DNA. Knots were observed to remain in close proximity for minutes at a time, allowing a free energy profile for the knot–knot attraction to be calculated that bore similarity to those predicted in simulations. In a more controlled replication study using a knot factory, Ma and Dorfman [187] also observed an attractive free-energy profile of knot–knot interaction, and ruled out the null hypothesis of two independent random walkers. The mechanism of this attraction is not fully understood.

4.2.4. Topological chromatography

Microfluidic devices have been designed *in silico* as topology filters with the purpose of separating chemically identical but topologically distinct macromolecules. Here, one does not resort to shear or extensional flows but rather to pressure-driven transport flows such as Poiseuille flow driven by a constant pressure gradient or body force acting on the solvent molecules. Weiss et al. [472] proposed corrugated channels with rows of attractive spots arranged along the flow direction as efficient filters to separate chains from knotted or unknotted rings. The device takes advantage of the fact that rings can transport by means of tank-treading motion (that is, moving like the tread of a tracked vehicle), an option not available to chains, which simply adsorb on the spots and become trapped on them, being therefore filtered out of the device. The main disadvantage of this concept is that it functions only at very dilute conditions, reducing device throughput. Accordingly, in a subsequent work, Weiss et al. [473] extended the ideas to concentrated ring–chain mixtures, taking advantage of the vorticity-swelling property of the rings in regions of high shear close to the channel walls, which produces strong lift forces and focuses them towards the channel centre. Separation of different knots, on the other hand, is more challenging, since none of the above propositions can distinguish between the knottedness of the polymer. To this end, Marenda et al. [474] simulated topographically corrugated channels and showed that, for suitable choices of the topography, one can drive rings of different knot-type through the channel with significantly different convection speeds, causing efficient topological separation. Although this work ignored hydrodynamics, subsequent MPCD-studies with the inclusion of hydrodynamic interactions confirmed the efficiency of the topological filter and also offered valuable insight on the mechanism of the translocation process of the knots through the channel constrictions [475].

4.3. Outlook on polymeric materials

Polymeric systems remain a plentiful source of fascinating scientific questions, despite the fact that they have been a focal point of scientific enquiry for several decades. We have reviewed the fundamental role played by topology in determining the material properties of polymeric systems and their unique relevance, as they impact the behaviour of the polymeric filaments from very dilute to very dense conditions. Many questions remain open for future research. First, recent results challenge the consolidated picture that explains the rheological response of ring polymer melts and push for experimental confirmation as well as for new theoretical approaches. We have also examined single-molecule experiments and the unique perspective on the properties of individual polymers they offer, especially when topology is involved. An exciting prospect regards the possibility of bridging macroscopic rheology and microscopic single-molecule experiments; such a connection could offer a comprehensive understanding of how topological signatures are manifest across different length- and time-scales. This perspective could be of pivotal importance out of equilibrium, where the behaviour of individual molecules may have a strong influence on the emergent properties of the entire system. An example may be the presence of knots in melts of linear chains that, upon elongation, may disturb the flow and cause unexpected behaviour. Real-world applications, such as extrusion moulding, could potentially be improved through this approach. In addition, out-of-equilibrium complex polymeric systems are ubiquitous in biology; in many cases, the role of topology has merely been postulated. Understanding the interplay between the different constituents of these systems will be crucial to achieve a better control and, eventually, to design bio-inspired topological materials.

5. Topological properties of living matter: DNA, chromatin and genome organization

The linear sizes of the genomes of viruses and of most of the living organisms in the two main realms of prokaryotes, e.g., bacteria, and eukaryotes, e.g., mammals, are orders of magnitude larger than their respective confining environments: capsids for viruses, the nucleoid for bacteria, and the nucleus for eukaryotes. Such spatial confinement implies that the packaging of genomes and the ensuing topological constraints — analogous to the ones of generic polymeric materials and fluids — markedly influence their function and organization. These topological constraints have a crucial biological

relevance because DNA needs to be accessed by proteins during gene transcription, duplicated during genome replication, and eventually segregated into daughter cells during cell division. Topological constraints can hinder these processes owing to the uncrossability constraint between physical polymers. The constraints can be lifted to some degree by topological enzymes (Section 3.3.7), but their presence, role, and extent of action are still being investigated for these various processes.

Accordingly, a precise and quantitative understanding of genome organization must take into account topological constraints and, more generally, polymer physics when interpreting and modelling experimental data. The most relevant experimental techniques that are being used to this end are (i) *fluorescence in situ hybridization* (FISH [233]), where fluorescent probes are attached to regions of interest along the genome of cells; (ii) *super-resolution microscopy*, e.g., STORM, STED and others [476,477], which can beat the light diffraction limit and achieve nm-scale resolution; (iii) *chromosome conformation capture* (3C) techniques, such as Hi-C [478] or GAM [479] where a combination of DNA breakage and ligation are used to identify spatial (3D) proximity of DNA fragments.

In this section, we review the efforts of the biophysical community to explore the extent of the biological relevance of topological constraints in viruses, prokaryotes, and eukaryotes using experimental data to inform and validate modelling strategies at scales from specific loci to entire genomes.

5.1. Viruses: DNA organization under extreme confinement

Genome packaging in viruses is a complex process and viral DNA has among the most impressive packaging in the biological world, with important differences between DNA and RNA viruses as well as between differently sized genomes [480]. For example, DNA packaging in bacteriophages involves a motor protein that inserts the genome into a pre-formed empty capsid where it assumes a more or less ordered configuration, often with an axial spool symmetry axis. This inverse spool configuration of confined DNA, first observed in T4 bacteriophage capsids but later in many others [481], is characterized by wrapping of the genome into a spool [482], and exhibits a substantial orientational ordering. However, other viruses, such as T5 bacteriophage, show a more complicated structure, exhibiting ordered domains without a fully developed inverse spool symmetry [482]. DNA packing in bacteriophage capsids, which can reach 50% volume fractions or higher — compared with 2% found in eukaryotic cells — could therefore exhibit a whole range of structures including axial inverse spool symmetries, spherical concentric symmetries, as well as liquid-crystalline polydomain phase mosaic structures characterized by an almost homogeneous DNA density. The important implication of DNA packaging in the inverse spool state is that it allows it to act as a coiled osmotic spring, therefore aiding the ejection process [483]. A quantitative model for inverse spool packing in bacteriophages was first formulated by Riemer and Bloomfield [484] and followed up by several papers. The inverse spool models are based on four additive free-energy contributions: (i) DNA elasticity [485], (ii) loss of entropy [484], (iii) DNA–DNA interactions [154], and (iv) DNA confinement [486].

Within the context of semiflexible polymer packaging, the possible states of condensed elastic chains *in vitro* have received a certain degree of attention [487,488]. The symmetry of the ground states can be ascribed to single spools, double spools comprising two nested tori with perpendicular axes, triply nested spools with perpendicular axes, as well as Hopf links with a symmetric partitioning into two equivalent, perpendicular, topologically linked tori [489]. This ordering mosaic of multiple homogeneously ordered domains composed of concentric spools is consistent with previous experiments and simulations of packing metallic wires into spheres, where ring-like coiling was observed, reminiscent of nested spools [490]. In addition, the observed complicated density and director configurations exhibit domain walls partitioning the interior of the capsid into multiple phase regions of the type observed recently by Leforestier et al. [482] in cryomicroscopy of T5 bacteriophage.

One of the most topologically interesting consequences of DNA packaging in viruses is that it induces a very large knotting probability, much larger than that of the genome of higher-order organisms. Arsuaga and colleagues [114] showed that the DNA in phage capsids displays a strong bias to forming torus knots. This can be explained by accounting for the near-crystalline packing of DNA and the chiral interactions induced by the DNA double helix [154], which also affect the ejection process [491]. Thus, beyond the geometric problem of packing semiflexible polymers in small spaces, DNA packaging in viruses and higher-order organisms leads to interesting exemplifications of knotting patterns and liquid-crystalline ordering, which have been explored in the soft-matter and polymer-physics communities (Section 2.7.1).

5.2. Prokaryotes: DNA organization, replication and topology

To discuss the role of topology in the organization of the genome in prokaryotes, we take as examples the widely studied bacterial species *Escherichia coli* and *Caulobacter crescentus*. First of all, bacterial DNA is folded into a compact membraneless body within the cell, the so-called *nucleoid*, which is a dynamic entity that alters its overall structure and shape in response to cell physiology [492]. The volume fraction occupied by naked DNA in the bacterial nucleoid is around 2%, much smaller than the one in viruses. Yet much of the nucleoid volume is also occupied by proteins that execute a range of functions on the DNA and that are absent in viruses. Although it is broadly accepted that the nucleoid is spatially organized under the combined influence of protein-mediated condensation [493], cell-boundary confinement [494] and, importantly, DNA supercoiling [495], understanding the finer structural features of the bacterial genome remains an outstanding challenge, reviewed in [496]. These finer features include plectonemes (see Section 3.3.6).

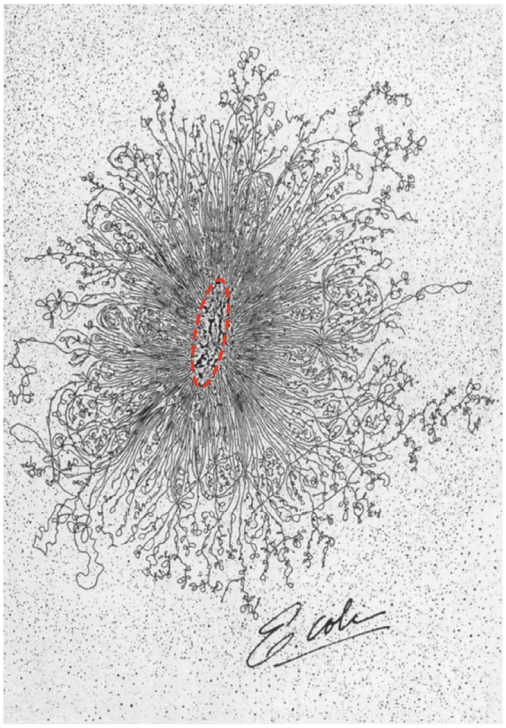

Fig. 58. A celebrated electron micrograph of a lysed *E. coli* cell by Ruth Kavenoff, showing supercoiled DNA sprouting from the burst *E. coli*, marked with dashed red line.
Source: Reproduced from [504]

The chromosome of an *E. coli* cell, a typical representative of prokaryotes, is approximately 4.6 mega base pairs (Mbp) long and has a circular topology [497]. If cut and fully extended, the DNA is approximately 1.5 mm long, which leads to the problem of packaging it within a $\sim$1 μm cell, 1000 times smaller. Studies using fluorescent microscopy show that the *E. coli* chromosome is confined by the cell wall, has a compact elliptical shape, and occupies a significant part of the available space inside the cell [494]. If one lyses, i.e., opens, the cells by removing the cell wall it is possible to appreciate that the diameter of the unconstrained chromosome becomes significantly larger, on the order of $\sim$10–20 μm (Fig. 58) [497,498]. A similar, yet more physiological, swelling of the nucleoid can be achieved by engineering strains of bacteria that acquire a more spherical shape in response to a certain stimulus [494]. Finer details based on electron-microscopy imaging have revealed that the nucleoid consists of hundreds of supercoiled DNA structures emerging from a dense condensed core [496]. From these experiments, it is clear that the cell boundary and supercoiling constrain the size of the bacterial chromosome.

The organization of the bacterial nucleoid into supercoiled domains was first proposed in 1981 [499]. The authors measured torsional tension in the nucleoid of live *E. coli* cells and in cells exposed to various levels of γ-irradiation to introduce random nicking sites in the DNA, i.e., sites in which the torsional tension is released. Based on the radiation rate, they estimated that around 160 nicks were sufficient to relax fully the *E. coli* genome, concluding that it must have been organized into *topologically insulated* supercoiled domains. This insulation is achieved by the binding of multivalent bridge proteins, such as H-NS, thought to be responsible for crosslinking and insulating DNA loops from the spreading of torsional stress [500]. If the domains were not topologically insulated, a single nick would have been enough to relax topologically the full genome. More recently, studies with chromosome conformation capture techniques such as Hi-C performed on *C. crescentus* reported similar results [501], indicating that the genome is partitioned in regions with larger-than-average contact probability, compatible with topologically insulated supercoiled domains [502].

The role of supercoiling in bacterial chromosomes and plasmids, i.e., shorter circular DNA, may not be restricted to their static organization. Recent numerical simulations and *in vitro* experiments have shown that supercoiling can have a strong influence on the relaxation dynamics of DNA [503] and can also speed up the dynamics of entangled DNA [121]. This suggests that during the cell cycle, in stages of intense replication or transcription, higher levels of supercoiling may effectively decrease the entanglement between unlinked supercoiled domains and help speed up segregation into domains or daughter cells.

5.2.1. The problem of DNA replication and segregation

Soon after the discovery of the DNA double helix, researchers puzzled over the biological consequence of such a structure. In their 1953 paper, Watson and Crick argued that the replication of DNA in living cells must pose a challenging, yet not *insuperable* problem [106], as Delbrück pointed out [505]. By unzipping the double helix and using two DNA strands as templates for two progeny strands, it is possible to replicate the genomic code faithfully and semi-conservatively, at the expense of obtaining two braided, tangled double helices winding around each other as many times as the parent strand was winding around itself [107]. This entanglement is particularly serious in bacteria; due to their closed circular chromosomes, the winding of the progeny strands necessarily leads to linking of replicated chromosomes, which would make cell division impossible were it not for proteins that can manipulate the topology of DNA. This topological problem is now known to require the help of special proteins, topoisomerases, that can relax and untangle newly replicated DNA and allow the daughter strands to be segregated in the daughter cells [113].

Bacteria are the simplest organisms that undergo DNA replication and are historically the organisms in which replication has been studied the most. Additionally, because bacteria have circular chromosomes, the tangling problem after DNA replication is present. Chromosome replication in bacteria initiates from a unique origin of replication and typically proceeds bi-directionally to a terminus region on the opposite side of the circular DNA [506]. Even though topoisomerases are typically positioned in front of the replication fork to relieve torsional stress [113], at the end of the replication process the progeny chromosomes need to be correctly segregated into the daughter cells. There are three largely opposing views describing DNA segregation in bacteria [507]. In the first model proposed by Dingman [506], the replication machinery — also referred to as the *replication factory* — is positioned near the cell centre, and the newly replicated DNA duplexes are pushed in opposite directions towards the cell poles to form two newly replicated chromosomes. Thus, segregation occurs in parallel to DNA replication. The second so-called *train track* model for replication [507] predicts that the two replisomes move along the chromosome arms and replicate the genomes independently. This model implies two distinct segregation mechanisms. The first is regulated by proteins: in certain species, e.g., *B. subtilis*, the so-called parABS system leads to chromosome segregation [507], while in *E. coli* this process may be driven by structural-maintenance-of-chromosome (SMC) proteins [508] (Section 5.3.3). In the third, so-called *entropic segregation* model [509], segregation is driven purely by entropy: newly replicated bacterial genomes can be viewed as circular polymers placed under geometric confinement. In certain conditions, there is a spontaneous de-mixing similar to that observed in melts of ring polymers (Section 4.1.3). There has been substantial interest in adopting ring-polymer models as proxies to study genome organization in bacteria and even eukaryotes [232]. Supercoiling itself, due to its ability to reduce overall entanglement, may be a route to induce segregation of newly replicated chromosomes more efficiently [121,510].

5.3. Genome organization and topology in eukaryotes

Genome organization in eukaryotic cells — i.e., in those organisms, such as mammals, that store their genetic information in a membraned nucleus — is considerably more complex than in prokaryotes. Here, the DNA is packaged into so-called chromatin fibres, a complex of DNA and histone octamers around which DNA is wrapped to form so-called nucleosomes. Nucleosomes are self-assembled heteromorphically along the genome, depending on the underlying sequence, post-translational histone modifications, cell line and stage [477,511]. The chromatin fibre is then itself looped and condensed into territories and topologically associated domains (TADs) [478]. Ultimately, in humans, 2 metres of DNA (6.6×10^9 base pairs in human diploids cells) must be packaged within a 10 μm nucleus, a 20 000-fold compaction, while remaining functional and accessible to various transcription and replication factors (Figs. 59 and 60). The volume fraction occupied by naked DNA in eukaryotic cells is around 1%–2%, much lower than the 50% found in viruses, yet the abundance of proteins and RNA renders the eukaryotic nucleus an extremely crowded and entangled environment. Accounting for proteins and RNA, the volume fraction of the genome can reach 20%–30% of the nuclear volume.

5.3.1. The nucleosome structure and the linking-number paradox

The very first layer of chromatin self-assembly, the nucleosome, presents a topological paradox: in each nucleosome, 146 bp of DNA wrap around a histone octamer core in 1.67 turns, in a conformation that resembles a shallow, wide but short, helix around a cylinder (Fig. 59**A–B**). As one can appreciate from Fig. 59**B**, this arrangement introduces writhe that is expected to affect the linking number in closed circular extrachromosomal DNA (Section 2.5). Experiments show that if circular DNA is topologically relaxed using Topoisomerase I in the presence of histone octamers and histones are subsequently removed, the DNA left behind displays a linking number deficit of about -1 per nucleosome, i.e., the DNA is underwound by one turn per nucleosome. This result presents a paradox since one would expect a -1.67 linking number deficit per nucleosome. The paradox is resolved with the CW theorem (Section 2.5): to explain the -1 linking number deficit per nucleosome, the DNA must twist as it wraps around the histone core yielding an equivalent of $+0.6$ in linking-number deficit. This prediction stemming from a topological conservation law proved correct and was confirmed in crystal structures of the nucleosome [107,514].

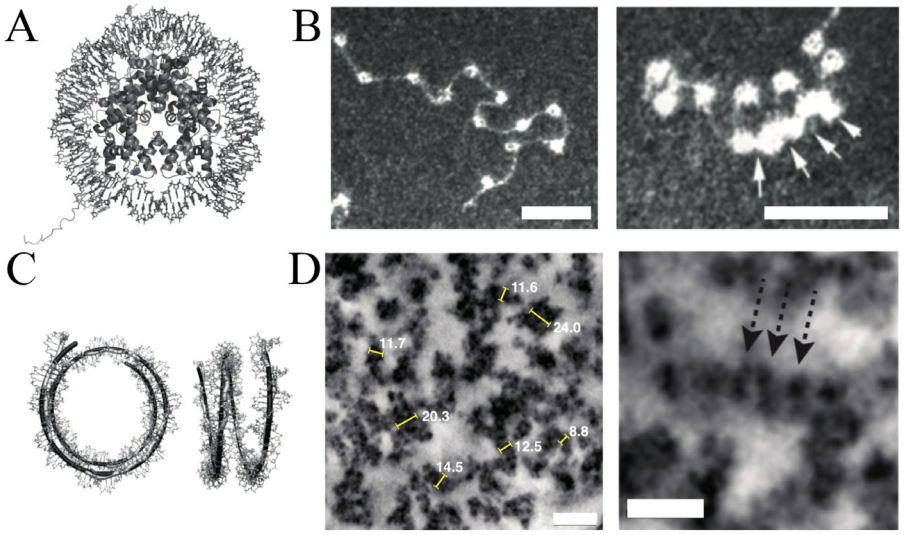

Fig. 59. **A** Crystal structure of DNA wrapped around a histone octamer core. **B** Electron micrograph of chromatin reconstituted *in vitro* using DNA and histone cores. Scale bars 50 nm. **C** Structure of the DNA showing the left-handed shallow helix around the core. **D** Chromatin organization *in vivo* captured using ChromEMT. Scale bars 50 nm on the left and 20 nm on the right.
Source: **A**,**C** reproduced from Ref. [107]; **B** reproduced from Ref. [512]; **D** reproduced from Ref. [477].

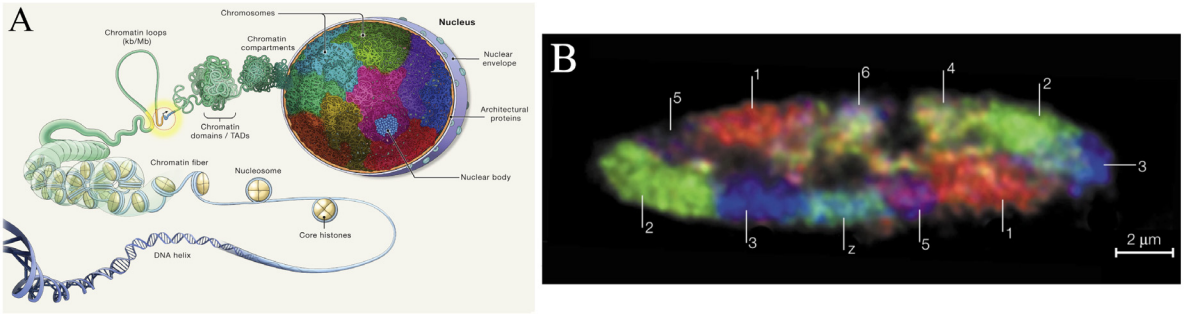

Fig. 60. **A** Chromosome folding in eukaryotic cells. Cartoon capturing the current understanding of DNA folding in the cell nucleus. **B** Chromosome territories in a chicken fibroblast nucleus.
Source: **A** reproduced from [513]; **B** reproduced from [233].

5.3.2. The chromatin fibre

The organizational layer above the nucleosome structure is the so-called *chromatin fibre*. This is made up by arrays of nucleosomes joined together by so-called linker DNA that is not wrapped around histones. The precise conformation of these arrays is largely debated, mostly due to its elusive nature [477]; it is remarkably difficult to assemble reconstituted chromatin fibres *in vitro* with non-artificial DNA sequences [515]. Arguably, the precise conformation of these poly-nucleosome fibres will depend on post-translational modifications appended to the histones [516]. As can be seen in Fig. 59, these fibres may assume various configurations: loose beads-on-a-string with thickness of about 10 nm (the so-called 10 nm fibre) or a more compact *zig-zag* arrangement (the so-called 30 nm fibre), by simply changing, for instance, salt conditions or the presence of linker histones [512,517]. Recent attempts to study chromatin structure *in vivo* have used super-resolution microscopy (STORM) [476] and ChromEMT [477] and have found a large variability of conformations and density. In all cases, chromatin fibres are typically seen to be rather heterogeneous and display a range of different configurations, which likely depend on factors such as gene content and histone post-translational modifications, which also probably vary with cell stage [511].

5.3.3. Physical domains and loops

Beyond the length-scale of a few nucleosomes and below the scale of one Mbp, indirect measurements of chromatin conformation may be obtained using chromosome conformation capture such as Hi-C; these have revealed the existence of structures called *topologically associating domains* (TADs) [518,519]. The term topology is here loosely employed to indicate the tendency of DNA segments inside TADs to be on average geometrically closer in 3D than equally distant segments

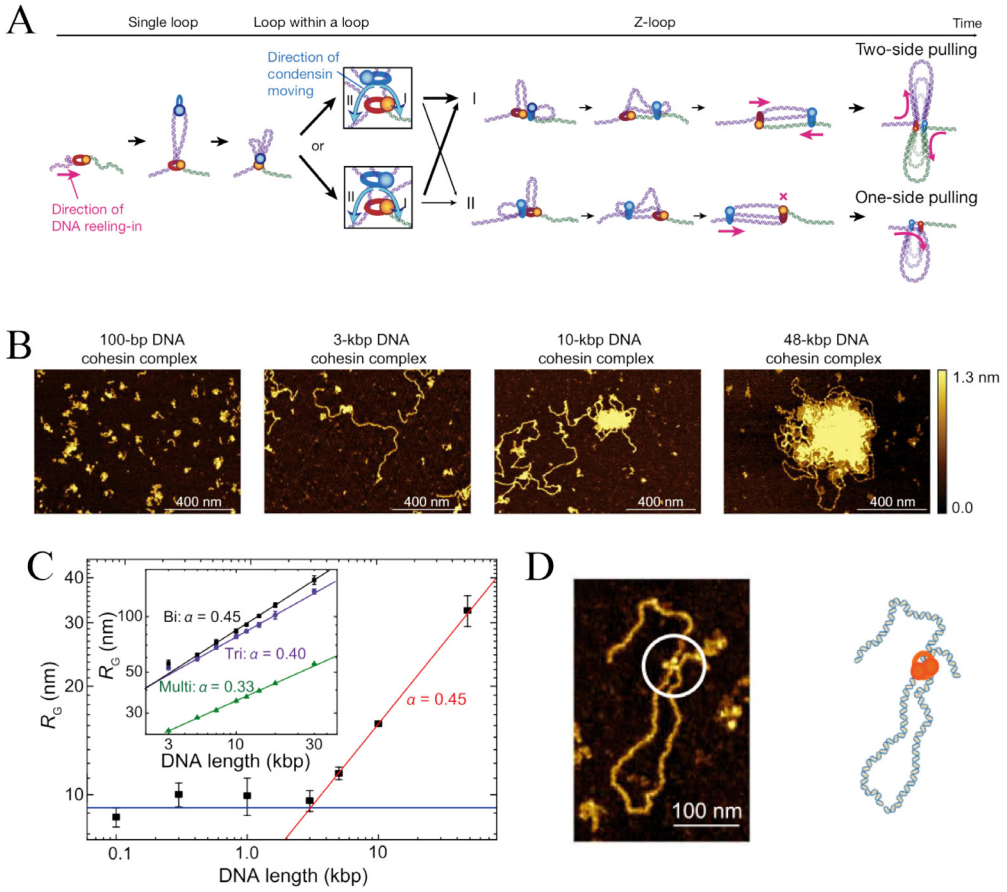

Fig. 61. Loop extrusion, Z loops, and bridging-induced attraction. **A** Model of DNA Z-loop formation by two loop-extruders (condensins). From left to right: a single extruder can form a single loop; additional loop extruders binding within single loops can form nested loops; depending on the mutual orientations of the two extruders (*zooms*), the formed Z-loop can reel in DNA either from both sides of DNA (two-side pulling from discordant extruder orientations) or from one side (one-side pulling from concordant extruder orientation). **B** AFM images showing that yeast, *S. Cerevisiae*, cohesin can form clusters when in the presence of long DNA substrates and no ATP. This behaviour, called *bridging induced phase separation*, is due to the non-specific multivalent binding of proteins to DNA. **C** Quantification of cluster size R_g from AFM images, showing that a critical DNA length of 3 kbp is needed to observe the onset of clustering. **D** AFM image showing a cohesin complex bridging a loop.
Source: **A** reproduced from [523]; **B–D** adapted from [524].

outside a TAD [519]. The physical origins of TADs are still debated, but protein bridges [520,521], supercoiling [502] and loop extrusion [522] are the most pursued.

The most popular hypotheses for the establishment of TADs and, in general, condensed domains in the eukaryotic genome, are either based on loop extrusion or on bridging-induced phase separation models. The former was conceptualized a few decades ago [525], and computational models were developed more recently [522,526,527]. In these models, loop extruding factors (LEFs), such as condensin or cohesin proteins, can consume energy (ATP) to drive the formation of DNA loops by extruding DNA, similarly to pulling a climbing rope through a carabiner (Fig. 61**A**). Recently, *in vitro* experiments have shown that condensin [528] and cohesin [529] can extrude loops at a speed of ∼1 kbp/s; these are fast but weak molecular motors. The precise mechanism through which loop extrusion is done remains unknown at a molecular/atomistic level, and different models, topological, pseudo-topological and non-topological, are currently being investigated [530,531]. Condensins have also been observed to form higher-order complex topological looped structures, so-called *Z-loops*, *in vitro* [523] (Fig. 61**A**). These are made by intersecting LEFs that hop over each other forming nested, zig-zagging loops. This allows for the formation of longer DNA loops within a busy genome and indirect evidence has been seen *in vivo* as well [508]. A possible mechanistic explanation for the appearance of these nested and intersecting loops is that LEFs may be able to *grab* DNA strands in 3D thereby bypassing the constraint to slide along a 1D DNA chain [532]. Alternatively, there may be other non-topological mechanisms through which some SMC proteins may organize the genome [524], e.g., via bridging-induced attraction or phase separation of DNA segments [533] (Fig. 61**B–D**). This behaviour is generically observed in systems of DNA and DNA-binding proteins that have more than one DNA binding site. The binding multivalency triggers a positive feedback loop through which a bound protein increases the local

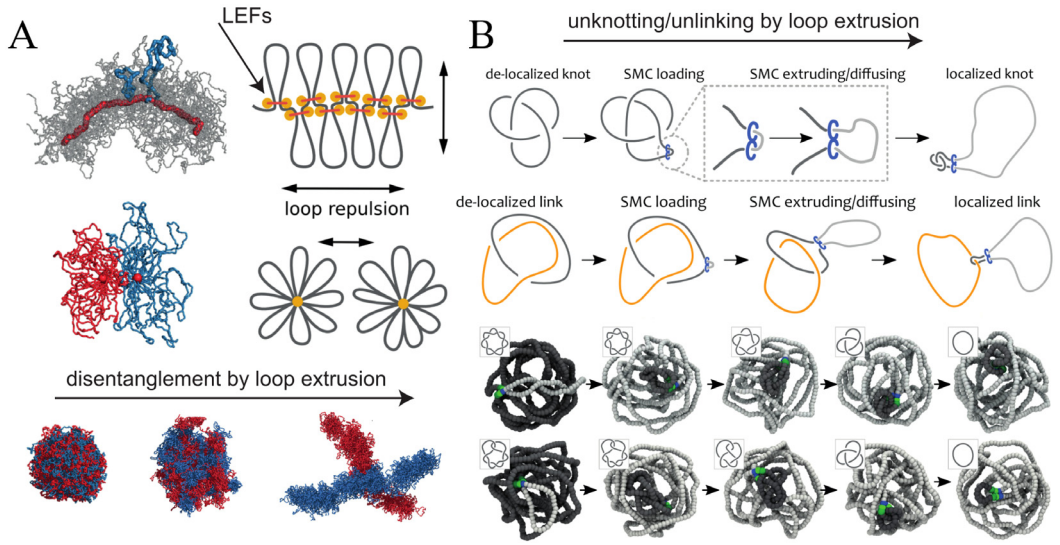

Fig. 62. Loop extrusion and entanglements. **A** Loop extruding factors (LEFs) can create structures resembling bottle-brush polymers with looped side chains. Due to their entropy and looped topology, the side chains effectively stiffen the backbone and increase the repulsion between different polymers. Because of this entropic repulsion and stiffening, sister chromatin may be more easily disentangled. **B** Loop extrusion may also play a key role in localizing entanglements, such as knots and links, and in directing the action of type II Topoisomerase in driving the topological simplification of the genome.
Source: **A** adapted from [535]; **B** adapted from [536].

concentration of DNA, which then recruits more proteins [533]. Eventually, a cluster — or a phase-separated condensate in the case of large systems — of proteins will appear (Fig. 61**B**). Ryu et al. [524] showed evidence that cohesin can bridge DNA, forming static loops, and that a critical DNA length of 3kbp is needed to observe the onset of cohesin clustering (Fig. 61**C,D**). The mechanism discovered does not require SMC activity, i.e., ATP consumption, and may thus represent an alternative organizing mode of condensin and cohesin. In spite of this, current evidence suggests that active (ATP-driven) loop extrusion is present *in vivo* and that TADs during interphase, the non-dividing stage of the cell cycle in which the cell spends most of its time, may be formed by actively loop extruding cohesin [534].

Loop extruding factors (LEFs) also appear to be involved in the organization of mitotic chromosomes, i.e., in the preparation for cell division [535,537]. The structure of mitotic chromosomes is even denser than that in interphase. They assume cylindrical conformations connected at the so-called centromere, yielding the commonly pictured X shapes [537]. Evidence suggests these are formed by a series of stacked loops spiralling around a central backbone that is densely populated by condensins (and, incidentally, Topoisomerase 2), in turn forming a structure resembling that of bottle-brush polymers [537,538] (Fig. 62**A**). Thanks to their effective increased rigidity and repulsion due to the presence of looped side chains, sister chromatids may be more easily disentangled in preparation for cell division [535,538] (Fig. 62**A**). Mitosis is a critical stage of the cell in terms of entanglements. Large forces are applied to the chromosomes from the spindles to drive segregation into daughter cells. If entanglements were not thoroughly resolved at this stage, DNA breaks would be inevitable and deadly for the cells. For this reason, loop extrusion and topoisomerase are both abundant at this stage of the cell cycle. Computational work has suggested that loop extrusion may help the localization of entanglements such as knots and links, thereby facilitating their downstream simplification by topoisomerase [532,536,539] (Fig. 62**B**). These computational works were verified experimentally using artificial minichromosomes in yeast where condensin could be inactivated [540]. The authors showed that the sole inactivation of condensin (but, importantly, not of topoisomerase) would increase the knotting probability of minichromosomes to the level that one would expect in equilibrium [540]. This paints a picture where both structural-maintenance-of-chromosomes (SMC) proteins and topoisomerase, two of the most well-conserved proteins across living organisms, are essential to drive the efficient topological simplification of genomes. Managing DNA topology is a vital task that life needed to learn to do efficiently in order to increase complexity.

5.3.4. Chromosome compartments

At the scale of tens of megabases, Hi-C contact maps suggest that the chromatin fibre condenses into compartments that consist of sub-chromosomal regions of the nucleus in which large portions of the genome are more often in contact than on the average [478]. Intriguingly, these compartments appear to be populated either by gene-rich and transcriptionally active or gene-poor and inactive regions of the genome but not by a mixture of the two [519]. This level of organization has been confirmed using super-resolution imaging, which additionally unveiled large cell-to-cell variability, i.e., two randomly chosen cells display different organization of the genome in compartments [541]. An outstanding

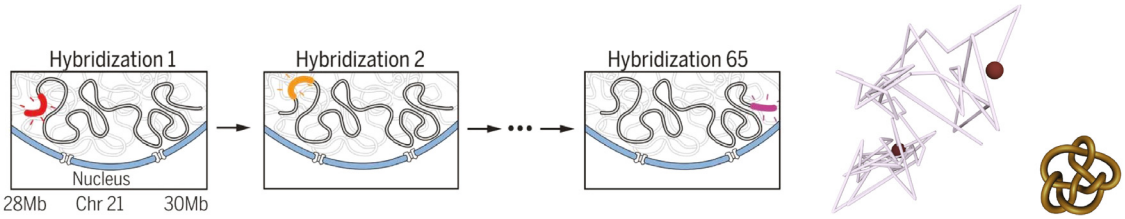

Fig. 63. Chromatin tracing. A fluorescent oligonucleotide is attached (hybridized) to DNA at the complementary sequence. After repeated rounds of washing and hybridization, a full segment of chromatin can be reconstructed at 30 nm resolution. The polygonal curve corresponding to one of the chromatin tracings in Ref. [549] is shown. Each vertex of the curve corresponds to the centroid of a 30-kb-long chromatin portion, as measured using the *oligopaint* method. Multiple-closure analysis reveals that it forms a 9_{30} knot. The minimal crossing representation of the 9_{30} knot is shown at the lower right.
Source: Adapted from [549], [153].

problem is to discover the molecular mechanisms driving the formation of such compartments. Among the currently most pursued hypotheses is the phase separation, demixing, of genomic regions [542] driven by DNA-binding proteins [533,543] or different interaction potentials due to epigenetic marks [521,544–546]. Integrating different models, e.g., accounting for supercoiling, variable interaction patterns, loop extrusion, etc., is a current challenge [511].

5.3.5. Chromosome territories

One of the most famous experiments in which chromosomes were first visualized inside the nucleus is that performed by the Cremer brothers in 2001 [233] (Fig. 60**B**). They labelled chromosomes with different combinations of fluorescent dyes and looked at their distribution in the nucleus. They observed that they occupy distinct regions, so-called *chromosome territories* (CTs), with minimal intermingling. Chromosome territories, and in general chromosome positioning within the nucleus, have been proposed to impact gene regulation [547] and even HIV integration [548]. The presence of chromosome territories has been confirmed by Hi-C experiments that showed inter-chromosomal interactions to be less frequent than intra-chromosomal ones [478]. Additionally, Hi-C experiments measured the exponent of the decay of the contact probability versus genomic separation to be $\gamma = 1$, where $\gamma = 3\nu$ for objects in three dimensions.

Chromosome territories and the large-scale scaling exponents $\nu = 1/3$ (Section 3.3.1), as well as $\gamma = 1$, can have topological origins [232,234,235]. A melt of unknotted rings exhibits territoriality and similar exponents to those seen in Hi-C experiments [478] (Section 4.1.3). Despite the fact that human chromosomes are effectively linear polymers, not rings, they are not in equilibrium on biological time-scales and so their state may be akin to that of a typical equilibrium state of a unknotted polymer ring (Section 4.1.1). Such considerations apply only to chromosomes much longer than the entanglement length. For example, the yeast genome is shorter or comparable to the entanglement length and does display the standard equilibrium globule exponent $\gamma = 3/2$, and much less clear territoriality [234].

As another way to explain the organization of long human chromosomes, and more specifically of loosely entangled chromosome territories, Grosberg proposed the idea of a *crumpled fractal globule* [235]. This model starts with the assumption that the underlying polymer is topologically simple due, for instance, to fast collapse from an extended state, to generate so-called fractal or crumpled globule ensembles. Within these conditions, the exponents expected in the theory are $\nu = 1/3$ and $\gamma = 1$, which coincide with those found in equilibrium for unknotted rings. When topological constraints are absent in the system and polymers can pass through each other, ring polymers in dense solutions recover the equilibrium exponents for linear chains $\nu = 1/2$ and $\gamma = 3/2$; in this case we expect the proliferation of knots and links [232]. A deeper connection between these exponents and the underlying topology of these polymer and DNA systems is still to be elucidated. For instance, we do not know whether some knotted ensembles of polymers can display the same exponents of the fractal globule, or if these can only be seen in unknotted chains.

Experiments done by the Roca group [144,540] on minichromosomes in yeast showed that they display a knotting probability much lower than that expected in equilibrium. As discussed above, it appears that the major player in maintaining a low topological complexity in these experiments is the action of SMCs [540], which may also have the indirect effect of maintaining a fractal globule-like arrangement of the genome. We expect that computational models and large-scale simulations will help clarify this question.

5.3.6. How to identify knots in eukaryotic chromosomes in vivo

During interphase, the expansion of chromosomes from the bottle-brush-like mitotic structure to the territorial interphase state may result in a increasingly crowded state in which knots and entanglements proliferate more easily than in the mitotic state due to the relaxation of polymer conformations. Knots may have a profound and detrimental impact on several biological processes such as transcription, gene regulation, and DNA replication [152], as argued by Delbrück [505]. It is therefore important to understand whether complex topologies appear *in vivo* and how they contribute to cell health.

One of the most successful techniques to quantify knotting probability is gel electrophoresis [144,540] (Section 3.2.2.), which relies on the fact that DNA of different length and topology travels at different speed through an agarose gel.

One can extract intact chromosomes and apply this technique. Unfortunately, this experiment is only feasible with yeast minichromosomes around 3–12 kbp. However, chromosomes, especially in higher order organisms, are typically 100–1000 times longer and it would not be possible to resolve them clearly using this technique.

In order to detect knotted structures in chromosomes in human live cells it is not even possible to rely on chromosome conformation capture techniques, as they require a large number of cells, i.e., population averages. Two techniques have been exploited to obtain chromosome conformations at single-cell resolution. The first is single-cell Hi-C [550,551], and these studies suggest that there could be some simple, loose, knots scattered across the genome. Yet the resolution of single-cell Hi-C is relatively low, about 100 kbp, meaning that it is impossible to "see" knots smaller than this length. Another method is so-called oligo-painting, an oligonucleotide-based fluorescent in-situ hybridization method, which has been used to trace the XYZ-coordinates of centroids of consecutive genomic sections at 30 kb resolution (Fig. 63). Oligo-painting super-resolution data generated in Ref. [549] was then used in Ref. [153] to quantify directly the topology of chromatin at single-cell resolution using random closure schemes followed by standard topological invariants (Fig. 63). In this way, it was found that most of the traces were unknotted, and over 10% of them remained unknotted even after perturbing the tracing data with stochastic noise, suggesting that, in analogy with the yeast data from the Roca lab [144], the human genome may also be topologically simple, showing robust unknotting at the megabase scale.

5.4. Outlook on DNA, chromatin and genome organization

We have seen how topology plays a role in DNA organization across scales and organisms from viruses, to bacteria and humans, and from the scale of a short double-stranded DNA molecule, to nucleosomes, chromatin, and chromosome territories. However, there are still a lot of unknowns in front of us waiting to be discovered especially when aspects of DNA dynamics are concerned. On the one hand, we are only starting to scratch the surface of how DNA and chromatin topology affect or are affected by chromatin transactions, such as transcription, DNA repair, and replication: how is the action of loop-extruders orchestrated with proteins and factors that regulate transcription? Do chromosome domains facilitate the interactions between genes and specific sequences that enhance or repress transcription or organize the process of DNA replications in the nuclear space? Is the super-coiling of DNA involved in fine-tuning functional interactions? On the other hand, topological constraints and the associated slow chromosome dynamics may contribute to maintaining a memory of chromosome organization over generations. The evidence that certain species adopt chromosome large-scale organization of different kinds, thanks to the action of chromatin extruders and large-scale mechanical manipulation during cell division is already pointing in the direction that re-acquiring a consistent overall chromosome shape at each cell cycle is important to preserve the cell state over time.

The stories of how life is written into our genomes and how DNA is topologically and geometrically organized into cells are strongly entangled. Nature has come up with ingenious and fascinating solutions to the topological problem caused by DNA packaging and entanglement. Thanks to interdisciplinary efforts involving biologists, mathematicians, and physicists we are now getting closer to a more complete understanding of these solutions and, in general, of how nature deals with its (un)knotted strands of life.

6. Topological properties of living matter: entangled proteins

6.1. Entangled proteins

The presence of knots in proteins poses at least three types of problems. First, knots in proteins must be identified starting from the native structure. As we have seen in the previous sections, several computational methods have been developed to tackle the issue of characterizing the degree of topological complexity of open chains. The second problem pertains to the formation of entanglements during folding. Experimental evidence has shown that certain proteins can knot and fold autonomously in the controlled environment of the test tube, and molecular simulations have provided important insights into their knotting mechanisms; other knotted proteins may require, or take advantage of, the presence of a class of molecular machines called chaperonins to reach their functional, knotted conformations. Furthermore, recent advances in simulation have also suggested that knotting may take place directly as the protein chain is synthesized, in the process of co-translational folding that is driven by another molecular machine, the ribosome. However, much remains to be understood of the specific features of each self-entangled protein's folding and knotting pathways, as each of them is a unique case *per se*. The third problem refers to the function of self-entangled proteins. Do knotted or otherwise entangled proteins benefit from having such topological features? Are knots frozen accidents of evolution, or do they represent a net gain for the protein's fitness? Can a knotted protein *de-evolve* into a knot-free structure? These questions still have to be answered.

Self-entangled proteins represent a fascinating area of research, and the impressive experimental and computational advances of the past 20 years have mostly only scratched its surface. A deeper understanding of topologically nontrivial polypeptides will not only boost our understanding of proteins in general — folding, function, dynamics, evolution, etc — , but may also represent a chance for practical industrial and pharmaceutical applications. The combination of the amazing structural and functional versatility of proteins, on the one hand, and the discreteness and resilience of topological properties, on the other, endow these molecules with great potential for the development of smart materials, hybrid artificial/biological responsive systems, novel pharmaceutical tools, and perhaps much more.

6.2. Where do knotted proteins come from?

Knotted protein structures occur in all kingdoms of life and homologous structures of knotted proteins, i.e., structures that can be traced back to a common ancestor due to their similarity in shape and sequence, tend to be knotted as well. For example, UCH-L3 contains the same fivefold knot in humans and yeast [552] even though they share only about one third of their sequences. This fact may be surprising at first, but typically a low degree of sequence similarity suffices to preserve the overall structure of any protein, including knotted proteins. Other examples include knotted homologues of CaCA transmembrane proteins [212], which have been found in archaea, bacteria and fungi, rendering a convergent evolution scenario unlikely. Thus, knotted protein structures tend to be preserved throughout evolution and, in many cases, have likely evolved from knotted precursor structures in organisms that lived hundreds of millions, if not billions, of years ago. There is also evidence that there are evolutionary mechanisms in which knotted structures emerged from unknotted predecessors, giving rise to theories on how knots evolved in the first place.

As already pointed out, some knotted structures are covalently linked homodimers, i.e., they consist of two structurally similar parts that are connected, which may have resulted from gene duplication and insertion mutations. Another potential evolutionary mechanism is circular permutation, by which the original termini of a protein are linked and new termini created elsewhere, as has been demonstrated recently by constructing an unknotted homologue from a trefoil knotted RNA methyltransferase [553]; the opposite process may also occur. Even though homologues of knotted proteins in the Protein Data Bank (PDB) are typically knotted as well, a single naturally occurring counterexample exists, which allows us to trace back its origin with a phylogenetic tree. The main difference in the knotted section of the bacterial transcarbamylase and its unknotted human homologue is an additional unstructured loop in the former through which the protein chain can thread to form a trefoil knot. An analysis of the corresponding phylogenetic tree [554] suggests that two knotted commonly rooted sub-branches exist that split from the unknotted main branch in a single evolutionary event.

Evidence from a simple protein toy model [555] and earlier comparisons of proteins with random compact loops [556] suggest that knots in proteins should be more abundant from an equilibrium statistical-mechanics point of view than is observed. These results imply that proteins evolved towards a mostly unknotted structural sub-space. Despite their statistical rarity, a complete solution of the protein folding problem must necessarily include knotted proteins, proteins with slipknots, and other topologically complex folds. In this section, we provide a review of our current understanding of the field based on experimental as well as theoretical results.

6.3. Folding of self-entangled proteins: Insights from experiments

A battery of different experimental techniques and approaches have been used to study both naturally occurring knotted and slip-knotted proteins as well as a few designed knotted proteins (Section 6.10.1). Here, we review the major findings obtained so far, which have contributed significantly over the past two decades to our understanding of the thermodynamic stabilities and folding kinetics of knotted proteins. Some examples of knotted proteins that have been studied experimentally are shown in Fig. 36.

6.3.1. Stability measurements: characterizing the structures and energies of denatured, intermediate, and native states under equilibrium conditions

Chemical denaturants such as urea and guanidinium chloride, as well as heat, have been used to unfold 3_1 (YibK, YbeA, MJ0366, and a single chain monomer of HP0242), 5_2 (numerous members of the UCH family) and 6_1 (DehI) knotted proteins under equilibrium conditions. In addition to measures of the global stability of the native state of the knotted proteins, these experiments provide information on whether there are any stable, intermediate, partially unfolded, states. In many cases, populated stable intermediate states have been observed [557–559] . In some of these cases, there is evidence that the intermediate states are likely knotted, whilst for other knotted proteins, particularly shallow knotted proteins, results suggest such partially structured states are unknotted. However, not all knotted proteins have stable intermediate states, and many have been shown to be simple two-state systems populating only native and denatured states [559–561] Overall, a very wide range of stabilities has been measured for the native folded states of knotted proteins, ranging from marginally stable with a free energy of unfolding of 6.3 kJ mol^{-1}, to extremely stable with a free energy of unfolding of over 80 kJ mol^{-1}[559]. This range is very similar to that found for unknotted proteins [559].

Other experimental methods, particularly nuclear magnetic resonance (NMR) spectroscopy, have also been used to study different aspects of the structure and stability of various populated states of knotted proteins, including the denatured, intermediate, and native states. In these cases, this experimental technique allows local stability to be probed, i.e., the stability associated with a single amino-acid residue or specific region within the structure, as well as the global stability. In one case, for the shallow trefoil-knotted protein MJ0366, NMR was used to establish that the knotted region is the most stable structural element within the overall structure [560]. However, in another system, the single-chain monomeric form of HP0242, the same technique demonstrated that the knotted region near a linker site was rather unstable [562]. For 5_2 knotted proteins from the UCH family, similar methods have been used to characterize the structure of partially unfolded intermediate states at high resolution [561,563].

6.3.2. Knots in the denatured states of knotted proteins

Even though most knotted proteins are open chains, i.e., the linear polypeptide chain is not circularized, in some cases, knots have been found to persist even in the denatured state in which there is little structure. This was first shown using a combination of different methods for two deeply trefoil-knotted proteins, YibK and YbeA, where the structure remained knotted for some time after the unfolding of almost all of the secondary and tertiary structure, before untying occurred [564]. This result was confirmed on another member of the same family of trefoil-knotted proteins, establishing that it is a general phenomenon for this family of knotted proteins [565]. NMR spectroscopy techniques have been used to investigate further this unusual behaviour and the side chains of residues just before the knotting loop and in the threaded region have been shown to interact in the denatured state, leading to the metastable knotted denatured state observed [565,566].

6.3.3. Dynamic processes within the native states of knotted protein structures

In addition to important information on the structures and relative stabilities of different populated states, NMR methods have also been used to study dynamic processes within the native structures of knotted proteins. In this case, the dynamics (flexibility and/or local unfolding events) of single-amino-acid residues within the structure can be probed. This experimental approach has been used to establish that the length of the cross-over loop that forms part of the knotted structure of 5_2 knotted (UCH) proteins correlates with disorder in the loop; higher levels of disorder being entropically stabilizing, resulting in changes in stability and slower unfolding rates [567].

6.3.4. Unfolding and refolding kinetics: measuring unfolding/folding rates and identifying transiently populated intermediate states and multiple folding pathways

The kinetics of unfolding and folding of knotted proteins have been studied experimentally using a number of methods, including using changes in chemical denaturant concentration to induce either unfolding or folding. The first study was on a trefoil-knotted protein with a deep knot (YibK). Kinetic analysis demonstrated that its folding pathway is complex with parallel folding pathways and a number of intermediate states [568]. Since that time, numerous other experimental studies have characterized the folding kinetics of different knotted proteins. In many cases, the kinetics are complex and similar, in some ways, to the original investigation [558,561,563,569,570]. However, in other cases, the folding kinetics are much simpler [560]. It is likely that these differences, also seen in the unfolding of unknotted proteins, are due to factors such as the depth of the knot, the knot type, and the intrinsic global stability of the protein or other aspects of the protein structure.

Unfolding rate constants measured in high concentrations of chemical denaturant can be extrapolated to 0 M denaturant, i.e., the unfolding rate constants in water can be estimated from unfolding data. Similarly to the results described above for the stability measurements, they have been determined for a number of knotted proteins and found to span many orders of magnitude from 2 s^{-1} to 6×10^{-7} s^{-1}, corresponding to half-lives of 350 ms to 14 days, and are within the range found for unknotted proteins [559]. Likewise, folding rate constants also vary over seven orders of magnitude, with the fastest folding example being a shallow 3_1-knotted protein (MJ0366) having a half-life of 64 μs whilst the slowest are the deeply 3_1-knotted (YibK and YbeA), which have folding half-lives of approximately 15 min in the absence of molecular chaperonins (Section 6.5).

In addition to determining the unfolding and folding rate constants, the number of partially structured species transiently populated during unfolding/folding, and whether there are multiple parallel pathways from the denatured to the native knotted state have been established using experimental approaches. In addition, experimental techniques have provided information on aspects of the folding mechanism. For example, kinetics has been used in conjunction with protein-engineering techniques to establish that deeply 3_1 knotted proteins YibK and YbeA knot by the C-terminus of the polypeptide chain threading through a knotting loop [571]. In this case, the C-terminus is closest to the knotted region of the protein. Further insight into the folding of this class of deeply trefoil-knotted proteins has also been obtained with results suggesting that threading involves the C-terminus of the chain even when the C-terminus is severely hindered by the addition of a large stable structure.

Protein-engineering techniques have also been used in other studies. Single point mutations in the 5_2 knotted UCH-L1 have been used to investigate its folding pathway [563], and results from these experiments suggest that the rate-limiting transition states have broad energy barriers consistent with the protein chain undergoing a conformational search prior to, or during, threading [563]. In other cases, experimental studies have established that, for a designed trefoil-knotted monomeric form of HP0242, misfolding occurs during folding and that the protein has to partially unfold in order to overcome the rate-limiting barrier to get to the native knotted state [569]. In this case, the protein has not evolved to have a knotted structure so its sequence has not been optimized by evolution to avoid kinetic traps.

Other protein engineering studies have *rewired* the structural elements within a knotted protein structure to generate what are known as circular permutants (CP), which have very similar secondary and tertiary structures to their knotted parents but are unknotted. These have enabled the effect of the knot on protein stability and folding rates to be determined experimentally. Two 3_1 deeply knotted proteins, YibK and YbeA, have been engineered such that the original N- and C-termini become covalently linked, whilst new N- and C-termini were introduced elsewhere. For YibK, the unknotted CP was shown to have undergone some structural changes which resulted in a lack of function [572]. It was less stable than the knotted wild type, but also folded with slightly faster kinetics, by a factor of two. However, it is hard to know whether

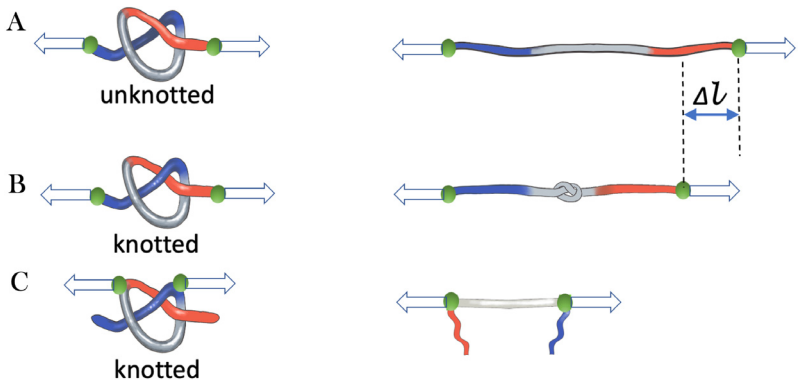

Fig. 64. SMFS allows for the manipulation of a protein knot by stretching the protein from two selected residues. **A** Stretching an unknotted protein leads to an unfolded and unknotted polypeptide chain. **B,C** Depending on the pulling direction, a protein knot can be tightened or untied. The length difference between the unknotted and knotted polypeptide chain measures the size of a protein knot.

this resulted from the absence of the knot or the structural change observed. For another member of the same family, YbeA, the unknotted CP was shown to fold into a non-functional domain-swapped dimer, with much reduced stability. It also folded with a slower rate than the knotted wild type [553]. Because of the structural rearrangements that occurred as a result of the untying of the knot in these circular permutated proteins, it is not possible to use the results unequivocally to assess whether the knot aided in the stabilization of these proteins or reduced the folding rate.

6.3.5. Single-molecule studies of knotted proteins

Single-molecule force spectroscopy (SMFS) techniques including atomic-force microscopy (AFM) and optical tweezers (OT) have developed over the last two decades into powerful tools to probe the folding–unfolding dynamics of proteins [573,574]. By stretching a protein from two specific residues, it is possible to manipulate mechanically a protein of interest, converting it from its folded state to an unfolded random coil-like state. The force at which the protein unfolds together with the length change associated with unfolding provide key signatures. For proteins that do not contain a knot or slipknot, mechanical unfolding will always lead to an unfolded and unknotted polypeptide chain. However, stretching a knotted or slip-knotted protein leads to an unfolded polypeptide chain that may be knotted or unknotted, depending on the position at which the forces are applied (Fig. 64**B-C**). Stretching a knotted protein from its N- and C-termini leads to an unfolded polypeptide chain with a tightened knot, which is shorter than the same polypeptide chain without a knot (Fig. 64**A–B**). This length difference Δl provides a straightforward way to detect the existence of a knot in a protein as well as to measure the size of a tightened knot. Bornschlögl et al. [575] used AFM to stretch the figure-eight knot in the chromophore-binding domain of the photoreceptor phytochrome. They found that, after unfolding, the unfolded phytochrome polypeptide is 6.2 nm shorter than an unknotted polypeptide chain without a knot, suggesting that the tightened figure-eight knot contains ~17 amino acid residues. AFM and OT techniques have also established the size of tightened knots in other knotted proteins including those with simple trefoil knots [576–578] and a more complex 5_2 knot [203]. The mechanical forces required to unfold knotted proteins have been found to cover a wide range of values and do not depend upon knot type. The values observed are well within the range found for unknotted proteins [559].

SMFS experiments have also been used to identify metastable intermediates on the unfolding pathways of these proteins as well as measure the folding rates from an unfolded but knotted state. Folding is measured after relaxation — the force that induced stretching is removed — and at this point the tightened knot undergoes a loosening process, suggesting that thermal energy is sufficient to loosen up the tightly knotted chain, thus facilitating refolding. In many cases, refolding is relatively rapid and consistent with solution folding studies of knotted proteins from their unfolded and knotted conformations [578,579].

In addition to stretching a knotted protein from its termini, or from two residues that are located in the two different knotting tails (Fig. 64**A–B**), proteins can be stretched from residues located in the knotted core (Fig. 64**C**) generating an unfolded and unknotted state. Refolding measurements from these states have shown that folding is slower than the folding from an unfolded polypeptide chain with a pre-formed knot, suggesting that knotting is the rate-limiting step for the folding of these proteins [203,577,578].

Using similar strategies, the unfolding–folding of slip-knotted protein has also been probed using SMFS techniques. Depending on the pulling direction, a protein slipknot can be untied or be converted into a real knot. Both scenarios have been observed in AFM experiments on the slip-knotted protein AFV3-109 [576,580]. The folding of a slipknot protein depends on the length of the threaded loop. A slipknot protein AFV3-109 with a short, threaded loop was observed to refold rapidly in optical tweezers experiments [581]. In contrast, the slipknot protein, pyruvoyl-dependent arginine decarboxylase (PADC) with a much longer threaded loop, was observed to fold very slowly, and only a small number of the unfolded protein molecules were able to refold on a time-scale of five minutes [582]. It remains to be seen whether this finding can be generalized to other slipknot proteins.

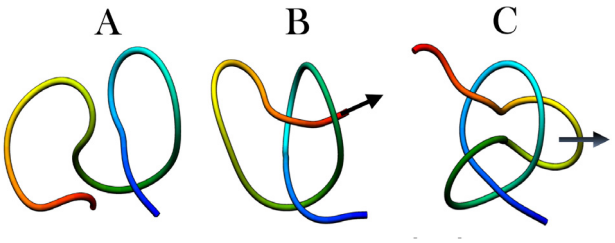

Fig. 65. Protein knotting step. The knotting loop **A** can be threaded by a bent terminus that forms a slipknotted conformation **C**, or directly by an extended chain terminus **B**.

6.4. Folding of self-entangled proteins: Insights from simulations

It is not yet possible to obtain a structurally resolved picture of the protein knotting mechanism in laboratory experiments. Thus, molecular simulation studies have been used as an important complement to experimental studies conducted *in vitro* by providing theoretical predictions for the knotting step. A wide range of theoretical models with different levels of structural resolution, from coarse-grained models on a lattice to full atomistic models with physics-based force fields (Section 6.10.2) have been combined with molecular simulation methods to study knotted proteins and proteins with other non-trivial topologies. One of the advantages of *in silico* approaches is the ability to determine unequivocally the topological state of a protein conformation. Additionally, it is considerably simpler to create an unknotted conformation from a knotted one in the framework of simulations [583] than experiments, which allows exploring the impact of the topological state on folding and function.

To date, around 10 proteins with different topology and knot depth have been investigated in simulations [214,584]. The first study focused on a protein, YibK, that embeds a deep trefoil knot [585]. It was found that a Gō potential, which is exclusively based on native interactions, was not able to knot the polypeptide chain in the time-scale employed in the simulations. A subsequent study reported a rather low, up to 2%, folding success rate [173] for the same protein, indicating that while non-native interactions may not be strictly necessary to fold a deeply knotted protein, they may be crucial to do so on a biologically relevant time-scale. Indeed, the folding success rate of YibK reached 100% when specific non-native interactions were considered in combination with the native ones. Moreover, it was found that sequence-dependent non-native interactions produced a detectable fraction of knotted structures in partially folded conformations of another deeply knotted trefoil protein, AOTCase [586], strengthening the view that they assist knotting in these cases. On the other hand, molecular simulations showed that proteins with rather shallow or medium depth of knots can self-tie when only native interactions are taken into account [587–589], and recent Monte Carlo simulations of a simple C-alpha model showed that a Gō potential is able to fold protein YibK with 100% efficiency, provided the simulation temperature is well below the folding transition temperature, i.e., in conditions that stabilize the folded state [590].

The picture emerging from *in silico* studies indicates that for proteins embedding a trefoil knot in their native structure, the knotting step proceeds through the formation of an almost native twisted loop, the knotting loop (Fig. 65**A**), which the remainder of the chain pierces (Fig. 65**B**). This step is rate-limiting and can be facilitated by the formation of an intermediate slipknot conformation (Fig. 65**C**), in which the kinked tail threads through the loop assisted by long-range native interactions [173], or pulled by non-native interactions [585]. In general, when the native twisted loop is loose in an extended conformation, the knotting step consists of a direct threading of the chain terminus that lies closer to the knotted core [585,586,591] (Fig. 65**C**). Detailed molecular simulations suggest that the conformational change from a slipknot to the fully threaded chain competes with the packing of the twisted loop. As a consequence, threading can be hindered when the twisted loop is too densely packed [214]. Knotting starting from random unfolded configurations has been observed using all-atom [592] and coarse-grained models [589,590,593]. In these cases, the native knotted structure is the most stable such that this can be considered to be driving knotting. In addition, in the case of protein MJ0366, which is the smallest knotted protein with a shallow trefoil knot, knotting has been observed from a slipknotted intermediate structure using unbiased all-atom explicit-solvent simulations [594]. In proteins with more complex topology, e.g., a protein with the 6_1 stevedore knot [216], and deeply slipknotted proteins [173,581], the knotting loop performs a *mousetrap-like* movement to establish the native knotted topology. This kind of loop-flipping movement has also been reported, albeit rarely, for MJ0366 [595].

Molecular simulation studies have also been used to study the folding and knotting mechanisms of proteins with other entanglements — lassos, links, and θ-curves — resulting from the formation of cysteine bridges (Fig. 66 and Section 2.6). The topological state of these proteins can be influenced by environmental factors, e.g., by changing the solution conditions from oxidizing (closed loop) to reducing (open loop). A considerable amount of work has been dedicated to leptin, the first protein discovered with a lasso motif in its native structure. A structure-based model indicated that folding with and without the covalently closed loop proceeds very similarly, with the polypeptide chain first adopting the lasso topology, followed by the formation of the disulfide bond. A structure-based modelling approach was also able to tie properly the chain of a more complex lasso topology, the supercoiled Pfu-542154 protein, but in this case a significant difference in

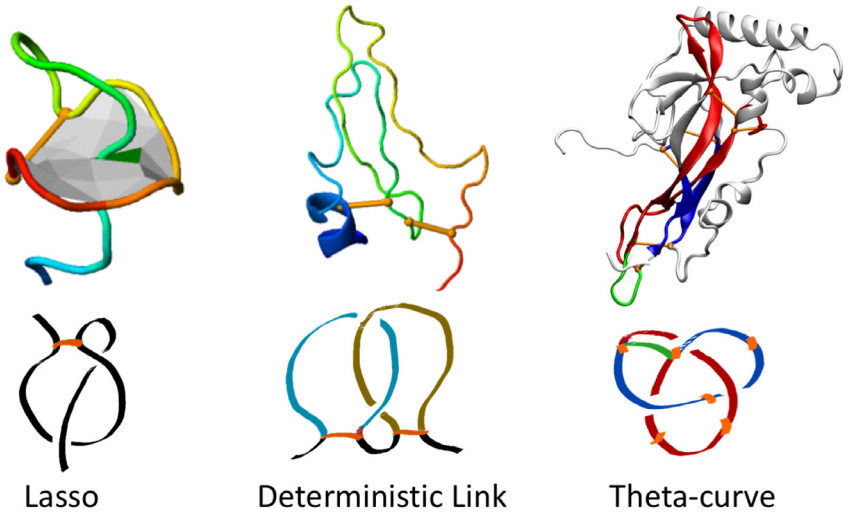

Fig. 66. Other types of entanglement in proteins: lasso (PDB id:5ZCN), link (PDB id:2LFK), knotoid (PDB id:3ONP), θ-curve (PDB id:1AOC).

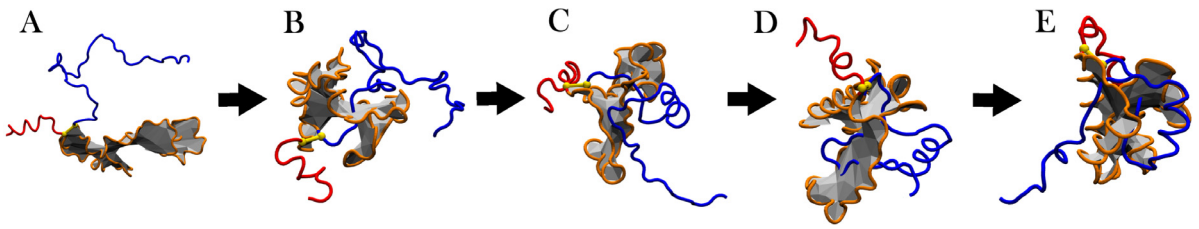

Fig. 67. Schematically presented key consecutive events characteristic for the folding process of the protein with supercoiling motif LS, Pfu-542154, observed based on a structure-based model: **A** conformation in the unfolded state, **B** first crossing of the covalent loop surface, **C** the covalent loop acquires the native-like structure, **D** slipknot-like threading of the N-terminal end through the loop, and **E** native state conformation. Tails are marked with red (N-terminus), and blue (C-terminus), the covalent loop is orange, the minimal surface spanning the covalent loop is coloured with shades of grey, cysteines forming the -S-S- bond are marked in yellow.
Source: Adapted from [596].

the folding mechanism was found under reducing and oxidizing conditions, as in the latter case the covalent loop was already closed at the beginning of the folding process [596] (Fig. 67). A protein exhibiting two lasso loops — a Hopf link (Secs 2.2.1 and 3.3.4) — the protease inhibitor TdPI, was also studied in the scope of a structure-based model [597], and the appropriate order of covalent loops closings proved critical to reach the correct fold. Finally, the free-energy landscape of a protein with a θ-curve topology, Japanese horseshoe crab coagulen, was shown to be only slightly influenced by the oxidative and reductive conditions. Independently of the latter, the native state was reached after crossing two short-lived intermediate states, each resulting from the formation of a particular subset of disulfide bonds. The examples outlined above indicate that even with simple coarse-grained models, insightful results have been obtained on the mechanism governing the folding of proteins with non-trivial topology, including those resulting from covalent loops.

6.5. Folding in vivo: chaperonin- and ribosome-assisted knotting

Although there have been no direct measurements of the folding of knotted proteins in cells, as there are many technical challenges to studying the folding of any protein *in vivo*, several *in vitro* and *in silico* studies have provided important information on the factors that might affect the folding of knotted proteins in their biological environments. The first such study was an experimental investigation of the post-translational folding of deeply knotted trefoil proteins YibK and YbeA using a cell-free translation system [579]. The cell-free system used contained only the cellular components required for transcription, where a copy of messenger RNA (mRNA) is produced from a DNA template, and translation, in which the mRNA is read by the large molecular machine, the ribosome, which synthesizes a polypeptide chain of the correct amino-acid sequence. Thus, this experimental method effectively probes the folding of proteins directly after they are synthesized by the ribosome. These experiments were crucial in establishing that these proteins could spontaneously self-tie, albeit slowly, in the absence of any other cellular factors such as molecular chaperones [579]. This approach, which enabled the addition of a specific class of purified molecular chaperone, was also crucial in demonstrating that molecular chaperones, particularly the chaperonin GroEL-GroES, can have a dramatic effect and accelerate the folding rate of at least

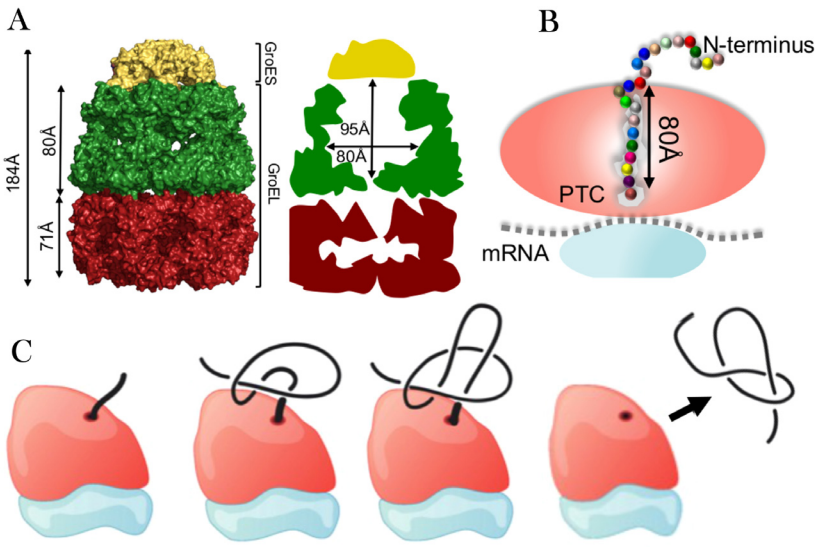

Fig. 68. Knotting *in vivo*. Three-dimensional representation of the *E. coli* chaperonin GroEL-GroES complex (PDB ID 1aon) and cross sectional view highlighting the cavity dimensions **A**, schematics of the ribosome's cross-sectional view highlighting the exit tunnel, and the peptidyl transferase centre (PTC) **B**, and ribossome-assisted knotting mechanism assisted predicted by molecular simulations **C**.
Source: **C** adapted from [214].

one class of deeply knotted proteins by at least an order of magnitude. In addition, GroEL-GroES was found to have no effect on the folding rate of denatured, yet knotted, conformations, providing further evidence that the chaperonins act on the knotting step, or another step closely associated with it [579].

Although these experimental studies provided the initial evidence that chaperonins might play an important role in the folding of knotted proteins *in vivo*, the first studies did not provide significant insight into the mechanism of action of the chaperonin on the folding pathway. A follow-up experimental study, using N- and C-terminal fusions of the trefoil-knotted proteins provided additional information. The effect of GroEL-GroES was found to be dependent upon the exact nature of the fusion protein in question, thus demonstrating that, at least for this family of knotted proteins, the chaperonin machinery acts on a specific state — either stabilizing it or destabilizing it — but is unlikely to act only by simply decreasing the entropic penalty to knotting through steric confinement [598]. A computational study on the same protein had already established that this protein populates kinetic traps during folding and has to *backtrack*, i.e., partially unfold from these trapped states, in order to fold to the native state, which is therefore consistent with a mechanism in which GroEL-GroES destabilizes the kinetically trapped misfolded intermediate.

Further mechanistic insight has come from several computational studies, and to understand these some knowledge of the general mechanism of action of chaperonins is required. Chaperonins are large cylindrical complexes with a central cavity within which either unfolded or misfolded substrate proteins with up to ~600 residues are allowed to fold in isolation. The best studied chaperonin is GroEL-GroES from *E. coli* [599]. GroEL is an oligomeric cylinder formed by two heptameric rings placed one on top of the other. GroES is a smaller heptameric dome-shaped ring, which caps one end of the GroEL forming a sealed cage (Fig. 68**A**). The substrate protein binds to hydrophobic residues located in the centre of the open ring of GroEL. The binding of ATP and GroES to GroEL triggers a conformational change upon which the cavity volume nearly doubles; concomitantly, the protein is displaced into this enlarged cage, whose inner surface becomes hydrophilic and highly negatively charged. Binding of ATP and GroES to the opposite GroEL ring triggers the detachment of GroES, and the cage opens to release the protein [599].

Initial computational studies [589,600] focused exclusively on the effects of steric confinement resulting from encapsulating the protein inside a rigid cage, and investigated small systems — e.g., MJ0366, VirC2, DnDE — featuring shallow trefoil knots [589,600] through Monte Carlo [589], and molecular-dynamics [600] simulations of CG C_α models. These proteins are all two-state systems, meaning that folding and knotting are coupled transitions limited by a single free-energy barrier, unlike the deeply trefoil-knotted MTases YibK and YbeA studied experimentally. As with unknotted proteins, it was shown that steric confinement increases thermal stability measured by the melting temperature, leads to compact denatured states, and stabilizes the transition state (TS) by facilitating the formation of non-local interactions [589]. In addition, it reduces backtracking [589,600], leading to higher observed folding rates.

In addition to the results on chaperonins, which clearly establish that this cellular factor can aid the folding of knotted proteins, it has also been suggested that other factors found *in vivo* may also promote knotting. Computational studies have suggested an elegant mechanism in which the ribosome can aid in co-translational folding that occurs at the same time as the protein chain is synthesized. The ribosome is a large, complex molecular machine made of many components.

Synthesis itself, the formation of peptide bonds between amino acids, occurs at the catalytic site (PCT) located at the bottom of a deep tunnel where the nascent chain, the polypeptide chain in the process of being synthesized, remains covalently attached to the ribosome and travels along this tunnel until it emerges at the open mouth (Fig. 68**B**). After the final amino acid has been added to the chain, the chain then detaches itself and is released relatively rapidly from the ribosome [601]. Limited folding can occur in the tunnel, which is approximately wide enough to accommodate an α-helix [601].

In the first study of cotranslational folding using a C_α structured-based model of the deeply trefoil-knotted protein YibK [602] the mouth of the ribosome was represented as an infinite repulsive plate that grows the protein chain at a steady rate. The latter was selected to yield a saturation in the knotting success rate S. Within an optimal range of temperatures, the nascent conditions enable knot formation, and the best S varied between 3 and 6%. The existence of the plate proved crucial for knotting, as it forced the positioning of the planar knotting loop in a way that allows for a penetration by the threading segment. This forms a slipknot which, upon detachment, becomes the proper knot. A structurally refined plate model [603], and a variant of that model which additionally considered electrostatics-mimicking contacts at the mouth of the ribosome [604], approximately doubled the S value.

In another study, based on a simple C_α model [605], a much larger protein, Tp0624, with three domains was studied. For this system, the knotted core is in the middle domain, which makes the knot very deep, 120 residues away from the nearest terminus. The smooth funnel-like repulsive potential of the tunnel with an axial pushing force yielded S of 60% at some selected temperature primarily because of the attractive centres placed at the exit. The latter causes the protruding chain to become wrapped around the exit tunnel and to stick onto the surface. The loop thus formed is then threaded by the nascent chain that is being pushed out of the tunnel with a constant force (Fig. 68**C**).

The results obtained so far for assisted knotting *in vivo* are interesting and informative, but certainly insufficient. The results from simulations outlined above support the view that proteins can become knotted co-translationally during their synthesis by the ribosome, with a mechanism in which the latter facilitates the formation of the knotting loop such that threading proceeds strictly via slip-knotting. However, there are not yet experimental results that corroborate this theoretical prediction, and the experimental studies on the effects of GroEL-GroES on the folding of YibK and YbeA are more compatible with a mechanism that occurs post-translationally [598]. It may be that some knotted proteins fold co-translationally via the slip-knotting mechanism identified in computational studies, whilst other knotted proteins fold post-translationally and use the cellular chaperonin machinery.

6.6. Knots and pores

The existence of entangled proteins raises questions about several cellular processes in which polypeptide chains must be pushed or pulled through a small pore, i.e., translocation through mitochondrial pores or degradation by the proteasome, a large protein complex in charge of protein degradation. During these processes the chain is subject to forces that can induce a change in its topological state. In the following, we present studies which tackle the problem of translocation of knotted proteins through a narrow pore, and a possible explanation of how it is overcome in nature.

6.6.1. Translocation experiments

Notwithstanding the biological relevance of protein translocation, experiments on the translocation of knotted proteins have been attempted only recently. The first such study was carried out by San Martin et al. [202], who analysed the translocation of the trefoil-knotted protein MJ0366 by the bacterial proteasome, ClpXP, which is responsible for the degradation of intracellular proteins. It was established that MJ0366 can be translocated on its own. However, when it is fused to the green fluorescent protein, GFP, placed downstream of MJ0366, the translocation stalls. Importantly, GFP itself can be degraded by the ClpXP machinery. Results suggest that ClpXP pushes the knot off the MJ0366 protein in a downstream direction towards GFP and, at the same time, tightens it. If the tightening takes place before the knot reaches GFP, then a tight knot can be translocated and degraded by ClpXP such that GFP is also subsequently degraded. However, if the linker between MJ0366 and GFP is too short then the knot does not tighten before it reaches GFP. The interaction of a knot with GFP apparently leads to pore jamming and prevents further progress of the molecular motor. The knot in MJ0366 protein is relatively shallow. However, in another study, Sivertsson et al. [205] showed that a much deeper trefoil knot in YbeA can relatively easily be degraded by ClpXP.

The degradation of proteins hosting a more complex Gordian knot (5_2) has also been studied experimentally by Sriramoju et al. [204] using human ubiquitin C-terminal hydrolases, UCHs; the results showed a high mechanical stability protecting these proteins from degradation. The authors associated this with the presence of the 5_2 knot. In this case, this tightened knot is significantly larger than the 3_1 knot studied earlier, and it was thought that this might potentially hinder the translocation process in a more significant way. This interpretation was subsequently challenged by Sivertsson et al. [205], who carried out similar experiments on UCH-L1, tagging it for degradation at both N- and C-termini. When UCH-L1 is degraded starting from the C-terminus they found, in agreement with Sriramoju et al. [204], elevated mechanical stability. However, if degradation is initiated at the N-terminus, the protein is easily degraded, which suggests that it is not the knotted topology itself, but rather the local stability of β-sheet structures near the C-terminus that prevents degradation. This was further supported by considering a destabilizing mutation in the β-sheet structure (F165A) near the C-terminus, which was shown to accelerate significantly the ClpXP-mediated degradation when pulled from the

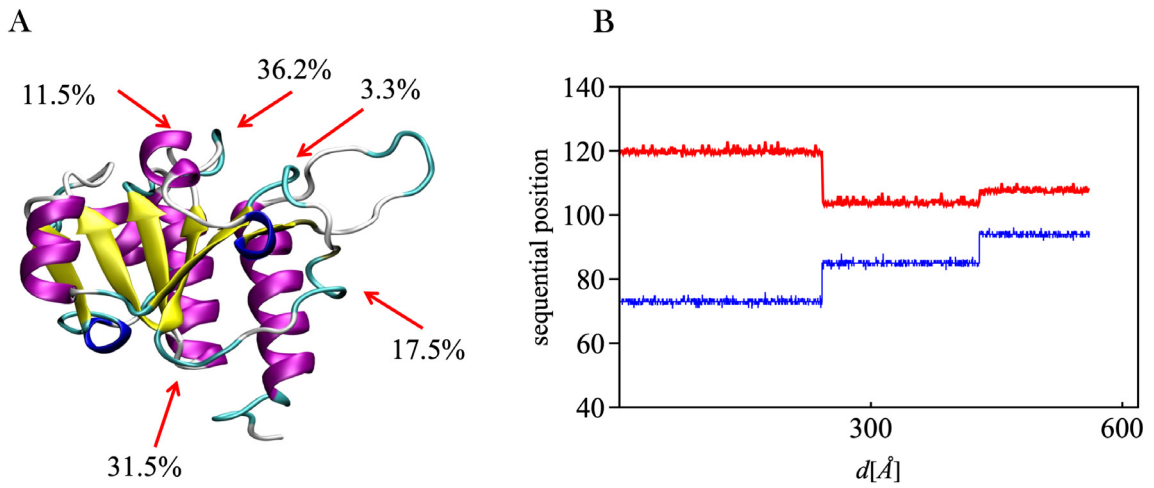

Fig. 69. **A** The protein YibK with the positions of pinning centres that arrest the movement of a knot during force-induced tightening. The numbers show percentages of situations (based on 700 trajectories) in which a knot's end is pinned at the feature after moving from the native state. **B** Motion of knot's ends during tightening of a knot in YibK.
Source: **B** adapted from [612].

C-terminus. In a subsequent paper, Sriramoju et al. [606] argued that the knotted topology might matter after all for UCH-L1. By comparing the F165A from Sivertsson et al. [205] with another unknotted mutant with a similar structure, they found that the unknotted construct was degraded twice as fast, which they attributed to a possible effect of the knot. However, this is a relatively small difference and some context is necessary. For example, single point mutations that have no effect on topology can have a much greater effect than that observed in this study. Sivertsson et al. [205] were also able to show that the bacterial degradation machinery is able to accommodate the tightened structure of a 5_2 knot, which is crucial for the debate on whether knots can indeed impair the degradation of proteins.

Recently, the translocation of the deeply trefoil-knotted proteins YibK and YibeA through nanopores of different sizes was characterized experimentally. In this case, the nanopores were between 2 to 7 nm, and the translocation behaviour was shown to depend critically upon pore size and the thermodynamic stability of the protein [607]. Unfortunately, no similar experimental data exist on the translocation of knotted proteins through mitochondrial pores, which are narrower than the smallest pores used in the study above; as such, depending on the flexibility of the pore, knotted proteins might have problems navigating it. A considerable number of simulations involving the pulling of knotted protein structures, some of them through pores, are available, providing some insight into the factors affecting such a process as well as an indication of what might be observed experimentally with smaller pores.

6.6.2. Pulling and translocation simulations

The first studies devoted to simulations of the mechanical stretching of knotted proteins were those of Ohta et al. [608], inspired by their earlier experiments on AFM-mediated unfolding of carbonic anhydrase [609]. The pulling direction was chosen so as to untie the knot, which resulted in a much lower resistance to pulling than analogous simulations in which carbonic anhydrase was pulled by its N- and C-termini, resulting in knot tightening, which was accompanied by a sharp rise in resisting force [610].

A more systematic numerical study of the pulling of a knotted protein along different directions was conducted by Sulkowska et al. [611] using a coarse-grained structure-based model. This study established that some pulling directions always resulted in untying or tightening of the knot, whereas for others the outcome was stochastic, with untying probability depending on the pulling speed and the temperature. A similar coarse-grained model was used to study the tightening dynamics of 20 different knotted proteins, paying special attention to the movement of the knot ends under the pulling force [612]. It was established that the motion of the ends along the protein backbone induced by the force is characterized by sudden jumps between pinning centres located at sharp turns in the peptide chain (Fig. 69). The jumps ceased as the knot fully tightened. Estimates of the size of the tightened knot were made in this and a follow-on study [613] and later verified by experiment (Section 6.3.5).

Pulling/stretching simulations have also been used to study the mechanical stability and unfolding of two proteins belonging to the transcarbamylase superfamily. The first protein, N-acetylornithine transcarbamylase, contains no knot, whereas the second one, human ornithine transcarbamylase, contains a trefoil knot located deep within its sequence, but is otherwise structurally nearly identical to the first (although it still differs in sequence). Numerical simulations based on a coarse-grained model show that for both pulling protocols the knotted protein exhibited a larger mechanical stability than its unknotted counterpart, suggesting that the presence of a knot has an overall stabilizing effect[591]. A similar

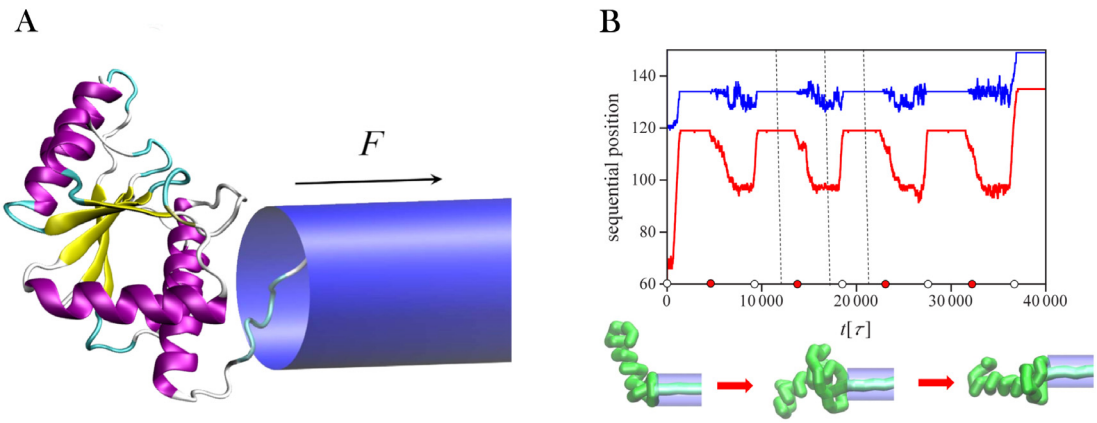

Fig. 70. **A** The protein YbeA pulled into a cylindrical pore. **B** Motion of knot's ends during translocation of YbeA under the action of repetitive force. The colours (red and blue) mark the two ends of the knot as they move along the chain. The circles on the time axis represent the moments of switching the force on (white) and off (red). The conformations below correspond to the time moments marked by the dashed lines. The knot makes several tightening-swelling cycles followed by a successful translocation.
Source: Adapted from [621].

study was performed by Xu et al. [614] using atomistic molecular-dynamics simulations. Here, the knotted/unknotted pair was formed by the protein YbeA from *E. coli* and an unknotted construct YbeA* designed by reversing one of the crossings of the backbone in such a way that the knot is removed. Again, it was found that the unknotted construct is less stable than the knotted one: it has shorter unfolding times in constant-force pulling and lower resistance forces in constant-velocity pulling.

Mechanical stretching simulations have also been applied to proteins with other entanglements, such as slipknots [615] and cysteine knots [616], as well as to multimeric units of entangled proteins [617]. In Ref. [615] the authors used a coarse-grained model to mechanically unfold thymidine kinase, which contains a slipknot motif. Two unfolding pathways were observed, one leading to the full unfolding of a slipknot and the other leading to a jammed configuration with a tightened slipknot. The force-dependent probability of each pathway depended upon the temperature as well as on the direction and value of the pulling force. In Ref. [616] cysteine motifs were analysed. Many such structures are characterized by an exceptional resistance to mechanical stretching. In Ref. [617] multimeric proteins with nontrivial topology were investigated. Stretching was used there not only to characterize the mechanical stability of the proteins but also to classify entanglement between protein pairs, by pulling on the ends of one protein while keeping the ends of the other protein fixed.

The fact that protein knots can tighten under tension brings up the question of whether such a tightened knot can get stuck during the translocation of a protein through a mitochondrial pore or the translocation pore in a cellular degradation machine, as hypothesized by Virnau et al. [552]. The experimental evidence that knots, even larger 5_2 knots, can be translocated through a narrow pore and therefore degraded has been discussed above. The first numerical study by Huang and Makarov [618] considered a rigid pore, the diameter of which was sufficiently large to accommodate two polypeptide chains at the same time. Translocation was shown to proceed through multiple slippage events, suggesting a rugged energy landscape with multiple metastable minima. The presence of a knot was found to increase considerably the translocation time, an effect increasing with knot complexity. Later studies [619–621] combined a simple model of a rigid, cylindrical pore with coarse-grained models of proteins. Using a constant force directed along the axis of the translocation channel and a pore diameter smaller than the size of the tight knot, the results were consistent with a simple, two-pathway model, with one pathway leading to the knot tightening and jamming and the other to successful translocation. The jamming probability dramatically increased as the magnitude of the driving force exceeded a critical value. Simulations have revealed that the translocation efficiency depends upon the pulling protocol [621]. Results from a simulation using a repetitive, on–off pulling force (Fig. 70), demonstrate that during the off-force period some stored length of chain becomes inserted into the knotted core, and the knot loosens, thus escaping the tightened configuration. Subsequently, during the next force-on period the protein makes another attempt at the translocation, with eventual success after sufficiently many attempts. Thus, it is possible that topological traps observed in earlier studies can be avoided. Such an intermittent pulling force is biologically relevant, since the mitochondrial import motor, like other molecular motors, transforms chemical energy into directed motions via nucleotide-hydrolysis-mediated conformational changes, which are cyclic in character.

6.7. Functional role of knotted proteins

For several decades, the potential functional roles of knots in protein structures have been speculated on and investigated through both experimental and computational studies. However, even now, the exact role of knots is

unclear. Many numerical studies have suggested that a knot can stabilize the native state of a protein with regards to its thermodynamic, kinetic, mechanical or other form of stability, e.g., against degradation [214]. Unfortunately, experimental studies have only shown that all forms of stabilities of knotted proteins are well within the range found for unknotted proteins [559]. Experimental attempts have been made to rewire a knotted protein structure such that it becomes unknotted — something that is trivial to do and has been done *in silico* — in order to make the most accurate comparison between the properties of knotted and unknotted but otherwise similar structures [553,572]. However, these have resulted in changes in structure and oligomeric state, making direct comparisons challenging. The area in which both experimental and computational studies have been most successful in determining the role of a knot in a protein is for the SPOUT class of methytransferases where the knotted structure has been shown to adopt a unique way of binding ligands [622,623].

6.7.1. The effect of a knot or entanglement on the stability of a protein

Let us provide a few highlights of such phenomena that will be discussed in more detail below, and can be found in a recent review [214]. The influence of entanglement on protein stability is not fully understood, in part due to the lack of unknotted counterparts of knotted and entangled proteins occurring naturally and/or that can be engineered for experimental investigation [559]. However, this is not an obstacle in theoretical studies where it is straightforward to create similar knotted and unknotted protein structures *in silico* for comparison. As well as the computational studies already described above, there are further examples. Based on the smallest protein with a Hopf link topology [624] it was possible to design an unknotted counterpart with the same fold and almost the same number of native contacts. It was found that the Hopf link structure has an unfolding energy barrier over 20% higher than the topologically trivial structure, consistent with other studies on knotted and unknotted members of the transcarbamylases [591]. However, simulations of lattice models of proteins have shown that the presence of knots does not increase thermal stability when compared to their unknotted counterparts [583,625]. In this case, enhanced kinetic stability (lower unfolding rates) of knotted structures was reported. Other experimental and computational studies on the stability of knotted proteins under force have been described above. Again, whereas theoretical studies have suggested that knotted topologies may be more resistant to mechanical unfolding [626], experimental studies have shown that the knotted proteins investigated to date lie well within the stabilities measured for unknotted proteins [569].

6.7.2. Examples of biological roles of entanglement in proteins

The influence of topology on biological function, although not easy to study, has been also investigated in enzymes. For these systems, entanglement may be helpful in shaping their active sites [212,627] or introducing additional structural rigidity [212,583], which may be crucial for carrying out enzymatic reactions [622,623]. Proteins from the SPOUT family have been studied extensively to unveil the role of entanglement in the catalytic activity of these enzymes. The SpoU-TrmD (SPOUT) enzyme family has a trefoil-knot fold in the catalytic domain that catalyses methyl transfer to RNA molecules [628]. The use of a topologically complex fold in the catalytic domain is unusual, because the majority of methyl transferases use the simpler open-sandwich structure of the Rossmann fold for catalysis. Even though the SPOUT proteins can differ significantly in terms of their sequence, the structure of the knot is strictly conserved [629]. Although SPOUT enzymes recognize different substrates and perform different types of methyl transfer reactions, the knotted region and its binding of AdoMet are similarly conserved. An examplary enzyme of the SPOUT family is the bacterial TrmD, which catalyses methyl transfer from AdoMet, a cofactor, to the N^1 position on a nucleotide in tRNA; and it is an essential enzyme. TrmD is an obligate dimer, where the two monomers, despite having the same amino-acid sequence, are functionally asymmetric with each other and only one monomer is active at a given time. Upon tRNA binding to one active site, the knot aligns the N^1 position on the tRNA substrate with the methyl donor of AdoMet to create the *ON* state of the monomer for methyl transfer. In this *ON* state, the conformation of AdoMet is in a bent shape that is accommodated by the knot. In contrast, the knot in the other monomer is switched to the *OFF* state, where AdoMet is bound in an inactive open conformation. This structural difference between the two knotted regions provides the basis for the *half-of-the-sites* mechanism of catalysis. It suggests propagation of the AdoMet binding signal from one monomer to the other to regulate catalysis. Free-energy calculations demonstrate that the substitution of a single amino acid (Y115A) within the knotted region is capable of breaking the communication between the two monomers. While this substitution creates a structural symmetry between the two monomers, the dimer is catalytically inactive [622].

TrmD is ranked as a high-priority antibacterial target [630], due to its fundamental structural and mechanistic distinction from the Rossman-fold-possessing human counterpart Trm5, which is conserved in the eukaryotic/archaeal domain. Additionally, inactivation of TrmD sensitizes bacteria to multiple antibiotics [631], further emphasizing the prominance of TrmD as an antibacterial target. Among many structural and mechanistic differences between bacterial TrmD and human Trm5, the knot in TrmD is a particularly promising feature for antibiotic research. Specifically, TrmD binds AdoMet in the unusual bent conformation [632] that is required for methyl transfer [622], whereas Trm5 and most methyl transferases bind AdoMet in the open conformation [622]. The bent conformation of AdoMet in TrmD is unique [633] and offers novel chemical space and diversity for antibiotic discovery.

Most eukaryotic counterparts of the SPOUT family in bacteria are largely unknotted with the exception of a knotted SPOUT enzyme, which is found in higher eukaryotes. This interspersed distribution of SPOUT enzymes in bacteria versus non-SPOUT enzymes in eukaryotes opens the door for drug targeting of the bacterial enzymes. In contrast, two SPOUT enzymes are conserved with the knot-fold throughout evolution, which are represented by TrmH and Trm10, although Trm10 is absent from bacteria. The preservation of the SPOUT knot-fold in these two enzymes across the evolutionary time-scale emphasizes a strong selective pressure for it to maintain cell fitness. Further research is necessary to understand the molecular basis for the evolutionary choice to replace or to preserve a SPOUT knot-fold from bacteria to humans.

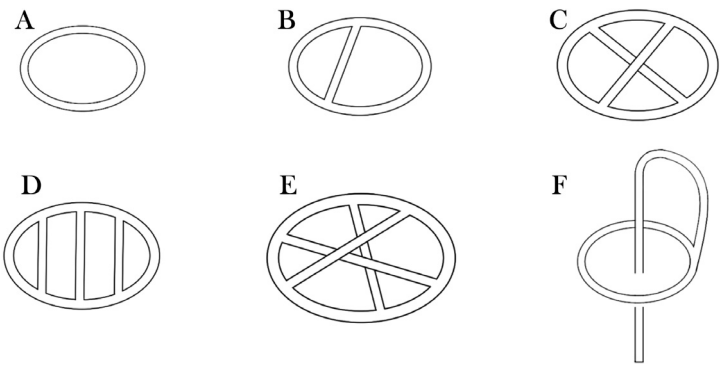

Fig. 71. Topologies of various classes of naturally occurring peptides. **A** Plant-derived orbitides (usually comprising nine amino acids) and bacterial bacteriocins (50–70 amino acids in size). **B** PawS-derived peptides exemplified by trypsin inhibitor 1 (SFTI-1), a 14 amino acid peptide from sunflower seeds. **C** Cyclized conotoxins. **D** θ-defensins. **E** Cyclotides. **F** Lasso peptides exemplified by microcin j25.

6.8. Pharmacological applications of tangled proteins and peptides

Peptides present several pharmacological advantages over traditional small-molecule drugs, including their ability to target pharmacological receptors with high potency and specificity [634]. These features can result in greater efficacy and fewer side effects. However, one of the disadvantages of linear peptides is their lack of stability and oral bioavailability, and so drug designers have turned to cyclic or topologically complex peptides, which typically show enhanced stability and specificity over linear peptides. Such peptides may come from natural sources or be synthetically designed [635]. Here, we focus on naturally occurring ones.

Fig. 71 shows six classes of topologically complex, i.e., nonlinear, peptides that have attracted attention as scaffolds in drug design. Five of the classes comprise naturally occurring peptides from bacteria, plants and animals that fall into the category of ribosomally synthesized and post-translationally modified peptides, commonly referred to as RiPPs [636]. They are biosynthetically assembled on the ribosome as conventional linear chains of amino acids and their topological complexity is introduced by post-translational processing such as cyclization or disulfide bond formation (cross linking). The sixth example, comprising cyclic conotoxins [637] and cyclic gomesins [638] (Fig. 71**C**), are naturally occurring peptides from marine snails and spiders, respectively, that have been synthetically cyclized by the addition of a short amino-acid linker between the termini of their parent linear peptides.

In their host organisms, these peptides typically have a role in defence against pests or pathogens, but aside from that natural function have been employed as drug leads for a diverse range of applications, including anti-microbial, insecticidal, and anti-cancer applications [639]. The simplest of the molecules have a circular topology (Fig. 71**A**) and include the orbitides [640] and the bacteriocins [641]. The PawS-derived peptides [642] (PDPs, Fig. 71**B**) contain a single disulfide bond in addition to having a head-to-tail cyclic backbone. The next most complex molecule shown in Fig. 71**C** is a synthetically cyclized conotoxin exemplified by Vc1.1, a 16-amino-acid naturally occurring peptide that was cyclized using a 6-amino-acid link to improve its stability and engender it with oral activity [643]. The θ-defensin shown in Fig. 71**D**, exemplified by RTD-1, comprises a cyclic backbone of around 18 amino acids including six cystine residues having a laddered arrangement of three disulfide bonds. This topology has been referred to as a cystine ladder [644]. The most complex framework is that of the cyclotides (Fig. 71**E**), which comprise around 30 amino acids including six cysteine residues connected in a cystine knot motif involving two disulfide bonds and their connecting backbone segments. The cyclic backbone and cystine knot are together referred to as a cyclic cystine knot [645], which is responsible for the exceptional stability of these molecules to proteolysis or thermal breakdown. Finally, the lasso peptides exemplified in Fig. 71**E** by microcin J25 comprise approximately 21 amino acids with a lasso-like structure brought about by a sidechain-to-backbone linkage forming a ring linking residues 1 and 8 that is threaded by the C-terminal tail. This molecular lasso does not readily unthread because the tail contains bulky amino acid side chains on either side of the ring that act as stoppers to prevent slippage. While several of these peptides have been proposed as drug leads themselves, a larger range of applications will probably come from their use as scaffolds onto which new amino-acid sequences can be inserted to introduce new therapeutic functionalities; a process referred to as grafting [645]. The popularity of molecular grafting [646] highlights the underpinning principle that topological complexity can introduce stability and overcome some of the deficiencies of linear peptides.

Proteins with a lasso topology (PLTs) are worth further mention. These are structures where the threading of the protein chain through a covalent loop formed by a disulfide bond [258,647] creates the native, active structure. PLTs are known to be involved in a number of human disorders such as obesity, cancer and neurodegeneration. The PLT leptin, associated with obesity, has been extensively studied [647,648] and it is known that breaking the disulfide bond in leptin decreases both its stability and biological activity [649], an effect attributed to an increase in conformational dynamics [647,648,650–652]. This work has led to the hypothesis that PLTs may act as molecular switches *in vivo*, i.e., the biological activity can

be switched on or off by the chemical environment, the redox potential in a cell. This is controlled by thioredoxin proteins (TXN) and the tripeptide glutathione (GSH), and it is well established that unhealthy conditions, such as inflammation and oxidative stress, may lead to a dysregulation of reactive oxygen species and the cellular redox environment. Since its discovery, more than 600 proteins with a disulfide-linked PLT have been found in nature [652,653] including in immune system proteins, cell-signalling proteins, bacterial proteins, toxins and viral proteins. For example, they are found within the cytokine protein family, in interleukins and chemokines, which play important roles in inflammation and oxidative stress. It has been suggested that the threaded topology of a PLT may block access to species which could otherwise break the disulfide bond, or inhibit degradation by proteases, thus potentially protecting proteins from proteasomal degradation [652]. However, further work is needed in this area to verify these hypotheses.

6.9. Design of knotted proteins

Until very recently, we have known of four classes of knotted proteins: those that adopt 3_1, 4_1, 5_2 and 6_1 knots in their polypeptide backbone chains, for all of which there are high-resolution structures. Recently, however, the structure of a tandem $3_1\#3_1$ knot has been solved and the structure deposited in the PDB (pdb code: 8BIN), demonstrating that a single polypeptide chain can thread multiple times to achieve a complex knotted state [654]. In addition to this, recently two papers have been published that have searched for novel knotted structures within the huge database of predicted protein structures created by the machine-learning algorithm AlphaFold 2.0 [655,656]. Both studies identified new knotted structures, particularly those with more complex topologies necessitating more challenging folding pathways. In the first case, Yeates, Virnau and coworkers highlighted proteins with possible 5_1 and 7_1 knotted structures [655], whilst Sulkowska and coworkers identified a human protein with a potential 6_3 topology [656]. Very recently, the structure of the 7_1 knot has been confirmed experimentally[657]; however, the other structures have yet to be verified but, if they exist, they show that the knotted protein world is larger and more diverse than we thought. However, caution is needed as, although AlphaFold 2.0 has been extremely successful in predicting many structures, knotted and otherwise, topologically complex structures may sometimes prove too challenging for it at the current time. This is illustrated by recent work by Bradley, Stoddard and coworkers who have designed *de novo* several novel knotted protein structures. In one case, where both the design and AlphaFold predict a 5_1-knotted topology, a 3_1 topology is observed experimentally [658]. Here, it may be possible that the design and AlphaFold consider the stability of the native folded structure but not the kinetic accessibility of this structure [658]. In addition, another recent paper has suggested that AlphaFold is blind to topological barriers, which affects its ability to correctly predict protein topology [659]. Clearly, there is still much to understand about the folding of these types of proteins.

The *de novo* design of knotted protein structures is still in its infancy and it is interesting to compare what has been achieved with proteins with what has been accomplished using synthetic chemistry. In the latter, considerable steps have been taken towards producing an array of knotted molecules using metal coordination and helically shaped ligands, even complex knots such as a 7_4 knot [660] and a knot with 12 crossings [585,661]. However, much less progress has been made with respect to designing novel knotted proteins. The most notable work has been using an approach pioneered by Yeates and coworkers, who created a new 3_1-knotted protein by linking the C- and N-termini within a highly symmetrical, but unknotted homodimer which had a specific geometry [600]. The central hypothesis of this work was that the duplication of domains in nature often forms knotted proteins. More recently Bradley, Stoddard and co-workers used a *de novo* design strategy and circular tandem repeat proteins to create several novel 3_1-knotted structures [658]. Despite these two studies, the rational design of knotted protein structures, particularly those with more complex topologies, remains a challenge.

Computational investigations may well play a key role in aiding the design of novel knotted protein structures in the future. Such approaches have already shown that self-assembly of helical templates, mimicking the helical ligands used in topological synthetic chemistry, reproduce a mixture of different knots including more complex ones [662,663]. Given the chemical heterogeneity of the 20 naturally occurring amino-acid building blocks, an enormous variety of sequence combinations is available to design a knotted protein. For this, computational studies using simpler building blocks, which still capture the features of amino acids, such as patchy polymers [664–666] are proving useful. In this approach, chains composed of different monomers are characterized by the presence of patches on their surface, which guarantees a directional interaction akin to hydrogen bonding in proteins. Monomer pairs interact not only via this short-range directional interaction but also through an alphabet of different isotropic attractions and repulsions. Computational studies have shown that patchy polymers can fold precisely into a variety of three-dimensional structures, including knotted structures, dictated by the heteropolymer sequence along the chain [664–666]. In one case, it was shown that a knotted structure externally locked by controlling the end monomers' interaction is stabilized with respect to thermal unfolding [665].

6.10. Methods used to study knotted proteins

We provide here lists of the experimental and numerical methods that have been used to study proteins with non-trivial topology.

6.10.1. Experimental methods

The following methods have been used to study proteins with non-trivial topology through experiments *in vitro*.

Chemical denaturation. A reversible process that uses chemical agents such as urea or guanidinium chloride, GdmCl to denature a protein. It is often used to measure thermodynamic stability, i.e., the free energy difference between native, intermediate, when present, and denatured states.

Thermal denaturation and differential scanning calorimetry (DSC). Uses heat to denature the protein. The process may be irreversible. By increasing the temperature in DSC, the difference in the heat capacity between sample and reference cells is recorded. The melting temperature, T_m, is the one for which the heat capacity (C_p) peaks. It records the energetic profile of unfolding directly in terms of the amount of energy transferred as heat that is necessary to denature a protein. Can be used to calculate the enthalpy and entropy change on unfolding at the T_m. May be irreversible if aggregation occurs. In that case accurate values for thermodynamic stability cannot be measured, and only apparent values of T_m are reported.

Fluorescence spectroscopy. Used to monitor protein folding and unfolding. The wavelength of the maximum fluorescence intensity (λ_{max}) for hydrophobic residues Trp (tryptophan) and Tyr (tyrosine) depends on their degree of exposure to the solvent. When buried within a protein core (as in the native state) there will be a large shift in (λ_{max}) compared to when they are exposed to the solvent (in intermediate or denatured states).

Far-UV circular dichroism (far-UV CD). Used commonly to rapidly evaluate the secondary structural content. CD is defined as the unequal absorption of left-handed and right-handed circularly polarized light by an optically active molecule. In proteins, the most commonly used chromophore is the peptide bond, whose CD signal depends critically on its secondary structure.

Hydrogen deuterium exchange (HDX). Powerful tool to study protein dynamics. The rate of hydrogen-to-deuterium exchange of the amide hydrogen on the backbone with the deuterated solvent D_2O provides information on solvent accessibility, hydrogen bonding, as well as local and global stability. Used in conjunction with NMR or mass spectrometry.

Nuclear magnetic resonance (NMR). Powerful tool to study protein dynamics and determine the three-dimensional structure with atomic resolution. NMR signals report on the variety of chemical environments experienced by nuclei in proteins through unique spectral signatures.

Atomic force microscopy (AFM) and optical tweezers (OT). AFM is a non-optical technique that allows accurate measurements of the mechanical properties of a single protein molecule with very high resolution. The protein of interest is attached to a surface and a cantilever tip. For optical tweezers, the protein of interest is covalently linked to two DNA handles, which are attached to polystyrene or silica beads held in laser traps. These techniques can be used to measure the force required to unfold the protein from different attachment points as well as the size of tightened knots.

Protein engineering. A technique that perturbs the sequence by introducing a single or multiple point mutations that are generally designed such that they do not disrupt the native structure and allow the role played by specific amino acids in the folding and knotting processes to be determined. Other modifications enabled by protein engineering include the introduction of fluorescent probes or handles to allow the employment of biophysical techniques (e.g., AFM and OT), as well as the fusion of a knotted protein with another protein.

Cell-free protein expression. A technique that allows the rapid expression of small amounts of native, functional proteins using the biological machinery, namely the ribosome. It can include the total cell extract, along with an energy source, supply of amino acids, cofactors as Mg^{2+}, and the gene coding the desired protein in a cell-free-translation system, that is, in the absence of living cells. Alternatively, a minimal system which consists of purified components of the transcription and translation machinery is employed. This has the advantage that no other cellular proteins, e.g chaperones, are present.

6.10.2. Computational methods

The following methods have been used to study proteins with non-trivial topology in the context of molecular simulation.

All-atom models. Proteins are represented by all their atoms, including hydrogen atoms. The most detailed representation of the system includes also all-atom representation of the surrounding environment: water, ions, lipid bilayer, etc. Possible simplifications of these models include implicit treatment of the environment (implicit solvent models).

Coarse-grained models. Neighbouring heavy atoms of simulated proteins are grouped and replaced by effective beads. The level of coarse-graining may depend on the problem under consideration and usually may vary between up to seven beads (as in the PRIMO force field [667]), through three united atoms per residue (in the UNRES force field [668]), to one bead per residue (in the SMOG force field [669]). The solvent is often represented implicitly, but in some models it is treated explicitly (e.g., four water molecules forming an effective solvent bead in the MARTINI force field [670]). In coarse-grained models the force-field can be physics-based or knowledge-based. Conformational space can be continuous or discrete (beads are placed in the vertices of a regular lattice). The advantage of simple models is that they allow to study thermodynamics transitions or comprehensive kinetics for larger or topologically more complex proteins.

Physics-based models. The force field is based on physico-chemical properties of atoms (charge, polarization, volume, …) represented by these beads. Examples of such models are: PRIMO, PaLaCe [671], UNRES and MARTINI.

Knowledge-based models. Force field is based on statistical potentials derived from structural data provided in the Protein Data Bank. CABS [672] is an example of a model in this category, which has been successfully applied in structure prediction, protein folding, and molecular docking.

Structure-based models. Energy function depends explicitly on experimentally determined protein structure. In the particular case of Gō or Gō-like models attractive non-bonded interactions between two beads not adjacent along the chain are taken into account only when they interact in the predefined native structure. These models can be used both with the all-atom or with a coarse-grained description of the system and they are used, in particular, for large systems where the study of the unbiased system would be unfeasible.

Elastic network model (ENMs). Effective beads form a network connected by elastic springs allowing only for harmonic fluctuations of the investigated system. These models can be used in coarse-grained systems (e.g. one bead per amino acid), as well as in systems represented by all heavy atoms.

Molecular dynamics. Simulates atomic motions by integrating Newtonian equations of motion using simple approximations in order to reduce computational complexity. As a result one gets trajectory describing time evolution of an investigated system.

Monte Carlo simulations. Random changes of positions of the simulated structures (atoms, molecules, etc.) generate new conformations and allow for an exploration of the configurational phase space of an investigated system. Using these methods one can calculate thermodynamic properties of studied systems.

Explicit solvent simulations. The solvent in which a protein system is immersed, including water, ions, lipid bilayers, other small molecules like cholesterol, etc., is simulated using all-atom representation. The approach in which the environment is introduced indirectly, by taking into account only average interactions between the solvent and the protein system, is called implicit solvent.

6.11. Outlook on entangled proteins

Nearly twenty years on from the first experimental and computational studies on knotted proteins, it is interesting to look back and reflect on how far we have come and what we now know about this intriguing class of proteins. The scientific community has been highly successful in developing numerous computational methods to detect and characterize knots in proteins and these approaches have recently been extended to other types of entangled protein structures. The number of proteins showing different topological features has grown and been extended and now includes examples of 3_1, 4_1, 5_2, 6_1 and 7_1 knots, slip-knots and knots created by covalent disulfide bonds. Most recently, the determination of a naturally occurring protein structure with two 3_1 knots in tandem, demonstrated that, at least for this structure, the protein chain can undergo two threading events. This structure highlights the fact that more complex structures such as those predicted by AlphaFold may well exist (see next paragraph). Indeed, the general level of entanglement in nature has begun to be much more appreciated by many different scientific communities.

Excellent databases now exist that catalogue and classify a range of knotted protein structures providing the community with an invaluable resource. These databases have recently been added to, with more knotted protein structures predicted by the machine-learning algorithm AlphaFold. The results of AlphaFold are exciting as they suggest that there may be more complex knotted structures in nature than we ever thought possible; recently one of the predicted structures, a 7_1 knot, was verified experimentally. However, it is now clear, at least in one case, that AlphaFold does not always predict knotted protein structures correctly. This means it is still essential to verify the novel 5_1 and 6_3 knots knotted topologies predicted by AlphaFold experimentally. If they exist, then this greatly increases the level of complexity of knotted proteins, and generates numerous questions on how such structures have evolved and how they fold.

Over the past 20 years, we have also established some of the evolutionary pathways by which several knotted protein structures are likely to have evolved. In one case, these results have been used to design a novel 3_1 knotted structure that does not exist in nature, providing further evidence that this is probably one route by which nature has evolved such complex structures. In other cases, although there exists convincing evidence from phylogenetic analysis of knotted and unknotted protein sequences, the putative mechanism — insertion of a knot-promoting loop — has yet to be demonstrated by experimentalists.

Major advances brought about by both experimental and computational work have been in understanding how these complex structures knot and fold. In particular, simulations have shown that a number of different folding pathways can be adopted, involving the formation of twisted loops and slipknots, which combined with threading events and loop flipping/mousetrap mechanisms can, in some cases, efficiently lead to the native knotted structure. In addition to these mechanisms, experimental studies have established that molecular chaperones, a large and diverse class of proteins that aid in the folding and maturation of proteins in cells, can significantly accelerate the folding of a class of knotted proteins. Together with a novel mechanism, in which the ribosome, the cellular protein synthesis machine, plays an active role in threading the protein chain through a loop stabilized by interactions with it, this suggests that many knotted proteins do not have any difficulty in folding *in vivo* as we once thought likely. If knotted proteins can and do fold efficiently *in vivo* then this raises issues on whether there have been any evolutionary pressures selecting against them.

Despite significant progress in many areas, there remain some major challenges in the field. Perhaps the most significant has been to establish whether there are any features and properties, unique to knotted protein structures, that provide some advantage over unknotted counterparts. With respect to this question, the jury is still out. Whereas computational studies have suggested that the thermodynamic, kinetic and mechanical stabilities, along with the ability of these structures to withstand degradation by cellular machines, of knotted proteins is greater than unknotted ones, there remains considerable experimental evidence that many knotted protein structures are not that stable in all these respects. The experimental evidence, in particular, has highlighted the vast diversity of properties that knotted proteins have. In many cases, it has been shown that thermodynamic and kinetic parameters associated with the stability and folding of this class of protein vary by up to seven orders of magnitude, making any conclusion about generic properties impossible. Nevertheless, there is one excellent example where the role of the knot in a trefoil-knotted protein is well established, and this is in the case of the SPOUT family of knotted methyltransferases where it has been demonstrated that the knotted structure binds substrate and cofactors in a different manner to that of unknotted proteins with a similar function. This raises the issue more broadly of why it has been so hard to establish the role, or roles, of the knot in other systems.

One of the limitations faced by the experimental community has been in engineering unknotted counterparts of knotted proteins that adopt a similar overall secondary, tertiary and quaternary structure but which are unknotted. In the two cases that have been reported, the engineered unknotted proteins fold to a different structure, making a comparative analysis of properties challenging. This is not an insurmountable problem, and such unknotted controls are likely to be generated at some point in the near future in order to address some of the remaining fundamental questions. The other limiting factor is that the number of knotted proteins that have been studied experimentally is still rather small. Assuming that there are any unique properties common to all knotted proteins may well be naïve, and knotted proteins may exist for multiple reasons. Certainly, the general behaviour of shallow-knotted proteins, where only a small amount of chain has to pass through the loop to form the knot, is different from deeply knotted proteins. More knotted proteins need to be studied, along with their unknotted counterparts, before we can truly establish the differences between these classes of protein and understand the role that entanglement and topology plays.

Compared to other areas in which molecular knots have been studied and designed, the design of knotted proteins remains some way behind. Using evolutionary approaches to engineer knots into proteins has been successful, but only in a single case. Very recently, the first example of a *de novo* designed knotted protein was published, providing evidence that it should be possible in the future to create from scratch knotted proteins with different topologies. In this respect, computational approaches using simple model systems to understand the rules governing knot formation in polymers are likely to greatly aid the design process. In conclusion, although we have made significant progress towards understanding these intriguing structures, much remains to be known. Both existing and novel computational and experimental approaches are required for us to address all the questions such that we can rationally design and manipulate the structures and properties of knotted and other entangled proteins to suit our purposes. Only then will it be possible to utilize our knowledge of these systems for a myriad of different purposes.

7. Topologically complex fluids

In Section 3, we presented the prime examples of continuum materials, where the nontrivial topology of fields leads to topologically protected states with distinct topological invariants, and to discrete objects that can be knotted or linked much like twine in the macro-world, or like polymers, proteins or DNA at the nanoscale. However, there are systems that deserve special mention, either due to particular material characteristics, such as extreme chirality in blue phases, the existence of specific geometric constraints, such as in droplet or shell-confined materials, or to activity found in artificial active matter and biological systems. We dedicate this section to them.

7.1. Blue phases in bulk, in thin layers and as hosts of colloidal dispersions

A long-known type of sophisticated ordering is seen in blue phases (BPs), chiral nematic material in which neighbouring molecules preferentially pack at a finite angle with respect to each other, like fusilli pasta. For many years, BPs were seen merely as a curiosity because they were stable only within a very narrow temperature window, say $\sim$1 K, but in 2005 one of them was discovered in a new type of liquid-crystalline material across a range of over 40 K [673]. This reinvigorated the interest in these structures, and in their applications.

BPs are a prime natural example of a topological soft material where the delicate balance of deformation modes characteristic of the anisotropic elasticity of highly chiral nematic liquid crystals leads to complex fluids with the order-parameter field characterized by 3D lattices of double twisted cylinders (DTs) interspaced by disclination lines [674,675]. DTs resemble skyrmions, discussed in Section 2.8.1, and could be called "quarter skyrmions", as they exhibit only a 45° twist of the director when progressing from the centre to the boundary along radial directions, rather than a full 180° [349]. The bulk structures of BPI and BPII phases are illustrated in Fig. 72. As the stability of these natural materials is limited to a very narrow range [676,677], interest in them remained limited until the discovery of complex molecules [673,678] and polymer stabilization [679] allowing for a broad temperature range of stability opened the door for potential applications [680,681]. Here, we focus on constrained BPs where the presence of colloidal particles or confinement to thin layers restrict the available space and impose particular boundary conditions.

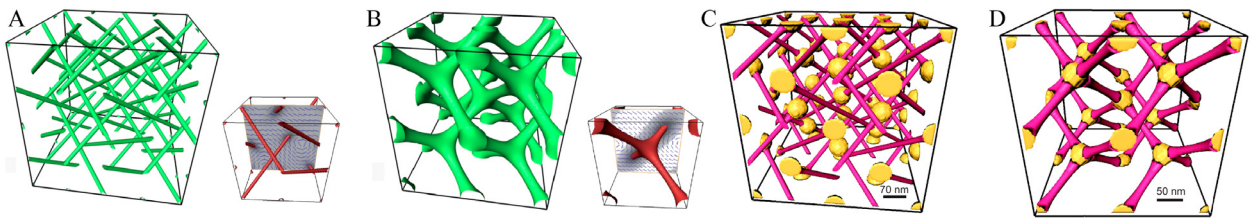

Fig. 72. Arrays of disclination lines in **A** blue phase I (BP I) and **B** blue phase II (BP II). Disclinations are visualized as iso-surfaces of degree of order $S = 0.3$ in BP I and $S = 0.17$ in BP II. Boxes constituted of $2 \times 2 \times 2$ unit cells are shown (one unit cell length is 360 nm in BP I and 680 nm in BP II). Insets show the corresponding conventional unit cells. In the insets the projection of the director on the given plane is shown. Note the hyperbolic director pattern around the defects characteristic of $-1/2$ disclination lines. Circular director fields characterize arrays of double twist cylinders. **C,D** Three-dimensional BP colloidal crystals (particles in yellow). **C** Energetically favourable FCC colloidal crystal, 4 particles per unit cell in BP I, **D** the most energetically favourable BCC colloidal crystal with 2 particles per unit cell in BP II, In BP I, disclination lines are drawn as isosurfaces of degree of order $S = 0.23$ ($S_{\text{bulk}} = 0.40$), particle radius is $r = 70$ nm. In BP II, disclination lines are visualized as isosurfaces of $S = 0.1$ ($S_{\text{bulk}} = 0.26$), $r = 50$ nm. In all cases $2 \times 2 \times 2$ unit cells have been shown better to illustrate the structure.
Source: **C,D** reproduced from [682].

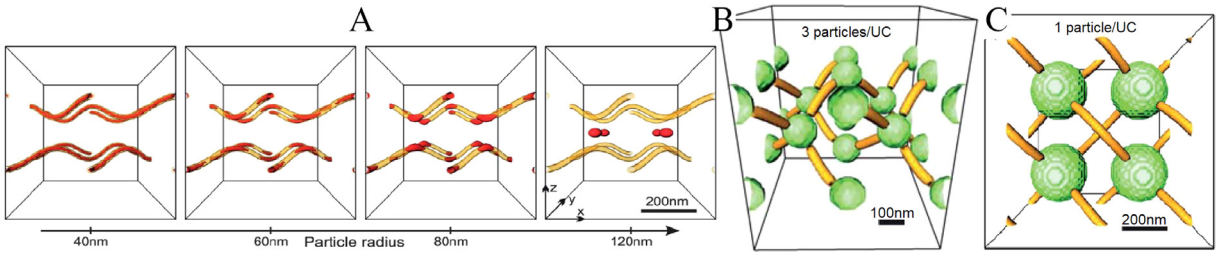

Fig. 73. Trapping of colloidal particles in BP confined to a thin layer. **A** Minima of the trapping potential (in red) for various colloidal particle sizes. All panels show 2×2 unit cells and disclination lines are drawn in yellow as isosurfaces of $S = 0.2$. **B** Side view of stable colloidal structure with medium-sized particles in green ($r = 60$ nm) in the undulating disclination structure with 3 particles per unit cell. **C** Top view of stable colloidal structure of large particles ($r = 120$ nm). Particles act as linkers for originally disconnected disclination lines.
Source: Reproduced from [686].

Trapping of the colloidal particles in disclination lines [683–685] is based on the principle that the free energy is reduced the most if the colloidal particles migrate into the defects, where the free-energy density is the highest due to the local melting of the liquid crystal to the isotropic phase. If anchoring on the particles is weak, sitting on the line is certainly the most favourable. For strong anchoring, sitting on the line is still favourable for small particles, but for large particles that more strongly perturb the neighbourhood director, this is not so evident. Therefore, the effects of particle size and surface anchoring properties were studied as main material tunability parameters [682]. Two specific roles of particles were identified: colloidal particles with weak surface anchoring increase the thermodynamic stability of BPs; larger particles and stronger surface anchoring give stronger binding of particles to the trapping sites in BPs. However, both the size of particles and surface anchoring affect the 3D profile of the trapping sites, which can change the relative metastability of various possible particle lattices. In a wider context, these results suggest a way to assemble complex 3D optical structures and their possible application in photonics and plasmonics. The small differences between different distributions in the case of a limited number of particles prevent the creation of a perfect 3D photonic crystal based on particle decorated BPs.

The situation is simpler in BPs confined to thin layers that are still thicker than the pitch. The thin geometry offers the possibly of laser-tweezer-assisted assembly. For a certain layer thickness [344,686,687] two orthogonal undulating layers of $-1/2$ disclination lines are stable. In Fig. 73 the optimal particle trapping positions are shown for selected particle radii, and two particle sizes and two numbers of particles per unit cell are illustrated. If the nanoparticles are too small — having radius of a few nm or smaller — the coupling becomes too weak compared to kT [685]. For additional possibilities, non-spherical nanoparticles can be used [688].

The possibility of producing skyrmions in monolayers of chiral magnets [689] stimulated the search for similar structures in highly confined BPs. Contrary to the above case, where DTs are still well defined and planar, in very thin layers the twist increases to 90° forming half skyrmions, called *merons*, with axes orthogonal to confining surfaces. The structure formation is driven by a free energy similar in form to that of the Frank model when all elastic constants are equal, or of a ferromagnet, Eq. (45)

$$f_{mag} = A|\nabla \mathbf{m}|^2 + D\mathbf{m} \cdot \nabla \times \mathbf{m},$$

$$f_{BP} = K|\nabla \mathbf{n}|^2 + Kq_0\mathbf{n} \cdot \nabla \times \mathbf{n}.$$

There is an important difference in the order parameter: magnetization $\mathbf{m}$ is a vector, whereas the director $\mathbf{n}$ has a $\mathbf{n} \rightarrow -\mathbf{n}$ symmetry. As a consequence, merons in magnetic structures can only form a square lattice, while the nematic director allows merons to form hexagonal lattices as well. Skyrmions can form both kinds of lattices in both cases. DTs, merons and skyrmions have double twist deformation while bend is more pronounced going from DTs to merons and skyrmions and consequently they are less optimal from the energy point of view. Nonetheless, in the case of very thin, subpitch, layers confined by surfaces with weak surface anchoring or degenerate planar anchoring, merons appear and form a hexagonal lattice. This was first predicted [687] and later experimentally proven [344]. In such a situation, a square lattice of merons is energetically less optimal and needs to be enforced by patterned surfaces [690]. Skyrmions and related *torons*, cholesteric solitons comprising two point defects and a double twist cylinder, appear in unwound cholesterics characterized by lower chirality in comparison to BPs [347,691].

7.2. Coupling of liquid-crystal topology with topology of other material or external fields

Liquid-crystalline materials are today used in a range of studies and applications, where the liquid-crystalline orientational fields (director, degree of order, …) become coupled to other non-liquid-crystalline fields, such as external electric or magnetic fields, or flow fields. These other non-liquid-crystalline fields can have different local order and obey different topological rules. As the nematic director has $\mathbf{n} \rightarrow -\mathbf{n}$ head–tail symmetry, whereas the electric field has full vector symmetry, this conditions different topology for the two fields. Research that links to this question includes soft-matter photonics, the role of electric charge in liquid-crystalline topological objects, and liquid-crystal microfluidics. Light has been shown to interact with the topological structure of liquid crystals, such as in q-plates [692], within the transfer of optical angular momentum in nematic droplets [693], and in liquid-crystal lasers [694]. Interaction of optical and topological solitons leading to their co-assembly has been demonstrated [695]. Topological defects in nematic electrolytes have been shown to perform as regions for local charge separation, forming charged defect cores and in some geometries even electric multilayers [696]. In nematic microfluidics, the interaction between the flow field and nematic topological defects has been shown, which can be explained at the topological level as the interaction of topological defects of different fields [697].

How do topologies of different fields mutually couple and does this lead to novel topology-conditioned phenomena? Such knowledge would open routes to control liquid-crystal topology via the topology of another field or, vice versa, to control the topology of another field with liquid-crystal topology. For example, can a knot in a liquid crystal create a knot in the light field, or can a structure of topological defects be used for the manipulation of microfluidic flow, such as with coupling to flow stagnation points? The relevance of coupling of liquid-crystalline topology with the topology of other fields will grow with the growing interdisciplinary use of liquid-crystalline materials.

7.3. Topology in liquid-crystal droplets

With the advent of liquid-crystal display technology in the 1960s, it became clear how best to employ suitably engineered confining surfaces and external fields so as to control the director structure within the flat liquid-crystalline cell constituting the display, and thus, its optical properties. On the more fundamental side, this era witnessed the development of homotopy theory as the mathematical framework best suited to the classification of topological defects [62]. In a topologically trivial sample of a nematic liquid crystal, such as flat cells constituting LC displays, defects tend to annihilate driven by the topological rules. However, once the plane-parallel geometry is replaced by a spherical confinement with a strong enough anchoring, defects can no longer be avoided for topological reasons. On the micrometre scale, such confinement is easily materialized in polymer-dispersed liquid-crystal (PDLC) films, developed in the 1980s, where nematic droplets are embedded within a polymer matrix [69,698]. By applying a suitable voltage, these films can be switched from the opaque, zero-field state where light is scattered by confinement-induced distorted nematic configurations to the translucent, field-aligned state. This prospect stimulated detailed theoretical studies of director structures within spherical cavities.

Defects can generally be nucleated and stabilized near solid boundaries, such as those provided by cell walls or dispersed particles. Yet, confining cavities with fluid boundaries, such as those found in liquid-crystalline droplets dispersed in aqueous solutions, provide extra degrees of freedom to stabilize and probe topological defects. Spherical confinement imposes restrictions on the topological charge in the droplet bulk, when the boundary conditions are homeotropic, or on the droplet surface, when the boundary conditions are planar [699]. On fluid boundaries, molecular anchoring is usually controlled by chemical additives to the continuous phase in contact with the liquid crystal. The combination of spherical confinement and strong boundary conditions typically results in geometrical frustration and the formation of topological defects. Consider a cholesteric droplet with strong homeotropic anchoring. Here the mismatch between the zero twist condition at the surface and the preferred helical order in the bulk stabilizes defects without the need for colloidal inclusions. Linked and knotted disclinations have been found in simulations of cholesteric and BP droplets [324,700]. Point defects and associated solutions in cholesteric droplets arrange into *topological molecules*, which can be observed and reconstructed in three dimensions from experimental data obtained with confocal microscopy [337]. The defects are not only based on homotopy theory, but Eliashberg and Thurston's theorem restricts which defects are compatible with a chiral environment. Higher-order chiral defects are possible, and can be classified according to singularity theory, while their breakup into elementary defects is described by unfoldings of each singularity [128].

While droplets provide an interesting platform to study topological defects, they have certain limitations stemming from the fact that the liquid crystal is bounded by a single surface, in contrast to classical flat cells where the liquid crystal is confined between two dissociated solid boundaries with independent boundary conditions. Progress in microfluidics has made possible the realization of spherical free-standing films of liquid crystal in water, so called liquid-crystal shells, which combine the advantages of both droplets and flat cells, offering a highly controlled environment to create, observe and manipulate topological defects, as explained below.

7.4. From confinement in shells to mesoscopic atoms

The last decade has seen the emergence of liquid-crystal shells as a new research area in the field of liquid crystals. They provide a powerful experimental platform in which to probe topological defects, as well as fascinating perspectives in terms of applications [701–703].

Confining a liquid crystal to the surface of a sphere inevitably entails geometrical frustration and the formation of topological defects. For nematic ordering and planar boundary conditions, the Poincaré–Hopf theorem enforces a total topological charge of $\chi = +2$, the Euler characteristic of the sphere. Among the possible defect structures allowed by the Poincaré–Hopf theorem for a spherical nematic, energy minimization predicts, in the one-elastic constant approximation, a structure with four $+1/2$ defects sitting at the vertices of a tetrahedron (Fig. 74**A**) [704]. This result, of fundamental interest, has attracted much attention because of its potential practical implications.

In a seminal paper, Nelson proposed using the predicted tetrahedral defect structure to produce colloids able to interact with a 4-fold valence, similar to the sp^3 hybridized chemical bonds associated with carbon or silicon atoms [705]. The strategy consists in coating colloidal particles with a nematic liquid-crystal shell and then attaching ligands to the four emerging defects, so that they become sticky patches [706]. The prospect of using liquid-crystal shells as mesoscopic atoms has triggered an important amount of research in the last ten years, on the experimental, numerical and theoretical fronts, aiming at controlling the defect structure of liquid-crystal shells. The interesting molecular arrangements observed in experimental liquid-crystal shells and their adaptability to external stimuli have inspired novel applications beyond Nelson's vision. Liquid-crystal shells offer promising perspectives as biochemical sensors [707], omnidirectional microlasers [708], micropumps [709], smart membranes [710], unclonable devices for secure authentication (Fig. 74**J**) [711] blueprints for nano-particle self-assembly [712], self-propelled particles (Fig. 74**K**) [713] or microcapsules for advanced textiles [714].

The first experimental liquid-crystal shells were produced by Fernández-Nieves et al. [715] using microfluidics. The shells were double emulsions [716], nematic liquid-crystal droplets containing an aqueous droplet inside, dispersed in an aqueous continuous phase (Fig. 74**C**). In these double emulsions, the liquid crystal is confined between two nested spheres, forming a spherical shell of average thickness $h = R - a$, where R and a are the radii of the outer and inner droplets respectively. The experiments were performed using 5CB (4-cyano-4'-pentylbiphenyl) as the nematic liquid crystal. Planar boundary conditions were enforced by adding a PVA (polyvinyl alcohol) to the two aqueous phases. These experimental shells displayed different types of defect structure. For small inner droplets, $a \lesssim R/2$, they showed a bipolar defect structure, similar to that observed in simple nematic droplets. For large inner droplets, $a \gtrsim R/2$, they exhibited three novel defect structures including $+1$ boojums [717] and/or $+1/2$ disclinations (Fig. 74**D–F**). Yet, because of the inherent thickness gradient of the shells, induced by buoyancy and nematic elasticity, the tetrahedral structure predicted for two-dimensional spherical nematics remained elusive. This structure was experimentally observed by López-León et al. [718] in very thin shells, $R \approx a$, obtained by osmotically swelling the inner droplet (Fig. 74**B**). The tetrahedral defect configuration was observed to coexist with bipolar and triangular defect structures, which emulate the symmetries of the hybridized sp^2 and sp orbitals of carbon, and provide exciting perspectives in terms of applications.

The molecular structures and energies of the different types of shells observed experimentally have been obtained using theory and numerical simulations, providing a full understanding of the system [719–722]. However, despite experimental efforts to functionalize the topological defects of liquid-crystal shells, to endow the shells with mechanical stability, or to bring their radii to the colloidal range [723–725], we are still far away from having a method to produce the *big atoms* envisioned by Nelson.

Besides their potential applications, liquid-crystal shells enable the stabilization and manipulation of topological defects, offering a playground to study fundamental questions on how defects interact, recombine or undergo topological transformations. The defect structure of the shells is controlled by a large palette of parameters, including shell thickness, boundary conditions, elastic constants of the liquid crystal, external fields, curvature gradients, etc. [701–703]. Combining the effects of the different parameters results in a plethora of new equilibrium configurations, whose complexity increases when increasing the degree of order of the liquid-crystal phase. Remarkable defect structures have been reported for nematic [701], cholesteric, and smectic shells [703,732]. By dynamically varying these control parameters, one can modify the energy landscape of the system and trigger transitions between different defect configurations, forcing the defects to evolve towards new states.

Osmotic swelling allows for a continuous variation of the shell average thickness and its gradient, quantified by the ratio h/R. Varying this parameter means modifying the relative weight of bulk elastic energy with respect to the other energy terms contributing to the free energy of the shell. The surface-energy term can be controlled by tuning the liquid-crystal molecular anchoring (MA) at the shell boundaries, both in terms of anchoring strength and molecular orientation. Anchoring transitions can be triggered by surfactant addition, temperature, or exposure to UV light [733–735]. Such

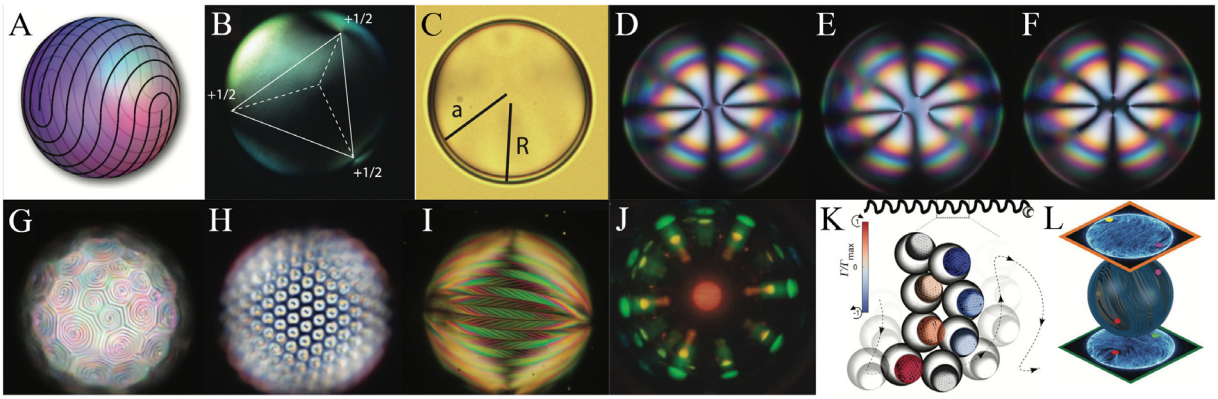

Fig. 74. **A** Two-dimensional spherical nematic with four $+1/2$ disclinations organized in a tetrahedral fashion. **B** Experimental nematic shell reproducing the tetrahedral defect structure shown in **A**. **C** Double emulsion with an inner radius a, an outer radius R, and an average thickness $h = R - a$. **D–F** Defect configurations in nematic shells with planar anchoring and thickness heterogeneity: **D** bivalent configuration with two pairs of $+1$ boojums on each spherical boundary, **E** trivalent configuration with a $+1$ boojum on each spherical boundary and two $+1/2$ disclinations that span the shell, and **F** tetravalent configuration with four $+1/2$ disclinations spanning the shell. **G** Cholesteric shell with hybrid boundary conditions displaying double-spiralled thin stripes inside focal conic domains. **H** Cholesteric shell with homeotropic anchoring showing a close-packed structure of axisymmetric topological solitons. **I** Smectic shell with planar boundary conditions, where curvature walls divide the sphere into crescent domains. **J** Photonic cross communication patterns in a cholesteric shell. **K** Swimming trajectory of a self-propelled nematic shell with homeotropic boundary conditions. **L** Two dimensional active nematic shell, where microtubule bundles are sheared by kinesin motors. The two projections show the positions of the four $+1/2$ disclinations, which continuously oscillate over time. **B** and **D–J** are crossed polarized images, while **C** is a bright-field image. The typical outer radii of the passive shells are around $100\,\mu$m, the active shell is five times smaller.
Source: **A** reproduced from [726]; **B** reproduced from [718]; **C–G** reproduced from [727]; **H** reproduced from [728]; **I** reproduced from [729]; **J** reproduced from [730]; **K** reproduced from [713]; **L** reproduced from [731].

control on the liquid-crystal orientation at the boundaries is key for two reasons. First, it enables tuning the balance between surface and bulk energy. Second, it sets the topological constraints for the system. The Poincaré–Hopf theorem applies when the boundary conditions are planar (**n** parallel to the surface), while a homeotropic (**n** perpendicular to the surface) three-dimensional nematic field obeys the Gauss–Bonnet theorem [699]. Since liquid-crystal shells are bounded by two spherical surfaces, they allow for hybrid boundary conditions, planar on one surface and homeotropic on the other. These two parameters, h/R and MA, control the response of the liquid crystal to geometrical frustration in the absence of external fields. Tuning this energy balance enables monitoring the dynamical restructuring of liquid crystals in a shell geometry.

A cholesteric shell itself beautifully illustrates the richness of behaviour that results from dynamically changing the shell thickness h and MA. In that case, the liquid crystal has a characteristic length scale given by the pitch, p, of the twisted molecular structure. Under planar boundary conditions, increasing h/p can lead to a process where two $+1$ defect lines wrap around each other to form a $+2$ defect with double-helix structure [736]. Changing MA from planar to homeotropic entails dramatic molecular rearrangements, since the condition of homeotropic MA is incompatible with the tendency of the cholesteric to twist. At moderate MA strength and confinement conditions, the cholesteric forms complex striped patterns (Fig. 74**G**) [737,738], while at strong MA and confinement conditions, the cholesteric unwinds to form a frustrated radial director field, in which solitonic structures appear in those regions where the local shell thickness is commensurate with p (Fig. 74**H**). Among those solitons, different types of cholesteric fingers and particle-like skyrmionic structures have been observed [728]. Dynamically changing MA and h/p allows switching between configurations: the cholesteric shell becomes a topological lab, where structures can be created, transformed, packed together and destroyed. Important findings have been reported regarding the mechanisms behind the association and interconversion of topological defects. The wide palette of parameters to which liquid-crystal shells are sensitive foreshadows a wide range of possibilities for future fundamental studies, especially in the case of smectic shells (Fig. 74**I**) and shells of more complex liquid-crystalline phases, where numerical simulations are still missing.

The potential applications of liquid-crystal shells open up further when considering the possibility of making the liquid crystal active. Recent advances in material science have enabled the self-assembly of a microtubule-kinesin active nematic on the surface of a sphere, forming a two-dimensional active nematic shell [731] (Fig. 74**L**). In this out-of-equilibrium material, the tetrahedral defect structure becomes dynamic and the nematic shell a robust micro-clock with tuneable frequency. How these micro-clocks synchronize or induce coupled dynamics in passive liquid crystals are questions to be explored. Active nematics are a fundamentally novel class of materials where topology and activity naturally merge, and whose fascinating properties, enriched by the complexity of the constraining surface, are yet to be uncovered.

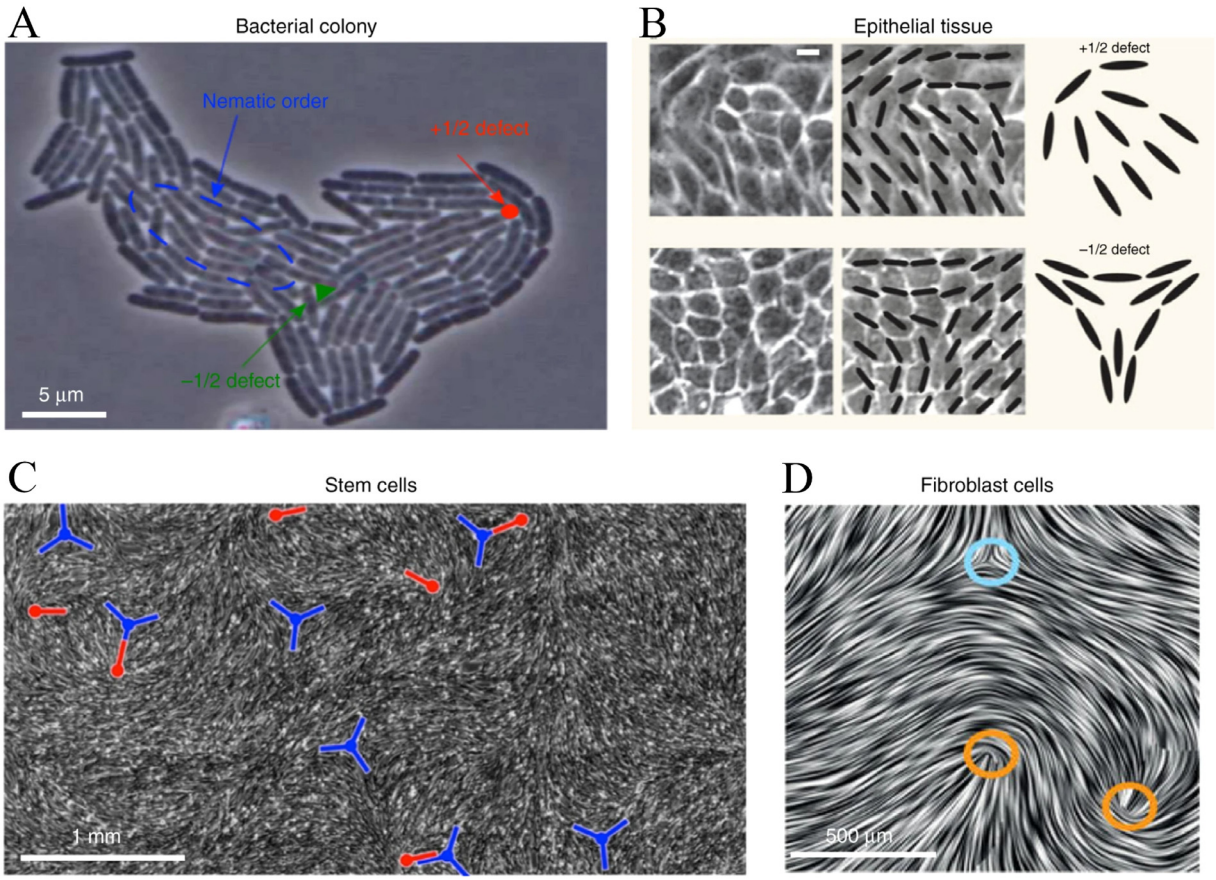

Fig. 75. Biological systems that exhibit active nematic order in two dimensions. $\pm 1/2$ topological defects are shown. *Source:* Reproduced from [741].

7.5. Active nematics, liquid-crystal fluidics and driven systems

Active matter is today a major growing field of interdisciplinary research with the fascination that active materials can self-move, self-rotate, change shape, swim and generally be active, by using energy from the environment; behaviour which we associate with the fundamentals of life. A range of active materials show extensive analogies with liquid crystals, such as the emergence of orientational order and of topological defects and the prime role of coupling between orientational order and material flow [739,740]. Examples of active liquid crystals include suspensions of bacteria, microtubule bundles, and cell layers, today developed and explored for various motivations [741]. Active agents such as bacteria can also be introduced into non-active liquid crystals, creating living liquid crystals where the non-active liquid-crystal environment — with its topology — couples with the active component [742,743]. The main current understanding of active liquid crystals is in two-dimensional or quasi-two-dimensional geometries such as layers or shells, but recently, full 3D active liquid crystal materials and systems are starting to be explored [310,744–746].

Active liquid crystals are a class of mesophase materials driven out of equilibrium by self-motility, or energy uptake, at the level of individual constituents. They arise in a range of biological and artificial settings, including bacterial swarms, cell monolayers and tissues (Fig. 75), synthetic microtubule suspensions, vibrated granular systems, and traditional liquid crystals doped with self-propelled particles [739,741,747]. Topology enters into active materials in several ways, but principally through the topological defects inherent in passive liquid crystals and confinement to channels, surfaces of spheres or tori, or in droplets. As we have seen, defects are a characteristic of liquid crystals that have underpinned much of the understanding of passive materials. They have gained an extra dimension in active systems, opening a new playground for topology in driven, non-equilibrium soft matter.

The most widely studied active liquid-crystal phase is the active nematic [741]. At the continuum level, the activity is captured in a minimal way by the addition of an active contribution to the stress tensor $\sigma^{\mathrm{a}}_{ij} = -\zeta Q_{ij}$, where ζ is a phenomenological parameter controlling the strength of the activity; the material is termed extensile if $\zeta > 0$ and contractile if $\zeta < 0$. Among the most striking features of active nematics is that defects are continually created and spontaneously self-propel [748,749]. Only the $+1/2$ and $+3/2$ defects are self-motile, as can be seen from symmetry

grounds since they are the only defects with a polar structure. The self-propulsion can be incorporated into an effective *particle dynamics* model of active nematics described solely in terms of the defects [750] and this description is now quite far advanced [751–753]. In unconfined systems defect proliferation and self-propulsion leads to complex dynamics [754,755], but this can be tamed by sufficiently strong confinement, determined by the active length-scale $\sim\sqrt{K/|\zeta|}$, with K the elastic term in Eq. (45), arising from the balance of active and elastic stresses.

The characteristic appearance of topological defects and their active dynamics has facilitated their identification in a variety of cell cultures and epithelial tissues [756–759]. Equally important as motility is that defects act as sources of additional localized stress, which have been shown to correlate with sites of cell death in epithelial layers [756]. A recent advance has been the demonstration that defects serve as organizing sites for feature formation in *Hydra* morphogenesis [760], suggesting their role as a *mechanical morphogen*.

Although the majority of research in active liquid crystals has been in two dimensions, three-dimensional active nematics have recently been experimentally obtained [310], stimulating an increase of activity in this area [745,746,761–763]. A significant difference in three dimensions is that the basic defects are lines and closed loops rather than points and this brings greater diversity and also richer dynamics. A model for simple defect loops was first introduced by Friedel and de Gennes [764] in which the director rotates about a vector $\boldsymbol{\Omega}$ and is given by $\mathbf{n} = \cos(\omega/4)\,\mathbf{e}_1 + \sin(\omega/4)\,\mathbf{e}_2$ where $\{\mathbf{e}_1, \mathbf{e}_2, \boldsymbol{\Omega}\}$ is an orthonormal frame and ω is the solid angle function for the loop [765]. The loop has different geometrical character depending on its orientation relative to $\boldsymbol{\Omega}$; when $\boldsymbol{\Omega}$ and the loop normal are parallel the defect loop is called wedge type, while when they are perpendicular it is called twist type. A self-propulsion dynamics for the defect loops has been developed by a local analysis and is able to capture the dynamics of full numerical simulations in simple cases [745].

The topology of non-active liquid crystals is evidently more complex in three spatial dimensions than in two dimensions, indicating exciting possibilities for transfer of knowledge from non-active to active liquid crystals. A range of singular and non-singular topological defects, topological objects or field structures are known to be topologically allowed in liquid-crystalline orientational order, and a first question is, can some of these emerge — i.e., be dynamically stable or metastable — in active liquid crystals? Active liquid crystals are also inherently out-of-equilibrium materials, posing a question as to how to apply topology to systems with a topologically non-trivial dynamic steady state, such as the topological turbulence in active nematics.

Beyond the active nematic phase, several of the other traditional liquid-crystal phases have also been extended to an active setting, principally smectics [766,767] and cholesterics [768–770]. The role of topology in these active phases has barely been explored to date and represents a natural avenue for further development.

7.6. Liquid-crystal structures in biology

Liquid-crystal structures are found in many biological systems [771]. One such instance is in biomineralized tissue [772]. Biomineralization gives us our bones and teeth, seashells, eggshells, corals, arthropod exoskeletons, and many other biological structures. One of the most celebrated of these biomineral structures is that of nacre, mother of pearl, which forms the inner layers of many seashells, as well as the pearls that the same organisms can produce. Nacre has a layered brick-wall structure consisting of bricks of calcium carbonate together with a mortar of proteins and the polysaccharide chitin. It has been seen that this brick-wall structure most probably begins from a precursor of a liquid crystal of nanorods of chitin [773]. Defects in this growth structure lead to spiral and target patterns visible in growth fronts [774]. In the case of pearls that are also formed of nacre, the spherical geometry of the pearl implies that there are necessarily defects in the nacreous growth structure, and these defects are found to drive the rotation of a growing pearl within its growth compartment. In turn, this rotation leads to the formation of different pearl morphologies [775]. As well as nacre, other mollusc biomineral structures are found to be compatible with having a liquid-crystalline precursor, including the cuttlebone of cuttlefish [776] and the crossed lamellar microstructure of mollusc shells [777].

Orientationally ordered and topological matter also plays an important role on the sub-cellular level, in biological processes essential for the cell's function. The cytoskeleton, in particular, is a polymeric structure that provides support to the cell. It is anchored both at the cell nucleus and at the plasma membrane, providing highways for mechanosensing, and means for the cell to exert force on the extracellular matrix and to move. The cytoskeleton is a topologically complex active fluid and has been modelled within the theoretical framework of liquid crystals.

7.7. Liquid-crystal models of the cytoskeleton

The eukaryotic cell's cytoskeleton is constituted by three types of fibres: microtubules, actin filaments and intermediate filaments. Microtubules are linear polar polymers constituted by α- and β-tubulin monomers [778]. They are rigid and play an important role in providing structure and rigidity to the cell. Moreover, they work as avenues for the transport of vesicles that carry loads in the cell [779]. Motor proteins such as kinesin and dynein link to the microtubules and transport these payloads to either the periphery or to the nucleus vicinity, respectively.

Actin filaments are the powerhouse for force deformation in the cell. They are polar filaments either aligned in bundles or organized in meshes that strengthen the cell's cortex. Myosins are motor proteins that bind actin (Fig. 76**A**) and, depending on the actin filament polarization, are able to either exert a tensile or compressive stress in the actin network. This is particularly relevant in the aligned fibre bundles that are able to exert either compressible or tensile forces at

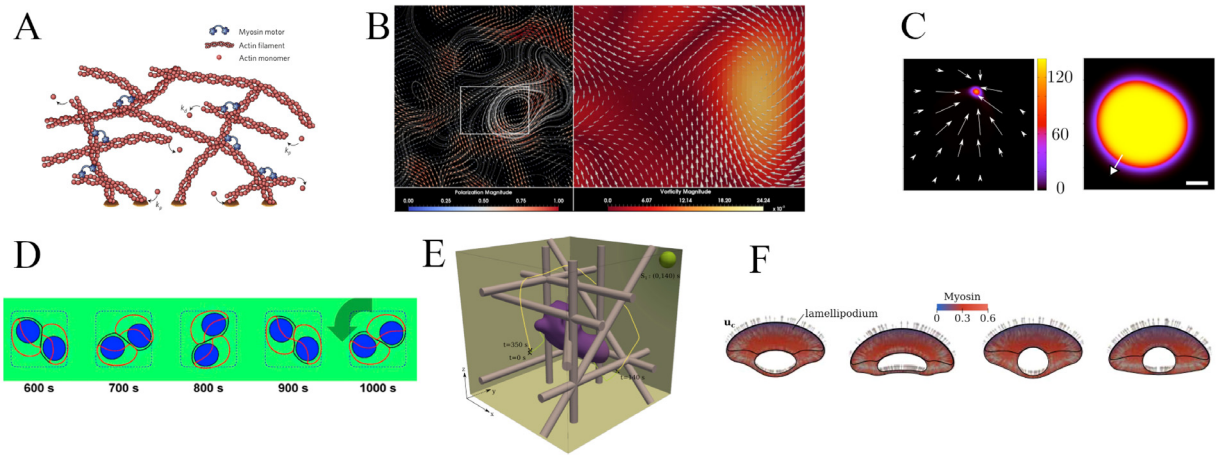

Fig. 76. **A** Active gel constituted by actin filaments, myosin motors and passive crosslinks. **B** Defects in the dynamics of active polar systems in a lattice Boltzmann simulation. On the left panel, the polarization field is represented by arrows; red/long arrows correspond to ordered regions, blue/short arrows are associated with the presence of topological defects. Velocity streamlines are also shown. On the right panel the polarization field is superimposed on to the vorticity contour plot. **C** Phase-field model of cell motion dependent on myosin activity. On the left the levels of myosin motors is shown — they concentrate at the back of the cell — and the arrows indicate the velocity field. On the right the cell is shown and the white arrow gives the direction of cell motion. **D** Phase-field model of two cells with nucleus in a cavity. The cells are able to rotate in the cavity in a concerted manner. **E** Simulation of 3D cell migration in a fibrous environment. The cell's path is identified by the thin line. **F** Shape of cell with nucleus for motion with different velocities. The myosin and the velocity (grey arrows) are indicated.
Source: **A** reproduced from [784]; **B** reproduced from [785]; **C** reproduced from [786]; **D** reproduced from [787]; **E** reproduced from [788]; **F** reproduced from [789].

their extremities. Actin cyloskeleton bundles are often linked to the cellular membrane at the adhesion complex. This adhesion complex is a set of proteins at the cell membrane that from a structure capable of binding the extracellular matrix (ECM) via integrins [780]. On the opposite side, the actin cytoskeleton binds the nuclear membrane through the LINC complexes [781,782]. In this way, the actin cytoskeleton is able to carry mechanical information from the cell's vicinity to the nucleus, being able to influence the nucleus size, and thus to condition gene transcription rates and cell fate [783]. The action of actin and myosin coupled with the secretion of metalloproteinases that locally remodel the ECM, is pivotal for the mobility of cells in tissues, and therefore essential to understand complex processes such as embryo development and tumour metastases formation.

Intermediate filaments are non-polarized filaments that form a cross-linked network that provides structure to the cell. They bind the myosin molecules in actin and are pushed along actin bundles in the direction of the cell nucleus [790–792]. In this way, most intermediate filaments are located at the vicinity of the nucleus and are often essential for specific cell signalling pathways, relevant, for example, in development and vessel growth [793,794].

The actin and myosin proteins can be modelled as an active elastomeric gel [784] and a variety of modelling approaches have been developed for this system. For example, Jülicher et al. [795] have introduced a vector field $\mathbf{p}$ with constant magnitude, set equal to 1 that defines the local polarization direction of the actin bundles. The active gel free energy is written as the free energy of a polarized nematic liquid crystal

$$F[\mathbf{p}] = \int \left\{ \frac{K_1}{2}(\nabla \cdot \mathbf{p})^2 + \frac{K_2}{2}\left[\mathbf{p} \cdot (\nabla \times \mathbf{p})\right]^2 + \frac{K_3}{2}\left[\mathbf{p} \times (\nabla \times \mathbf{p})\right]^2 + k\nabla \cdot \mathbf{p} - \frac{h_\parallel}{2}|\mathbf{p}|^2 \right\} dV, \tag{71}$$

where, as in Eq. (44), K_1, K_2, and K_3 are parameters for the splaying, twisting, and bending of the fibres, k describes the spontaneous splay of the nematic fluid and $\mathbf{p}$ is a vector field instead of a director field. The authors implement a viscoelastic Maxwell model description for the local velocity. The local stress is driven by both the field $\mathbf{h} = -\delta F/\delta \mathbf{p}$ (akin to liquid crystals) and by the local ATP consumption. The presence of ATP in the medium leads to the myosin working to contract the actin fibres. This is indicated in the constitutive viscoelastic equation for the velocity by an increase in the local stress at locations with high ATP consumption [795], which also drives the local alignment of the actin polarization. In simulations, the polarization magnitude is kept constant by the component of $\mathbf{h}$ parallel to the polarization field, $h_\parallel$, in Eq. (71), which works as a Lagrange multiplier.

This model is able to create spontaneous flows driven by ATP levels as well as topological defects (Fig. 76**B**) such as polarization vortices and spirals. It has been applied to describe the evolution of lamellipodia [796] in planar cell migration [797], where it predicts the shape of a lamellipodium as well as the cytoskeleton velocities and stresses within the migrating active gel. Besides gel movement driven by aligned actin bundles, the model is able describe the propagation of actin contraction waves in cells [798–800], and the existence of the cellular cortex, the region of actin at the vicinity of the cellular membrane, constituted by randomly oriented actin fibres [795]. The study of actin flow at the cell surface

yields solutions that describe contractile rings which can exert force and play a crucial role in cellular division [801]. These type of models have been explored through a variety of computational methods [802,803] such as lattice Boltzmann simulations [785].

7.8. Modelling cell locomotion

The cellular membrane limits the cell, and its mechanical properties and adhesion to the ECM determine cell shape and cell movement. The cell membrane is constituted by a lipid bilayer, which can be in different phases depending on temperature and composition. The simpler scenario is when the membrane phospholipids are free to rearrange themselves within the bilayer when the membrane is deformed. In this scenario, and for small deformations, the energy of the membrane is proportional to its local curvature, as described by the Canham–Helfrich free energy [804].

The bending energy of such membranes can be conveniently represented using phase-field models [805,806]. Phase-field models originated in materials science, and gained popularity due to their flexibility to model a wide range of systems [807]. They describe the interfacial dynamics between the different domains in the system. The equations are derived from a free-energy functional and the inclusion of new biological and mechanical phenomena can be made directly in such functional. These models are compact, accurate, and require a moderate number of parameters. Thus, they are suitable to model morphology and growth of biological systems, e.g., cell shape and movement [787,808,809], blood-vessel growth [810–812], and solid tumour growth [813–815].

A possible route to include the Canham–Helfrich energy in a phase-field model is to implement the free energy functional [805]

$$F[\phi] = \kappa \int \left[-\phi + \phi^3 - \epsilon^2 \nabla^2 \phi + \epsilon c_0 (1 - \phi^2)\right]^2 \mathrm{d}V \ , \tag{72}$$

where ϕ is an order parameter that distinguishes the inside from the outside of the cell, c_0 is the equilibrium local curvature of the membrane, κ is a coefficient proportional to the membrane bending rigidity, and ϵ is the membrane width within the model. This phase-field free energy can also include terms that describe adhesion and hard-core repulsion from neighbouring cells and from the ECM [787,808,809]. The evolution of the shape of the cell is driven by the field $\mu(\mathbf{r}) = \delta F/\delta\phi(\mathbf{r})$, using conserved dynamics [805], non-conserved dynamics [809] or through coupling the order parameter field with a velocity field driven by $\mu(\mathbf{r})$ [787,806], akin to models A, B, and H of the Hohenberg–Halperin classification [816].

Phase-field models describing cell shape can then be coupled with an internal implementation of an active gel model for the cytoskeleton. For example in [817] the authors delineate a strategy to introduce the full active gel model introduced in [795] in a cell capable of changing shape. Other works opt for a simpler description of a cell's actomyosin dynamics. In [786] the authors present a minimal model of actomyosin as a non-polar viscoelastic gel (Fig. 76C). The concentration of myosin is responsible for generating the local cell contraction, and the actin is considered uniformly distributed within the cell.

In [787,806,818] the authors have a non-polar viscous two-component model that distinguishes myosin and actin concentrations to calculate the cell velocity at every point. The cell membrane is described by the Canham–Helfrich free energy, Eq. (72), and in [787] a second-order parameter is introduced to describe the cell nucleus. In [787] the authors also introduce the interaction between two cells (Fig. 76**D**), and in [809,819] the authors address the interaction between cell and ECM during cell movement.

The polymerization and de-polymerization of actin filaments (Fig. 76**A**) is also taken into account in several works. In [788] the authors implement a 3D phase-field model with actin described as a viscous fluid, similar to [787], and taking into account the polymerization dynamics of actin, as well as the interaction with ECM fibres, which are interpreted as obstacles to cell movement (Fig. 76**E**). This model permits addressing the strategies used by the cell to move between ECM fibres. By adding the cell nucleus to their model [789] (Fig. 76**F**), they were able to explore the cell nucleus' role as an anchorage place for actin in promoting cell migration.

Topologically complex fluids are therefore determinant to cell life. Processes in heath and disease that depend on cell migration, e.g., embryo development, wound healing, leukocyte motion, or tumour metastasis, are essentially the result of actin dynamics. Due to the complexity of the system, a variety of modelling choices have been used to address these mechanisms quantitatively. These choices may explore the interplay between the actomyosin network and the dynamics of the cellular membrane, the presence of the cell nucleus, the interaction with other cells and the ECM, the remodelling of the ECM and dynamics of the intermediate filament network. Simple models focused on how each one of these specific interplays regulates cell migration are still extremely useful at this stage.

7.9. Topological fluid dynamics: Topological edge modes in active fluids

The band structure of waves in active fluids can be classified using the same topological ideas that are used for defects, solitons, and knots in real space. For more details, see the dedicated review [820]. Sound waves in a fluid can be classified according to how their shape, i.e., eigenvector, and frequency ω, i.e., eigenvalue, depend on their wavevector $\mathbf{q}$, i.e., point in *reciprocal* space. Topological invariants that classify these bulk bands give rise to physical phenomena associated with the

fluid's boundary via the *bulk-boundary correspondence* principle. Active fluids provide a unique playground for designing new topological states of matter owing to their complex acoustics combined with broken time-reversal symmetry.

Many analogies can be drawn between the collective excitations of active fluids and those of electronic fluids, in which time-reversal symmetry can be broken by an applied external magnetic field [821]. A landmark discovery for electronic topological states was the quantum Hall effect; its photonic [822] and soft-matter analogues have only recently begun to be explored. Different topological invariants can be designed depending on global symmetries. One key example is time-reversal symmetry, which is naturally broken in active fluids due to violation of detailed balance at the microscopic scale.

One strategy for creating topological band structures using active fluids is to confine a fluid of self-propelled particles to a periodic network of channels; an example is shown in Fig. 77**A**. Each ring-shaped channel acts as an *atom* in this lattice, with acoustic bands emerging from coupling between neighbouring rings [823–825]. However, even without periodic order, fluids can support topological band structures. For polar active fluids, confining them to the surface of a sphere or another curved manifold creates an interplay between real-space and reciprocal-space topological invariants, resulting in protected modes [826,827]. As another example, topological bands exist in chiral active fluids in which each particle rotates around its own axis and exchanges its intrinsic rotation with fluid vorticity (Fig. 77**B**). In these active-rotor fluids, a rotational background flow endows the acoustics with a band gap and intrinsic rotation compactifies reciprocal space, resulting in a well-defined topological invariant [828,829]. This compactification is possible because of the presence of so-called odd viscosity, an exotic transport coefficient which arises in fluids in which both time-reversal and chiral symmetries are broken [830,831].

A prominent topological invariant arises in two-dimensional fluids with broken time-reversal symmetry that exhibit an acoustic band gap (i.e., for a range of frequencies, no sound waves propagate). This invariant is called the Chern number, defined for each band n as

$$\mathcal{C}_n \equiv \frac{1}{2\pi}\int \mathcal{B}_n(\mathbf{q})\,\mathrm{d}\mathbf{q}, \tag{73}$$

where $\mathcal{B}_n \equiv i\boldsymbol{\nabla}_{\mathbf{q}} \times [\mathbf{u}_n(\mathbf{q})]^{\dagger} \cdot [\boldsymbol{\nabla}_{\mathbf{q}}\mathbf{u}_n(\mathbf{q})]$ is called the Berry curvature, which can be computed directly from the band eigenvectors $\mathbf{u}_n(\mathbf{q})$ (Fig. 77**C**). *Bulk-boundary correspondence* relates the value and sign of the Chern number to the number and direction of chiral states propagating along an edge, or interface between two distinct topological states. A heuristic argument says that these edge states are manifestations of a local closing of the band gap at the topological material's edge. A nonzero Chern number guarantees the existence of these chiral edge modes because a topological invariant can only change when the band gap closes. The power of this topological argument is that it does not rely on any detail of the boundary: the edge states exist independently of boundary conditions. One fundamental property of these topological edge states is their unidirectional nature leading to a non-reciprocal transport of energy and information. The edge states are also guaranteed to be protected against scattering because inside the bulk band gap these unidirectional modes have no other state to scatter into.

More recent developments in topological active matter have explored how to classify invariants in *non-Hermitian* band structures [820,832–835]. This non-Hermiticity occurs naturally in active materials due to a combination of energy injection and dissipation. Strikingly, in addition to invariants associated with eigenvectors, non-Hermitian systems can have topological winding numbers associated with the complex phases of their eigenvalues (i.e., frequencies) around so-called exceptional points. One connection between Chern numbers and non-Hermiticity comes about in systems that violate bulk-boundary correspondence [836], resulting in perfect absorption (Fig. 77**D**) [837].

Topological edge states promise a range of exotic applications to be developed from these fundamental scientific discoveries. Unidirectional edge modes herald devices in which sound transport is robust and protected against scattering. Another potential application is acoustic lasing, for which topological protection can be exploited to develop sharp lasing modes [838,839]. More generally, principles of active and non-reciprocal matter underlie the design of novel smart and reconfigurable materials, giving rise to future applications at the intersection of materials science and robotics.

7.10. Outlook on complex fluids

In this section, we demonstrated that fluid systems without positional order can exhibit complex structural features, some of which share topological properties with polymeric systems and crystalline solids. Fluids are ideally suited for use in soft composites, such as emulsions and colloidal dispersions, where the topological properties gain additional complexity due to boundary conditions. We focused on fluids with orientational order, which covers a lot of materials of technological interest, as well as some aspects of living and biological matter, where anisotropy is accompanied with active motion driven by a constant source of energy. The demonstrated advances in different liquid-crystal systems — from colloids, to metamaterials, to blue phases and biological systems — have contributed to opening novel perspectives on their use in devices, sensors, biomimetic systems and fluidics. Although incomplete, the selection of topics presented should elucidate the different ways topology plays a role in flowing soft matter.

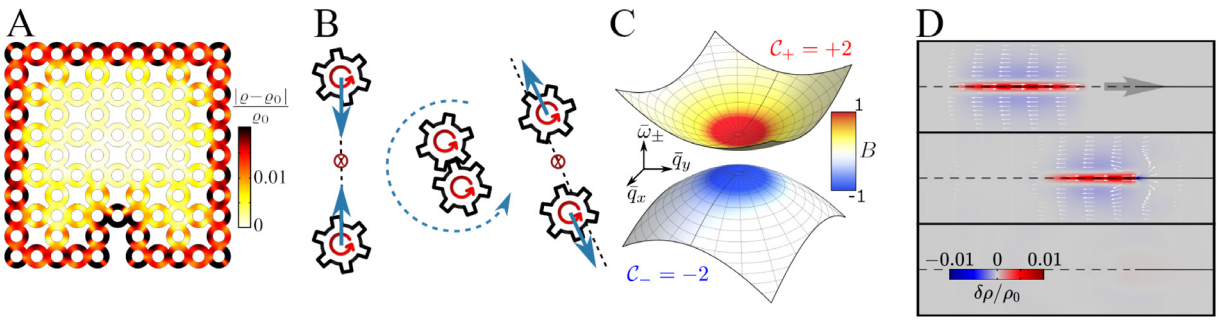

Fig. 77. Topological edge modes in active fluids. **A** Confining a polar active fluid in a periodic array of microchannels results in chiral edge states, which are protected against scattering. **B** Particles in a chiral active fluid can exchange their intrinsic rotation for orbital angular momentum, resulting in exotic effects such as odd viscosity and topological edge states. **C** The acoustics in a chiral active fluid involves bands characterized by a topological invariant called a Chern number. **D** Violating bulk-boundary correspondence can result in topological edge states losing their protection, which in turn can be used to design perfect absorption.
Source: **A** adapted from [824]; **B** adapted from [831]; **C** adapted from [828]; **D** adapted from [837].

8. Summary and outlook

The field of topological soft matter is growing rapidly, with novel experimental and computational techniques allowing researchers to gain deeper insight into the workings of disparate systems such as proteins, DNA, the genome, artificial polymeric materials, and liquid crystals. We hope that with this text we have succeeded to give not only a concise account about the recent advances in the characterization of these systems, but also to merge them in the context of previous research, in a form that is understandable for a wide interdisciplinary audience of scientists working in the field of soft and biological matter. Following this aim, the first sections of the review have been dedicated to a detailed overview of topology in soft matter, while the remaining ones went in depth into more specialized topics.

Section 2 introduced the mathematical concepts needed to study the topology of soft materials, both in polymers and in the continuum. The definitions of knots and links, their generalization to open curves, and the topological invariants used to characterize them have been introduced. These were followed by the definition of topological defects in field theories, necessary to treat complex fluids. Care has been taken in presenting the material in a way that is accessible to soft-matter physicists without sacrificing the formal correctness of the definitions.

Section 3 presented an overview of topological objects in different soft-matter systems, discussing their consequences. We discussed the properties of the different physical substrates considered in this review: polymers, DNA, proteins, and complex liquids such as nematic liquid crystals.

The effects of topological constraints on the viscoelastic properties of polymer melts were treated in Section 4. The results presented there have general validity, and offer a physical basis for results about the organization of the genome presented in Section 5. Given the importance of these topics for biophysics and soft matter, a considerable effort was made to present them in an accessible way, condensing a debate on the rheological properties of melts that has been ongoing for the better part of three decades. The impact of topological constraints on the microfluidics properties of single polymers was also discussed here in Section 4.2.

Section 5 journeyed into the complexity of DNA *in vitro* and *in vivo*. The Călugăreanu–White theorem was introduced in Section 2.5 in the context of dsDNA, and its generalization to fluids was discussed in Section 3.5.5. The central part of Section 5 presented an overview of the current understanding of the organization of DNA in bacteria and eukaryotes. We discussed how recent developments in computer simulations and knot theory integrate the results from advanced imaging and chromosome conformation capture techniques and help to characterize the role of topology in the structure and function of DNA.

Section 6 was dedicated to several aspects of the research on topology in proteins. A large effort has been made to clarify issues that are still under debate, namely the mechanisms of the formation of knots in proteins and the biological motivations of the emergence of topological structures in enzymes. The particular case of proteins from the SPOUT family was discussed in detail in Section 6.7.2.

Section 7 focused on complex fluids, and the role of topological defects in their behaviour. Despite having very different microscopic composition, various types of molecular liquid crystals, colonies and suspensions of cells, and intracellular structures, all share similar mesoscopic behaviour and similar topological features. A large portion of the section is dedicated to active materials found in biological systems, where influx of energy drives the fluid out of equilibrium, producing flowing steady states with dynamical evolution of defects, collectively described as *active nematics*.

8.1. Topology in other areas of physics

Topology has played, and continues to play, an important role in many other areas of physics. We mention a few examples here, to offer interesting connections to the reader. In superconductors and superfluids such as ^{3}He, the

existence of vortex and other topological solutions can be understood through homotopy theory; see for instance [840]. In relativistic quantum field theory, topological solitons such as monopoles and strings appear very often [841], and instantons play a crucial role in quantum chromodynamics [842]. On the largest scales in cosmology, topological solutions such as cosmic strings can leave important observational effects that are currently looked for with different experiments such as gravitational wave interferometers and cosmic microwave background probes [843]. On the more theoretical side, the connections between supersymmetric quantum field theory and topology have led to important advances in mathematics [60]. The results presented in Sections 2.8, 3.5, and 7, as well as the short discussion in Section 2.8.1 begin to offer a connection between ongoing research in theoretical physics, fluid dynamics, cosmology, and soft materials, but much more could certainly be said. For example, conformal methods and conformal field theories have been applied to the statistics of entangled random walks in a series of remarkable works whose results have been summarized in a book by Nechaev [844]. The mathematics of knots is also deeply connected to topological quantum field theories; we refer the interested reader to the book by Kauffman [3].

8.2. Topology in other areas of biology

Knots are found throughout the natural world [845]. In some instances knots in nature have no purpose as such, but are merely accidental byproducts of how something has grown or evolved. In this case they may be harmless side effects, or even harmful ones. But in other instances nature has hit upon a way of using knots to do something in particular.

For an animal to knot its own body it must be long, thin, and flexible enough. Snakes can, and do, tie themselves into knots. Pythons and constrictors are noted anecdotally to have been seen knotting themselves. Some snakes, especially sea snakes, form a knot to shed their old skin and perhaps to remove parasites [846,847]. The brown treesnake *Boiga irregularis* ascends large smooth treetrunks using a knot in *lasso locomotion* [848]. Eels too form self-knots. One method of moray eel feeding is to latch onto its prey, then form a figure-eight knot and pull its head back through the knot to tear its prey [849,850]. Hagfish knot themselves to dig burrows and to leverage themselves when feeding [851]. They also slide a knot along their body to release slime. Uyeno et al. classified hagfish self-knots by getting hagfish to knot themselves in the laboratory. 45% of the time they formed a trefoil knot, 33% a figure-eight knot, and about 4% a three-twist knot [852]. Likewise the parasitic gastropod mollusc *Thyonicola dogieli*, which has the form of a long tube and parasitizes sea cucumbers, also forms knots [853].

Darwin wrote about knots in climbing plants [854], "As the spiral contraction travelled down the main stem and down the branches of the tendril, all the lower branches, one after another, were brought into contact with the stick, and were wound round it and round their own branches until the whole was tied together in an inextricable knot round the stick. The branches of a tendril, though at first so flexible, after having clasped a support for a time, become rigid and even stronger than they were at first. Thus the plant is secured to its support in a perfect manner". These climbing plants certainly exploit topological laws in their growth [855], but do they utilize actual knots? It seems so [856]; they form lassos like those of the treesnakes above [857].

Some nonhuman great apes can tie knots. Strand knotting behaviour seen during bed construction from foliage in orangutans, bonobos and chimpanzees has been observed both in zoos [858] and in the wild [859]. Of course, we humans, also great apes, are forming a trefoil knot when we fold our arms, and the same behaviour is observed in other great apes.

Many animals have evolved mechanisms to avoid problems with self-knotting. A study of octopus tentacles showed that they avoid tangling and knotting their limbs by utilizing a chemical self-recognition system [860]. Under conditions of illness or strange situations like microgravity, this knotting avoidance mechanism can be overridden. "Some snakes, in the genera *Thamnophis* and *Elaphe*, which typically thrashed and rolled in μg [microgravity], managed to knot their own bodies with their tails and immediately became quiescent. [...] The fact that they became quiet upon self-embrace further suggests a failure to distinguish self from non-self" [861].

Another, unwanted, knot in the human body can sometimes be found in the umbilical cord [862]. The umbilical cord is found knotted in approximately 1% of deliveries in human pregnancy according to a study [863]. This is undesirable, since it is associated with a higher incidence of stillbirth deliveries [864]. Diagnosis and imaging of these knots has been performed *in utero* [865].

The vast topological topic in biology that we have not covered in this review is network topology. Biological networks range from biochemistry through taxonomy to populations and ecosystems. We direct the reader to review articles [866–869].

8.3. Other topological aspects of soft matter

Despite its length, this review could not cover all topology-related topics in soft matter. Examples have been left out, or treated in less detail that we would have liked. This was by no means motivated by a judgement of value, but simply by the expertise of the authors and the scientific focus of the EUTOPIA Cost Action. Below, we report a few notable examples which would deserve a review of their own, pointing the interested reader to some relevant sources to learn more about them.

The first prominent topic which was left out is the application of topological tools such as graph theory to describe the architectural properties of biomolecules. Despite the fact that we extensively discuss topology for proteins and DNA,

we did not present here applications to RNA, for which graph theory [870,871] and matrix field theory [872–874] have been used to characterize the architecture of the molecule given by the network of base pairing. Since the existence of knots for RNA molecules is also quite uncertain [875,876], we did not discuss the application of topology to RNA at all and left the topic to specialized publications devoted to these systems.

Another prominent, vast topic that was only mentioned, but deserves much greater attention, is that of topologically complex synthetic molecules. These include self-assembled knots [877,878], weavings, and different kinds of mechanically interlocked molecules and polymers, formed either by interlocked rings, such as polycatenanes [272], or by rings (rotaxanes) sliding on linear polymers. These systems can be formed through various self-assembly techniques [879] and particularly through metallo-template synthesis [272] and have shown to be of key importance for the developments of nanomachines [880–882], stimuli-reactive nanomaterials, and advanced, shape-memory gels. There are excellent reviews on these topics, some very recent, which we encourage the reader to check, for example [883–885].

The topological aspects of liquids and amorphous solids is another topic we have not touched on. There is important recent work highlighting how phase transitions in these systems are reflected in topological metrics [886].

Finally, we need to mention an emerging parallel field which we think offers the possibility for fruitful exchanges: the physics of textiles, wearable and soft robotics [887].

8.4. Looking ahead

The wealth of results related to the topology of soft and biological matter is generating a growing interest for potential technological applications, several of which were mentioned throughout the review, in particular near the end of each section. Here we mention a few global aspects which we believe contribute to make this field especially exciting.

In polymer physics, and particularly in relation to single-molecule experiments, the concurrent advancement of microfluidic assays [171,184,189] and nano-pore devices [175,888] on the experimental side, and the availability of reliable algorithms to localize physical knots on the theoretical side (Section 2) is encouraging a very fruitful discussion between experimental and computational physicists, working both on DNA and on proteins (Section 6), with positive technological repercussions in the development of DNA barcoding and sequencing apparatuses, as well as in the characterization of polypeptide chains.

In the context of proteins, Section 6, research is focusing on more complex topologies, like lassos and θ-curves, which promise intriguing pharmaceutical possibilities, as well as on the physical linkage between different chains in a protein complex. At the same time, there are still several open questions regarding the influence of knots on the behaviour of proteins beyond their influence on the folded state, and how knotted proteins could be designed.

In the context of chromosome organization, described in Section 5, the development of Hi-C and other experimental techniques, which now allow biologists to map the position and partially the dynamics of chromosomes, are opening the possibility for the computational modelling of whole chromosomes. This endeavour, of fundamental importance to understand the functioning and regulation of our genomes, is based on polymer physics models and benefits significantly from the knowledge derived in the study of polymer melts and of their topological interactions, described in Section 4. This topic is further related to another exciting problem in biological physics, namely the characterization of active materials. There are several enzymes that constantly act on chromatine, influencing its organization and keeping the genome functional. Some of them, topoisomerases (Topo2), actively control the knotting and linking of DNA.

The above research offers several interesting prompts for the development of novel smart soft materials, which are exemplified by kinetoplast DNA, described in Section 3.3.5. This is formed by several thousand DNA mini-rings linked together with a conserved topology, and is currently being studied as a candidate topological soft material. As demonstrated by the group of Spakowitz [274], its elastic properties can be actively modified through the action of Topo2 enzymes.

Understanding the role of activity, and how to control the properties of the material through external fields are two open questions in relation to liquid crystals and topologically complex fluids. As we saw in Section 7, on the one hand the framework of active liquid crystals can be used to model the cytoskeleton of cells, and, on the other, recent advances in material science have enabled the construction of two-dimensional active nematic shells formed by microtubules and kinesin, whose topological defects can be dynamically tuned. In three dimensions, the inclusion of colloidal particles in a twisted nematic now allows researchers to knot and link the disclination lines that are formed around the colloids, thus creating a tunable disclination textile; this is the micrometre-size equivalent of our scarf from Section 1.

CRediT authorship contribution statement

Luca Tubiana: Conceptualization, Supervision, Writing – original draft, Writing – review & editing, Visualization. **Gareth P. Alexander:** Writing – original draft. **Agnese Barbensi:** Visualization, Writing – original draft, Writing – review & editing. **Dorothy Buck:** Writing – original draft. **Julyan H.E. Cartwright:** Writing – review & editing. **Mateusz Chwastyk:** Writing – original draft. **Marek Cieplak:** Writing – original draft. **Ivan Coluzza:** Writing – original draft, Writing – review & editing. **Simon Čopar:** Conceptualization, Supervision, Visualization, Writing – original draft, Writing – review & editing. **David J. Craik:** Writing – original draft. **Marco Di Stefano:** Conceptualization, Visualization, Writing – original draft, Writing – review & editing. **Ralf Everaers:** Writing – original draft, Writing – review & editing.

Patrícia F.N. Faísca: Conceptualization, Visualization, Writing – original draft, Writing – review & editing, Supervision. **Franco Ferrari:** Conceptualization, Writing – original draft, Writing – review & editing, Supervision. **Achille Giacometti:** Conceptualization, Writing – original draft, Writing – review & editing. **Dimos Goundaroulis:** Writing – original draft, Writing – review & editing. **Ellinor Haglund:** Writing – original draft. **Ya-Ming Hou:** Writing – original draft. **Nevena Ilieva:** Writing – original draft, Writing – review & editing. **Sophie E. Jackson:** Writing – original draft, Writing – review & editing, Supervision. **Aleksandre Japaridze:** Writing – original draft. **Noam Kaplan:** Writing – original draft. **Alexander R. Klotz:** Writing – review & editing. **Hongbin Li:** Writing – original draft. **Christos N. Likos:** Writing – original draft, Writing – review & editing. **Emanuele Locatelli:** Conceptualization, Supervision, Visualization, Writing – original draft, Writing – review & editing. **Teresa López-León:** Writing – original draft, Writing – review & editing. **Thomas Machon:** Supervision, Writing – original draft, Conceptualization. **Cristian Micheletti:** Writing – original draft. **Davide Michieletto:** Conceptualization, Supervision, Writing – original draft, Writing – review & editing, Visualization. **Antti Niemi:** Writing – original draft, Writing – review & editing. **Wanda Niemyska:** Writing – original draft. **Szymon Niewieczerzal:** Writing – original draft. **Francesco Nitti:** Conceptualization, Writing – original draft, Writing – review & editing. **Enzo Orlandini:** Writing – original draft, Writing – review & editing. **Samuela Pasquali:** Conceptualization, Writing – original draft, Writing – review & editing. **Agata P. Perlinska:** Writing – original draft. **Rudolf Podgornik:** Writing – original draft. **Raffaello Potestio:** Writing – original draft. **Nicola M. Pugno:** Writing – original draft. **Miha Ravnik:** Writing – original draft. **Renzo Ricca:** Visualization, Writing – original draft, Writing – review & editing. **Christian M. Rohwer:** Conceptualization, Writing – original draft, Supervision. **Angelo Rosa:** Conceptualization, Supervision, Visualization, Writing – original draft, Writing – review & editing. **Jan Smrek:** Writing – original draft, Writing – review & editing. **Anton Souslov:** Writing – original draft. **Andrzej Stasiak:** Writing – original draft. **Danièle Steer:** Writing – original draft. **Joanna Sułkowska:** Conceptualization, Supervision, Writing – original draft, Writing – review & editing. **Piotr Sułkowski:** Writing – original draft, Writing – review & editing. **De Witt L. Sumners:** Writing – original draft, Writing – review & editing. **Carsten Svaneborg:** Writing – original draft. **Piotr Szymczak:** Writing – original draft. **Thomas Tarenzi:** Software, Writing – original draft. **Rui Travasso:** Writing – original draft. **Peter Virnau:** Writing – original draft. **Dimitris Vlassopoulos:** Writing – original draft, Writing – review & editing. **Primož Ziherl:** Writing – original draft. **Slobodan Žumer:** Conceptualization, Writing – original draft, Writing – review & editing.

Declaration of competing interest

The authors declare that they have no known competing financial interests or personal relationships that could have appeared to influence the work reported in this paper.

Acknowledgements

This review is dedicated to the memory of Marek Cieplak, coauthor of this paper, who died before its submission. He will be remembered by many of us as a dear colleague, and by some of us as a dear friend and mentor.

This manuscript is based upon work from COST Action CA17139 (EUTOPIA), supported by COST (European Cooperation in Science and Technology). The members of EUTOPIA who have participated in this endeavour are deeply grateful to COST for the invaluable help in connecting research initiatives across Europe and beyond and in enabling researchers and innovators to grow their ideas in any science and technology field by sharing them with their peers. Without this help, the present publication would not have been possible.

Several of the reported results are the outcome of national and international research projects. While it is not possible to acknowledge here all the related funding agencies, mention is deserved for those projects that are closely related to EUTOPIA:

1. Austrian Science Fund (FWF), Lise-Meitner Fellowship No. M 2470-N28 (Jan Smrek);
2. Italian MIUR grant Rita Levi-Montalcini (Emanuele Locatelli)
3. Polish National Science Centre under grant OPUS 19, grant no. 2020/37/B/ST3/01471 (Franco Ferrari);
4. European Research Council (ERC) under the European Union's Horizon 2020 research and innovation programme (grant agreement No 947918, TAP) and Royal Society University Research Fellowship (Davide Michieletto);
5. EMBO Installation Grant 2057, the Polish Ministry for Science and Higher Education 0003/ID3/2016/64, Polish National Science Centre: COVID-19 EXPRESS CALL and OPUS 16, 2018/31/B/NZ1/04016 (Joanna I. Sułkowska);
6. TEAM programme of the Foundation for Polish Science co-financed by the European Union under the European Regional Development Fund POIR.04.04.00-00-5C55/17-00 (Piotr Sułkowski);
7. Grant KP-06-COST-9/2019 of the Bulgarian National Science Fund, a National Co-funding for participation in approved COST Actions (Nevena Ilieva)
8. Fundação para a Ciência e a Tecnologia under the projects UIDB/04564/2020 and UIDP/04564/2020 with DOI identifiers [http://dx.doi.org/10.54499/UIDB/04564/2020] and [http://dx.doi.org/10.54499/UIDP/04564/2020] (Rui D. M. Travasso);
9. ICSC — Centro Nazionale di Ricerca in High Performance Computing, Big Data and Quantum Computing, funded by European Union — NextGenerationEU (Luca Tubiana, Raffaello Potestio)

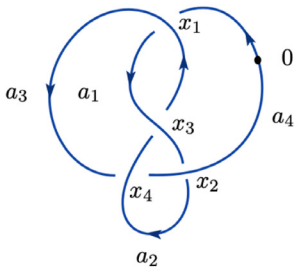

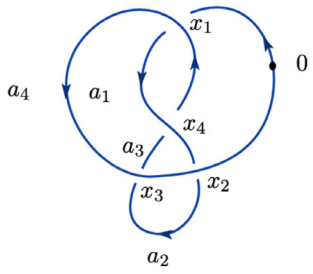

$$\mathbf{M}(t;4_1) = \begin{pmatrix} t & 0 & 1-t & -1 \\ t & -1 & 0 & 1-t \\ 1-t & -1 & t & 0 \\ 0 & 1-t & t & -1 \end{pmatrix} \qquad \mathbf{M}(t;0_1) = \begin{pmatrix} -1 & 0 & 0 & 1 \\ t & -1 & 0 & 1-t \\ 0 & -1 & t & 1-t \\ 1-t & 0 & -1 & t \end{pmatrix}$$

$$\begin{vmatrix} 0 & 1-t & -1 \\ -1 & 0 & 1-t \\ -1 & t & 0 \end{vmatrix} = -t^2+3t-1 \qquad \begin{vmatrix} -1 & 0 & 0 \\ t & -1 & 0 \\ 0 & -1 & t \end{vmatrix} = t$$

$$\Delta(t;4_1) = t^2-3t+1 \qquad \Delta(t;0_1) = +1$$

Fig. A.78. Alexander polynomial for a 4_1 knot, on the left, and an unknot, on the right. The latter is not represented by its minimal diagram.

10. NSF-CLP under the projects CHE2145906 CAREER A Novel Twist in Nature; Proteins with a Pierced Lasso Topology (Ellinor Haglund)
11. Fundação para a Ciência e a Tecnologia under the project UIDB/04046/2020[(https://doi.org/10.54499/UIDB/04046/2020)] (Patrícia F. N. Faísca)
12. Leverhulme Trust Grant under the project RP2013-K-017 (Dorothy Buck)
13. Slovenian Research and Innovation Agency (ARIS) under the project P1-0099 Physics of soft matter, surfaces and nanostructures (Simon Copar, Miha Ravnik, Slobodan Zumer)
14. Engineering and Physical Sciences Research Council (EPSRC) under the project EP/ T000961/1 (Anton Souslov)
15. European Research Council (ERC) under the European Union's Horizon 2020 Research and Innovation Programme Grant Agreement 758588 (Raffaello Potestio).

Finally, Luca Tubiana would like to acknowledge support from the Italian MIUR grant Rita Levi-Montalcini.

Appendix A. The Alexander polynomial

The Alexander polynomial is defined for a diagram of a knot K in terms of a single variable t. The algorithm maps the diagram onto a matrix $\mathbf{M}(t;K)$; the polynomial is then obtained by calculating a minor of $\mathbf{M}$ [9]:

1. Assign an orientation to the knot diagram and establish the sign of each crossing following the convention in Fig. 5**A**.
2. Starting from an arbitrary non-crossing point of the diagram, let us call it 0, follow the ring orientation and assign an increasing numbering index to all the n *undercrossings*, i.e., the crossings in which the current segment passes below another one.
3. Define *arcs* as strands going from an undercrossing to the next one. Starting from point 0 and following the orientation of the curve, assign an increasing numbering index to all the n arcs in the diagram. Arc a_i goes from undercrossing x_i to undercrossing x_{i+1}, with $i+1=1$ when $i=n$ (periodic boundary conditions).
4. Define an $n\times n$ matrix $\mathbf{M}(t;K)$. The rows of $\mathbf{M}$ correspond to the undercrossings of the diagram, and the columns to its arcs. For each undercrossing the labelling defines three arcs, one passing over the crossing, a_k, and two passing below, a_i and a_{i-1}, with $i-1=n$ when $i=1$. Starting from a matrix with all entries equal to zero we can construct $\mathbf{M}$ by summing the following values for the entries $\mathbf{M}_{x_i,a_k}$, $\mathbf{M}_{x_i,a_{i-1}}$, $\mathbf{M}_{x_i,a_i}$ of all crossings x_i.
   - If x_i is a positive crossing, $\mathbf{M}_{x_i,a_k}=+1-t$, $\mathbf{M}_{x_i,a_{i-1}}=-1$, $\mathbf{M}_{x_i,a_i}=+t$.
   - If x_i is a negative crossing, $\mathbf{M}_{x_i,a_k}=+1-t$, $\mathbf{M}_{x_i,a_{i-1}}=+t$, $\mathbf{M}_{x_i,a_i}=-1$.
   - If the index of the overpassing arc $k=i$ or $k=i-1$, $\mathbf{M}_{x_i,a_{i-1}}=1$ and $\mathbf{M}_{x_i,a_i}=-1$ irrespective of the crossing's sign (in the simplest case, this corresponds to a Reidemeister type I move, see Fig. 2**B**).

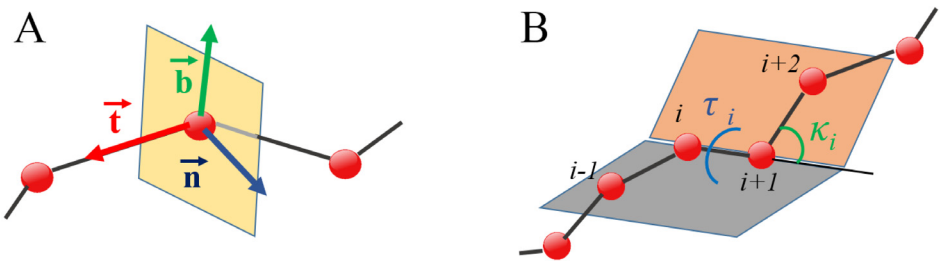

Fig. B.79. **A** The Frenet frame; **B** The virtual bond and torsion angles. The Cα-atoms are represented as red spheres.

5. Compute any minor of order $n-1$ of the matrix **M** and multiply it by a quantity $\pm t^{-m}$, $m \in \mathbb{N}$ in such a way that the resulting polynomial does not contain negative powers, and has a positive constant term. Such a minor is the (irreducible) Alexander polynomial $\Delta(t; K)$ of the knot K.

In Fig. A.78 we show the calculation of an Alexander polynomial for a projection of the 4_1 knot and for a similar projection of the unknot. The Alexander polynomial is very effective in distinguishing knots with low crossing number. Indeed, even its values in $t = -1$ and $t = -2$, $\Delta(-1; K)$ and $\Delta(-2; K)$ alone allow distinguishing knots up to 8_{19}. A drawback of this polynomial invariant, however, is that it is unable to distinguish a knot from its mirror image or chiral enantiomer, i.e., the knot type obtained from a knot K by changing all the crossings in a diagram representing K.

Appendix B. A field-theoretical, topological approach to protein folding and dynamics

As described in Section 3.1.3, the standard description of protein folding is based on the free-energy landscape theory of protein folding [125], which assumes that the folded state of a protein is located at the bottom of a rugged free-energy landscape.

Recently, advanced deep-learning tools trained on large databases of experimentally known protein structures, such as AlphaFold [889], have obtained extremely precise prediction of folded structures starting from the primary sequence of a protein. However, results obtained through these approaches, while useful in applications, do not provide an insight into the folding mechanism of proteins and the principle guiding them.

Furthermore, since algorithms like AlphaFold are trained on static protein structures, the biological relevance of these predictions for protein function is limited to the static native conformation. However, most proteins are dynamical when biologically active. Proteins in living cells often behave as nanomachines: their segments need to move collectively, in a given fashion, in order to accomplish a desired biological function. It remains a challenge to extend the learning algorithms to include dynamics, and more generally to model proteins that are *intrinsically disordered* under physiological conditions.

Here we discuss a possible alternative way to understand protein structure and dynamics, through the use of a soliton — or more precisely, the soliton solutions of a generalized discrete nonlinear Schrödinger equation. As explained in Section 2.8.1, a soliton often provides a methodical approach to describe both structural and dynamical self-organization in a physical system.

In order for these collective modes to emerge, suitable key variables must be determined and, through the symmetries of the system and the separation of scales, the dynamics of such key variables can become simple and be described by a self-consistent effective theory. This theory can reveal qualitatively new features including structural self-organization and emerging topological order.

In the case of proteins, the nonlinear difference equations that support solitons as stable solutions emerge from such an *effective theory* description based on the backbone-trace representation of the protein. In this representation, the entire protein is approximated with a discrete curve in three-dimensional space, with vertices at the positions of the α carbons. The protein is then akin to a linear polymer with appropriate steric restrictions. The side chains can often be added and accounted for at appropriate levels of coarse-graining. The Cα representation allows describing protein geometry and its evolution in terms of discrete Frenet frames $(\mathbf{t}_i, \mathbf{b}_i, \mathbf{n}_i)$, located at the positions of the Cα atoms Fig. B.79 (Section 2.4).

It is worth noting that the Frenet angles (κ, τ) (Eq. (10)) are quite different from the conventional Ramachandran angles (ϕ, ψ) [890]. The definition of Frenet angles involves four consecutive Cα atoms, while the definition of Ramachandran angles does not extend beyond the peptide plane connecting two neighbouring Cα atoms. Furthermore, the topology of the virtual bond and torsion angles (κ, τ) is that of the sphere S^2 of spherical coordinates in $\mathbb{R}^3$, while the Ramachandran angles are coordinates on a torus T^2. As a consequence the (κ, τ) pairs are a sufficient coordinate set for reconstructing the original fractal protein geometry, while the (ϕ, ψ) pairs are not [890]. The discrete Frenet frames provide an effective methodology to describe the geometry of a protein backbone, which is now also being employed in the development of effective protein language-based AI approaches for structure prediction [891]. Furthermore, since they provide a complete description of the protein backbone, they can also be used to develop effective theory approaches to describe protein dynamics, in the tradition of theoretical physics, with the bond and torsion angles as the reduced set of dynamical

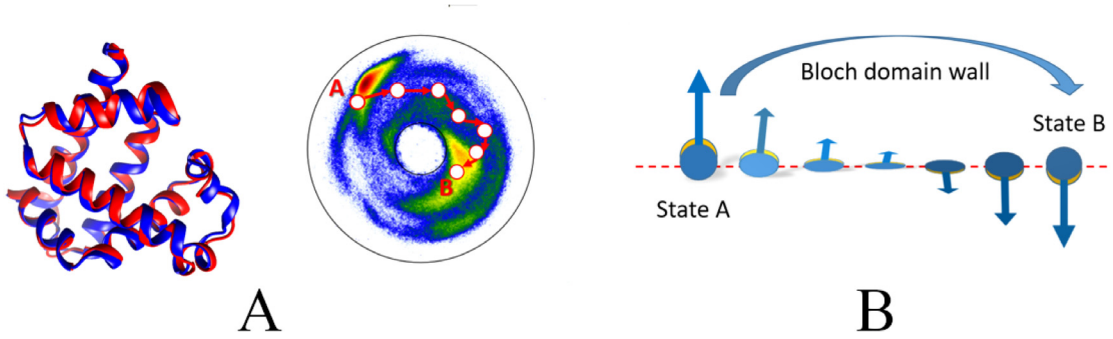

Fig. B.80. A Comparison between the crystallographic structure of myoglobin (in blue), PDB ID 1ABS [896], and the multi-soliton reconstruction (in red); **B** A generic loop on the (κ, τ) sphere for all structures in PDB with a higher than 1 Å resolution, between an α-helix and a β-strand.

variables. A symmetry principle states that the free energy should have the same form, irrespective of which local frame is used for describing the protein backbone. That is, the free energy should be covariant under local frame rotations. In the long-wave-length limit of slow modes, the free energy is then uniquely approximated by the discretized Abelian Higgs model Hamiltonian

$$F = \sum_{i=1}^{N-1} (\kappa_{i+1} - \kappa_i)^2 + \sum_{i=1}^{N} \left\{ \lambda\,(\kappa_i^2 - m^2)^2 + \frac{d}{2}\,\kappa_i^2 \tau_i^2 - b\,\kappa_i^2\,\tau_i - a\,\tau_i + \frac{c}{2}\tau_i^2 \right\} + \dots . \tag{B.1}$$

In Eq. (B.1), a discretized version of the nonlinear Schrödinger (DNLS) energy is seen [892]. In particular, the first two terms coincide with the soliton model described in Section 2.8.1. In addition, it contains the conserved momentum (4th term) and helicity (5th term) terms of the DNLS hierarchy, as well as the Proca mass term (6th term). The former account for the chirality, i.e., right-handedness of the protein backbone, and the Proca mass term acts as a regulator. In principle, the coefficients in Eq. (B.1) can be computed from atomic-level data or, alternatively, can be obtained by training the energy function on a known structure.

Further, the nonlinear Schrödinger equation is a paradigmatic equation for supporting topological solitons. For the critical points of Eq. (B.1), the ensuing equations for (κ_i, τ_i) can be solved numerically, and an excellent approximation is obtained by discretizing the topological soliton of the nonlinear Schrödinger equation

$$\kappa_i \approx \frac{m_1 \cdot e^{c_1(i-s)} - m_2 \cdot e^{-c_2(i-s)}}{e^{c_1(i-s)} + e^{-c_2(i-s)}} \qquad \Rightarrow \qquad \tau_i \approx \frac{a + b\kappa_i^2}{c + d\kappa_i^2}. \tag{B.2}$$

For any super-secondary motif the parameters in Eq. (B.2) are determined by the asymptotic κ-values of the topological soliton, its position, the adjacent bond and torsion angles, and the length of the corresponding bond-angle profile. Accounting for the rather limited number of folds as compared to the total number of resolved protein structures, it is proposed that these solutions are the modular building blocks of a folded protein; that is, the super-secondary modular building blocks are fully characterized by a topological soliton profile in terms of the above parameter set. For example, in the case of the two most common regular structures, α-helices and β-strands, the virtual bond and torsion angles are $(\kappa, \tau) \approx (\pi/2, 1)$ and $(\kappa, \tau) \approx (1, \pi)$, respectively.

For a proof of concept, a multistage *in silico* approach was developed [893], building on the complementarity of deterministic molecular dynamics, MD [104] and stochastic MCMC [894] methods. The protocol allows for accelerated sampling of the conformation space and convergence to the biological fold. The RMSD[35] accuracy for the backbone Cα atoms of the topological multi-soliton representation is extremely high, within an Ångström (Fig. B.80**A**). Comparison of the generated synthetic data with the available structural statistics, e.g., from PDB [895], affirms the sampling quality.

A folding trajectory, then, represents a loop on the stereographically projected (κ, τ) sphere, corresponding to a sequence of certain regular secondary structures and endowed with certain topological characteristics. The super-secondary-structure formation during the folding process can be conveniently interpreted and its physical properties analysed in terms of a Bloch domain wall, moving along a Heisenberg spin chain (Fig. B.80**B**); the side chains are akin to the *spin variables*.

[35] The root mean square deviation (RMSD) is given by

$$RMSD(\mathbf{r}_i, \mathbf{r}_i^{ref}) = \left[\frac{1}{\sum_{i=1}^{N} m_i} \sum_{i=1}^{N} m_i \|\mathbf{r}_i - \mathbf{r}_i^{ref}\|^2 \right]^{1/2},$$

where N is the number of atoms, $\{\mathbf{r}_i, \mathbf{r}_i^{ref}\}$ are the atomic positions in the compared structures, and m_i are the respective masses.

The introduction of a folding index, Ind_f [897],

$$Ind_f = [\,\Gamma\,], \tag{B.3}$$

where

$$\Gamma = \frac{1}{\pi}\sum_{i=n_1+2}^{n_2-2}\begin{cases}\tau_i - \tau_{i-1} - 2\pi & \text{if } \tau_i - \tau_{i-1} > \pi \\ \tau_i - \tau_{i-1} + 2\pi & \text{if } \tau_i - \tau_{i-1} < -\pi \\ \tau_i - \tau_{i-1} & \text{otherwise}\end{cases} \tag{B.4}$$

allows for the classification of different loop structures, but also the protein backbone as a whole. This is an integer, which takes negative values by clockwise rotation and positive values otherwise and differs by a factor of two from the number of times the vector in Fig. B.80**B** rotates around its axis when traversing a domain wall. Thus, for loops connecting uniform structures such as two α-helices, or two β-strands, the folding index is an even integer, and an odd integer otherwise. E.g., for the sample loop in Fig. B.80**B**, $Ind_f = -1$. For a more detailed analysis, a folding index can be associated with the side-chain geometry as well [893].

Evidence gained through both analytical considerations and multistage *in silico* experiments thus far strongly supports the proposal that topological solitons may have a pivotal role in understanding the origin of self organization in protein structure and dynamics.

References

[1] C.W. Ashley, The Ashley Book of Knots, Doubleday, 1944.
[2] C.C. Adams, The Knot Book, Freeman, 1994.
[3] L.H. Kauffman, Knots and Applications, World Scientific, 1995.
[4] B.A. Burton, The next 350 million knots, in: 36th International Symposium on Computational Geometry (SoCG 2020), Schloss Dagstuhl-Leibniz-Zentrum für Informatik, 2020, pp. 25:1–-25:17.
[5] V.F.R. Jones, Hecke algebra representations of braid groups and link polynomials, in: New Developments in the Theory of Knots, World Scientific, 1987, pp. 20–73.
[6] L.H. Kauffman, Knots and Physics, vol. 1, World Scientific, 2001.
[7] P. Freyd, D. Yetter, J. Hoste, W.B.R. Lickorish, K. Millett, A. Ocneanu, A new polynomial invariant of knots and links, Bull. (new series) Am. Math. Soc. 12 (2) (1985) 239–246.
[8] J.H. Przytycki, P. Traczyk, Invariants of links of conway type, Kobe J. Math. 4 (1987) 115–139.
[9] A.V. Vologodskii, A.V. Lukashin, M.D. Frank-Kamenetskii, V.V. Anshelevich, The knot problem in statistical mechanics of polymer chains, Sov. Phys.-JETP 39 (1974) 1059–1063.
[10] L. Tubiana, G. Polles, E. Orlandini, C. Micheletti, Kymoknot: A web server and software package to identify and locate knots in trajectories of linear or circular polymers, Eur. Phys. J. E 41 (6) (2018) 72.
[11] C. Micheletti, D. Marenduzzo, E. Orlandini, Polymers with spatial or topological constraints: Theoretical and computational results, Phys. Rep. 504 (2011) 1–73.
[12] P. Dabrowski-Tumanski, P. Rubach, W. Niemyska, B.A. Gren, J.I. Sulkowska, Topoly: Python package to analyze topology of polymers, Brief. Bioinform. 000 (2020) 1–8.
[13] R.G. Scharein, Knotplot, 1998, https://www.knotplot.com/.
[14] W. Stein, D. Joyner, Sage: System for algebra and geometry experimentation, Acm Sigsam Bull. 39 (2) (2005) 61–64.
[15] B. Trefz, J. Siebert, P. Virnau, How molecular knots can pass through each other, Proc. Natl. Acad. Sci. 111 (22) (2014) 7948–7951.
[16] L. Tubiana, Computational study on the progressive factorization of composite polymer knots into separated prime components, Phys. Rev. E 89 (5) (2014) 052602.
[17] S. Najafi, R. Podgornik, R. Potestio, L. Tubiana, Role of bending energy and knot chirality in knot distribution and their effective interaction along stretched semiflexible polymers, Polymers 8 (10) (2016) 347.
[18] R.L. Ricca, B. Nipoti, Gauss' linking number revisited, J. Knot Theory Ramifications 20 (10) (2011) 1325–1343.
[19] J. Douglas, Solution of the problem of plateau, Trans. Amer. Math. Soc. 33 (1) (1931) 263–321.
[20] J. Smrek, A.Y. Grosberg, Minimal surfaces on unconcatenated polymer rings in melt, ACS Macro Lett. 5 (6) (2016) 750–754.
[21] M. Lang, Ring conformations in bidisperse blends of ring polymers, Macromolecules 46 (3) (2013) 1158–1166.
[22] K.A. Brakke, The surface evolver, Exp. Math. 1 (2) (1992) 141–165.
[23] J.J. Van Wijk, A.M. Cohen, Visualization of seifert surfaces, IEEE Trans. Vis. Comput. Graph. 12 (2006) 485.
[24] J.H. Conway, An enumeration of knots and links, and some of their algebraic properties, in: Computational Problems in Abstract Algebra, Elsevier, 1970, pp. 329–358.
[25] D.W. Sumners, Lifting the curtain: Using topology to probe the hidden action of enzymes, Notices Amer. Math. Soc. 42 (1995) 528–537.
[26] S. Hu, M. Lundgren, A.J. Niemi, Discrete frenet frame, inflection point solitons, curve visualization with applications to folded proteins, Phys. Rev. E 83 (2011) 061908.
[27] G. Călugăreanu, Sur les classes d'isotopie des noeuds tridimensionnels et leurs invariants, Czechoslovak Math. J. 11 (4) (1961) 588–625.
[28] H.K. Moffatt, R.L. Ricca, Helicity and the Călugăreanu invariant, Proc. R. Soc. London. Ser. A: Math. Phys. Sci. 439 (1906) (1992) 411–429.
[29] J.H. White, Self-linking and the Gauss integral in higher dimensions, Am. J. Math. 91 (1969) 683–728.
[30] F.B. Fuller, The writhing number of a space curve, Proc. Natl. Acad. Sci. U S A 68 (1971) 815–819.
[31] M.R. Dennis, J.H. Hannay, Geometry of Călugăreanu's theorem, Proc. R. Soc. A: Math., Phys. Eng. Sci. 461 (2062) (2005) 3245–3254.
[32] R.D. Kamien, The geometry of soft materials: A primer, Rev. Modern Phys. 74 (4) (2002) 953–971.
[33] H. Moriuchi, An enumeration of theta-curves with up to seven crossings, J. Knot Theory Ramifications 18 (2) (2009).
[34] S. Yamada, An invariant of spatial graphs, J. Graph Theory 13 (5) (1989) 537–551.
[35] L. Tubiana, E. Orlandini, C. Micheletti, Probing the entanglement and locating knots in ring polymers: A comparative study of different arc closure schemes, Progr. Theoret. Phys. Suppl. 191 (2011) 192–204.
[36] D.W. Sumners, S.G. Whittington, Detecting knots in self-avoiding walks, J. Phys. A: Math. Gen. 23 (1990) 1471–1472.
[37] E.J.J. Van Rensburg, D.W. Sumners, E. Wasserman, S.G. Whittington, Entanglement complexity of self-avoiding walks, J. Phys. A: Math. Gen. 25 (1992) 6557–6566.

[38] M.L. Mansfield, Are there knots in proteins? Nature Structural Biology 1 (4) (1994) 213–214.
[39] B. Marcone, E. Orlandini, A.L. Stella, F. Zonta, What is the length of a knot in a polymer? J. Phys. A: Math. Gen. 38 (2005) L15–L21.
[40] K. Millett, A. Dobay, A. Stasiak, Linear random knots and their scaling behavior, Macromolecules 38 (2) (2005) 601–606.
[41] L. Tubiana, E. Orlandini, C. Micheletti, Multiscale entanglement in ring polymers under spherical confinement, Phys. Rev. Lett. 107 (2011) 188302.
[42] L. Tubiana, H. Kobayashi, R. Potestio, B. Dünweg, K. Kremer, P. Virnau, K. Daoulas, Comparing equilibration schemes of high-molecular-weight polymer melts with topological indicators, J. Phys.: Condens. Matter 33 (20) (2021) 204003.
[43] M. Caraglio, C. Micheletti, E. Orlandini, Physical links: defining and detecting inter-chain entanglement, Sci. Rep. 7 (2017) art no. 1156.
[44] A. Barbensi, N. Yerolemou, O. Vipond, B.I. Mahler, P. Dabrowski-Tumanski, D. Goundaroulis, A topological selection of folding pathways from native states of knotted proteins, Symmetry 13 (2021) 1670.
[45] D. Goundaroulis, J. Dorier, F. Benedetti, A. Stasiak, Studies of global and local entanglements of individual protein chains using the concept of knotoids, Sci. Rep. 7 (1) (2017) 6309.
[46] D. Goundaroulis, N. Gügümcü, S. Lambropoulou, J. Dorier, A. Stasiak, L. Kauffman, Topological models for open-knotted protein chains using the concepts of knotoids and bonded knotoids, Polymers 9 (9) (2017) 444.
[47] J. Dorier, D. Goundaroulis, F. Benedetti, A. Stasiak, Knoto-ID: A tool to study the entanglement of open protein chains using the concept of knotoids, Bioinformatics 34 (19) (2018) 3402–3404.
[48] A. Barbensi, D. Goundaroulis, f-distance of knotoids and protein structure, Proc. R. Soc. Lond. Ser. A Math. Phys. Eng. Sci. 477 (2246) (2021) 20200898.
[49] V. Turaev, Knotoids, Osaka J. Math. 49 (1) (2012) 195–223.
[50] N. Gügümcü, L.H. Kauffman, New invariants of knotoids, European J. Combin. 65 (2017) 186–229.
[51] D. Goundaroulis, J. Dorier, A. Stasiak, A systematic classification of knotoids on the plane and on the sphere, 2019, arXiv preprint arXiv:1902.07277.
[52] A. Barbensi, D. Buck, H.A. Harrington, M. Lackenby, Double branched covers of knotoids, Comm. Anal. Geom. (2018).
[53] D. Goundaroulis, J. Dorier, A. Stasiak, Knotoids and protein structure, Topol. Geom. Biopolym. 746 (2020) 185.
[54] P. Dabrowski-Tumanski, P. Rubach, D. Goundaroulis, J. Dorier, P. Sułkowski, K.C. Millett, E.J. Rawdon, A. Stasiak, J.I. Sulkowska, KnotProt 2.0: A database of proteins with knots and other entangled structures, Nucleic Acids Res. 47 (D1) (2018) D367–D375.
[55] E. Panagiotou, L.H. Kauffman, Knot polynomials of open and closed curves, Proc. R. Soc. Lond. Ser. A Math. Phys. Eng. Sci. 476 (2240) (2020) 20200124.
[56] E. Panagiotou, L.H. Kauffman, Vassiliev measures of complexity of open and closed curves in 3-space, Proc. R. Soc. Lond. Ser. A Math. Phys. Eng. Sci. 477 (2254) (2021) 20210440.
[57] O. Viro, Khovanov homology, its definitions and ramifications, Fund. Math. 184 (2004) 317–342.
[58] N.P. King, E.O. Yeates, T.O. Yeates, Identification of rare slipknots in proteins and their implications for stability and folding, J. Mol. Biol. 373 (1) (2007) 153–166.
[59] J.I. Sulkowska, E.J. Rawdon, K.C. Millett, J.N. Onuchic, A. Stasiak, Conservation of complex knotting and slipknotting patterns in proteins, Proc. Natl. Acad. Sci. 109 (26) (2012) E1715–E1723.
[60] E. Witten, Quantum field theory and the jones polynomial, in: A.N. Mitra (Ed.), Comm. Math. Phys. 121 (1989) 351–399.
[61] M. Kleman, O.D. Lavrentovich, Soft Matter Physics: An Introduction, Springer, New York, 2003.
[62] N.D. Mermin, The topological theory of defects in ordered media, Rev. Modern Phys. 51 (3) (1979) 591–648.
[63] T. Vachaspati, A class of kinks in SU(N) x Z(2), Phys. Rev. D 63 (2001) 105010.
[64] L. Pogosian, T. Vachaspati, Space of kink solutions in SU(N) * Z(2), Phys. Rev. D 64 (2001) 105023.
[65] R.D. Kamien, J.V. Selinger, Order and frustration in chiral liquid crystals, J. Phys.: Condens. Matter 13 (3) (2001) R1.
[66] F.C. Frank, I. Liquid crystals. On the theory of liquid crystals, Discuss. Faraday Soc. 25 (1958) 19–28.
[67] S. Čopar, S. Žumer, Quaternions and hybrid nematic disclinations, Proceedings of the Royal Society A: Mathematical, Physical and Engineering Sciences 469 (2156) (2013) 20130204.
[68] C. Nash, S. Sen, Topology and Geometry for Physicists, Academic Press, 1988.
[69] G.E. Volovik, O.D. Lavrentovich, Topological dynamics of defects: boojums in nematic drops, Sov. Phys.—JETP 58 (December 1983) (1983) 1159–1166.
[70] R. Ondris-Crawford, E.P. Boyko, B.G. Wagner, J.H. Erdmann, S. Žumer, J.W. Doane, Microscope textures of nematic droplets in polymer dispersed liquid crystals, J. Appl. Phys. 69 (9) (1991) 6380–6386.
[71] M. Škarabot, M. Ravnik, S. Žumer, U. Tkalec, I. Poberaj, D. Babič, N. Osterman, I. Muševič, Two-dimensional dipolar nematic colloidal crystals, Phys. Rev. E 76 (2007) 051406.
[72] G.P. Alexander, B.G. Chen, E.A. Matsumoto, R.D. Kamien, Colloquium: Disclination loops, point defects, all that in nematic liquid crystals, Rev. Modern Phys. 84 (2) (2012) 497.
[73] B. Göbel, I. Mertig, O.A. Tretiakov, Beyond skyrmions: Review and perspectives of alternative magnetic quasiparticles, Phys. Rep. 895 (2021) 1.
[74] J.-S. Wu, I.I. Smalyukh, Hopfions, heliknotons, skyrmions, torons and both abelian and nonabelian vortices in chiral liquid crystals, Liquid Cryst. Rev. (2022) 1–35.
[75] P.J. Ackerman, I.I. Smalyukh, Diversity of knot solitons in liquid crystals manifested by linking of preimages in torons and Hopfions, Phys. Rev. X 7 (1) (2017) 011006.
[76] B.G.-g. Chen, P.J. Ackerman, G.P. Alexander, R.D. Kamien, I.I. Smalyukh, Generating the Hopf fibration experimentally in nematic liquid crystals, Phys. Rev. Lett. 110 (23) (2013) 237801.
[77] P.J. Ackerman, I.I. Smalyukh, Static three-dimensional topological solitons in fluid chiral ferromagnets and colloids, Nature Mater. 16 (4) (2017) 426–432.
[78] J.-S.B. Tai, I.I. Smalyukh, Static Hopf solitons and knotted emergent fields in solid-state noncentrosymmetric magnetic nanostructures, Phys. Rev. Lett. 121 (2018) 401.
[79] J.H.C. Whitehead, An expression of Hopf's invariant as an integral, Proc. Natl. Acad. Sci. 33 (5) (1947) 117–123.
[80] L. Woltjer, A theorem on force-free magnetic fields, Proc. Natl. Acad. Sci. 44 (6) (1958) 489–491.
[81] H.K. Moffatt, The degree of knottedness of tangled vortex lines, J. Fluid Mech. 35 (1) (1969) 117–129.
[82] J.J. Moreau, Constantes d'un îlot tourbillonnaire en fluide parfait barotrope, C. R. Hebd. Séances l'Acad. Sci. 252 (1961) 2810–2812.
[83] M.A. Berger, G.B. Field, The topological properties of magnetic helicity, J. Fluid Mech. 147 (1984) 133–148.
[84] X. Liu, R.L. Ricca, The Jones polynomial for fluid knots from helicity, J. Phys. A: Math. Theor. 45 (2012) 205501.
[85] X. Liu, R.L. Ricca, On the derivation of the HOMFLYPT polynomial invariant for fluid knots, J. Fluid Mech. 773 (2015) 34–48.
[86] R.L. Ricca, X. Liu (Eds.), Knotted fields, in: Lecture Notes in Mathematics, Springer-Verlag, in press.
[87] M. Rubinstein, R.H. Colby, Polymer Physics, Oxford University Press, New York, 2003.
[88] S.F. Edwards, Statistical mechanics with topological constraints: I, Proc. Phys. Soc. 91 (3) (1967) 513–519.

[89] S.F. Edwards, Statistical mechanics with topological constraints: II, J. Phys. A: Math. Gen. 1 (1968) 15–28.
[90] M. Doi, S.F. Edwards, The Theory of Polymer Dynamics, Clarendon, Oxford, 1986.
[91] J. Cloizeaux, G. Jannink, Polymers in Solution : their Modelling and Structure, Clarendon Press Oxford University Press, Oxford New York, 1990.
[92] H. Kleinert, Path Integrals in Quantum Mechanics, Statistics, Polymer Physics, World Scientific, Singapore Teaneck, NJ, 1990.
[93] G. Vernizzi, H. Orland, A. Zee, Classification and predictions of RNA pseudoknots based on topological invariants, Phys. Rev. E 94 (2016) 042410.
[94] A. Molochkov, A. Begun, A. Niemi, Gauge symmetries and structure of proteins, in: Y. Foka, N. Brambilla, V. Kovalenko (Eds.), in: EPJ Web of Conferences, vol. 137, EDP Sciences, 2017, p. 04004.
[95] R.K. Manna, P.B.S. Kumar, Emergent topological phenomena in active polymeric fluids, Soft Matter 15 (3) (2019) 477–486.
[96] P.G. De Gennes, Exponents for the excluded volume problem as derived by the Wilson method, Phys. Lett. A 38 (5) (1972) 339–340.
[97] L. Schäfer, Renormalized perturbation theory and field-theoretic renormalization group, in: Excluded Volume Effects in Polymer Solutions, Springer, Berlin, Heidelberg, 1999, pp. 179–205.
[98] F. Ferrari, J. Paturej, M. Piątek, Y. Zhao, Knots, links, anyons and statistical mechanics of entangled polymer rings, Nuclear Phys. B 945 (2019) 114673.
[99] F. Ferrari, A new strategy to microscopic modeling of topological entanglement in polymers based on field theory, Nuclear Phys. B 948 (2019) 114778.
[100] P.J. Flory, Statistical Mechanics of Chain Molecules, Hanser, 1969.
[101] A.Y. Grosberg, A.R. Khokhlov, Statistical physics of macromolecules, AIP series in polymers and complex materials, American Institute of Physics, New York, 1994.
[102] P.-G. De Gennes, Scaling Concepts in Polymer Physics, Cornell University Press, Ithaca, New York, 1979.
[103] G.S. Grest, K. Kremer, Molecular dynamics simulation for polymers in the presence of a heat bath, Phys. Rev. A 33 (1986) 3628–3631.
[104] D. Frenkel, B. Smit, Understanding Molecular Simulation, 2nd Edition, Academic Press, San Diego, 2002.
[105] D. Michieletto, Make or break: building soft materials with DNA, Phys. World 34 (3) (2021) 48–52.
[106] J.D. Watson, F.H.C. Crick, Molecular structure of nucleic acids, Nature 171 (1953) 737–738.
[107] A.D. Bates, A. Maxwell, DNA Topology, Oxford University Press, 2005.
[108] C.R. Calladine, H. Drew, F.B. Luisi, A.A. Travers, Understanding DNA: the Molecule and How It Works, Elsevier Academic Press, 1997.
[109] Wikipedia contributors, Dna, 2024, https://en.wikipedia.org/wiki/DNA,
[110] X. Gao, Y. Hong, F. Ye, J.T. Inman, M.D. Wang, Torsional stiffness of extended and plectonemic DNA, Phys. Rev. Lett. 127 (2) (2021) 28101.
[111] S.B. Smith, Y. Cui, C. Bustamante, Overstretching B-DNA: The elastic response of individual double-stranded and single-stranded DNA molecules, Science 271 (5250) (1996) 795–799.
[112] C.J. Bustamante, Y.R. Chemla, S. Liu, M.D. Wang, Optical tweezers in single-molecule biophysics, Nat. Rev. Methods Primers 1 (1) (2021) 25.
[113] J.C. Wang, Untangling the Double Helix: DNA Entanglement and the Action of the DNA Topoisomerases, Cold Spring Harbor Laboratory Press, 2009.
[114] J. Arsuaga, M. Vázquez, P. McGuirk, S. Trigueros, D.W. Sumners, J. Roca, DNA knots reveal a chiral organization of DNA in phage capsids, Proc. Natl. Acad. Sci. USA 102 (2005) 9165–9169.
[115] M. Gellert, Formation of covalent circles of lambda DNA by E. coli extracts, Proc. Natl. Acad. Sci. 57 (1) (1967) 148–155.
[116] A. Becker, H. Murialdo, Bacteriophage lambda DNA: the beginning of the end, J. Bacteriol. 172 (6) (1990) 2819–2824.
[117] D. Michieletto, P. Neill, S. Weir, D. Evans, N. Crist, V.A. Martinez, R.M. Robertson-Anderson, Topological digestion drives time-varying rheology of entangled DNA fluids, Nature Commun. 13 (1) (2022).
[118] K.N. Kreuzer, N.R. Cozzarelli, Formation and resolution of DNA catenanes by DNA gyrase, Cell 20 (May) (1980) 245–254.
[119] P.D. Dans, J. Walther, H. Gómez, M. Orozco, Multiscale simulation of DNA, Curr. Opin. Struct. Biol. 37 (2016) 29–45.
[120] T. Schlick, S. Portillo-Ledesma, Biomolecular modeling thrives in the age of technology, Nat. Comput. Sci. 1 (5) (2021) 321–331.
[121] J. Smrek, J. Garamella, R. Robertson-Anderson, D. Michieletto, Topological tuning of DNA mobility in entangled solutions of supercoiled plasmids, Sci. Adv. 7 (20) (2021).
[122] J.F. Marko, E.D. Siggia, Bending and twisting elasticity of DNA, Macromolecules 27 (4) (1994) 981–988.
[123] B.E. Snodin, F. Randisi, M. Mosayebi, P. Šulc, J.S. Schreck, F. Romano, T.E. Ouldridge, R. Tsukanov, E. Nir, A.A. Louis, et al., Introducing improved structural properties and salt dependence into a coarse-grained model of DNA, J. Chem. Phys. 142 (23) (2015).
[124] E. Skoruppa, S.K. Nomidis, J.F. Marko, E. Carlon, Bend-induced twist waves and the structure of nucleosomal DNA, Phys. Rev. Lett. 121 (8) (2018) 2–6.
[125] J.N. Onuchic, Z. Luthey-Schulten, P.G. Wolynes, Theory of protein folding: The energy landscape perspective, Annu. Rev. Phys. Chem. 48 (1) (1997) 545–600.
[126] T.C. Lubensky, D. Pettey, N. Currier, H. Stark, Topological defects and interactions in nematic emulsions, Phys. Rev. E 57 (1998) 610.
[127] U. Tkalec, M. Ravnik, S. Čopar, S. Žumer, I. Muševič, Reconfigurable knots and links in chiral nematic colloids, Science 333 (2011) 62.
[128] J. Pollard, G. Posnjak, S. Čopar, I. Muševič, G.P. Alexander, Point defects, topological chirality, and singularity theory in cholesteric liquid-crystal droplets, Phys. Rev. X 9 (2019) 1442.
[129] I. Muševič, Nematic colloids, topology and photonics, Phil. Trans. R. Soc. A 371 (2013) 20120266.
[130] Wikipedia contributors, Liquid crystal, 2022, https://en.wikipedia.org/wiki/Liquid_crystal,
[131] M. Nikkhou, M. Škarabot, S. Čopar, I. Muševič, Dynamics of topological monopoles annihilation on a fibre in a thick and thin nematic layer, Eur. Phys. J. E 39 (10) (2016) 1–7.
[132] P.M. Chaikin, T.C. Lubensky, Principles of Condensed Matter Physics, vol. 10, Cambridge University Press, Cambridge, 1995.
[133] M. Ravnik, S. Žumer, Landau–De Gennes modelling of nematic liquid crystal colloids, Liq. Cryst. 36 (10–11) (2009) 1201–1214.
[134] H.L. Frisch, E. Wasserman, Chemical topology, J. Am. Chem. Soc. 83 (1961) 3789–3795.
[135] M. Delbruck, Knotting problems in biology, Plant Genome Data Inf. Cent. Collect. Comput. Mol. Biol. Genet. (1961).
[136] L.F. Liu, D.R. E., W.J. C., Knotted single-stranded DNA rings: A novel topological isomer of circular single-stranded DNA formed by treatment with Escherichia coli ω protein, J. Mol. Biol. 106 (2) (1976) 439–452.
[137] L.F. Liu, L. Perkocha, R. Calendar, J.C. Wang, Knotted DNA from bacteriophage capsids, Proc. Natl. Acad. Sci. 78 (9) (1981) 5498–5502.
[138] L.F. Liu, J.L. Davis, R. Calendar, Novel topologically knotted DNA from bacteriophage P4 capsids: studies with DNA topoisomerases, Nucleic Acids Res. 9 (16) (1981) 3979–3989.
[139] D.W. Sumners, S.G. Whittington, Knots in self-avoiding walks, J. Phys. A: Math. Gen. 21 (1988) 1689–1694.
[140] Y. Diao, N. Pippenger, D.W. Sumners, On random knots, J. Knot Theory Ramifications 3 (03) (1994) 419–429.
[141] Y. Diao, The knotting of equilateral polygons in R^3, J. Knot Theory Ramifications 4 (1995) 189–196.
[142] E. Orlandini, M.C. Tesi, E.J.J. Van Rensburg, S.G. Whittington, Asymptotics of knotted lattice polygons, J. Phys. A: Math. Gen. 31 (1998) 5953–5967.
[143] S.A. Wasserman, N.R. Cozzarelli, Biochemical topology: applications to DNA recombination and replication, Science 232 (1986) 951–960.

[144] A. Valdés, J. Segura, S. Dyson, B. Martínez-García, J. Roca, DNA knots occur in intracellular chromatin, Nucleic Acids Res. 46 (2) (2018) 650–660.
[145] C. Ernst, D.W. Sumners, A calculus for rational tangles: Applications to DNA recombination, Math. Proc. Camb. Phil. Soc. 108 (3) (1990) 489–515.
[146] V.V. Rybenkov, N.R. Cozzarelli, A.V. Vologodskii, Probability of DNA knotting and the effective diameter of the DNA double helix, Proc. Natl. Acad. Sci. USA 90 (1993) 5307–5311.
[147] M.C. Tesi, E.J.J. Van Rensburg, E. Orlandini, D.W. Sumners, S.G. Whittington, Knotting and supercoiling in circular DNA: A model incorporating the effect of added salt, Phys. Rev. E 49 (1) (1994) 868.
[148] J. Vinograd, J. Lebowitz, R. Radloff, R. Watson, P. Laipis, The twisted circular form of polyoma viral DNA, Proc. Natl. Acad. Sci. USA 53 (5) (1965) 1104–1111.
[149] J. Menissier, G. De Murcia, G. Lebeurier, L. Hirth, Electron microscopic studies of the different topological forms of the cauliflower mosaic virus DNA: knotted encapsidated DNA and nuclear minichromosome, EMBO J. 2 (7) (1983) 1067–1071.
[150] J. Arsuaga, M. Vázquez, S. Trigueros, D. Sumners, J. Roca, Knotting probability of DNA molecules confined in restricted volumes: DNA knotting in phage capsids, Proc. Natl. Acad. Sci. USA 99 (8) (2002) 5373–5377.
[151] K. Shishido, N. Komiyama, S. Ikawa, Increased production of a knotted form of plasmid pBR322 DNA in Escherichia coli DNA topoisomerase mutants, J. Mol. Biol. 195 (1) (1987) 215–218.
[152] J.M. Sogo, A. Stasiak, M.L. Martínez-Robles, D.B. Krimer, P. Hernández, J.B. Schvartzman, Formation of knots in partially replicated DNA molecules, J. Mol. Biol. 286 (3) (1999) 637–643.
[153] D. Goundaroulis, E. Lieberman Aiden, A. Stasiak, Chromatin is frequently unknotted at the megabase scale, Biophys. J. 118 (9) (2020) 2268–2279.
[154] D. Marenduzzo, E. Orlandini, A. Stasiak, d.W. Sumners, L. Tubiana, C. Micheletti, DNA-DNA interactions in bacteriophage capsids are responsible for the observed DNA knotting, Proc. Natl. Acad. Sci. U. S. A. 106 (52) (2009) 22269–22274.
[155] A.Y. Grosberg, Critical exponents for random knots, Phys. Rev. Lett. 85 (2000) 3858–3862.
[156] J.M. Deutsch, Equilibrium size of large ring molecules, Phys. Rev. E 59 (3) (1999) R2539–R2541.
[157] J. des Cloizeaux, Ring polymers in solution: Topological effects, J. Physique – Lett. 42 (1981) L433–L436.
[158] C.M. Rohwer, K.K. Müller-Nedebock, Operator formalism for topology-conserving crossing dynamics in planar knot diagrams, J. Stat. Phys. 159 (1) (2015) 120–157.
[159] A.Y. Grosberg, A. Feigel, Y. Rabin, Flory-type theory of a knotted ring polymer, Phys. Rev. E 54 (1996) 6618–6622.
[160] V. Katritch, J. Bednar, D. Michoud, R.G. Scharein, J. Dubochet, A. Stasiak, Geometry and physics of knots, Nature 384 (1996) 142–145.
[161] A. Stasiak, V. Katritch, J. Bednar, D. Michoud, J. Dubochet, Electrophoretic mobility of DNA knots, Nature 384 (6605) (1996) 122.
[162] L. Tubiana, A. Rosa, F. Fragiacomo, C. Micheletti, Spontaneous knotting and unknotting of flexible linear polymers: Equilibrium and kinetic aspects, Macromolecules 46 (2013) 3669–3678.
[163] E. Orlandini, Statics and dynamics of DNA knotting, J. Phys. A 51 (5) (2017) 053001.
[164] E. Orlandini, S.G. Whittington, Statistical topology of closed curves: Some applications in polymer physics, Rev. Modern Phys. 79 (2) (2007) 611.
[165] K. Kremer, G.S. Grest, Dynamics of entangled linear polymer melts: A molecular-dynamics simulation, J. Chem. Phys. 92 (8) (1990) 5057.
[166] F.C. Rieger, P. Virnau, A Monte Carlo study of knots in long double-stranded DNA chains, PLoS Comput. Biol. 12 (9) (2016) e1005029.
[167] P. Virnau, Y. Kantor, M. Kardar, Knots in globule and coil phases of a model polyethylene, J. Am. Chem. Soc. 127 (2005) 15102–15106.
[168] C. Micheletti, E. Orlandini, Numerical study of linear and circular model DNA chains confined in a slit: Metric and topological properties, Macromolecules 45 (2012) 2113–2121.
[169] A.Y. Grosberg, Y. Rabin, Metastable tight knots in a wormlike polymer, Phys. Rev. Lett. 99 (2007) 217801.
[170] J. Tang, D. Ning, P.S. Doyle, Compression and self-entanglement of single DNA molecules under uniform electric field, Proc. Natl. Acad. Sci. U. S. A. 108 (39) (2011) 16153–16158.
[171] C.B. Renner, P.S. Doyle, Untying knotted DNA with elongational flows, ACS Macro Lett. 3 (2014) 963—-967.
[172] L. Dai, C.B. Renner, P.S. Doyle, Origin of metastable knots in single flexible chains, Phys. Rev. Lett. 114 (2015) 037801.
[173] J.I. Sulkowska, P. Sułkowski, J. Onuchic, Dodging the crisis of folding proteins with knots, Proc. Natl. Acad. Sci. 106 (9) (2009) 3119–3124.
[174] S. Wettermann, M. Brems, J.T. Siebert, G.T. Vu, T.J. Stevens, P. Virnau, A minimal Gō-model for rebuilding whole genome structures from haploid single-cell Hi-C data, Comput. Mater. Sci. 173 (April 2019) (2020).
[175] C. Plesa, D. Verschueren, S. Pud, J. van der Torre, J.W. Ruitenberg, M.J. Witteveen, M.P. Jonsson, A.Y. Grosberg, Y. Rabin, C. Dekker, Direct observation of DNA knots using a solid-state nanopore, Nature Nanotechnol. 11 (12) (2016) 1093–1097.
[176] R. Kumar Sharma, I. Agrawal, L. Dai, P.S. Doyle, S. Garaj, Complex DNA knots detected with a nanopore sensor, Nat. Commun. 10 (1) (2019) 4473.
[177] X.R. Bao, H.J. Lee, S.R. Quake, Behavior of complex knots in single DNA molecules, Phys. Rev. Lett. 91 (2003) 265506.
[178] J.G. Reifenberger, K.D. Dorfman, H. Cao, Topological events in single molecules of e. coli DNA confined in nanochannels, Analyst 140 (14) (2015) 4887–4894.
[179] R.L. Welch, R. Sladek, K. Dewar, W.W. Reisner, Denaturation mapping of saccharomyces cerevisiae, Lab Chip 12 (18) (2012) 3314–3321.
[180] Y. Arai, R. Yasuda, K. Akashi, Y. Harada, H. Miyata, T. Kinosita, H. Itoh, Tying a molecular knot with optical tweezers, Nature 399 (1999) 446–448.
[181] S. Amin, A. Khorshid, L. Zeng, P. Zimny, W. Reisner, A nanofluidic knot factory based on compression of single DNA in nanochannels, Nature Commun. 9 (1) (2018) 1506.
[182] Z. Ma, K.D. Dorfman, Diffusion of knots along DNA confined in nanochannels, Macromolecules 53 (15) (2020) 6461–6468.
[183] A.R. Klotz, B.W. Soh, P.S. Doyle, An experimental investigation of attraction between knots in a stretched DNA molecule, Europhys. Lett. 129 (2020) 68001.
[184] C.B. Renner, P.S. Doyle, Stretching self-entangled DNA molecules in elongational fields, Soft Matter 11 (2015) 3105–3114.
[185] R. Metzler, W. Reisner, R. Riehn, R. Austin, J.O. Tegenfeldt, I.M. Sokolov, Diffusion mechanisms of localised knots along a polymer, Europhys. Lett. 76 (4) (2006) 696.
[186] Z. Ma, K.D. Dorfman, Diffusion of knotted DNA molecules in nanochannels in the extended de gennes regime, Macromolecules 54 (9) (2021) 4211–4218.
[187] Z. Ma, K.D. Dorfman, Interactions between two knots in nanochannel-confined DNA molecules, J. Chem. Phys. 155 (15) (2021) 154901.
[188] J. Rothörl, S. Wettermann, P. Virnau, A. Bhattacharya, Knot formation of dsDNA pushed inside a nanochannel, Sci. Rep. 12 (1) (2022) 5342.
[189] A.R. Klotz, V. Narsimhan, B.W. Soh, P.S. Doyle, Dynamics of DNA knots during chain relaxation, Macromolecules 50 (10) (2017) 4074–4082.
[190] D. Michieletto, D. Marenduzzo, E. Orlandini, Topological patterns in two-dimensional gel electrophoresis of DNA knots, Proc. Natl. Acad. Sci. USA (2015) E5471—-E5477.
[191] L. Dai, P.S. Doyle, Universal knot spectra for confined polymers, ACS Macro Lett. 51 (2018) 6327—-6333.
[192] M.L. Mansfield, J.F. Douglas, Properties of knotted ring polymers. I. Equilibrium dimensions, J. Chem. Phys. 133 (4) (2010) 044903.
[193] K. Radhakrishnan, S.P. Singh, Compression of a confined semiflexible polymer under direct and oscillating fields, Phys. Rev. E 108 (1) (2023) 014501.

[194] V. Narsimhan, A.R. Klotz, P.S. Doyle, Steady-state and transient behavior of knotted chains in extensional fields, ACS Macro Lett. 6 (11) (2017) 1285–1289.
[195] B.W. Soh, A.R. Klotz, P.S. Doyle, Untying of complex knots on stretched polymers in elongational fields, Macromolecules 51 (2018) 9562–9571.
[196] M. Caraglio, F. Baldovin, B. Marcone, E. Orlandini, A.L. Stella, Topological disentanglement dynamics of torus knots on open linear polymers, ACS Macro Lett. 8 (5) (2019) 576–581.
[197] A.R. Klotz, B.W. Soh, P.S. Doyle, Motion of knots in DNA stretched by elongational fields, Phys. Rev. Lett. 120 (120) (2018) 188003.
[198] B.W. Soh, A.R. Klotz, L. Dai, P.S. Doyle, Conformational state hopping of knots in tensioned polymer chains, ACS Macro Lett. 8 (2019) 905–911.
[199] B.W. Soh, A. Khorshid, D. Al Sulaiman, P.S. Doyle, Ionic effects on the equilibrium conformation of catenated DNA networks, Macromolecules 53 (19) (2020) 8502–8508.
[200] R. Matthews, A.A. Louis, J.M. Yeomans, Knot-controlled ejection of a polymer from a virus capsid, Phys. Rev. Lett. 102 (2009) 088101.
[201] A. Rosa, M. Di Ventra, C. Micheletti, Topological jamming of spontaneously knotted polyelectrolyte chains driven through a nanopore, Phys. Rev. Lett. 109 (2012) 118301.
[202] Á. San Martín, P. Rodriguez-Aliaga, J.A. Molina, A. Martin, C. Bustamante, M. Baez, Knots can impair protein degradation by ATP-dependent proteases, Proc. Natl. Acad. Sci. 114 (37) (2017) 9864–9869.
[203] F. Ziegler, N.C.H. Lim, S.S. Mandal, B. Pelz, W.-P. Ng, M. Schlierf, S.E. Jackson, M. Rief, Knotting and unknotting of a protein in single molecule experiments, Proc. Natl. Acad. Sci. USA 113 (27) (2016) 7533–7538.
[204] M.K. Sriramoju, Y. Chen, Y.-T.C. Lee, S.-T.D. Hsu, Topologically knotted deubiquitinases exhibit unprecedented mechanostability to withstand the proteolysis by an aaa+ protease, Sci. Rep. 8 (1) (2018) 1–9.
[205] E.M. Sivertsson, S.E. Jackson, L.S. Itzhaki, The AAA+ protease clpxp can easily degrade a 3 1 and a 5 2-knotted protein, Sci. Rep. 9 (1) (2019) 1–14.
[206] S.E. Jackson, Why are there knots in proteins? Topol. Geom. Biopolym. 746 (2020) 129.
[207] B.W. Soh, V. Narsimhan, A.R. Klotz, P.S. Doyle, Knots modify the coil-stretch transition in linear DNA polymers, Soft Matter 14 (2018) 1689–1698.
[208] M. Caraglio, E. Orlandini, C. Micheletti, Stretching response of knotted and unknotted polymer chains, Phys. Rev. Lett. 115 (2015) 188301.
[209] M. Di Stefano, L. Tubiana, M. Di Ventra, C. Micheletti, Driving knots on DNA with AC/DC electric fields: topological friction and memory effects, Soft Matter 10 (2014) 6491–6498.
[210] J.S. Richardson, β-Sheet topology and the relatedness of proteins, Nature 268 (5620) (1977) 495–500.
[211] W.R. Taylor, A deeply knotted protein structure and how it might fold, Nature 406 (2000) 916–919.
[212] A.I. Jarmolinska, A.P. Perlinska, R. Runkel, B. Trefz, H.M. Ginn, P. Virnau, J.I. Sulkowska, Proteins' knotty problems, J. Mol. Biol. 431 (2) (2019) 244–257.
[213] S.E. Jackson, A. Suma, C. Micheletti, How to fold intricately: using theory and experiments to unravel the properties of knotted proteins, Current opinion in structural biology 42 (2017) 6–14.
[214] J.I. Sulkowska, On folding of entangled proteins: knots, lassos, links and θ-curves, Curr. Opin. Struct. Biol. 60 (2020) 131–141.
[215] J.W. Schmidberger, J.A. Wilce, A.J. Weightman, J.C. Whisstock, M.C.J. Wilce, The crystal structure of dehi reveals a new α-haloacid dehalogenase fold and active-site mechanism, J. Mol. Biol. 378 (1) (2008) 284–294.
[216] D. Bölinger, J.I. Sulkowska, H.-P. Hsu, L.A. Mirny, M. Kardar, J.N. Onuchic, P. Virnau, A Stevedore's protein knot, PLoS Comput. Biol. 6 (4) (2010) e1000731.
[217] A.V. Vologodskii, A.V. Lukashin, M.D. Frank-Kamenetskii, Topological interaction between polymer chains, Sov. Phys.-JETP 40 (5) (1975) 932–936.
[218] A.R. Khokhlov, S.K. Nechaev, Polymer chain in an array of obstacles, Phys. Lett. A 112 (3) (1985) 156–160.
[219] M. Rubinstein, Dynamics of ring polymers in the presence of fixed obstacles, Phys. Rev. Lett. 57 (1986) 3023–3026.
[220] M.E. Cates, J.M. Deutsch, Conjectures on the statistics of ring polymers, J. Physique 47 (12) (1986) 2121–2128.
[221] T. Sakaue, Ring polymers in melts and solutions: Scaling and crossover, Phys. Rev. Lett. 106 (2011) 167802.
[222] M. Kapnistos, M. Lang, D. Vlassopoulos, W. Pyckhout-Hintzen, D. Richter, D. Cho, C. T., M. Rubinstein, Unexpected power-law stress relaxation of entangled ring polymers, Nature Mater. 7 (2008) 997–1002.
[223] S.T. Milner, J.D. Newhall, Stress relaxation in entangled melts of unlinked ring polymers, Phys. Rev. Lett. 105 (2010) 208302.
[224] G. Tsolou, N. Stratikis, C. Baig, P.S. Stephanou, V.G. Mavrantzas, Melt structure and dynamics of unentangled poluethylene rings: Rouse theory, atomistic molecular dynamics simulation, comparison with the linear analogues, Macromolecules 43 (2010) 10692.
[225] J.D. Halverson, W.B. Lee, G.S. Grest, A.Y. Grosberg, K. Kremer, Molecular dynamics simulation study of nonconcatenated ring polymers in a melt. II. Dynamics, J. Chem. Phys. 134 (2011) 204905.
[226] S. Goossen, A.R. Brás, M. Krutyeva, M. Sharp, P. Falus, A. Feoktystov, U. Gasser, W. Pyckhout-Hintzen, A. Wischnewski, D. Richter, Molecular scale dynamics of large ring polymers, Phys. Rev. Lett. 113 (16) (2014) 168302.
[227] J. Smrek, A.Y. Grosberg, Understanding the dynamics of rings in the melt in terms of the annealed tree model, J. Phys.: Condens. Matter 27 (6) (2015) 064117.
[228] T. Ge, S. Panyukov, M. Rubinstein, Self-similar conformations and dynamics in entangled melts and solutions of nonconcatenated ring polymers, Macromolecules 49 (2) (2016) 708–722.
[229] D.G. Tsalikis, T. Koukoulas, V.G. Mavrantzas, R. Pasquino, D. Vlassopoulos, W. Pyckhout-Hintzen, A. Wischnewski, M. Monkenbusch, D. Richter, Microscopic structure, conformation, dynamics of ring and linear poly(ethylene oxide) melts from detailed atomistic molecular dynamics simulations: Dependence on chain length and direct comparison with experimental data, Macromolecules 50 (6) (2017) 2565–2584.
[230] M.Q. Tu, O. Davydovich, B. Mei, P.K. Singh, G.S. Grest, K.S. Schweizer, T.C. O'Connor, C.M. Schroeder, Unexpected slow relaxation dynamics in pure ring polymers arise from intermolecular interactions, ACS Polym. Au 3 (4) (2023) 307–317.
[231] D. Chen, K. Molnar, H. Kim, C.A. Helfer, G. Kaszas, J.E. Puskas, J.A. Kornfield, G.B. McKenna, Linear viscoelastic properties of putative cyclic polymers synthesized by reversible radical recombination polymerization (R3P), Macromolecules 56 (3) (2023) 1013–1032.
[232] J.D. Halverson, J. Smrek, K. Kremer, A.Y. Grosberg, From a melt of rings to chromosome territories: The role of topological constraints in genome folding, Rep. Progr. Phys. 77 (2) (2014) 022601.
[233] T. Cremer, C. Cremer, Chromosome territories, nuclear architecture and gene regulation in mammalian cells, Nature Rev. Genet. 2 (4) (2001) 292–301.
[234] A. Rosa, R. Everaers, Structure and dynamics of interphase chromosomes, PLOS Comp. Biol. 4 (2008) e1000153.
[235] A. Grosberg, Y. Rabin, S. Havlin, A. Neer, Crumpled globule model of the three-dimensional structure of DNA, Europhys. Lett. 23 (5) (1993) 373–378.
[236] D. Needleman, Z. Dogic, Active matter at the interface between materials science and cell biology, Nat. Rev. Mater. 2 (9) (2017) 1–14.
[237] R.D. Vale, The molecular motor toolbox for intracellular transport, Cell 112 (4) (2003) 467–480.
[238] A. Zidovska, D.A. Weitz, T.J. Mitchison, Micron-scale coherence in interphase chromatin dynamics, Proc. Natl. Acad. Sci. 110 (39) (2013) 15555–15560.
[239] R.G. Winkler, G. Gompper, The physics of active polymers and filaments, J. Chem. Phys. 153 (4) (2020) 040901.

[240] A. Joshi, E. Putzig, A. Baskaran, M.F. Hagan, The interplay between activity and filament flexibility determines the emergent properties of active nematics, Soft Matter 15 (1) (2019) 94–101.
[241] R. Zhang, S.A. Redford, P.V. Ruijgrok, N. Kumar, A. Mozaffari, S. Zemsky, A.R. Dinner, V. Vitelli, Z. Bryant, M.L. Gardel, J.J. de Pablo, Spatiotemporal control of liquid crystal structure and dynamics through activity patterning, Nat. Mater. 20 (6) (2021) 875–882.
[242] G.A. Vliegenthart, A. Ravichandran, M. Ripoll, T. Auth, G. Gompper, Filamentous active matter: Band formation, bending, buckling, and defects, Sci. Adv. 6 (30) (2020) eaaw9975.
[243] J. Smrek, I. Chubak, C.N. Likos, K. Kremer, Active topological glass, Nature Commun. 11 (1) (2020) 26.
[244] D. Saintillan, M.J. Shelley, A. Zidovska, Extensile motor activity drives coherent motions in a model of interphase chromatin, Proc. Natl. Acad. Sci. USA 115 (45) (2018) 11442–11447.
[245] V.P. Patil, H. Tuazon, E. Kaufman, T. Chakrabortty, D. Qin, J. Dunkel, M.S. Bhamla, Ultrafast reversible self-assembly of living tangled matter, Science 380 (6643) (2023) 392–398.
[246] A. Deblais, A.C. Maggs, D. Bonn, S. Woutersen, Phase separation by entanglement of active polymerlike worms, Phys. Rev. Lett. 124 (20) (2020) 208006.
[247] A. Mahajan, W. Yan, A. Zidovska, D. Saintillan, M.J. Shelley, Euchromatin activity enhances segregation and compaction of heterochromatin in the cell nucleus, Phys. Rev. X 12 (4) (2022) 041033.
[248] I. Chubak, C.N. Likos, K. Kremer, J. Smrek, Emergence of active topological glass through directed chain dynamics and nonequilibrium phase segregation, Phys. Rev. Res. 2 (2020) 043249.
[249] D. Michieletto, M.S. Turner, A topologically driven glass in ring polymers, Proc. Natl. Acad. Sci. USA 113 (19) (2016) 5195–5200.
[250] D. Michieletto, N. Nahali, A. Rosa, Glassiness and heterogeneous dynamics in dense solutions of ring polymers, Phys. Rev. Lett. 119 (2017) 197801.
[251] E. Locatelli, V. Bianco, P. Malgaretti, Activity-induced collapse and arrest of active polymer rings, Phys. Rev. Lett. 126 (9) (2021) 097801.
[252] A.R. Tejedor, J. Ramirez, Reptation of active entangled polymers, Macromolecules 52 (22) (2019) 8788–8792.
[253] A.R. Tejedor, R. Carracedo, J. Ramírez, Molecular dynamics simulations of active entangled polymers reptating through a passive mesh, Polymer (2023) 125677.
[254] W. Savoie, H. Tuazon, I. Tiwari, M.S. Bhamla, D.I. Goldman, Amorphous entangled active matter, Soft Matter (2023).
[255] A. Deblais, S. Woutersen, D. Bonn, Rheology of entangled active polymer-like t. tubifex worms, Phys. Rev. Lett. 124 (18) (2020) 188002.
[256] A. Deblais, K. Prathyusha, R. Sinaasappel, H. Tuazon, I. Tiwari, V.P. Patil, M.S. Bhamla, Worm blobs as entangled living polymers: from topological active matter to flexible soft robot collectives, Soft Matter 19 (37) (2023) 7057–7069.
[257] M. Baiesi, E. Orlandini, A. Trovato, F. Seno, Linking in domain-swapped protein dimers, Sci. Rep. 6 (1) (2016) 1–11.
[258] W. Niemyska, P. Dabrowski-Tumanski, M. Kadlof, E. Haglund, P. Sułkowski, J.I. Sulkowska, Complex lasso: new entangled motifs in proteins, Sci. Rep. 6 (1) (2016) 36895.
[259] P. Dabrowski-Tumanski, J.I. Sulkowska, To tie or not to tie? That is the question, Polymers 9 (9) (2017).
[260] D.A. Nissley, Y. Jiang, F. Trovato, I. Sitarik, K.B. Narayan, P. To, Y. Xia, S.D. Fried, E.P. O'Brien, Universal protein misfolding intermediates can bypass the proteostasis network and remain soluble and less functional, Nat. Commun. 13 (1) (2022) 3081.
[261] Y. Jiang, S.S. Neti, I. Sitarik, P. Pradhan, P. To, Y. Xia, S.D. Fried, S.J. Booker, E.P. O'Brien, How synonymous mutations alter enzyme structure and function over long timescales, Nature Chem. 15 (3) (2023) 308–318.
[262] M. Baiesi, E. Orlandini, F. Seno, A. Trovato, Sequence and structural patterns detected in entangled proteins reveal the importance of co-translational folding, Sci. Rep. 9 (1) (2019) 1–12.
[263] M. Baiesi, E. Orlandini, F. Seno, A. Trovato, Exploring the correlation between the folding rates of proteins and the entanglement of their native states, J. Phys. A 50 (2017) 504001.
[264] L.P. Simpson, Morphogenesis and the function of the kinetoplast in "leishmania", Atlas Symposia Sobre Biota Amazonica (Pathologia) 6 (1967) 231–234.
[265] J. Chen, C.A. Rauch, J.H. White, P.T. Englund, N.R. Cozzarelli, The topology of the kinetoplast DNA network, Cell 80 (1995) 61–69.
[266] C. Brack, E. Delain, G. Riou, B. Festy, Molecular organization of the kinetoplast DNA of trypanosoma cruzi treated with berenil, a DNA interacting drug, J. Ultrasruct. Res. 39 (5–6) (1972) 568–579.
[267] L. Simpson, A. da Silva, Isolation and characterization of kinetoplast DNA from leishmania tarentolae, J. Mol. Biol. 56 (3) (1971) 443–473.
[268] A.R. Klotz, B.W. Soh, P.S. Doyle, Equilibrium structure and deformation response of 2D kinetoplast sheets, Proc. Natl. Acad. Sci. USA 117 (1) (2020) 121–127.
[269] P. He, A.J. Katan, L. Tubiana, C. Dekker, D. Michieletto, Single-molecule structure and topology of kinetoplast DNA networks, Phys. Rev. X 13 (2023) 021010.
[270] Y. Diao, K. Hinson, R. Kaplan, M. Vazquez, J. Arsuaga, The effects of density on the topological structure of the mitochondrial DNA from trypanosomes, J. Math. Biol. 64 (2012) 1087–1108.
[271] D. Michieletto, D. Marenduzzo, E. Orlandini, Is the kinetoplast DNA a percolating network of linked rings at its critical point? Phys. Biol. 12 (1) (2015) 036001.
[272] Q. Wu, P.M. Rauscher, X. Lang, R.J. Wojtecki, J.J. de Pablo, M.J.A. Hore, S.J. Rowan, Poly[n]catenanes: Synthesis of molecular interlocked chains, Science 358 (6369) (2017) 1434–1439.
[273] M.A. Krasnow, N.R. Cozzarelli, Catenation of DNA rings by topoisomerases. Mechanism of control by spermidine, J. Biol. Chem. 257 (5) (1982) 2687–2693.
[274] B.A. Krajina, A. Zhu, S.C. Heilshorn, A.J. Spakowitz, Active DNA olympic hydrogels driven by topoisomerase activity, Phys. Rev. Lett. 121 (14) (2018) 148001.
[275] T.A. Vilgis, M. Otto, Elasticity of entangled polymer loops: Olympic gels, Phys. Rev. E 56 (1997) R1314–R1317.
[276] M. Lang, J. Fischer, M. Werner, J.-U. Sommer, Swelling of olympic gels, Phys. Rev. Lett. 112 (2014) 238001.
[277] Z. Ahmadian Dehaghani, I. Chubak, C.N. Likos, M.R. Ejtehadi, Effects of topological constraints on linked ring polymers in solvents of varying quality, Soft Matter 16 (2020) 3029–3038.
[278] B. Alberts, A. Johnson, J. Lewis, M. Raff, K. Roberts, P. Walter, Molecular Biology of the Cell: fifth edition, (Garland Science (Taylor and Francis)), New York, 2007.
[279] L. Postow, C.D. Hardy, J. Arsuaga, N.R. Cozzarelli, Topological domain structure of the Escherichia coli chromosome, Genes Dev. 18 (14) (2004) 1766–1779.
[280] B.J. Peter, J. Arsuaga, A.M. Breier, A.B. Khodursky, P.O. Brown, N.R. Cozzarelli, Genomic transcriptional response to loss of chromosomal supercoiling in *Escherichia coli*, Genome Biol. 5 (11) (2004) R87.
[281] A. Goriely, Twisted elastic rings and the rediscoveries of Michell's instability, J. Elasticity 84 (2006) 281–299.
[282] S. Wasserman, J. Dungan, N. Cozzarelli, Discovery of a predicted DNA knot substantiates a model for site-specific recombination, Science 229 (4709) (1985) 171–174.
[283] F.J. Olorunniji, D.E. Buck, S.D. Colloms, A.R. McEwan, M.C. Smith, W.M. Stark, S.J. Rosser, Gated rotation mechanism of site-specific recombination by ΦC31 integrase, Proc. Natl. Acad. Sci. USA 109 (48) (2012) 19661–19666.

[284] N.R. Cozzarelli, S. De Witt, N.R. Cozzarelli, Analysis of the mechanism of DNA recombination using tangles, Q. Rev. Biophys. 28 (3) (1995) 253–313.
[285] Y. Saka, M. Vazquez, TangleSolve: topological analysis of site-specific recombination, Bioinformatics 18 (7) (2002) 1011–1012.
[286] I.K. Darcy, R.G. Scharein, TopoICE-R: 3D visualization modeling the topology of DNA recombination, Bioinformatics 22 (14) (2006) 1790–1791.
[287] I.K. Darcy, Modeling protein–DNA complexes with tangles, Comput. Math. Appl. 55 (5) (2008) 924–937.
[288] W.M. Stark, D.J. Sherratt, M.R. Boocock, Site-specific recombination by Tn3 resolvase: topological changes in the forward and reverse reactions, Cell 58 (4) (1989) 779–790.
[289] S.D. Colloms, J. Bath, D.J. Sherratt, Topological selectivity in xer site-specific recombination, Cell 88 (6) (1997) 855–864.
[290] M. Vazquez, S.D. Colloms, D.W. Sumners, Tangle analysis of xer recombination reveals only three solutions, all consistent with a single three-dimensional topological pathway, J. Mol. Biol. 346 (2) (2005) 493–504.
[291] P. Pieranski, S. Kasas, G. Dietler, J. Dubochet, A. Stasiak, Localization of breakage points in knotted strings, New J. Phys. 3 (1) (2001) 10.
[292] H. Uehara, H. Kimura, A. Aoyama, T. Yamanobe, T. Komoto, Effects of knot characteristics on tensile breaking of a polymeric monofilament, New J. Phys. 9 (3) (2007) 65.
[293] A.M. Saitta, P.D. Soper, E. Wasserman, M.L. Klein, Influence of a knot on the strength of a polymer strand, Nature 399 (6731) (1999) 46–48.
[294] M.K. Jawed, P. Dieleman, B. Audoly, P.M. Reis, Untangling the mechanics and topology in the frictional response of long overhand elastic knots, Phys. Rev. Lett. 115 (11) (2015) 118302.
[295] B. Audoly, N. Clauvelin, S. Neukirch, Elastic knots, Phys. Rev. Lett. 99 (16) (2007) 164301.
[296] P. Johanns, C. Baek, P. Grandgeorge, S. Guerid, S.A. Chester, P.M. Reis, The strength of surgical knots involves a critical interplay between friction and elastoplasticity, Sci. Adv. 9 (23) (2023) eadg8861.
[297] V.P. Patil, J.D. Sandt, M. Kolle, J. Dunkel, Topological mechanics of knots and tangles, Science 367 (6473) (2020) 71–75.
[298] W.P. Moestopo, S. Shaker, W. Deng, J.R. Greer, Knots are not for naught: Design, properties, and topology of hierarchical intertwined microarchitected materials, Sci. Adv. 9 (10) (2023) eade6725.
[299] O. Farago, Y. Kantor, M. Kardar, Pulling knotted polymers, Europhys. Lett. 60 (2002) 53–59.
[300] P. Pierański, S. Przybył, A. Stasiak, Tight open knots, Eur. Phys. J. E 6 (2001) 123–128.
[301] J.H. Maddocks, J.B. Keller, Ropes in equilibrium, SIAM J. Appl. Math. 47 (6) (1987) 1185–1200.
[302] U.G. Wegst, H. Bai, E. Saiz, A.P. Tomsia, R.O. Ritchie, Bioinspired structural materials, Nat. Mater. 14 (1) (2015) 23–36.
[303] G. Greco, M.F. Pantano, B. Mazzolai, N.M. Pugno, Imaging and mechanical characterization of different junctions in spider orb webs, Sci. Rep. 9 (2019) 5776.
[304] S.W. Cranford, A. Tarakanova, N.M. Pugno, M.J. Buehler, Nonlinear material behaviour of spider silk yields robust webs, Nature 482 (2012) 72–78.
[305] N.M. Pugno, The “egg of columbus” for making the world’s toughest fibres, PLoS One 9 (4) (2014) e93079.
[306] I. Agnarsson, M. Kuntner, T.A. Blackledge, Bioprospecting finds the toughest biological material: Extraordinary silk from a giant riverine orb spider, PLoS One 5 (9) (2010) e11234.
[307] R.O. Ritchie, The conflicts between strength and toughness, Nat. Mater. 10 (11) (2011) 817–822.
[308] R. Snyder, A.N. Pargellis, P.A. Graham, B. Yurke, Light-transmission study of coarsening in a nematic liquid crystal, Phys. Rev. A 45 (1992) R2169.
[309] I. Chuang, B. Yurke, A. Pargellis, N. Turok, Coarsening dynamics in uniaxial nematic liquid crystals, Phys. Rev. E 47 (1993) 3343.
[310] G. Duclos, R. Adkins, D. Banerjee, M.S.E. Peterson, M. Varghese, I. Kolvin, A. Baskaran, R.A. Pelcovits, T.R. Powers, A. Baskaran, F. Toschi, M.F. Hagan, S.J. Streichan, V. Vitelli, D.A. Beller, Z. Dogic, Topological structure and dynamics of three-dimensional active nematics, Science 367 (2020) 1120.
[311] N. Kralj, M. Ravnik, Ž. Kos, Defect line coarsening and refinement in active nematics, Phys. Rev. Lett. 130 (2023) 128101.
[312] K. Jänich, Topological properties of ordinary nematics in 3-space, Acta Appl. Math. 8 (1) (1987) 65–74.
[313] S. Čopar, Topology and geometry of nematic braids, Phys. Rep. 538 (2014) 1.
[314] T. Machon, G.P. Alexander, Global defect topology in nematic liquid crystals, Proc. R. Soc. A: Math., Phys. Eng. Sci. 472 (2191) (2016) 20160265.
[315] Y. Bouligand, Recherches sur les textures des états mésomorphes: Dislocations coins et signification des cloisons de Grandjean-Cano dans les cholestériques, J. Phys. France 35 (1974) 959.
[316] P. Poulin, H. Stark, T.C. Lubensky, D.A. Weitz, Novel colloidal interactions in anisotropic fluids, Science 275 (1997) 1770–1773.
[317] R.W. Ruhwandl, E.M. Terentjev, Long-range forces and aggregation of colloid particles in a nematic liquid crystal, Phys. Rev. E 55 (1997) 2958–2961.
[318] E. Terentjev, Disclination loops, standing alone and around solid particles, in nematic liquid crystals, Phys. Rev. E 51 (2) (1995) 1330.
[319] H. Stark, Physics of colloidal dispersions in nematic liquid crystals, Phys. Rep. 351 (2001) 387–474.
[320] I. Muševič, M. Škarabot, U. Tkalec, M. Ravnik, S. Žumer, Two-dimensional nematic colloidal crystals self-assembled by topological defects, Science 313 (2006) 954–958.
[321] M. Ravnik, M. Škarabot, S. Žumer, U. Tkalec, I. Poberaj, D. Babič, N. Osterman, I. Muševič, Entangled nematic colloidal dimers and wires, Phys. Rev. Lett. 99 (2007) 247801.
[322] B. Senyuk, Q. Liu, S. He, R.D. Kamien, R.B. Kusner, T.C. Lubensky, I.I. Smalyukh, Topological colloids, Nature 493 (2013) 200.
[323] T. Machon, G.P. Alexander, Knots and nonorientable surfaces in chiral nematics, Proc. Natl. Acad. Sci. USA 110 (2013) 14174–14179.
[324] D. Seč, S. Čopar, S. Žumer, Topological zoo of free-standing knots in confined chiral nematic fluids, Nature Commun. 5 (2014) 3057.
[325] M. Škarabot, M. Ravnik, S. Žumer, U. Tkalec, I. Poberaj, D. Babič, N. Osterman, I. Muševič, Interactions of quadrupolar nematic colloids, Phys. Rev. E 77 (2008) 031705.
[326] U. Ognysta, A. Nych, V. Nazarenko, I. Muševič, M. Škarabot, M. Ravnik, S. Žumer, I. Poberaj, D. Babič, 2D interactions and binary crystals of dipolar and quadrupolar nematic colloids, Phys. Rev. Lett. 100 (2008) 217803.
[327] A. Nych, U. Ognysta, M. Škarabot, M. Ravnik, S. Žumer, I. Muševič, Assembly and control of 3D nematic dipolar colloidal crystals, Nature Commun. 4 (2013) 1489.
[328] S. Čopar, N.A. Clark, M. Ravnik, S. Žumer, Elementary building blocks of nematic disclination networks in densely packed 3D colloidal lattices, Soft Matter 9 (2013) 8203.
[329] S. Čopar, U. Tkalec, I. Muševič, S. Žumer, Knot theory realizations in nematic colloids, Proc. Natl. Acad. Sci. 112 (2015) 1675.
[330] A. Martinez, M. Ravnik, B. Lucero, R. Visvanathan, S. Žumer, I.I. Smalyukh, Mutually tangled colloidal knots and induced defect loops in nematic fields, Nature Mater. 13 (2014) 258.
[331] Ž. Kos, J. Dunkel, Nematic bits and universal logic gates, Sci. Adv. 8 (33) (2022) eabp8371.
[332] T. Machon, G.P. Alexander, Woven nematic defects, skyrmions, and the abelian sandpile model, Phys. Rev. Lett. 121 (2018) 237801.
[333] Y. Bouligand, B. Derrida, V. Poenaru, Y. Pomeau, G. Toulouse, Distortions with double topological character: the case of cholesterics, J. Physique 39 (8) (1978) 863–867.
[334] T. Machon, Contact topology and the structure and dynamics of cholesterics, New J. Phys. 19 (11) (2017) 113030.

[335] J. Pollard, G. Posnjak, S. Čopar, I. Muševič, G.P. Alexander, Point defects, topological chirality, singularity theory in cholesteric liquid-crystal droplets, Phys. Rev. X 9 (2) (2019) 021004.
[336] P.J. Ackerman, I.I. Smalyukh, Reversal of helicoidal twist handedness near point defects of confined chiral liquid crystals, Phys. Rev. E 93 (5) (2016) 052702.
[337] G. Posnjak, S. Čopar, I. Muševič, Hidden topological constellations and polyvalent charges in chiral nematic droplets, Nat. Commun. 8 (2017) 14594.
[338] M.N. Krakhalev, V.Y. Rudyak, O.O. Prishchepa, A.P. Gardymova, A.V. Emelyanenko, J.-H. Liu, V.Y. Zyryanov, Orientational structures in cholesteric droplets with homeotropic surface anchoring, Soft Matter 15 (28) (2019) 5554–5561.
[339] M.O. Lavrentovich, L. Tran, Undulation instabilities in cholesteric liquid crystals induced by anchoring transitions, Phys. Rev. Res. 2 (2) (2020) 023128.
[340] Y. Han, J. Dalby, A. Majumdar, B.M.G.D. Carter, T. Machon, Uniaxial versus biaxial pathways in one-dimensional cholesteric liquid crystals, Phys. Rev. Res. 4 (2022) L032018.
[341] J. Pollard, G.P. Alexander, Contact topology and the classification of disclination lines in cholesteric liquid crystals, Phys. Rev. Lett. 130 (22) (2023) 228102.
[342] T. Machon, G.P. Alexander, Knotted defects in nematic liquid crystals, Phys. Rev. Lett. 113 (2) (2014) 027801.
[343] J.-S.B. Tai, I.I. Smalyukh, Three-dimensional crystals of adaptive knots, Science 365 (6460) (2019) 1449–1453.
[344] A. Nych, J. Fukuda, U. Ognysta, S. Žumer, I. Muševič, Spontaneous formation and dynamics of half-skyrmions in a chiral liquid-crystal film, Nat. Phys. 13 (2017) 1215.
[345] T. Machon, G.P. Alexander, Umbilic lines in orientational order, Phys. Rev. X 6 (2016) 011033.
[346] D. Foster, C. Kind, P.J. Ackerman, J.-S.B. Tai, M.R. Dennis, I.I. Smalyukh, Two-dimensional skyrmion bags in liquid crystals and ferromagnets, Nat. Phys. 15 (2019) 655.
[347] S. Afghah, J.V. Selinger, Theory of helicoids and skyrmions in confined cholesteric liquid crystals, Phys. Rev. E 96 (1) (2017) 012708.
[348] A. Varanytsia, L.-C. Chien, Photoswitchable and dye-doped bubble domain texture of cholesteric liquid crystals, Opt. Lett. 40 (19) (2015) 4392–4395.
[349] J. Pišljar, S. Ghosh, S. Turlapati, N.V.S. Rao, M. Škarabot, A. Mertelj, A. Petelin, A. Nych, M. Marinčič, A. Pusovnik, M. Ravnik, I. Muševič, Blue phase III: Topological fluid of skyrmions, Phys. Rev. X 12 (1) (2022) 011003.
[350] B. Khesin, V.I. Arnold, Topological Methods in Hydrodynamics, Springer-Verlag, Berlin, 1992.
[351] R.L. Ricca (Ed.), Lectures on topological fluid mechanics, CIME Lecture Notes in Mathematics **1973**, Springer-Verlag, 2009.
[352] A. Enciso, D. Peralta-Salas, Knots and links in steady solutions of the Euler equation, Ann. Math. 175 (2012) 345–367.
[353] P. Pieranski, In search of ideal knots, in: A. Stasiak, V. Katrich, L.H. Kauffmann (Eds.), Ideal Knots, in: Series on Knots and Everything, vol. 19, World Scientific, Singapore, 1998, pp. 20–41.
[354] V.I. Arnold, The asymptotic Hopf invariant and its applications, in: Proc. Summer School in Diff. Eqs. At Dilizhan, Armenian Academy of Sciences, Erevan, 1974, pp. 229–256, [In Russian.], 1986 *Sel. Math. Sov.* **5**, 327–345 [English translation].
[355] H.K. Moffatt, The energy spectrum of knots and links, Nature 347 (1990) 367–369.
[356] M.H. Freedman, Z.-X. He, Divergence-free fields: energy and asymptotic crossing number, Ann. Math. 134 (1991) 189–229.
[357] R. Battye, P.M. Sutcliffe, Knots as stable soliton solutions in a three-dimensional classical field theory, Phys. Rev. Lett. 81 (1998) 4798–4801.
[358] T. Ashton, J. Cantarella, M. Piatek, E.J. Rawdon, Knot tightening by constrained gradient descent, Exp. Math. 20 (2011) 57–90.
[359] R.L. Ricca, F. Maggioni, On the groundstate energy spectrum of magnetic knots and links, J. Phys. A: Math. Theor. 47 (2014) 205501.
[360] R.V. Buniy, J. Cantarella, T.W. Kephart, E.J. Rawdon, Tight knot spectrum in QCD, Phys. Rev. D 89 (2014) 054513.
[361] M.A. Berger, Topological magnetohydrodynamics and astrophysics, in: R. Meyers (Ed.), Encyclopedia of Complexity and Systems Science, Springer, 2009, pp. 9268–9282.
[362] A.L. Wilmot-Smith, D.I. Pontin, G. Hornig, Dynamics of braided coronal loops I. Onset of magnetic reconnection, Astron. Astrophys. 516 (2010) A5.
[363] A.R. Yeates, G. Hornig, Unique topological characterization of braided magnetic fields, Phys. Plasmas 20 (2013) 012102.
[364] M.A. Berger, Energy-crossing number relations for braided magnetic fields, Phys. Rev. Lett. 70 (1993) 705–708.
[365] A.L. Wilmot-Smith, D.I. Pontin, A.R. Yeates, G. Hornig, Heating of braided coronal loops, Astron. Astrophys. 536 (2011).
[366] H. Aref, J.R. Blake, M. Budišić, S.S.S. Cardoso, J.H.E. Cartwright, H.J.H. Clercx, K. El Omari, U. Feudel, R. Golestanian, E. Gouillart, G.J.F. van Heijst, T.S. Krasnopolskaya, Y. Le Guer, R.S. MacKay, V.V. Meleshko, G. Metcalfe, I. Mezić, A.P.S. de Moura, O. Piro, M.F.M. Speetjens, R. Sturman, J.-L. Thiffeault, I. Tuval, Frontiers of chaotic advection, Rev. Modern Phys. 89 (2) (2017) 025007.
[367] P.L. Boyland, H. Aref, M.A. Stremler, Topological fluid mechanics of stirring, J. Fluid Mech. 403 (2000) 277–304.
[368] J.-L. Thiffeault, Measuring topological chaos, Phys. Rev. Lett. 94 (2005) 084502.
[369] M. Arrayás, D. Bouwmeester, J.L. Trueba, Knots in electromagnetism, Phys. Rep. 667 (2017) 1–61.
[370] A.M. Kamchatnov, Topological solitons in magnetohydrodynamics, Sov. Phys.-JETP 55 (1) (1982) 59–73.
[371] A.F. Rañada, A topological theory of the electromagnetic field, Lett. Math. Phys. 18 (2) (1989) 97–106.
[372] M.R. Dennis, R.P. King, B. Jack, K. O'Holleran, M.J. Padgett, Isolated optical vortex knots, Nature Phys. 6 (2010) 118–121.
[373] H. Kedia, D. Foster, M.R. Dennis, W.T.M. Irvine, Weaving knotted vector fields with tunable helicity, Phys. Rev. Lett. 117 (2016) 274501.
[374] M. Arrayás, D. Bouwmeester, J.L. Trueba, Knots in electromagnetism, Phys. Rep. 667 (2017) 1–61.
[375] B. Bode, M.R. Dennis, D. Foster, R.P. King, Knotted fields and explicit fibrations for lemniscate knots, Proc. R. Soc. Lond. Ser. A Math. Phys. Eng. Sci. 473 (2017) 20160829.
[376] D. Kleckner, W.T.M. Irvine, Creation and dynamics of knotted vortices, Nature Phys. 9 (2013) 253–258.
[377] S. Zuccher, R. Ricca, Creation of quantum knots and links driven by minimal surfaces, J. Fluid Mech. 942 (2022) A8.
[378] S. Kida, A vortex filament moving without change of form, J. Fluid Mech. 112 (1981) 397–409.
[379] J.P. Keener, Knotted vortex filaments in an ideal fluid, J. Fluid Mech. 211 (1990) 629–651.
[380] R.L. Ricca, Torus knots and polynomial invariants for a class of soliton equations, Chaos 3 (1993) 83–91.
[381] R.L. Ricca, D.C. Samuels, C.F. Barenghi, Evolution of vortex knots, J. Fluid Mech. 391 (1999) 29–44.
[382] H. Aref, I. Zawadzki, Linking of vortex rings, Nature 354 (1991) 50–53.
[383] J. Yao, Y. Yang, F. Hussain, Dynamics of a trefoil knotted vortex, J. Fluid Mech. 923 (2021).
[384] X. Zhao, Z. Yu, C. J.-B., C. Scalo, Direct numerical and large-eddy simulation of trefoil knotted vortices, J. Fluid Mech. 910 (2021).
[385] C.F. Barenghi, R.L. Ricca, D.C. Samuels, How tangled is a tangle? Physica D 157 (2001) 197–206.
[386] D. Kleckner, L.H. Kauffman, W.T.M. Irvine, How superfluid vortex knots untie, Nat. Phys. 12 (2016) 650–655.
[387] W.-K. Bai, T. Yang, W.-M. Liu, Topological transition from superfluid vortex rings to isolated knots and links, Phys. Rev. A 102 (2020) 063318.
[388] R.G. Cooper, M. Mesgarnezhad, A.W. Baggaley, C.F. Barenghi, Knot spectrum of turbulence, Sci. Rep. 9 (2019) 10545.
[389] R. Everaers, S.K. Sukumaran, G.S. Grest, C. Svaneborg, A. Sivasubramanian, K. Kremer, Rheology and microscopic topology of entangled polymeric liquids, Science 303 (5659) (2004) 823–826.
[390] P.G. De Gennes, Reptation of a polymer chain in the presence of fixed obstacles, J. Chem. Phys. 55 (2) (1971) 572–579.

[391] G. Marrucci, Relaxation by reptation and tube enlargement: A model for polydisperse polymers, J. Polym. Sci.: Polym. Phys. Ed. 23 (1) (1985) 159–177.
[392] J.L. Viovy, M. Rubinstein, R.H. Colby, Constraint release in polymer melts: tube reorganization versus tube dilation, Macromolecules 24 (12) (1991) 3587–3596.
[393] H. Watanabe, Viscoelasticity and dynamics of entangled polymers, Prog. Polym. Sci. 24 (9) (1999) 1253–1403.
[394] A.E. Likhtman, T.C.B. McLeish, Quantitative theory for linear dynamics of linear entangled polymers, Macromolecules 35 (16) (2002) 6332–6343.
[395] V.A. Boudara, D.J. Read, J. Ramírez, REPTATE rheology software: Toolkit for the analysis of theories and experiments, J. Rheol. 64 (3) (2020) 709–722.
[396] D. Parisi, J. Ahn, T. Chang, D. Vlassopoulos, M. Rubinstein, Stress relaxation in symmetric ring-linear polymer blends at low ring fractions, Macromolecules 53 (5) (2020) 1685–1693.
[397] A. Herrmann, B. Kresse, M. Wohlfahrt, I. Bauer, A.F. Privalov, D. Kruk, N. Fatkullin, F. Fujara, E.A. Rössler, Mean square displacement and reorientational correlation function in entangled polymer melts revealed by field cycling 1H and 2H NMR relaxometry, Macromolecules 45 (16) (2012) 6516–6526.
[398] C. Svaneborg, R. Everaers, Characteristic time and length scales in melts of kremer–grest bead–spring polymers with wormlike bending stiffness, Macromolecules 53 (6) (2020) 1917.
[399] R. Everaers, H.A. Karimi-Varzaneh, F. Fleck, N. Hojdis, C. Svaneborg, Kremer–grest models for commodity polymer melts: Linking theory, experiment, simulation at the kuhn scale, Macromolecules 53 (6) (2020) 1901–1916.
[400] T.C.B. McLeish, Tube theory of entangled polymer dynamics, Adv. Phys. 51 (2002) 1379–1527.
[401] N. Uchida, G.S. Grest, R. Everaers, Viscoelasticity and primitive path analysis of entangled polymer liquids: From F-actin to polyethylene, J. Chem. Phys. 128 (4) (2008) 044902.
[402] S.F. Edwards, The theory of rubber elasticity, Br. Polym. J. 9 (1977) 140.
[403] M. Rubinstein, E. Helfand, Statistics of the entanglement of polymers: Concentration effects, J. Chem. Phys. 82 (5) (1985) 2477–2483.
[404] M. Kröger, Shortest multiple disconnected path for the analysis of entanglements in two- and three-dimensional polymeric systems, Comput. Phys. Comm. 168 (2005) 209–232.
[405] S. Shanbhag, R.G. Larson, Chain retraction potential in a fixed entanglement network, Phys. Rev. Lett. 94 (7) (2005) 076001.
[406] C. Tzoumanekas, D.N. Theodorou, Topological analysis of linear polymer melts: A statistical approach, Macromolecules 39 (13) (2006) 4592–4604.
[407] R.S. Hoy, G.S. Grest, Entanglements of an end-grafted polymer brush in a polymeric matrix, Macromolecules 40 (23) (2007) 8389.
[408] C. Svaneborg, R. Everaers, G.S. Grest, J.G. Curro, Connectivity and entanglement stress contributions in strained polymer networks, Macromolecules 41 (13) (2008) 4920.
[409] R.S. Hoy, K. Foteinopoulou, M. Kröger, Topological analysis of polymeric melts: Chain-length effects and fast-converging estimators for entanglement length, Phys. Rev. E. 80 (3) (2009) 031803.
[410] R. Everaers, Topological versus rheological entanglement length in primitive-path analysis protocols, tube models, slip-link models, Phys. Rev. E. 86 (2) (2012) 022801.
[411] J.-X. Hou, Note: Determine entanglement length through monomer mean-square displacement, J. Chem. Phys. 146 (2) (2017) 026101.
[412] H.-P. Hsu, K. Kremer, Static and dynamic properties of large polymer melts in equilibrium, J. Chem. Phys. 144 (15) (2016) 154907.
[413] J.-X. Hou, C. Svaneborg, R. Everaers, G.S. Grest, Stress relaxation in entangled polymer melts, Phys. Rev. Lett. 105 (6) (2010) 068301.
[414] A.N. Semenov, Dynamics of concentrated solutions of rigid-chain polymers. I: Brownian motion of persistent macromolecules in isotropic solution, J. Chem. Soc., Faraday Trans. 82 (1986) 317–329.
[415] D.C. Morse, Tube diameter in tightly entangled solutions of semiflexible polymers, Phys. Rev. E 63 (2001) 031502.
[416] Y.H. Lin, Number of entanglement strands per cubed tube diameter, a fundamental aspect of topological universality in polymer viscoelasticity, Macromolecules 20 (12) (1987) 3080–3083.
[417] T.A. Kavassalis, J. Noolandi, New view of entanglements in dense polymer systems, Phys. Rev. Lett. 59 (1987) 2674–2677.
[418] D.J. Read, K. Jagannathan, A.E. Likhtman, Entangled polymers: Constraint release, mean paths, tube bending energy, Macromolecules 41 (18) (2008) 6843–6853.
[419] A.E. Likhtman, The tube axis and entanglements in polymer melts, Soft Matter 10 (12) (2014) 1895.
[420] A.E. Likhtman, M. Ponmurugan, Microscopic definition of polymer entanglements, Macromolecules 47 (4) (2014) 1470–1481.
[421] D. Michieletto, T. Sakaue, Dynamical entanglement and cooperative dynamics in entangled solutions of ring and linear polymers, ACS Macro Lett. 10 (2020) 129.
[422] J.D. Halverson, G.S. Grest, A.Y. Grosberg, K. Kremer, Rheology of ring polymer melts: From linear contaminants to ring-linear blends, Phys. Rev. Lett. 108 (3) (2012) 038301.
[423] A. Rosa, R. Everaers, Ring polymers in the melt state: The physics of crumpling, Phys. Rev. Lett. 112 (2014) 118302.
[424] R.D. Schram, A. Rosa, R. Everaers, Local loop opening in untangled ring polymer melts: A detailed "feynman test" of models for the large scale structure, Soft Matter 15 (2019) 2418–2429.
[425] J. Wang, T. Ge, Crazing reveals an entanglement network in glassy ring polymers, Macromolecules 54 (16) (2021) 7500–7511.
[426] J.D. Halverson, W.B. Lee, G.S. Grest, A.Y. Grosberg, K. Kremer, Molecular dynamics simulation study of nonconcatenated ring polymers in a melt. 1. Statics, J. Chem. Phys. 134 (2011) 204904.
[427] J. Smrek, K. Kremer, A. Rosa, Threading of unconcatenated ring polymers at high concentrations: double-folded vs time-equilibrated structures, ACS Macro Lett. 8 (2) (2019) 155–160.
[428] S.P. Obukhov, M. Rubinstein, T. Duke, Dynamics of a ring polymer in a gel, Phys. Rev. Lett. 73 (1994) 1263–1266.
[429] T. Chang, Polymer characterization by interaction chromatography, J. Polym. Sci. Part B: Polym. Phys. 43 (13) (2005) 1591–1607.
[430] H.C. Lee, H. Lee, W. Lee, T. Chang, J. Roovers, Fractionation of cyclic polystyrene from linear precursor by HPLC at the chromatographic critical condition, Macromolecules 33 (22) (2000) 8119–8121.
[431] Y. Doi, K. Matsubara, Y. Ohta, T. Nakano, D. Kawaguchi, Y. Takahashi, A. Takano, Y. Matsushita, Melt rheology of ring polystyrenes with ultrahigh purity, Macromolecules 48 (9) (2015) 3140–3147.
[432] Y. Doi, A. Matsumoto, T. Inoue, T. Iwamoto, A. Takano, Y. Matsushita, Y. Takahashi, H. Watanabe, Re-examination of terminal relaxation behavior of high-molecular-weight ring polystyrene melts, Rheol. Acta 56 (6) (2017) 567–581.
[433] D.G. Tsalikis, V.G. Mavrantzas, D. Vlassopoulos, Analysis of slow modes in ring polymers: Threading of rings controls long-time relaxation, ACS Macro Lett. 5 (6) (2016) 755–760.
[434] D.G. Tsalikis, V.G. Mavrantzas, Threading of ring poly(ethylene oxide) molecules by linear chains in the melt, ACS Macro Lett. 3 (8) (2014) 763–766.
[435] D. Michieletto, D. Marenduzzo, E. Orlandini, G.P. Alexander, M.S. Turner, Dynamics of self-threading ring polymers in a gel, Soft Matter 10 (2014) 5936–5944.
[436] S. Gooßen, M. Krutyeva, M. Sharp, A. Feoktystov, J. Allgaier, W. Pyckhout-Hintzen, A. Wischnewski, D. Richter, Sensing polymer chain dynamics through ring topology: A neutron spin echo study, Phys. Rev. Lett. 115 (14) (2015) 148302.

[437] S.P. Obukhov, Talk at KITP santa barbara, 1997, accessed Apr. 2019.
[438] W.-C. Lo, M.S. Turner, The topological glass in ring polymers, Europhys. Lett. 102 (5) (2013) 58005.
[439] A. Borger, W. Wang, T.C. O'Connor, T. Ge, G.S. Grest, G.V. Jensen, J. Ahn, T. Chang, O. Hassager, K. Mortensen, D. Vlassopoulos, Q. Huang, Threading–unthreading transition of linear-ring polymer blends in extensional flow, ACS Macro Lett. 9 (10) (2020) 1452–1457.
[440] T.C. O'Connor, T. Ge, M. Rubinstein, G.S. Grest, Topological linking drives anomalous thickening of ring polymers in weak extensional flows, Phys. Rev. Lett. 124 (2020) 027801.
[441] Q. Huang, J. Ahn, D. Parisi, T. Chang, O. Hassager, S. Panyukov, M. Rubinstein, D. Vlassopoulos, Unexpected stretching of entangled ring macromolecules, Phys. Rev. Lett. 122 (20) (2019) 208001.
[442] A. Narros, A.J. Moreno, C.N. Likos, Effective interactions of knotted ring polymers, Biochem. Soc. Trans. 41 (2) (2013) 630–634.
[443] M. Lang, J. Fischer, J.-U. Sommer, Effect of topology on the conformations of ring polymers, Macromolecules 45 (18) (2012) 7642–7648.
[444] E. Lee, S. Kim, Y. Jung, Slowing down of ring polymer diffusion caused by inter-ring threading, Macromol. Rapid Commun. 36 (11) (2015) 1115–1121.
[445] A. Rosa, J. Smrek, M.S. Turner, D. Michieletto, Threading-induced dynamical transition in tadpole-shaped polymers, ACS Macro Lett. 9 (5) (2020) 743–748.
[446] D.G. Tsalikis, V.G. Mavrantzas, Size and diffusivity of polymer rings in linear polymer matrices: The key role of threading events, Macromolecules 53 (3) (2020) 803–820.
[447] H.R. Parks, Soap-film-like minimal surfaces spanning knots, J. Geom. Anal. 2 (3) (1992) 267–290.
[448] I. Chubak, C.N. Likos, J. Smrek, Topological and threading effects in polydisperse ring polymer solutions, Mol. Phys. (2021) e1883140.
[449] D. Parisi, S. Costanzo, Y. Jeong, J. Ahn, T. Chang, D. Vlassopoulos, J.D. Halverson, K. Kremer, T. Ge, M. Rubinstein, G.S. Grest, W. Srinin, A.Y. Grosberg, Nonlinear shear rheology of entangled polymer rings, Macromolecules 54 (6) (2021) 2811–2827.
[450] N.-T. Nguyen, S.T. Wereley, S.A.M. Shaegh, Fundamentals and Applications of Microfluidics, Artech House, 2019.
[451] B.W. Soh, A.R. Klotz, P.S. Doyle, Topological simplification of complex knots untied in elongational flows, Macromolecules 53 (2020) 7389–7398.
[452] C.M. Schroeder, Single polymer dynamics for molecular rheology, J. Rheol. 62 (2018) 371–403.
[453] Y. Li, K.-W. Hsiao, C.A. Brockman, D.Y. Yates, R.M. Robertson-Anderson, J.A. Kornfield, M.J. San Francisco, C.M. Schroeder, G.B. McKenna, When ends meet: Circular DNA stretches differently in elongational flows, Macromolecules 48 (2015) 5997–6001.
[454] A.G. Balducci, J. Tang, P.S. Doyle, Electrophoretic stretching of DNA molecules in cross-slot nanoslit channels, Macromolecules 41 (24) (2008) 9914–9918.
[455] J.M. Dealy, Weissenberg and deborah numbers - their definition and use, Rheol. Bull. 79 (2010) 14–18.
[456] M. Tanyeri, C.M. Schroeder, Manipulation and confinement of sinlge particles using fluid flow, Nano Lett. 13 (2013) 2357–2364.
[457] P. De Gennes, Molecular individualism, Science 276 (5321) (1997) 1999–2000.
[458] K.-W. Hsiao, C.M. Schroeder, C.E. Sing, Ring polymer dynamics are governed by a couling between architecture and hydrodynamic interactions, Macromolecules 49 (2016) 1961–1971.
[459] M. Liebetreu, C.N. Likos, Hydrodynamic inflation of ring polymers under shear, Commun. Mater. 1 (2020) 4.
[460] A. Malevanets, R. Kapral, Mesoscopic model for solvent dynamics, J. Chem. Phys. 110 (17) (1999) 8605–8613.
[461] G. Gompper, T. Ihle, D.M. Kroll, R.G. Winkler, Multi-particle collision dynamics - a particle-based mesoscale simulation approach to the hydrodynamics of complex fluids, Adv. Polym. Sci. 221 (2008) 1–91.
[462] M. Liebetreu, M. Ripoll, C.N. Likos, Trefoil knot hydrodynamic delocalization on sheared ring polymers, ACS Macro Lett. 7 (2018) 447–452.
[463] C.D. Young, J.R. Qian, M. Marvin, C.E. Sing, Ring polymer dynamics and tumbling-strecth transitions in planar mixed flows, Phys. Rev. E 99 (2019) 062502.
[464] M.Q. Tu, M. Lee, R.M. Robertson-Anderson, C.M. Schroeder, Direct obesrvation of ring polymer dynamics in the flow-gradient plane of shear flow, Macromolecules 53 (2020) 9406–9419.
[465] B.W. Soh, A.R. Klotz, R.M. Robertson-Anderson, P.S. Doyle, Long-lived self-entanglements in ring polymers, Phys. Rev. Lett. 123 (2019) 048002.
[466] B.W. Soh, I.R. Gengaro, A.R. Klotz, P.S. Doyle, Self-entanglement of a tumbled circular chain, Phys. Rev. Res. 1 (2019) 033194.
[467] V. Narsimhan, C.B. Renner, P.S. Doyle, Jamming of knots along a tensioned chain, ACS Macro Lett. 5 (2016) 123–127.
[468] L. Dai, C.B. Renner, P.S. Doyle, Metastable tight knots in semiflexible chains, Macromolecules 47 (17) (2014) 6135–6140.
[469] R.K. Sharma, I. Agrawal, L. Dai, P. Doyle, S. Garaj, DNA knot malleability in single-digit nanopores, Nano Lett. 21 (9) (2021) 3772–3779.
[470] S.N. Rheaume, A.R. Klotz, Nanopore translocation of topologically linked DNA catenanes, Phys. Rev. E 107 (2) (2023) 024504.
[471] S. Najafi, L. Tubiana, R. Podgornik, R. Potestio, Chirality modifies the interaction between knots, Europhys. Lett. 114 (5) (2016) 50007.
[472] L.B. Weiss, A. Nikoubashman, C.N. Likos, Topology-sensitive microfluidic filter for polymers of varying stiffness, ACS Macro Lett. 6 (2017) 1426–1431.
[473] L.B. Weiss, C.N. Likos, A. Nikoubashman, Spatial demixing of ring and chain polymers in pressure-driven flow, Macromolecules 52 (2019) 7858–7869.
[474] M. Marenda, E. Orlandini, C. Micheletti, Sorting ring polymers by knot type with modulated nanochannels, Soft Matter 13 (2017) 795–802.
[475] L.B. Weiss, M. Marenda, C. Micheletti, C.N. Likos, Hydrodynamics and filtering of knotted ring polymers in nanochannels, Macromolecules 52 (2019) 4111–4119.
[476] A.N. Boettiger, B. Bintu, J.R. Moffitt, S. Wang, B.J. Beliveau, G. Fudenberg, M. Imakaev, L.A. Mirny, C.-t. Wu, X. Zhuang, Super-resolution imaging reveals distinct chromatin folding for different epigenetic states, Nature 529 (7586) (2016) 418–422.
[477] H.D. Ou, S. Phan, T.J. Deerinck, A. Thor, M.H. Ellisman, C.C. O'Shea, Chromemt: Visualizing 3D chromatin structure and compaction in interphase and mitotic cells, Science 357 (6349) (2017).
[478] E. Lieberman-Aiden, N.L. Van Berkum, L. Williams, M. Imakaev, T. Ragoczy, A. Telling, I. Amit, B.R. Lajoie, P.J. Sabo, M.O. Dorschner, R. Sandstrom, B. Bernstein, M.A. Bender, M. Groudine, A. Gnirke, J. Stamatoyannopoulos, L.A. Mirny, E.S. Lander, J. Dekker, Comprehensive mapping of long-range interactions reveals folding principles of the human genome, Science 326 (5950) (2009) 289–293.
[479] R.A. Beagrie, A. Scialdone, M. Schueler, D.C.A. Kraemer, M. Chotalia, S.Q. Xie, M. Barbieri, I. de Santiago, L.-M. Lavitas, M.R. Branco, J. Fraser, J. Dostie, L. Game, N. Dillon, P.A.W. Edwards, M. Nicodemi, A. Pombo, Complex multi-enhancer contacts captured by genome architecture mapping, Nature 543 (7646) (2017) 519–524.
[480] V.B. Rao, M. Feiss, The bacteriophage DNA packaging motor, Annu. Rev. Genet. 42 (2008) 647–681.
[481] R. Zandi, B. Dragnea, A. Travesset, R. Podgornik, On virus growth and form, Phys. Rep. 847 (2020) 1–102.
[482] A. Leforestier, S. Brasiles, M. de Frutos, E. Raspaud, L. Letellier, P. Tavares, F. Livolant, Bacteriophage T5 DNA ejection under pressure, J. Mol. Biol. 384 (3) (2008) 730–739.
[483] I.J. Molineux, D. Panja, Popping the cork: Mechanisms of phage genome ejection, Nat. Rev. Microbiol. 11 (2013) 194–204.
[484] S.C. Riemer, V.A. Bloomfield, Packaging of DNA in bacteriophage heads: Some considerations on energetics, Biopolymers 17 (1978) 785–794.
[485] P.A. Wiggins, T. van der Heijden, F. Moreno-Herrero, A. Spakowitz, R. Phillips, J. Widom, C. Dekker, P.C. Nelson, High flexibility of DNA on short length scales probed by atomic force microscopy, Nature Nanotechnol. 1 (2006) 137.
[486] A. Leforestier, A. Šiber, F. Livolant, R. Podgornik, Protein-DNA interactions determine the shapes of DNA toroids condensed in virus capsids, Biophys. J. 100 (9) (2011) 2209–2216.

[487] N.V. Hud, K.H. Downing, R. Balhorn, A constant radius of curvature model for the organization of DNA in toroidal condensates, Proc. Natl. Acad. Sci. 92 (8) (1995) 3581–3585.
[488] A. Leforestier, F. Livolant, Structure of toroidal DNA collapsed inside the phage capsid, Proc. Natl. Acad. Sci. U. S. A. 106 (23) (2009) 9157–9162.
[489] T. Curk, J.D. Farrell, J. Dobnikar, R. Podgornik, Spontaneous domain formation in spherically confined elastic filaments, Phys. Rev. Lett. 123 (2019) 047801.
[490] N. Stoop, J. Najafi, F.K. Wittel, M. Habibi, H.J. Herrmann, Packing of elastic wires in spherical cavities, Phys. Rev. Lett. 106 (2011) 214102.
[491] D. Marenduzzo, C. Micheletti, E. Orlandini, D.W. Sumners, Topological friction strongly affects viral DNA ejection, Proc. Natl. Acad. Sci. 110 (50) (2013) 20081–20086.
[492] D.J. Mason, D.M. Powelson, Nuclear division a s observed in live bacteria by a new technique, J. Bacteriol. 71 (4) (1956) 474.
[493] T.A. Azam, A. Ishihama, Twelve species of the nucleoid-associated protein from Escherichia coli. Sequence recognition specificity and DNA binding affinity, J. Biol. Chem. 274 (46) (1999) 33105–33113.
[494] F. Wu, P. Swain, L. Kuijpers, X. Zheng, K. Felter, M. Guurink, J. Solari, S. Jun, T.S. Shimizu, D. Chaudhuri, B. Mulder, C. Dekker, Cell boundary confinement sets the size and position of the E. coli Chromosome, Curr. Biol. 29 (13) (2019) 2131–2144.e4.
[495] R. Stuger, C.L. Woldringh, C.C. Van der Weijden, N.O. Vischer, B.M. Bakker, R.J. Van Spanning, J.L. Snoep, H.V. Weterhoff, DNA supercoiling by gyrase is linked to nucleoid compaction, Mol. Biol. Rep. 29 (1–2) (2002) 79–82.
[496] X. Wang, P.M. Llopis, D.Z. Rudner, Organization and segregation of bacterial chromosomes, Nature Rev. Genet. 14 (3) (2013) 191–203.
[497] J. Cairns, The bacterial chromosome and its manner of replication as seen by autoradiography, J. Mol. Biol. 6 (3) (1963) 208–213.
[498] R. Kavenoff, O.A. Ryder, Electron microscopy of membrane-associated folded chromosomes of Escherichia coli, Chromosoma 55 (1) (1976) 13–25.
[499] R.R. Sinden, D.E. Pettijohn, Chromosomes in living Escherichia coli cells are segregated into domains of supercoiling, Proc. Natl. Acad. Sci. USA 78 (1 II) (1981) 224–228.
[500] M.C. Noom, W.W. Navarre, T. Oshima, G.J.L. Wuite, R.T. Dame, H-NS promotes looped domain formation in the bacterial chromosome, Curr. Biol. 17 (21) (2007) 913–914.
[501] T.B.K. Le, M.V. Imakaev, L.A. Mirny, M.T. Laub, High-resolution mapping of the spatial organization of a bacterial chromosome, Science 342 (6159) (2013) 731–734.
[502] F. Benedetti, J. Dorier, Y. Burnier, A. Stasiak, Models that include supercoiling of topological domains reproduce several known features of interphase chromosomes, Nucleic Acids Res. 42 (5) (2014) 2848–2855.
[503] Y.A.G. Fosado, D. Michieletto, C.A. Brackley, D. Marenduzzo, Nonequilibrium dynamics and action at a distance in transcriptionally driven DNA supercoiling, Proc. Natl. Acad. Sci. USA 118 (10) (2021).
[504] A. Griswold, Genome packaging in prokaryotes: the circular chromosome of e. coli, Nature Education 1 (1) (2008) 57.
[505] M. Delbrück, On the replication of desoxyribonucleic acid (DNA), Proc. Natl. Acad. Sci. 40 (9) (1954) 783–788.
[506] C.W. Dingman, Bidirectional chromosome replication: some topological considerations, J. Theoret. Biol. 43 (1) (1974) 187–195.
[507] C. Gogou, A. Japaridze, C. Dekker, Mechanisms for chromosome segregation in bacteria, Front. Microbiol. 12 (June) (2021) 1–15.
[508] H.B. Brandão, Z. Ren, X. Karaboja, L.A. Mirny, X. Wang, DNA-loop-extruding SMC complexes can traverse one another in vivo, Nat. Struct. Mol. Biol. 28 (8) (2021) 642–651.
[509] S. Jun, B. Mulder, Entropy-driven spatial organization of highly confined polymers: lessons for the bacterial chromosome, Proc. Natl. Acad. Sci. USA 103 (33) (2006) 12388–12393.
[510] Y.A.G. Fosado, J. Howard, S. Weir, A. Noy, M.C. Leake, D. Michieletto, Fluidification of entanglements by a DNA bending protein, Phys. Rev. Lett. 130 (5) (2023) 58203.
[511] A. Buckle, C.A. Brackley, S. Boyle, D. Marenduzzo, N. Gilbert, Polymer simulations of heteromorphic chromatin predict the 3D folding of complex genomic loci, Mol. Cell 72 (4) (2018) 786–797.
[512] S.A. Grigoryev, G. Arya, S. Correll, C.L. Woodcock, T. Schlick, Evidence for heteromorphic chromatin fibers from analysis of nucleosome interactions, Proc. Natl. Acad. Sci. USA 106 (32) (2009) 13317–13322.
[513] T. Misteli, The self-organizing genome: Principles of genome architecture and function, Cell (2020).
[514] A. Prunell, A topological approach to nucleosome structure and dynamics: the linking number paradox and other issues, Biophys. J. 74 (5) (1998) 2531–2544.
[515] A. Lusser, J.T. Kadonaga, Strategies for the reconstitution of chromatin, Nature Methods 1 (1) (2004) 19–26.
[516] A. Bertin, A. Leforestier, D. Durand, F. Livolant, Role of histone tails in the conformation and interactions of nucleosome core particles, Biochemistry 43 (16) (2004) 4773–4780.
[517] H. Schiessel, The physics of chromatin, J. Phys. Condens. Matter 15 (R699) (2003).
[518] J.R. Dixon, S. Selvaraj, F. Yue, A. Kim, Y. Li, Y. Shen, M. Hu, J.S. Liu, B. Ren, Topological domains in mammalian genomes identified by analysis of chromatin interactions, Nature 485 (7398) (2012) 376–380.
[519] S.S. Rao, M.H. Huntley, N.C. Durand, E.K. Stamenova, I.D. Bochkov, J.T. Robinson, A.L. Sanborn, I. Machol, A.D. Omer, E.S. Lander, E. Lieberman Aiden, A 3D map of the human genome at kilobase resolution reveals principles of chromatin looping, Cell 159 (7) (2014) 1665–1680.
[520] C.A. Brackley, B. Liebchen, D. Michieletto, F. Mouvet, P.R. Cook, D. Marenduzzo, Ephemeral protein binding to DNA shapes stable nuclear bodies and chromatin domains, Biophys. J. 112 (6) (2017) 1085–1093.
[521] D. Michieletto, E. Orlandini, D. Marenduzzo, Polymer model with epigenetic recoloring reveals a pathway for the de novo establishment and 3D organization of chromatin domains, Phys. Rev. X 6 (4) (2016) 041047.
[522] G. Fudenberg, M. Imakaev, C. Lu, A. Goloborodko, N. Abdennur, L.A. Mirny, Formation of chromosomal domains by loop extrusion, Cell Rep. 15 (9) (2016) 2038–2049.
[523] E. Kim, J. Kerssemakers, I.A. Shaltiel, C.H. Haering, C. Dekker, DNA-loop extruding condensin complexes can traverse one another, Nature 579 (7799) (2020) 438–442.
[524] J.-K. Ryu, C. Bouchoux, H.W. Liu, E. Kim, M. Minamino, R. de Groot, A.J. Katan, A. Bonato, D. Marenduzzo, D. Michieletto, F. Uhlmann, C. Dekker, Bridging-induced phase separation induced by cohesin SMC protein complexes, Sci. Adv. 7 (7) (2021) eabe5905.
[525] K. Nasmyth, Disseminating the genome: joining, resolving, separating sister chromatids during mitosis and meiosis, Annu. Rev. Genet. 35 (1) (2001) 673–745.
[526] E. Alipour, J.F. Marko, Self-organization of domain structures by DNA-loop-extruding enzymes, Nucleic Acids Res. 40 (22) (2012) 11202–11212.
[527] A.L. Sanborn, S.S. Rao, S.-C. Huang, N.C. Durand, M.H. Huntley, A.I. Jewett, I.D. Bochkov, D. Chinnappan, A. Cutkosky, J. Li, K.P. Geeting, A. Gnirke, A. Melnikov, D. McKenna, E.K. Stamenova, E.S. Lander, E. Lieberman Aiden, Chromatin extrusion explains key features of loop and domain formation in wild-type and engineered genomes, Proc. Natl. Acad. Sci. 112 (47) (2015) E6456–E6465.
[528] M. Ganji, I.A. Shaltiel, S. Bisht, E. Kim, A. Kalichava, C.H. Haering, C. Dekker, Real-time imaging of DNA loop extrusion by condensin, Science 360 (6384) (2018).
[529] I.F. Davidson, B. Bauer, D. Goetz, W. Tang, G. Wutz, J.M. Peters, DNA loop extrusion by human cohesin, Science 366 (6471) (2019) 1338–1345.

[530] S.K. Nomidis, E. Carlon, S. Gruber, J.F. Marko, DNA tension-modulated translocation and loop extrusion by SMC complexes revealed by molecular dynamics simulations, Nucleic Acids Res. 50 (9) (2022) 4974–4987.
[531] I.A. Shaltiel, S. Datta, L. Lecomte, M. Hassler, M. Kschonsak, S. Bravo, C. Stober, J. Ormanns, S. Eustermann, C.H. Haering, A hold-and-feed mechanism drives directional DNA loop extrusion by condensin, Science 376 (6597) (2022) 1087–1094.
[532] A. Bonato, D. Michieletto, Three-dimensional loop extrusion, Biophys. J. 120 (24) (2021) 5544–5552.
[533] C.A. Brackley, S. Taylor, A. Papantonis, P.R. Cook, D. Marenduzzo, Nonspecific bridging-induced attraction drives clustering of DNA-binding proteins and genome organization, Proc. Natl. Acad. Sci. USA 110 (38) (2013) E3605–11.
[534] S.S.P. Rao, S.-C. Huang, B.G.S. Hilaire, J.M. Engreitz, E.M. Perez, K.-R. Kieffer-Kwon, A.L. Sanborn, S.E. Johnstone, G.D. Bascom, I.D. Bochkov, X. Huang, M.S. Shamim, J. Shin, D. Turner, Z. Ye, A.D. Omer, J.T. Robinson, T. Schlick, B.E. Bernstein, R. Casellas, E.S. Lander, E.L. Aiden, Cohesin loss eliminates all loop domains, Cell 171 (2) (2017) 305–320.e24.
[535] A. Goloborodko, M.V. Imakaev, J.F. Marko, L.A. Mirny, Compaction and segregation of sister chromatids via active loop extrusion, eLife (2016) 1–20.
[536] E. Orlandini, D. Marenduzzo, D. Michieletto, Synergy of topoisomerase and structural-maintenance-of-chromosomes proteins creates a universal pathway to simplify genome topology, Proc. Natl. Acad. Sci. 116 (17) (2019) 8149–8154.
[537] J.H. Gibcus, K. Samejima, A. Goloborodko, I. Samejima, N. Naumova, J. Nuebler, M.T. Kanemaki, L. Xie, J.R. Paulson, W.C. Earnshaw, L.A. Mirny, J. Dekker, A pathway for mitotic chromosome formation, Science 359 (6376) (2018).
[538] J.F. Marko, E.D. Siggia, Polymer models of meiotic and mitotic chromosomes, Mol. Biol. Cell 8 (11) (1997) 2217–2231.
[539] D. Racko, F. Benedetti, D. Goundaroulis, A. Stasiak, Chromatin loop extrusion and chromatin unknotting, Polymers 10 (10) (2018) 1–11.
[540] S. Dyson, J. Segura, B. Martínez-García, A. Valdés, J. Roca, Condensin minimizes topoisomerase II-mediated entanglements of DNA in vivo, EMBO J. 40 (1) (2021) 1–14.
[541] G. Nir, I. Farabella, C. Pérez Estrada, C.G. Ebeling, B.J. Beliveau, H.M. Sasaki, S.H. Lee, S.C. Nguyen, R.B. McCole, S. Chattoraj, J. Erceg, J. AlHaj Abed, N.M. Martins, H.Q. Nguyen, M.A. Hannan, S. Russell, N.C. Durand, S.S.P. Rao, J.Y. Kishi, P. Soler-Vila, M. Di Pierro, J.N. Onuchic, S.P. Callahan, J.M. Schreiner, J.A. Stuckey, P. Yin, E.L. Aiden, M.A. Marti-Renom, C.T. Wu, Walking along chromosomes with super-resolution imaging, contact maps, integrative modeling, PLoS Genetics 14 (12) (2018) e1007872.
[542] C.P. Brangwynne, T.J. Mitchison, A.A. Hyman, Active liquid-like behavior of nucleoli determines their size and shape in xenopus laevis oocytes, Proc. Natl. Acad. Sci. 108 (11) (2011) 4334–4339.
[543] M. Barbieri, M. Chotalia, J. Fraser, L.-M. Lavitas, J. Dostie, A. Pombo, M. Nicodemi, Complexity of chromatin folding is captured by the strings and binders switch model, Proc. Natl. Acad. Sci. USA 109 (40) (2012) 16173–16178.
[544] D. Jost, P. Carrivain, G. Cavalli, C. Vaillant, Modeling epigenome folding: formation and dynamics of topologically associated chromatin domains, Nucleic Acids Res. 42 (15) (2014) 9553–9561.
[545] D. Michieletto, D. Colì, D. Marenduzzo, E. Orlandini, Nonequilibrium theory of epigenomic microphase separation in the cell nucleus, Phys. Rev. Lett. 123 (22) (2019) 831396.
[546] M. Di Stefano, H.-W. Nützmann, M.A. Marti-Renom, D. Jost, Polymer modelling unveils the roles of heterochromatin and nucleolar organizing regions in shaping 3D genome organization in Arabidopsis thaliana, Nucleic Acids Res. 49 (4) (2021) 1840–1858.
[547] C. Uhler, G.V. Shivashankar, Chromosome intermingling: Mechanical hotspots for genome regulation, Trends Cell Biol. 27 (11) (2017) 810–819.
[548] D. Michieletto, M. Lusic, D. Marenduzzo, E. Orlandini, Physical principles of retroviral integration in the human genome, Nature Commun. 10 (1) (2019) 575.
[549] B. Bintu, L.J. Mateo, J.-H. Su, N.A. Sinnott-Armstrong, M. Parker, S. Kinrot, K. Yamaya, A.N. Boettiger, X. Zhuang, Super-resolution chromatin tracing reveals domains and cooperative interactions in single cells, Science 362 (6413) (2018).
[550] T.J. Stevens, D. Lando, S. Basu, L.P. Atkinson, Y. Cao, S.F. Lee, M. Leeb, K.J. Wohlfahrt, W. Boucher, A. O'Shaughnessy-Kirwan, J. Cramard, A.J. Faure, M. Ralser, E. Blanco, L. Morey, M. Sansó, M.G.S. Palayret, B. Lehner, L. Di Croce, A. Wutz, B. Hendrich, D. Klenerman, E.D. Laue, 3D structures of individual mammalian genomes studied by single-cell Hi-C, Nature 544 (7648) (2017) 59–64.
[551] J.T. Siebert, A.N. Kivel, L.P. Atkinson, T.J. Stevens, E.D. Laue, P. Virnau, Are there knots in chromosomes? Polymers 9 (8) (2017) 1–10.
[552] P. Virnau, L.A. Mirny, M. Kardar, Intricate knots in proteins: Function and evolution, PLoS Comput. Biol. 2 (9) (2006) e122.
[553] K.-T. Ko, I.-C. Hu, K.-F. Huang, P.-C. Lyu, S.-T.D. Hsu, Untying a knotted SPOUT RNA methyltransferase by circular permutation results in a domain-swapped dimer, Structure 27 (8) (2019) 1224–1233.e4.
[554] R. Potestio, C. Micheletti, H. Orland, Knotted vs. Unknotted proteins: Evidence of knot-promoting loops, Plos Comput. Biol. 6 (7) (2010) e1000864.
[555] T. Wüst, D. Reith, P. Virnau, Sequence determines degree of knottedness in a coarse-grained protein model, Phys. Rev. Lett. 114 (2015) 028102.
[556] R.C. Lua, A.Y. Grosberg, Statistics of knots, geometry of conformations, evolution of proteins, PLoS Comput. Biol. 2 (5) (2006).
[557] A.L. Mallam, S.E. Jackson, Folding studies on a knotted protein, J. Mol. Biol. 346 (5) (2005) 1409–1421.
[558] I. Wang, S.-Y. Chen, S.-T.D. Hsu, Folding analysis of the most complex Stevedore's protein knot, Sci. Rep. 6 (1) (2016) 31514.
[559] S. Jackson, Why are there knots in proteins? Contemp. Math. 746 (2020) 129–153.
[560] I. Wang, S.-Y. Chen, S.-T.D. Hsu, Unraveling the folding mechanism of the smallest knotted protein, MJ0366, J. Phys. Chem. B 119 (12) (2015) 4359–4370.
[561] S.-C. Lou, S. Wetzel, H. Zhang, E.W. Crone, Y.-T. Lee, S.E. Jackson, S.-T.D. Hsu, The knotted protein UCH-L1 exhibits partially unfolded forms under native conditions that share common structural features with its kinetic folding intermediates, J. Mol. Biol. 428 (11) (2016) 2507–2520.
[562] S.-T.D. Hsu, Protein knotting through concatenation significantly reduces folding stability, Sci. Rep. 6 (1) (2016) 39357.
[563] H. Zhang, S.E. Jackson, Characterization of the folding of a 5_2-knotted protein using engineered single-tryptophan variants, Biophys. J. 111 (12) (2016) 2587–2599.
[564] A.L. Mallam, J.M. Rogers, S.E. Jackson, Experimental detection of knotted conformations in denatured proteins, Proc. Natl. Acad. Sci. 107 (18) (2010) 8189–8194.
[565] D.J. Burban, E. Haglund, D.T. Capraro, P.A. Jennings, Heterogeneous side chain conformation highlights a network of interactions implicated in hysteresis of the knotted protein, minimal tied trefoil, J. Phys.: Condens. Matter 27 (35) (2015) 354108.
[566] D.T. Capraro, D.J. Burban, P.A. Jennings, Unraveling allostery in a knotted minimal methyltransferase by nmr spectroscopy, J. Mol. Biol. 432 (9) (2020) 3018–3032.
[567] Y.-T.C. Lee, C.-Y. Chang, S.-Y. Chen, Y.-R. Pan, M.-R. Ho, S.-T.D. Hsu, Entropic stabilization of a deubiquitinase provides conformational plasticity and slow unfolding kinetics beneficial for functioning on the proteasome, Sci. Rep. 7 (1) (2017) 45174.
[568] A.L. Mallam, S.E. Jackson, Probing nature's knots: The folding pathway of a knotted homodimeric protein, J. Mol. Biol. 359 (5) (2006) 1420–1436.
[569] N.P. King, A.W. Jacobitz, M.R. Sawaya, L. Goldschmidt, T.O. Yeates, Structure and folding of a designed knotted protein, Proc. Natl. Acad. Sci. 107 (48) (2010) 20732–20737.
[570] L.-W. Wang, Y.-N. Liu, P.-C. Lyu, S.E. Jackson, S.-T.D. Hsu, Comparative analysis of the folding dynamics and kinetics of an engineered knotted protein and its variants derived from HP0242 ofhelicobacter pylori, J. Phys.: Condens. Matter 27 (35) (2015) 354106.
[571] A.L. Mallam, S.C. Onuoha, J.G. Grossmann, S.E. Jackson, Knotted fusion proteins reveal unexpected possibilities in protein folding, Mol. Cell 30 (5) (2008) 642–648.

[572] Y.-C. Chuang, I.-C. Hu, P.-C. Lyu, S.-T.D. Hsu, Untying a protein knot by circular permutation, J. Mol. Biol. 431 (4) (2019) 857–863.
[573] G. Žoldák, M. Rief, Force as a single molecule probe of multidimensional protein energy landscapes, Curr. Opin. Struct. Biol. 23 (1) (2013) 48–57.
[574] J. Schönfelder, A. Alonso-Caballero, D. De Sancho, R. Perez-Jimenez, The life of proteins under mechanical force, Chem. Soc. Rev. 47 (2018) 3558–3573.
[575] T. Bornschlögl, D.M. Anstrom, E. Mey, J. Dzubiella, M. Rief, K.T. Forest, Tightening the knot in phytochrome by single-molecule atomic force microscopy, Biophys. J. 96 (4) (2009) 1508–1514.
[576] C. He, G. Lamour, A. Xiao, J. Gsponer, H. Li, Mechanically tightening a protein slipknot into a trefoil knot, J. Am. Chem. Soc. 136 (34) (2014) 11946–11955.
[577] M. Rivera, Y. Hao, R.A. Maillard, M. Baez, Mechanical unfolding of a knotted protein unveils the kinetic and thermodynamic consequences of threading a polypeptide chain, Sci. Rep. 10 (1) (2020) 9562.
[578] H. Wang, H. Li, Mechanically tightening, untying and retying a protein trefoil knot by single-molecule force spectroscopy, Chem. Sci. 11 (2020) 12512–12521.
[579] A.L. Mallam, S.E. Jackson, Knot formation in newly translated proteins is spontaneous and accelerated by chaperonins, Nat. Chem. Biol. 8 (2) (2012) 147–153.
[580] C. He, G.Z. Genchev, H. Lu, H. Li, Mechanically untying a protein slipknot: Multiple pathways revealed by force spectroscopy and steered molecular dynamics simulations, J. Am. Chem. Soc. 134 (25) (2012) 10428–10435.
[581] C. He, S. Li, X. Gao, A. Xiao, C. Hu, X. Hu, X. Hu, H. Li, Direct observation of the fast and robust folding of a slipknotted protein by optical tweezers, Nanoscale 11 (2019) 3945–3951.
[582] H. Wang, X. Gao, X. Hu, X. Hu, C. Hu, H. Li, Mechanical unfolding and folding of a complex slipknot protein probed by using optical tweezers, Biochemistry 58 (47) (2019) 4751–4760.
[583] M.A. Soler, A. Nunes, P.F.N. Faísca, Effects of knot type in the folding of topologically complex lattice proteins, J. Chem. Phys. 141 (2) (2014) 025101.
[584] P.F. Faísca, Knotted proteins: A tangled tale of structural biology, Comput. Struct. Biotechnol. J. 13 (2015) 459–468.
[585] S. Wallin, K.B. Zeldovich, E.I. Shakhnovich, The folding mechanics of a knotted protein, J. Mol. Biol. 368 (3) (2007) 884–893.
[586] T. Škrbić, C. Micheletti, P. Faccioli, The role of non-native interactions in the folding of knotted proteins, PLoS Comput. Biol. 8 (6) (2012) e1002504.
[587] J.K. Noel, J.I. Sulkowska, J.N. Onuchic, Slipknotting upon native-like loop formation in a trefoil knot protein, Proc. Natl. Acad. Sci. 107 (35) (2010) 15403–15408.
[588] P. Dabrowski-Tumanski, A.I. Jarmolinska, J.I. Sulkowska, Prediction of the optimal set of contacts to fold the smallest knotted protein, J. Phys.: Condens. Matter 27 (35) (2015) 354109.
[589] M.A. Soler, A. Rey, P.F.N. Faísca, Steric confinement and enhanced local flexibility assist knotting in simple models of protein folding, Phys. Chem. Chem. Phys. 18 (2016) 26391–26403.
[590] J.N.C. Especial, P.F.N. Faísca, Effects of sequence-dependent non-native interactions in equilibrium and kinetic folding properties of knotted proteins, J. Chem. Phys. 159 (6) (2023) 065101.
[591] J.I. Sulkowska, P. Sulkowski, P. Szymczak, M. Cieplak, Stabilizing effect of knots on proteins, Proc. Natl. Acad. Sci. U. S. A. 105 (50) (2008) 19714–19719.
[592] S. a Beccara, T. Škrbić, R. Covino, C. Micheletti, P. Faccioli, Folding pathways of a knotted protein with a realistic atomistic force field, PLoS Comput. Biol. 9 (3) (2013) e1003002.
[593] S. Najafi, R. Potestio, Folding of small knotted proteins: Insights from a mean field coarse-grained model, J. Chem. Phys. 143 (24) (2015) 243121.
[594] J.K. Noel, J. Onuchic, J.I. Sulkowska, Knotting a protein in explicit solvent, 4 (21) (2013) 3570–3573.
[595] R. Covino, T. Škrbić, S. a Beccara, P. Faccioli, C. Micheletti, The role of non-native interactions in the folding of knotted proteins: insights from molecular dynamics simulations, Biomolecules 4 (1) (2014) 1–19.
[596] S. Niewieczerzał, J.I. Sulkowska, Supercoiling in a protein increases its stability, Phys. Rev. Lett. 123 (2019) 138102.
[597] P. Dabrowski-Tumanski, A.I. Jarmolinska, W. Niemyska, E.J. Rawdon, K.C. Millett, J.I. Sulkowska, Linkprot: A database collecting information about biological links, Nucleic Acids Res. 45 (2017) D243–D249.
[598] N.C.H. Lim, S.E. Jackson, Mechanistic insights into the folding of knotted proteins in vitro and in vivo, J. Mol. Biol. 427 (2) (2015) 248–258.
[599] G. Stan, G.H. Lorimer, D. Thirumalai, Friends in need: How chaperonins recognize and remodel proteins that require folding assistance, Front. Mol. Biosci. 9 (2022).
[600] S. Niewieczerzal, J.I. Sulkowska, Knotting and unknotting proteins in the chaperonin cage: Effects of the excluded volume, PLoS One 12 (5) (2017) 1–23.
[601] A.M. Cassaignau, L.D. Cabrita, J. Christodoulou, How does the ribosome fold the proteome? Annu. Rev. Biochem. 89 (1) (2020) 389–415.
[602] M. Chwastyk, M. Cieplak, Cotranslational folding of deeply knotted proteins, J. Phys.: Condens. Matter 27 (35) (2015) 354105.
[603] P.T. Bui, T.X. Hoang, Protein escape at the ribosomal exit tunnel: Effect of the tunnel shape, J. Chem. Phys. 153 (4) (2020) 045105.
[604] M. Chwastyk, M. Cieplak, Nascent folding of proteins across the three domains of life, Front. Mol. Biosci. 8 (2021) 508.
[605] P. Dabrowski-Tumanski, M. Piejko, S. Niewieczerzal, A. Stasiak, J.I. Sulkowska, Protein knotting by active threading of nascent polypeptide chain exiting from the ribosome exit channel, J. Phys. Chem. B 122 (49) (2018) 11616–11625.
[606] M.K. Sriramoju, Y. Chen, S.-T.D. Hsu, Protein knots provide mechano-resilience to an AAA+ protease-mediated proteolysis with profound ATP energy expenses, Biochim. Biophys. Acta (BBA)-Proteins Proteomics 1868 (2) (2020) 140330.
[607] P. Tripathi, B. Mehrafrooz, A. Aksimentiev, S.E. Jackson, M. Gruebele, M. Wanunu, A marcus-Type Inverted Region in the translocation kinetics of a knotted protein, J. Phys. Chem. Lett. 14 (47) (2023) 10719–10726.
[608] S. Ohta, M.T. Alam, H. Arakawa, A. Ikai, Origin of mechanical strength of bovine carbonic anhydrase studied by molecular dynamics simulation, Biophys. J. 87 (6) (2004) 4007–4020.
[609] M.T. Alam, T. Yamada, U. Carlsson, A. Ikai, The importance of being knotted: effects of the C-terminal knot structure on enzymatic and mechanical properties of bovine carbonic anhydrase II, FEBS Lett. 519 (1–3) (2002) 35–40.
[610] J. Dzubiella, Sequence-specific size, structure, stability of tight protein knots, Biophys. J. 96 (2009) 831–839.
[611] J.I. Sulkowska, P. Sułkowski, P. Szymczak, M. Cieplak, Untying knots in proteins, J. Am. Chem. Soc. 132 (40) (2010) 13954–13956.
[612] J.I. Sułkowska, P. Sułkowski, P. Szymczak, M. Cieplak, Tightening of knots in proteins, Physical review letters 100 (5) (2008) 058106.
[613] J. Dzubiella, Tightening and untying the knot in human carbonic anhydrase III, J. Phys. Chem. Lett. 4 (11) (2013) 1829–1833.
[614] Y. Xu, S. Li, Z. Yan, Z. Luo, H. Ren, B. Ge, F. Huang, T. Yue, Stabilizing effect of inherent knots on proteins revealed by molecular dynamics simulations, Biophys. J. 115 (9) (2018) 1681–1689.
[615] J.I. Sułkowska, P. Sułkowski, J.N. Onuchic, Jamming proteins with slipknots and their free energy landscape, Physical review letters 103 (26) (2009) 268103.

[616] M. Sikora, J.I. Sulkowska, M. Cieplak, Mechanical strength of 17 134 model proteins and cysteine slipknots, PLoS Comput. Biol. 5 (10) (2009) e1000547.
[617] Y.I. Zhao, M. Chwastyk, M. Cieplak, Structural entanglements in protein complexes, J. Chem. Phys. 146 (22) (2017) 225102.
[618] L. Huang, D.E. Makarov, Translocation of a knotted polypeptide through a pore, J. Chem. Phys. 129 (2008) 121107.
[619] P. Szymczak, Tight knots in proteins: can they block the mitochondrial pores? Biochem. Soc. Trans. 41 (2) (2013) 620–624.
[620] P. Szymczak, Translocation of knotted proteins through a pore, Eur. Phys. J. Spec. Top. 223 (2014) 1805–1821.
[621] P. Szymczak, Periodic forces trigger knot untying during translocation of knotted proteins, Sci. Rep. 6 (1) (2016) 21702.
[622] T. Christian, R. Sakaguchi, A.P. Perlinska, G. Lahoud, T. Ito, E.A. Taylor, S. Yokoyama, J.I. Sulkowska, Y.-M. Hou, Methyl transfer by substrate signaling from a knotted protein fold, Nat. Struct. Mol. Biol. 23 (10) (2016) 941–948.
[623] A.P. Perlinska, A. Stasiulewicz, E.K. Nawrocka, K. Kazimierczuk, P. Setny, J.I. Sulkowska, Restriction of S-adenosylmethionine conformational freedom by knotted protein binding sites, PLoS Comput. Biol. 16 (5) (2020) e1007904.
[624] P. Dabrowski-Tumanski, J.I. Sulkowska, Topological knots and links in proteins, Proc. Natl. Acad. Sci. 114 (13) (2017) 3415–3420.
[625] M.A. Soler, P.F. Faísca, Effects of knots on protein folding properties, PLoS One 8 (9) (2013) e74755.
[626] J.I. Sulkowska, M. Cieplak, Mechanical stretching of proteins - A theoretical survey of the protein data bank, J. Phys.: Condens. Matt. 19 (28) (2007) 283201.
[627] O. Nureki, M. Shirouzu, K. Hashimoto, R. Ishitani, T. Terada, M. Tamakoshi, T. Oshima, M. Chijimatsu, K. Takio, D.G. Vassylyev, T. Shibata, Y. Inoue, S. Kuramitsu, S. Yokoyama, An enzyme with a deep trefoil knot for the active-site architecture, Acta Crystallogr. D 58 (7) (2002) 1129–1137.
[628] H. Hori, Transfer RNA methyltransferases with a SpoU-TrmD (SPOUT) fold and their modified nucleosides in tRNA, Biomolecules 7 (1) (2017) 23.
[629] K.L. Tkaczuk, S. Dunin-Horkawicz, E. Purta, J.M. Bujnicki, Structural and evolutionary bioinformatics of the SPOUT superfamily of methyltransferases, BMC Bioinform. 8 (1) (2007) 1–31.
[630] T.A. White, D.B. Kell, Comparative genomic assessment of novel broad-spectrum targets for antibacterial drugs, Comp. Funct. Genomics 5 (4) (2004) 304–327.
[631] I. Masuda, R. Matsubara, T. Christian, E.R. Rojas, S.S. Yadavalli, L. Zhang, M. Goulian, L.J. Foster, K.C. Huang, Y.-M. Hou, tRNA methylation is a global determinant of bacterial multi-drug resistance, Cell Syst. 8 (4) (2019) 302–314.
[632] H.J. Ahn, H.-W. Kim, H.-J. Yoon, B.I. Lee, S.W. Suh, J.K. Yang, Crystal structure of tRNA (m1G37) methyltransferase: insights into tRNA recognition, EMBO J. 22 (11) (2003) 2593–2603.
[633] G. Lahoud, S. Goto-Ito, K.-i. Yoshida, T. Ito, S. Yokoyama, Y.-M. Hou, Differentiating analogous tRNA methyltransferases by fragments of the methyl donor, RNA 17 (7) (2011) 1236–1246.
[634] D.J. Craik, D.P. Fairlie, S. Liras, D. Price, The future of peptide-based drugs, Chem. Biol. Drug Des. 81 (1) (2013) 136–147.
[635] C.K. Wang, D.J. Craik, Designing macrocyclic disulfide-rich peptides for biotechnological applications, Nat. Chem. Biol. 14 (5) (2018) 417–427.
[636] P.G. Arnison, M.J. Bibb, G. Bierbaum, A.A. Bowers, T.S. Bugni, G. Bulaj, J.A. Camarero, D.J. Campopiano, G.L. Challis, J. Clardy, P.D. Cotter, D.J. Craik, M. Dawson, E. Dittmann, S. Donadio, P.C. Dorrestein, K.-D. Entian, M.A. Fischbach, J.S. Garavelli, U. Göransson, C.W. Gruber, D.H. Haft, T.K. Hemscheidt, C. Hertweck, C. Hill, A.R. Horswill, M. Jaspars, W.L. Kelly, J.P. Klinman, O.P. Kuipers, A.J. Link, W. Liu, M.A. Marahiel, D.A. Mitchell, G.N. Moll, B.S. Moore, R. Müller, S.K. Nair, I.F. Nes, G.E. Norris, B.M. Olivera, H. Onaka, M.L. Patchett, J. Piel, M.J.T. Reaney, S. Rebuffat, R.P. Ross, H.-G. Sahl, E.W. Schmidt, M.E. Selsted, K. Severinov, B. Shen, K. Sivonen, L. Smith, T. Stein, R.D. Süssmuth, J.R. Tagg, G.-L. Tang, r.W. Truman, J.C. Vederas, C.T. Walsh, J.D. Walton, S.C. Wenzel, J.M. Willey, W.A. van der Donk, Ribosomally synthesized and post-translationally modified peptide natural products: overview and recommendations for a universal nomenclature, Nat. Prod. Rep. 30 (2013) 108–160.
[637] X. Wu, Y.-H. Huang, Q. Kaas, D.J. Craik, Cyclisation of disulfide-rich conotoxins in drug design applications, Eur. J. Org. Chem. 2016 (21) (2016) 3462–3472.
[638] A.H. Benfield, S. Defaus, N. Lawrence, S. Chaousis, N. Condon, O. Cheneval, Y.-H. Huang, L.Y. Chan, D. Andreu, D.J. Craik, S.T. Henriques, Cyclic gomesin, a stable redesigned spider peptide able to enter cancer cells, Biochim. Biophys. Acta (BBA) - Biomembranes 1863 (1) (2021) 183480.
[639] D.J. Craik, J. Du, Cyclotides as drug design scaffolds, Curr. Opin. Chem. Biol. 38 (2017) 8–16.
[640] Y.Y. Shim, Z. Song, P.D. Jadhav, M.J. Reaney, Orbitides from flaxseed (Linum usitatissimum L.): A comprehensive review, Trends Food Sci. Technol. 93 (2019) 197–211.
[641] R.H. Perez, T. Zendo, K. Sonomoto, Circular and leaderless bacteriocins: Biosynthesis, mode of action, applications, prospects, Front. Microbiol. 9 (2018) 2085.
[642] S.J. de Veer, r.M. White, D.J. Craik, Sunflower trypsin inhibitor-1 (SFTI-1): Sowing seeds in the fields of chemistry and biology, Angew. Chem. Int. Ed. 60 (15) (2021) 8050–8071.
[643] R.J. Clark, J. Jensen, S.T. Nevin, B.P. Callaghan, D.J. Adams, D.J. Craik, The engineering of an orally active conotoxin for the treatment of neuropathic pain, Angew. Chem. Int. Ed. 49 (37) (2010) 6545–6548.
[644] A.C. Conibear, D.J. Craik, The chemistry and biology of theta defensins, Angew. Chem. Int. Ed. 53 (40) (2014) 10612–10623.
[645] D.J. Craik, N.L. Daly, T. Bond, C. Waine, Plant cyclotides: A unique family of cyclic and knotted proteins that defines the cyclic cystine knot structural motif1 1edited by P. E. Wright, J. Mol. Biol. 294 (5) (1999) 1327–1336.
[646] C.K. Wang, C.W. Gruber, M. Cemazar, C. Siatskas, P. Tagore, N. Payne, G. Sun, S. Wang, C.C. Bernard, D.J. Craik, Molecular grafting onto a stable framework yields novel cyclic peptides for the treatment of multiple sclerosis, ACS Chem. Biol. 9 (1) (2014) 156–163.
[647] E. Haglund, J.I. Sułkowska, Z. He, G.-S. Feng, P.A. Jennings, J.N. Onuchic, The unique cysteine knot regulates the pleotropic hormone leptin, PLoS One 7 (9) (2012) 1–13.
[648] E. Haglund, J.I. Sulkowska, J.K. Noel, H. Lammert, J.N. Onuchic, P.A. Jennings, Pierced lasso bundles are a new class of knot-like motifs, PLoS Comput. Biol. 10 (6) (2014) 1–11.
[649] D. Reith, P. Cifra, A. Stasiak, P. Virnau, Effective stiffening of DNA due to nematic ordering causes DNA molecules packed in phage capsids to preferentially form torus knots, Nucleic Acids Res. 40 (11) (2012) 5129–5137.
[650] E. Haglund, Engineering covalent loops in proteins can serve as an on/off switch to regulate threaded topologies, J. Phys.: Condens. Matter 27 (35) (2015) 354107.
[651] E. Haglund, A. Pilko, R. Wollman, P.A. Jennings, J. Onuchic, Pierced lasso topology controls function in leptin, J. Phys. Chem. B 121 (4) (2017) 706–718.
[652] J.M. Simien, E. Haglund, Topological twists in nature, Trends Biochem. Sci. 46 (6) (2021) 461–471.
[653] P. Dabrowski-Tumanski, W. Niemyska, P. Pasznik, J.I. Sulkowska, LassoProt: server to analyze biopolymers with lassos, Nucleic Acids Res. 44 (W1) (2016) W383–W389.
[654] F.B.d. Silva, I. Lewandowska, A. Kluza, S. Niewieczerzal, R. Augustyniak, J.I. Sulkowska, First crystal structure of double knotted protein trmd-tm1570 – inside from degradation perspective, 2023, http://dx.doi.org/10.1101/2023.03.13.532328.
[655] M.A. Brems, R. Runkel, T.O. Yeates, P. Virnau, AlphaFold predicts the most complex protein knot and composite protein knots, Prot. Sci. 31 (8) (2022) e4380.

[656] A.P. Perlinska, W.H. Niemyska, B.A. Gren, M. Bukowicki, S. Nowakowski, P. Rubach, J.I. Sulkowska, AlphaFold predicts novel human proteins with knots, Prot. Sci. 32 (5) (2023) e4631.
[657] M.-F. Hsu, M.K. Sriramoju, C.-H. Lai, Y.-R. Chen, J.-S. Huang, T.-P. Ko, K.-F. Huang, S.-T.D. Hsu, Structure, dynamics, and stability of the smallest and most complex 71 protein knot, Journal of Biological Chemistry 300 (1) (2024).
[658] L.A. Doyle, B. Takushi, R.D. Kibler, L.F. Milles, C.T. Orozco, J.D. Jones, S.E. Jackson, B.L. Stoddard, P. Bradley, De novo design of knotted tandem repeat proteins, Nature Commun. 14 (1) (2023) 6746.
[659] P. Dabrowski-Tumanski, A. Stasiak, Alphafold blindness to topological barriers affects its ability to correctly predict proteins' topology, Molecules 28 (22) (2023).
[660] D.A. Leigh, J.J. Danon, S.D.P. Fielden, J.-F. Lemonnier, G.F.S. Whitehead, S.L. Woltering, A molecular endless (7_4) knot, Nat. Chem. 13 (2) (2021) 117–122.
[661] Z. Ashbridge, E. Kreidt, L. Pirvu, F. Schaufelberger, J.H. Stenlid, F. Abild-Pedersen, D.A. Leigh, Vernier template synthesis of molecular knots, Science 375 (6584) (2022) 1035–1041.
[662] G. Polles, D. Marenduzzo, E. Orlandini, C. Micheletti, Self-assembling knots of controlled topology by designing the geometry of patchy templates, Nature Commun. 6 (1) (2015) 6423.
[663] M. Marenda, E. Orlandini, C. Micheletti, Discovering privileged topologies of molecular knots with self-assembling models, Nature Commun. 9 (1) (2018) 3051.
[664] I. Coluzza, P.D.J. van Oostrum, B. Capone, E. Reimhult, C. Dellago, Design and folding of colloidal patchy polymers, Soft Matter 9 (2013) 938–944.
[665] I. Coluzza, P.D.J. van Oostrum, B. Capone, E. Reimhult, C. Dellago, Sequence controlled self-knotting colloidal patchy polymers, Phys. Rev. Lett. 110 (2013) 075501.
[666] C. Cardelli, V. Bianco, L. Rovigatti, F. Nerattini, L. Tubiana, C. Dellago, I. Coluzza, The role of directional interactions in the designability of generalized heteropolymers, Sci. Rep. 7 (1) (2017) 4986.
[667] P. Kar, S.M. Gopal, Y.-M. Cheng, A. Predeus, M. Feig, PRIMO: A transferable coarse-grained force field for proteins, J. Chem. Theory Comput. 9 (8) (2013) 3769–3788.
[668] A. Liwo, M. Baranowski, C. Czaplewski, E. Gołaś, Y. He, D. Jagieła, P. Krupa, M. Maciejczyk, M. Makowski, M.A. Mozolewska, A. Niadzvedtski, S. Ołdziej, H.A. Scheraga, A.K. Sieradzan, R. Ślusarz, T. Wirecki, Y. Yin, B. Zaborowski, A unified coarse-grained model of biological macromolecules based on mean-field multipole–multipole interactions, J. Mol. Model. 20 (8) (2014) 1–15.
[669] J.K. Noel, M. Levi, M. Raghunathan, H. Lammert, R.L. Hayes, J.N. Onuchic, P.C. Whitford, SMOG 2: A versatile software package for generating structure-based models, PLoS Comput. Biol. 12 (3) (2016) e1004794.
[670] L. Monticelli, S.K. Kandasamy, X. Periole, R.G. Larson, D.P. Tieleman, S.-J. Marrink, The MARTINI coarse-grained force field: Extension to proteins, J. Chem. Theory Comput. 4 (5) (2008) 819–834.
[671] M. Pasi, R. Lavery, N. Ceres, Palace: A coarse-grain protein model for studying mechanical properties, J. Chem. Theory Comput. 9 (1) (2013) 785–793.
[672] A. Kolinski, Protein modeling and structure prediction with a reduced representation, Acta Biochim. Pol. 51 (2) (2004) 349–371.
[673] H.J. Coles, M.N. Pivnenko, Liquid crystal 'blue phases' with a wide temperature range, Nature 436 (2005) 997–1000.
[674] D. Wright, N. Mermin, Crystalline liquids: the blue phases, Rev. Modern Phys. 61 (1989) 385.
[675] G.P. Alexander, J.M. Yeomans, Stabilizing the blue phases, Phys. Rev. E 74 (2006) 061706.
[676] D.K. Yang, P.P. Crooker, Chiral-racemic phase diagrams of blue-phase liquid crystals, Phys. Rev. A 35 (1987) 4419.
[677] J. Thoen, Adiabatic scanning calorimetric results for the blue phases of cholesteryl nonanoate, Phys. Rev. A 37 (1988) 1754.
[678] F. Castles, S. Morris, H. Coles, Flexoelectro-optic properties of chiral nematic liquid crystals in the uniform standing helix configuration, Phys. Rev. E 80 (2009) 031709.
[679] H. Kikuchi, M. Yokota, Y. Hisakado, H. Yang, T. Kajiyama, Polymer-stabilized liquid crystal blue phases, Nature Mater. 1 (2002) 64.
[680] Y. Huang, H. Chen, G. Tan, H. Tobata, S.-I. Yamamoto, E. Okabe, Y.-F. Lan, C.-Y. Tsai, S.-T. Wu, Optimized blue-phase liquid crystal for field-sequential-color displays, Opt. Mater. Express 7 (2017) 641.
[681] D.-Y. Guo, C.-W. Chen, C.-C. Li, H.-C. Jau, K.-H. Lin, T.-M. Feng, C.-T. Wang, T.J. Bunning, I.C. Khoo, T.-H. Lin, Reconfiguration of three-dimensional liquid-crystalline photonic crystals by electrostriction, Nature Mater. 19 (2020) 94.
[682] M. Ravnik, G.P. Alexander, J.M. Yeomans, S. Žumer, Three-dimensional colloidal crystals in liquid crystalline blue phases, Proc. Natl. Acad. Sci. 108 (2011) 5188.
[683] D. Pires, J.-B. Fleury, Y. Galerne, Colloid particles in the interaction field of a disclination line in a nematic phase, Phys. Rev. Lett. 98 (2007) 247801.
[684] M. Škarabot, M. Ravnik, S. Žumer, U. Tkalec, I. Poberaj, D. Babič, I. Muševič, Hierarchical self-assembly of nematic colloidal superstructures, Phys. Rev. E 77 (2008) 061706.
[685] M. Ravnik, G.P. Alexander, J.M. Yeomans, S. Žumer, Mesoscopic modelling of colloids in chiral nematics, Faraday Discuss. 144 (2009) 159.
[686] M. Ravnik, J. Fukuda, J.M. Yeomans, S. Žumer, Confining blue phase colloids to thin layers, Soft Matter 7 (2011) 10144.
[687] J. Fukuda, S. Žumer, Quasi-two-dimensional skyrmion lattices in a chiral nematic liquid crystal, Nat. Commun. 2 (1) (2011) 1–5.
[688] M. Lavrič, G. Cordoyiannis, V. Tzitzios, I. Lelidis, S. Kralj, G. Nounesis, S. Žumer, M. Daniel, Z. Kutnjak, Blue phase stabilization by CoPt-decorated reduced-graphene oxide nanosheets dispersed in a chiral liquid crystal, J. Appl. Phys. 127 (2020) 095101.
[689] S. Muhlbauer, B. Binz, F. Jonietz, C. Pfleiderer, A. Rosch, A. Neubauer, R. Georgii, P. Boni, Skyrmion lattice in a chiral magnet, Science 323 (2009) 915.
[690] S. Wang, M. Ravnik, S. Žumer, Surface-patterning generated half-skyrmion lattices in cholesteric blue phase thin films, Liq. Cryst. 45 (2018) 2329.
[691] P.J. Ackerman, R.P. Trivedi, B. Senyuk, J. van de Lagemaat, I.I. Smalyukh, Two-dimensional skyrmions and other solitonic structures in confinement-frustrated chiral nematics, Phys. Rev. E 90 (1) (2014) 012505.
[692] S. Slussarenko, A. Murauski, T. Du, V. Chigrinov, L. Marrucci, E. Santamato, Tunable liquid crystal q-plates with arbitrary topological charge, Opt. Express 19 (2011) 4085.
[693] C. Loussert, U. Delabre, E. Brasselet, Manipulating the orbital angular momentum of light at the micron scale with nematic disclinations in a liquid crystal film, Phys. Rev. Lett. 111 (2013) 037802.
[694] M. Humar, I. Muševič, 3D microlasers from self-assembled cholesteric liquid-crystal microdroplets, Opt. Express 18 (2010) 26995.
[695] G. Poy, A.J. Hess, A.J. Seracuse, M. Paul, S. Žumer, I.I. Smalyukh, Interaction and co-assembly of optical and topological solitons, Nature Photon. 16 (2022) 454.
[696] J.C. Everts, M. Ravnik, Ionically charged topological defects in nematic fluids, Phys. Rev. X 11 (1) (2021) 011054.
[697] L. Giomi, Ž. Kos, M. Ravnik, A. Sengupta, Cross-talk between topological defects in different fields revealed by nematic microfluidics, Proc. Natl. Acad. Sci. USA 114 (2017) E5771.
[698] J.W. Doane, N.A. Vaz, B.G. Wu, S. Žumer, Field controlled light scattering from nematic microdroplets, Appl. Phys. Lett. 48 (1986) 269–271.

[699] O.D. Lavrentovich, Topological defects in dispersed words and worlds around liquid crystals, or liquid crystal drops, Liq. Cryst. 24 (1) (1998) 117–126.
[700] J.A. Martínez-González, Y. Zhou, M. Rahimi, E. Bukusoglu, N.L. Abbott, J.J. de Pablo, Blue-phase liquid crystal droplets, Proc. Natl. Acad. Sci. 112 (2015) 13195.
[701] T. Lopez-Leon, A. Fernandez-Nieves, Drops and shells of liquid crystal, Colloid Polym. Sci. 289 (4) (2011) 345–359.
[702] L.V. Mirantsev, E.J.L. de Oliveira, I.N. de Oliveira, M.L. Lyra, Defect structures in nematic liquid crystal shells of different shapes, Liquid Cryst. Rev. 4 (1) (2016) 35–58.
[703] M. Urbanski, C.G. Reyes, J. Noh, A. Sharma, Y. Geng, V.S.R. Jampani, J.P.F. Lagerwall, Liquid crystals in micron-scale droplets, shells and fibers, J. Phys.: Condens. Matter 29 (13) (2017) 133003.
[704] T.C. Lubensky, J. Prost, Orientational order and vesicle shape, J. Phys. II 2 (3) (1992) 371–382.
[705] D.R. Nelson, Toward a tetravalent chemistry of colloids, Nano Lett. 2 (10) (2002) 1125–1129.
[706] G.R. Yi, D.J. Pine, S. Sacanna, Recent progress on patchy colloids and their self-assembly, J. Phys.: Condens. Matter 25 (19) (2013).
[707] J.G. Kim, S.-Y. Park, Photonic spring-like shell templated from cholesteric liquid crystal prepared by microfluidics, Adv. Opt. Mater. 5 (13) (2017) 1–8.
[708] Y. Uchida, Y. Takanishi, J. Yamamoto, Controlled fabrication and photonic structure of cholesteric liquid crystalline shells, Adv. Mater. 25 (23) (2013) 3234–3237.
[709] E.-K. Fleischmann, H.-L. Liang, N. Kapernaum, F. Giesselmann, J. Lagerwall, R. Zentel, One-piece micropumps from liquid crystalline core-shell particles, Nature Commun. 3 (1) (2012) 1178.
[710] V.S.R. Jampani, R.H. Volpe, K. Reguengo de Sousa, J. Ferreira Machado, C.M. Yakacki, J.P.F.F. Lagerwall, Liquid crystal elastomer shell actuators with negative order parameter, Sci. Adv. 5 (4) (2019) eaaw2476.
[711] M. Schwartz, G. Lenzini, Y. Geng, P.B. Rønne, P.Y.A. Ryan, J.P.F. Lagerwall, Cholesteric liquid crystal shells as enabling material for information-rich design and architecture, Adv. Mater. 1707382 (2018) 1707382–1.
[712] L. Tran, K.J.M. Bishop, Swelling cholesteric liquid crystal shells to direct the assembly of particles at the interface, ACS Nano (2020).
[713] B.V. Hokmabad, K.A. Baldwin, C. Krüger, C. Bahr, C.C. Maass, Topological stabilization and dynamics of self-propelling nematic shells, Phys. Rev. Lett. 123 (17) (2019) 178003.
[714] M. Sheng, L. Zhang, S. Jiang, L. Yang, F. Zaaboul, S. Fu, Bioinspired electro-responsive multispectral controllable dye-doped liquid crystal yolk-shell microcapsules for advanced textiles, ACS Appl. Mater. Interfaces 13 (11) (2021) 13586–13595.
[715] A. Fernandez-Nieves, V. Vitelli, A.S. Utada, D.R. Link, M. Márquez, D.R. Nelson, D.A. Weitz, Novel defect structures in nematic liquid crystal shells, Phys. Rev. Lett. 99 (15) (2007) 157801.
[716] A.S. Utada, E. Lorenceau, D.R. Link, P.D. Kaplan, H.A. Stone, D.A. Weitz, Monodisperse double emulsions generated from a microcapillary device, Science 308 (5721) (2005) 537–541.
[717] N.D. Mermin, E pluribus boojum: the physicist as neologist, Phys. Today 34 (4) (1981) 46–53.
[718] T. Lopez-Leon, V. Koning, K.B.S. Devaiah, V. Vitelli, A. Fernandez-Nieves, Frustrated nematic order in spherical geometries, Nat. Phys. 7 (5) (2011) 391–394.
[719] V. Vitelli, D.R. Nelson, Nematic textures in spherical shells, Phys. Rev. E 74 (2) (2006) 1–18.
[720] H. Shin, M.J. Bowick, X. Xing, Topological defects in spherical nematics, Phys. Rev. Lett. 101 (3) (2008) 1–4.
[721] Y. Zhou, A. Guo, R. Zhang, J.C. Armas-Pérez, J.A. Martínez-González, M. Rahimi, M. Sadati, J.J. de Pablo, Mesoscale structure of chiral nematic shells, Soft Matter (2016).
[722] L.N. Carenza, G. Gonnella, D. Marenduzzo, G. Negro, E. Orlandini, Cholesteric shells: two-dimensional blue fog and finite quasicrystals, Phys. Rev. Lett. 128 (2022) 497.
[723] Y. Iwai, Y. Uchida, N. Nishiyama, Self-assembled magnetic control lever embedded in photonic liquid crystalline microcapsule, Adv. Opt. Mater. 4 (12) (2016) 1961–1964.
[724] J. Noh, B. Henx, J.P.F. Lagerwall, Taming liquid crystal self-assembly: The multifaceted response of nematic and smectic shells to polymerization, Adv. Mater. 28 (46) (2016) 10170–10174.
[725] K. He, F. Campo-Cortés, M. Goral, T. López-León, J.M. Gordillo, Micron-sized double emulsions and nematic shells generated via tip streaming, Phys. Rev. Fluids 4 (12) (2019) 124201.
[726] R.D. Kamien, Colloidal inclusions in liquid crystals, in: Proceedings of the International School of Physics “Enrico Fermi”, Course 193: Soft Matter Assembly, 2015.
[727] G. Durey, Stripes, Fingers and Skyrmions: Taming Cholesteric Liquid Crystal Shells Under Perpendicular Anchoring (Ph.D. thesis), Université PSL, 2018, p. 234.
[728] G. Durey, H.R.O. Sohn, P.J. Ackerman, E. Brasselet, I.I. Smalyukh, T. Lopez-Leon, Topological solitons, cholesteric fingers and singular defect lines in janus liquid crystal shells, Soft Matter 16 (11) (2020) 2669–2682.
[729] T. Lopez-Leon, A. Fernandez-Nieves, M. Nobili, C. Blanc, Smectic shells, J. Phys.: Condens. Matter 24 (28) (2012) 284122.
[730] Y. Geng, J. Noh, I. Drevensek-Olenik, R. Rupp, G. Lenzini, J.P.F. Lagerwall, High-fidelity spherical cholesteric liquid crystal bragg reflectors generating unclonable patterns for secure authentication, Sci. Rep. 6 (2016) 26840.
[731] F.C. Keber, E. Loiseau, T. Sanchez, S.J. DeCamp, L. Giomi, M.J. Bowick, M.C. Marchetti, Z. Dogic, A.R. Bausch, Topology and dynamics of active nematic vesicles, Science 345 (6201) (2014) 1135–1139.
[732] C. Blanc, G. Durey, R.D. Kamien, T. Lopez-Leon, M.O. Lavrentovich, L. Tran, Helfrich-hurault elastic instabilities driven by geometrical frustration, Rev. Modern Phys. 95 (2023) 85.
[733] A. Sharma, J.P.F. Lagerwall, Influence of head group and chain length of surfactants used for stabilising liquid crystal shells, Liq. Cryst. (2018) 1–10.
[734] G. Durey, Y. Ishii, T. Lopez-Leon, Temperature-driven anchoring transitions at liquid crystal/water interfaces, Langmuir 36 (2020) 9368.
[735] J. Noh, V.S.R. Jampani, O. Haba, K. Yonetake, H. Takezoe, J.P.F. Lagerwall, Sub-second dynamic phototuning of alignment in azodendrimer-doped nematic liquid crystal shells, J. Mol. Liq. 267 (2018) 197–204.
[736] A. Darmon, M. Benzaquen, D. Seč, S. Čopar, O. Dauchot, T. Lopez-Leon, Waltzing route toward double-helix formation in cholesteric shells, Proc. Natl. Acad. Sci. 113 (34) (2016) 9469–9474.
[737] L. Tran, M.O. Lavrentovich, G. Durey, A. Darmon, M.F. Haase, N. Li, D. Lee, K.J. Stebe, R.D. Kamien, T. Lopez-Leon, Change in stripes for cholesteric shells via anchoring in moderation, Phys. Rev. X 7 (4) (2017) 041029.
[738] B. Gollapelli, J. Vallamkondu, Electric field-driven structural changes in cholesteric shells for optical applications, Curr. Appl. Phys. 19 (12) (2019) 1399–1403.
[739] M.C. Marchetti, J.F. Joanny, S. Ramaswamy, T.B. Liverpool, J. Prost, M. Rao, R.A. Simha, Hydrodynamics of soft active matter, Rev. Modern Phys. 85 (2013) 1143.
[740] N.P. Group, Nature research collection active matter, 2019.
[741] A. Doostmohammadi, J. Ignés-Mullol, J.M. Yeomans, F. Sagués, Active nematics, Nature Commun. 9 (2018) 3246.

[742] M.M. Genkin, A. Sokolov, O.D. Lavrentovich, I.S. Aranson, Topological defects in a living nematic ensnare swimming bacteria, Phys. Rev. X 7 (2017) 011029.
[743] O.D. Lavrentovich, Active colloids in liquid crystals, Curr. Opin. Colloid Interface Sci. 21 (2016) 97.
[744] S. Čopar, J. Aplinc, Ž. Kos, S. Žumer, M. Ravnik, Topology of three-dimensional active nematic turbulence confined to droplets, Phys. Rev. X 9 (3) (2019) 031051.
[745] J. Binysh, Ž. Kos, S. Čopar, M. Ravnik, G.P. Alexander, Three-dimensional active defect loops, Phys. Rev. Lett. 124 (2020) 257.
[746] L.J. Ruske, J.M. Yeomans, Morphology of active deformable 3D droplets, Phys. Rev. X 11 (2021) 021001.
[747] S. Ramaswamy, The mechanics and statistics of active matter, Annu. Rev. Condens. Matter Phys. 1 (2010) 323–345.
[748] V. Narayan, S. Ramaswamy, N. Menon, Long-lived giant number fluctuations in a swarming granular nematic, Science 317 (2007) 105–108.
[749] T. Sanchez, D. Chen, S. DeCamp, M. Heymann, Z. Dogic, Spontaneous motion in hierarchically assembled active matter, Nature 491 (2012) 431.
[750] L. Giomi, M.J. Bowick, P. Mishra, R. Sknepnek, M.C. Marchetti, Defect dynamics in active nematics, Phil. Trans. R. Soc. A 372 (2014) 20130365.
[751] D. Khoromskaia, G.P. Alexander, Vortex formation and dynamics of defects in active nematic shells, New J. Phys. 19 (10) (2017) 103043.
[752] D. Cortese, J. Eggers, T. Liverpool, Pair creation, motion, annihilation of topological defects in two-dimensional nematic liquid crystals, Phys. Rev. E 97 (2018) 022704.
[753] S. Shankar, M.C. Marchetti, Hydrodynamics of active defects: From order to chaos to defect ordering, Phys. Rev. X 9 (2019) 041047.
[754] H.H. Wensink, J. Dunkel, S. Heidenreich, K. Drescher, R.E. Goldstein, H. Löwen, J.M. Yeomans, Meso-scale turbulence in living fluids, Proc. Natl. Acad. Sci. USA 109 (2012) 14308.
[755] L. Giomi, Geometry and topology of turbulence in active nematics, Phys. Rev. X 5 (2015) 031003.
[756] T.B. Saw, A. Doostmohammadi, V. Nier, L. Kocgozlu, S. Thampi, Y. Toyama, P. Marcq, C.T. Lim, J.M. Yeomans, B. Ladoux, Topological defects in epithelia govern cell death and extrusion, Nature 544 (2017) 212.
[757] K. Kawaguchi, R. Kageyama, M. Sano, Topological defects control collective dynamics in neural progenitor cell cultures, Nature 545 (2017) 327.
[758] G. Duclos, C. Erlenkämper, J.-F. Joanny, P. Silberzan, Topological defects in confined populations of spindle-shaped cells, Nat. Phys. 13 (2017) 58.
[759] O.J. Meacock, A. Doostmohammadi, K.R. Foster, J.M. Yeomans, W.M. Durham, Bacteria solve the problem of crowding by moving slowly, Nat. Phys. 17 (2021) 205.
[760] Y. Maroudas-Sachs, L. Garion, L. Shani-Zerbib, A. Livshits, E. Braun, K. Keren, Topological defects in the nematic order of actin fibres as organization centres of *Hydra* morphogenesis, Nat. Phys. 17 (2021) 251.
[761] S. Chandragiri, A. Doostmohammadi, J.M. Yeomans, S.P. Thampi, Flow states and transitions of an active nematic in a three-dimensional channel, Phys. Rev. Lett. 125 (2020) 148002.
[762] P. Chandrakar, M. Varghese, S. Aghvami, A. Baskaran, Z. Dogic, G. Duclos, Confinement controls the bend instability of three-dimensional active liquid crystals, Phys. Rev. Lett. 125 (2020) 257801.
[763] M. Varghese, A. Baskaran, M. Hagan, A. Baskaran, Confinement-induced self-pumping in 3D active fluids, Phys. Rev. Lett. 125 (2020) 268003.
[764] J. Friedel, P. De Gennes, Boulces de disclinations dans les cristaux liquides, C. R. Acad. Sc. Paris B 268 (1969) 257–259.
[765] J. Binysh, G.P. Alexander, Maxwell's theory of solid angle and the construction of knotted fields, J. Phys. A 51 (2018) 385202.
[766] T.C. Adhyapak, S. Ramaswamy, J. Toner, Live soap: Stability, order, fluctuations in apolar active smectics, Phys. Rev. Lett. 110 (2013) 118102.
[767] L. Chen, J. Toner, Universality for moving stripes: A hydrodynamic theory of polar active smectics, Phys. Rev. Lett. 111 (2013) 088701.
[768] C.A. Whitfield, T.C. Adhyapak, A. Tiribocchi, G.P. Alexander, D. Marenduzzo, S. Ramaswamy, Hydrodynamic instabilities in active cholesteric liquid crystals, Eur. Phys. J. E 40 (2017) 50.
[769] L. Metselaar, A. Doostmohammadi, J.M. Yeomans, Topological states in chiral active matter: Dynamic blue phases and active half-skyrmions, J. Chem. Phys. 150 (2019) 064909.
[770] L.N. Carenza, G. Gonella, D. Marenduzzo, G. Negro, Rotation and propulsion in 3D active chiral droplets, Proc. Natl. Acad. Sci. USA 116 (2019) 22065.
[771] Y. Bouligand, Twisted fibrous arrangements in biological materials and cholesteric mesophases, Tissue Cell 4 (2) (1972) 189–217.
[772] A.C. Neville, Biology of Fibrous Composites: Development Beyond the Cell Membrane, Cambridge University Press, 1993.
[773] J.H.E. Cartwright, A.G. Checa, The dynamics of nacre self-assembly, J. R. Soc. Interface 4 (14) (2007) 491–504.
[774] J.H.E. Cartwright, A.G. Checa, B. Escribano, C.I. Sainz-Díaz, Spiral and target patterns in bivalve nacre manifest a natural excitable medium from layer growth of a biological liquid crystal, Proc. Natl. Acad. Sci. 106 (26) (2009) 10499–10504.
[775] J.H.E. Cartwright, A.G. Checa, M. Rousseau, Pearls are self-organized natural ratchets, Langmuir 29 (26) (2013) 8370–8376.
[776] A.G. Checa, J.H.E. Cartwright, I. Sánchez-Almazo, J.P. Andrade, F. Ruiz-Raya, The cuttlefish sepia officinalis (sepiidae, cephalopoda) constructs cuttlebone from a liquid-crystal precursor, Sci. Rep. 5 (1) (2015) 1–13.
[777] I. Almagro, J.H.E. Cartwright, A.G. Checa, E. Macías-Sánchez, C.I. Sainz-Díaz, Evidence for a liquid-crystal precursor involved in the formation of the crossed-lamellar microstructure of the mollusc shell, Acta Biomater. 120 (2021) 12–19.
[778] C.P. Garnham, A. Roll-Mecak, The chemical complexity of cellular microtubules: tubulin post-translational modification enzymes and their roles in tuning microtubule functions, Cytoskeleton 69 (7) (2012) 442–463.
[779] M.A. Welte, Bidirectional transport along microtubules, Curr. Biol. 14 (13) (2004) R525–R537.
[780] M. Vicente-Manzanares, C.K. Choi, A.R. Horwitz, Integrins in cell migration–the actin connection, J. Cell Sci. 122 (2) (2009) 199–206.
[781] M. Crisp, Q. Liu, K. Roux, J.B. Rattner, C. Shanahan, B. Burke, P.D. Stahl, D. Hodzic, Coupling of the nucleus and cytoplasm: role of the LINC complex, J. Cell Biol. 172 (1) (2006) 41–53.
[782] T. Bouzid, E. Kim, B.D. Riehl, A.M. Esfahani, J. Rosenbohm, R. Yang, B. Duan, J.Y. Lim, The LINC complex, mechanotransduction, mesenchymal stem cell function and fate, J. Biol. Eng. 13 (1) (2019) 1–12.
[783] H. Gerardo, A. Lima, J. Carvalho, J.R. Ramos, S. Couceiro, R.D.M. Travasso, R.P. das Neves, M. Grãos, Soft culture substrates favor stem-like cellular phenotype and facilitate reprogramming of human mesenchymal stem/stromal cells (hMSCs) through mechanotransduction, Sci. Rep. 9 (1) (2019) 1–18.
[784] J. Prost, F. Jülicher, J.-F. Joanny, Active gel physics, Nat. Phys. 11 (2) (2015) 111–117.
[785] L.N. Carenza, G. Gonnella, A. Lamura, G. Negro, A. Tiribocchi, Lattice Boltzmann methods and active fluids, Eur. Phys. J. E 42 (6) (2019) 1–38.
[786] T. Le Goff, B. Liebchen, D. Marenduzzo, Actomyosin contraction induces in-bulk motility of cells and droplets, Biophys. J. 119 (5) (2020) 1025–1032.
[787] B.A. Camley, Y. Zhang, Y. Zhao, B. Li, E. Ben-Jacob, H. Levine, W.-J. Rappel, Polarity mechanisms such as contact inhibition of locomotion regulate persistent rotational motion of mammalian cells on micropatterns, Proc. Natl. Acad. Sci. 111 (41) (2014) 14770–14775.
[788] A. Moure, H. Gomez, Three-dimensional simulation of obstacle-mediated chemotaxis, Biomech. Model. Mechanobiol. 17 (5) (2018) 1243–1268.
[789] A. Moure, H. Gomez, Dual role of the nucleus in cell migration on planar substrates, Biomech. Model. Mechanobiol. 19 (2020) 1491–1508.
[790] S. Portet, A. Madzvamuse, y. Chung, R.E. Leube, R. Windoffer, Keratin dynamics: modeling the interplay between turnover and transport, PLoS One 10 (3) (2015) e0121090.

[791] M. Gouveia, Š. Zemljič-Jokhadar, M. Vidak, B. Stojkovič, J. Derganc, R. Travasso, M. Liovic, Keratin dynamics and spatial distribution in wild-type and K14 R125P mutant cells—A computational model, Int. J. Mol. Sci. 21 (7) (2020) 2596.
[792] Š. Zemljič Jokhadar, B. Stojković, M. Vidak, T. Sorčan, M. Liovic, M. Gouveia, R.D.M. Travasso, J. Derganc, Cortical stiffness of keratinocytes measured by lateral indentation with optical tweezers, PLoS One 15 (12) (2020) e0231606.
[793] D. Antfolk, M. Sjöqvist, F. Cheng, K. Isoniemi, C.L. Duran, A. Rivero-Muller, C. Antila, R. Niemi, S. Landor, C.V.C. Bouten, K.J. Bayless, J.E. Eriksson, C.M. Sahlgren, Selective regulation of notch ligands during angiogenesis is mediated by vimentin, Proc. Natl. Acad. Sci. 114 (23) (2017) E4574–E4581.
[794] N.C.A. van Engeland, F.S. Rodriguez, A. Rivero-Müller, T. Ristori, C.L. Duran, O.M.J.A. Stassen, D. Antfolk, R.C.H. Driessen, S. Ruohonen, S.T. Ruohonen, S. Nuutinen, E. Savontaus, S. Loerakker, K.J. Bayless, M. Sjöqvist, C.V.C. Bouten, J.E. Eriksson, C.M. Sahlgren, Vimentin regulates notch signaling strength and arterial remodeling in response to hemodynamic stress, Sci. Rep. 9 (1) (2019) 1–14.
[795] F. Jülicher, K. Kruse, J. Prost, J.-F. Joanny, Active behavior of the cytoskeleton, Phys. Rep. 449 (1–3) (2007) 3–28.
[796] M. Krause, A. Gautreau, Steering cell migration: lamellipodium dynamics and the regulation of directional persistence, Nat. Rev. Mol. Cell Biol. 15 (9) (2014) 577–590.
[797] K. Kruse, J.F. Joanny, F. Jülicher, J. Prost, Contractility and retrograde flow in lamellipodium motion, Phys. Biol. 3 (2) (2006) 130.
[798] K. Kruse, J.-F. Joanny, F. Jülicher, J. Prost, K. Sekimoto, Generic theory of active polar gels: A paradigm for cytoskeletal dynamics, Eur. Phys. J. E 16 (1) (2005) 5–16.
[799] T. Bretschneider, S. Diez, K. Anderson, J. Heuser, M. Clarke, A. Müller-Taubenberger, J. Köhler, G. Gerisch, Dynamic actin patterns and Arp2/3 assembly at the substrate-attached surface of motile cells, Curr. Biol. 14 (1) (2004) 1–10.
[800] G. Salbreux, J.-F. Joanny, J. Prost, P. Pullarkat, Shape oscillations of non-adhering fibroblast cells, Phys. Biol. 4 (4) (2007) 268.
[801] G. Salbreux, J. Prost, J.-F. Joanny, Hydrodynamics of cellular cortical flows and the formation of contractile rings, Phys. Rev. Lett. 103 (5) (2009) 058102.
[802] M.R. Shaebani, A. Wysocki, R.G. Winkler, G. Gompper, H. Rieger, Computational models for active matter, Nat. Rev. Phys. 2 (4) (2020) 181–199.
[803] R. Ramaswamy, G. Bourantas, F. Jülicher, I.F. Sbalzarini, A hybrid particle-mesh method for incompressible active polar viscous gels, J. Comput. Phys. 291 (2015) 334–361.
[804] S. Safran, Statistical Thermodynamics of Surfaces, Interfaces, Membranes, CRC Press, 2018.
[805] F. Campelo, A. Hernandez-Machado, Dynamic model and stationary shapes of fluid vesicles, Eur. Phys. J. E 20 (1) (2006) 37–45.
[806] D. Shao, H. Levine, W.-J. Rappel, Coupling actin flow, adhesion, morphology in a computational cell motility model, Proc. Natl. Acad. Sci. 109 (18) (2012) 6851–6856.
[807] N. Provatas, K. Elder, Phase-Field Methods in Materials Science and Engineering, John Wiley & Sons, 2011.
[808] M. Nonomura, Study on multicellular systems using a phase field model, PLoS One 7 (4) (2012) e33501.
[809] M. Moreira-Soares, S.P. Cunha, J.R. Bordin, R.D.M. Travasso, Adhesion modulates cell morphology and migration within dense fibrous networks, J. Phys.: Condens. Matter 32 (31) (2020) 314001.
[810] P. Santos-Oliveira, A. Correia, T. Rodrigues, T.M. Ribeiro-Rodrigues, P. Matafome, J.C. Rodríguez-Manzaneque, R. Seiça, H. Girão, R.D.M. Travasso, The force at the tip-modelling tension and proliferation in sprouting angiogenesis, PLoS Comput. Biol. 11 (8) (2015) e1004436.
[811] G. Vilanova, I. Colominas, H. Gomez, Capillary networks in tumor angiogenesis: From discrete endothelial cells to phase-field averaged descriptions via isogeometric analysis, Int. J. Numer. Methods Biomed. Eng. 29 (10) (2013) 1015–1037.
[812] M. Moreira-Soares, R. Coimbra, L. Rebelo, J. Carvalho, R.D.M. Travasso, Angiogenic factors produced by hypoxic cells are a leading driver of anastomoses in sprouting angiogenesis–A computational study, Sci. Rep. 8 (1) (2018) 1–12.
[813] H. Gomez, K.G. van der Zee, Computational phase-field modeling, in: Encyclopedia of Computational Mechanics, Second Edition, Wiley Online Library, 2018, pp. 1–35.
[814] R.D. Travasso, M. Castro, J.C.R.E. Oliveira, The phase-field model in tumor growth, Phil. Mag. 91 (1) (2011) 183–206.
[815] G. Lorenzo, T.J. Hughes, P. Dominguez-Frojan, A. Reali, H. Gomez, Computer simulations suggest that prostate enlargement due to benign prostatic hyperplasia mechanically impedes prostate cancer growth, Proc. Natl. Acad. Sci. 116 (4) (2019) 1152–1161.
[816] P.C. Hohenberg, B.I. Halperin, Theory of dynamic critical phenomena, Rev. Modern Phys. 49 (3) (1977) 435.
[817] Q. Wang, X. Yang, D. Adalsteinsson, T.C. Elston, K. Jacobson, M. Kapustina, M.G. Forest, Computational and modeling strategies for cell motility, in: Computational Modeling of Biological Systems, Springer, 2012, pp. 257–296.
[818] B.A. Camley, Y. Zhao, B. Li, H. Levine, W.-J. Rappel, Crawling and turning in a minimal reaction-diffusion cell motility model: coupling cell shape and biochemistry, Phys. Rev. E 95 (1) (2017) 012401.
[819] J. Kim, Y. Cao, C. Eddy, Y. Deng, H. Levine, W.-J. Rappel, B. Sun, The mechanics and dynamics of cancer cells sensing noisy 3D contact guidance, Proc. Natl. Acad. Sci. 118 (10) (2021).
[820] S. Shankar, A. Souslov, M.J. Bowick, M.C. Marchetti, V. Vitelli, Topological active matter, Nat. Rev. Phys. 4 (2022) 380–398.
[821] M.Z. Hasan, C.L. Kane, Colloquium: Topological insulators, Rev. Modern Phys. 82 (2010) 3045–3067.
[822] T. Ozawa, H.M. Price, A. Amo, N. Goldman, M. Hafezi, L. Lu, M.C. Rechtsman, D. Schuster, J. Simon, O. Zilberberg, I. Carusotto, Topological photonics, Rev. Modern Phys. 91 (2019) 015006.
[823] R. Fleury, D.L. Sounas, C.F. Sieck, M.R. Haberman, A. Alù, Sound isolation and giant linear nonreciprocity in a compact acoustic circulator, Science 343 (2014) 516–519.
[824] A. Souslov, B.C. van Zuiden, D. Bartolo, V. Vitelli, Topological sound in active-liquid metamaterials, Nat. Phys. 13 (2017) 1091.
[825] K. Sone, Y. Ashida, Anomalous topological active matter, Phys. Rev. Lett. 123 (2019) 205502.
[826] P. Delplace, J.B. Marston, A. Venaille, Topological origin of equatorial waves, Science 358 (2017) 1075–1077.
[827] S. Shankar, M.J. Bowick, M.C. Marchetti, Topological sound and flocking on curved surfaces, Phys. Rev. X 7 (2017) 031039.
[828] A. Souslov, K. Dasbiswas, M. Fruchart, S. Vaikuntanathan, V. Vitelli, Topological waves in fluids with odd viscosity, Phys. Rev. Lett. 122 (12) (2019) 128001.
[829] C. Tauber, P. Delplace, A. Venaille, A bulk-interface correspondence for equatorial waves, J. Fluid Mech. 868 (2019) R2.
[830] J.E. Avron, Odd viscosity, J. Stat. Phys. 92 (1998) 543–557.
[831] D. Banerjee, A. Souslov, A.G.P. Abanov, V. Vitelli, Odd viscosity in chiral active fluids, Nat. Commun. 8 (1) (2017) 1–12.
[832] M. Brandenbourger, X. Locsin, E. Lerner, C. Coulais, Non-reciprocal robotic metamaterials, Nature Commun. 10 (2019) 4608.
[833] A. Ghatak, M. Brandenbourger, J. van Wezel, C. Coulais, Observation of non-hermitian topology and its bulk-edge correspondence in an active mechanical metamaterial, Proc. Natl. Acad. Sci. U.S.A 117 (2020) 29651–29658.
[834] C. Scheibner, A. Souslov, D. Banerjee, P. Surówka, W.T.M. Irvine, V. Vitelli, Odd elasticity, Nat. Phys. 16 (4) (2020) 475–480.
[835] C. Scheibner, W.T.M. Irvine, V. Vitelli, Non-hermitian band topology and skin modes in active elastic media, Phys. Rev. Lett. 125 (2020) 118001.
[836] C. Tauber, P. Delplace, A. Venaille, Anomalous bulk-edge correspondence in continuous media, Phys. Rev. Res. 2 (2020) 013147.
[837] G. Baardink, G. Cassella, L. Neville, P.A. Milewski, A. Souslov, Complete absorption of topologically protected waves, Phys. Rev. E 104 (1) (2021) 014603.
[838] H. Abbaszadeh, A. Souslov, J. Paulose, H. Schomerus, V. Vitelli, Sonic Landau levels and synthetic gauge fields in mechanical metamaterials, Phys. Rev. Lett. 119 (2017) 195502.

[839] M.A. Bandres, S. Wittek, G. Harari, M. Parto, J. Ren, M. Segev, D.N. Christodoulides, M. Khajavikhan, Topological insulator laser: Experiments, Science 359 (6381) (2018).
[840] G.E. Volovik, The universe in a helium droplet, in: International Series of Monographs on Physics, OUP Oxford, 2009.
[841] S. Coleman, Aspects of Symmetry: Selected Erice Lectures, Cambridge University Press, Cambridge, U.K., 1985.
[842] S. Weinberg, The quantum theory of fields. Vol. 2: Modern applications, Cambridge University Press, 2013.
[843] A. Vilenkin, E.P.S. Shellard, Cosmic Strings and Other Topological Defects, Cambridge University Press, 2000.
[844] S.K. Nechaev, Statistics of Knots and Entangled Random Walks, World Scientific, 1996.
[845] D. Meluzzi, D.E. Smith, G. Arya, Biophysics of knotting, Annu. Rev. Biophys. 39 (2010) 349–366.
[846] G.V. Pickwell, Knotting and coiling behavior in the pelagic sea snake pelamis platurus (L.), Copeia 1971 (2) (1971) 348–350.
[847] H.B. Lillywhite, Unusual shedding behaviors in an aquatic snake, Acrochordus granulatus, Copeia 1989 (3) (1989) 768–770.
[848] J.A. Savidge, T.F. Seibert, M. Kastner, B.C. Jayne, Lasso locomotion expands the climbing repertoire of snakes, Curr. Biol. 31 (1) (2021) R7–R8.
[849] T.J. Miller, Knotting: A previously undescribed feeding behavior in muraenid eels, Copeia 1987 (4) (1987) 1055–1057.
[850] S.C. Barley, R.S. Mehta, J.J. Meeuwig, M.G. Meekan, To knot or not? Novel feeding behaviours in moray eels, Mar. Biodivers. 46 (3) (2016) 703–705.
[851] A.J. Clark, C.H. Crawford, B.D. King, A.M. Demas, T.A. Uyeno, Material properties of hagfish skin, with insights into knotting behaviors, Biol. Bull. 230 (3) (2016) 243–256.
[852] W.A. Haney, A.J. Clark, T.A. Uyeno, Characterization of body knotting behavior used for escape in a diversity of hagfishes, J. Zool. 310 (4) (2020) 261–272.
[853] P. Lambert, Sea cucumbers of British Columbia, Southeast Alaska and Puget Sound, UBC Press, 1997.
[854] C. Darwin, The Movements and Habits of Climbing Plants, John Murray, 1875.
[855] P. Pieranski, J. Baranska, A. Skjeltorp, Tendril perversion—A physical implication of the topological conservation law, Eur. J. Phys. 25 (5) (2004) 613.
[856] J. Feng, W. Zhang, C. Liu, M. Guo, C. Zhang, Homoclinic and heteroclinic orbits in climbing cucumber tendrils, Sci. Rep. 9 (1) (2019) 1–14.
[857] J. Feng, Q. Zhang, W. Wang, S. Hao, Nonlinear dynamics behavior analysis of the spatial configuration of a tendril-bearing plant, Eur. Phys. J. Plus 132 (3) (2017) 1–14.
[858] C. Herzfeld, D. Lestel, Knot tying in great apes: etho-ethnology of an unusual tool behavior, Soc. Sci. Inf. 44 (4) (2005) 621–653.
[859] M.R. McLennan, Tie one on: 'nest tying' by wild chimpanzees at Bulindi — A variant of a universal great ape behavior? Primates 59 (3) (2018) 227–233.
[860] N. Nesher, G. Levy, F.W. Grasso, B. Hochner, Self-recognition mechanism between skin and suckers prevents octopus arms from interfering with each other, Curr. Biol. 24 (11) (2014) 1271–1275.
[861] R.J. Wassersug, L. Roberts, J. Gimian, E. Hughes, R. Saunders, D. Devison, J. Woodbury, J.C. O'Reilly, The behavioral responses of amphibians and reptiles to microgravity on parabolic flights, Zoology 108 (2) (2005) 107–120.
[862] A. Goriely, Knotted umbilical cords, in: Physical and Numerical Models in Knot Theory: Including Applications To the Life Sciences, World Scientific, 2005, pp. 109–126.
[863] W.N. Spellacy, H. Gravem, R.O. Fisch, The umbilical cord complications of true knots, nuchal coils, and cords around the body: report from the collaborative study of cerebral palsy, Am. J. Obstet. Gynecol. 94 (8) (1966) 1136–1142.
[864] G. Clerici, I. Koutras, R. Luzietti, G.C. Di Renzo, Multiple true umbilical knots: A silent risk for intrauterine growth restriction with anomalous hemodynamic pattern, Fetal Diagn. Ther. 22 (6) (2007) 440–443.
[865] C. López Ramón y Cajal, R. Ocampo Martínez, Four-dimensional ultrasonography of a true knot of the umbilical cord, Am. J. Obstet. Gynecol. 195 (4) (2006) 896–898.
[866] A.-L. Barabasi, Z.N. Oltvai, Network biology: understanding the cell's functional organization, Nat. Rev. Genet. 5 (2) (2004) 101–113.
[867] C. Mitrea, Z. Taghavi, B. Bokanizad, S. Hanoudi, R. Tagett, M. Donato, C. Voichiţa, S. Drăghici, Methods and approaches in the topology-based analysis of biological pathways, Front. Physiol. 4 (2013) 278.
[868] W. Winterbach, P.V. Mieghem, M. Reinders, H. Wang, D.d. Ridder, Topology of molecular interaction networks, BMC Syst. Biol. 7 (2013) 1–15.
[869] M. Gosak, R. Markovič, J. Dolenšek, M.S. Rupnik, M. Marhl, A. Stožer, M. Perc, Network science of biological systems at different scales: A review, Phys. Life Rev. 24 (2018) 118–135.
[870] H.H. Gan, S. Pasquali, T. Schlick, Exploring the repertoire of RNA secondary motifs using graph theory with implications for RNA design, Nucleic Acids Res. 31 (2003) 2926–2943.
[871] H.H. Gan, D. Fera, J. Zorn, N. Shiffeldrim, M. Tang, U. Laserson, N. Kim, T. Schlick, RAG: RNA-As-graphs database - concepts, analysis, and features, Bioinformatics 20 (8) (2004) 1285–1291.
[872] H. Orland, A. Zee, RNA folding and largenmatrix theory, Nuclear Phys. B 620 (2002) 456–476.
[873] G. Vernizzi, P. Ribeca, H. Orland, A. Zee, Topology of pseudoknotted homopolymers, Phys. Rev. E 73 (2016) 031902.
[874] G. Vernizzi, H. Orland, A. Zee, Classification and predictions of RNA pseudoknots based on topological invariants, Phys. Rev. E 94 (2016) 042410.
[875] C. Micheletti, M. Di Stefano, H. Orland, Absence of knots in known RNA structures, Proc. Natl. Acad. Sci. 112 (7) (2015) 2052–2057.
[876] A. Burton, M. Di Stefano, N. Lehman, H. Orland, C. Micheletti, The elusive quest for RNA knots, RNA Biol. 13 (2) (2016) 134–139.
[877] J.-F. Ayme, J.E. Beves, D.A. Leigh, R.T. McBurney, K. Rissanen, D. Schultz, A synthetic molecular pentafoil knot, Nature Chem. 4 (1) (2012) 15–20.
[878] S.D.P. Fielden, D.A. Leigh, S.L. Woltering, Molecular knots, Angew. Chem. Int. Ed. 56 (37) (2017) 11166–11194.
[879] S. Datta, Y. Kato, S. Higashiharaguchi, K. Aratsu, A. Isobe, T. Saito, D.D. Prabhu, Y. Kitamoto, M.J. Hollamby, A.J. Smith, R. Dalgliesh, N. Mahmoudi, L. Pesce, C. Perego, G.M. Pavan, S. Yagai, Self-assembled poly-catenanes from supramolecular toroidal building blocks, Nature 583 (7816) (2020) 400–405.
[880] J.-P. Sauvage, J.-P. Collin, S. Durot, J. Frey, V. Heitz, A. Sour, C. Tock, From chemical topology to molecular machines, C. R. Chim. 13 (3) (2010) 315–328.
[881] S. Erbas-Cakmak, S.D.P. Fielden, U. Karaca, D.A. Leigh, C.T. McTernan, D.J. Tetlow, M.R. Wilson, Rotary and linear molecular motors driven by pulses of a chemical fuel, Science 358 (6361) (2017) 340–343.
[882] D.A. Leigh, J.K.Y. Wong, F. Dehez, F. Zerbetto, Unidirectional rotation in a mechanically interlocked molecular rotor, Nature 424 (6945) (2003) 174–179.
[883] N.H. Evans, P.D. Beer, Progress in the synthesis and exploitation of catenanes since the millennium, Chem. Soc. Rev. 43 (13) (2014) 4658–4683.
[884] S. Mena-Hernando, E.M. Pérez, Mechanically interlocked materials. Rotaxanes and catenanes beyond the small molecule, Chem. Soc. Rev. 48 (19) (2019) 5016–5032.
[885] L.F. Hart, J.E. Hertzog, P.M. Rauscher, B.W. Rawe, M.M. Tranquilli, S.J. Rowan, Material properties and applications of mechanically interlocked polymers, Nat. Rev. Mater. 6 (6) (2021) 508–530.
[886] A. Neophytou, D. Chakrabarti, F. Sciortino, Topological nature of the liquid–liquid phase transition in tetrahedral liquids, Nat. Phys. 18 (10) (2022) 1248–1253.

[887] A.S. Gladman, E.A. Matsumoto, R.G. Nuzzo, L. Mahadevan, J.A. Lewis, Biomimetic 4D printing, Nature Mater. 15 (4) (2016) 413–418.
[888] G.F. Schneider, C. Dekker, DNA sequencing with nanopores, Nat. Biotechnol. 30 (4) (2012) 326–328.
[889] A.W. Senior, R. Evans, J. Jumper, J. Kirkpatrick, L. Sifre, T. Green, C. Qin, A. Zidek, A.W.R. Nelson, A. Bridgland, H. Penedones, S. Petersen, K. Simonyan, S. Crossan, P. Kohli, D.T. Jones, D. Silver, K. Kavukcuoglu, D. Hassabis, Improved protein structure prediction using potentials from deep learning, Nature 577 (2020) 706–710.
[890] K. Hinsen, S. Hu, G.R. Kneller, A.J. Niemi, A comparison of reduced coordinate sets for describing protein structure, J. Chem. Phys. 139 (2013) 124115.
[891] R. Chowdhury, N. Bouatta, S. Biswas, C. Floristean, A. Kharkar, K. Roy, C. Rochereau, G. Ahdritz, J. Zhang, G.M. Church, P.K. Sorger, M. AlQuraishi, Single-sequence protein structure prediction using a language model and deep learning, Nature Biotechnol. 40 (2022) 1617–1623.
[892] N. Molkenthin, S. Hu, A.J. Niemi, Discrete nonlinear Schrödinger equation and polygonal solitons with applications to collapsed proteins, Phys. Rev. Lett. 106 (2011) 078102.
[893] J. Dai, A.J. Niemi, J. He, A. Sieradzan, N. Ilieva, Bloch spin waves and emergent structure in protein folding with HIV envelope glycoprotein as an example, Phys. Rev. E 93 (2016) 032409.
[894] N. Metropolis, A.W. Rosenbluth, M.N. Rosenbluth, A.H. Teller, Equation of state calculations by fast computing machines, J. Chem. Phys. 21 (1953) 1087–1092.
[895] H.M. Berman, J. Westbrook, Z. Feng, G. Gilliland, T. Bhat, H. Weissig, I.N. Shindyalov, P.E. Bourne, Protein data bank, Nucleic Acids Res. 28 (1) (2000) 235–242.
[896] I. Schlichting, J. Berendzen, G.N. Phillips, Jr., R.M. Sweet, Crystal structure of photolysed carbonmonoxy-myoglobin, Nature 371 (1994) 808–812.
[897] M. Lundgren, A. Krokhotin, A.J. Niemi, Topology and structural self-organization in folded proteins, Phys. Rev. E 88 (2013) 042709.